Politecnico di Milano
Department of Mathematics
Doctoral Programme in Mathematical Models and Methods in Engineering

---

Reduced-order models for patient-specific haemodynamics of coronary artery bypass grafts

Doctoral Dissertation of:
Francesco Ballarin

Supervisors:
Prof. Alfio Quarteroni
Dr. Roberto Scrofani

Co-advisors:
Dr. Elena Faggiano
Dr. Andrea Manzoni
Prof. Gianluigi Rozza

The Chair of the Doctoral Program:
Prof. Roberto Lucchetti

2015 – XXVII Cycle

Abstract

Coronary artery disease represents one of the leading causes of mortality worldwide. In fact, coronary arteries are the only source of blood supply to the heart, and the occlusion of one or more major coronary arteries may lead to angina pectoris, heart attack and heart failure. *Coronary artery bypass grafting* is a surgical procedure to create new paths around narrowed coronary arteries to restore sufficient blood flow to the heart.

Understanding fluid dynamics in biomedical configurations can be a valuable tool in the study of the human circulatory system and in the improvement of prosthetic devices such as coronary artery bypass grafts (CABGs). Clinical studies and experience suggest that bypass grafts tend to fail after some years due to the process of *restenosis*. *Computational fluid dynamics* can help to assess unfavorable flow conditions near the anastomosis of the CABG, which can be strictly related to the onset of restenosis.

A *computational framework* for the simulation of blood flows in three-dimensional *patient-specific* CABGs is proposed in this thesis. A close collaboration with clinicians at Ospedale Luigi Sacco (Divisions of Cardiac Surgery and Radiology) has been established to study clinically relevant patient-specific cases. This framework is based on the combination of:

1. *clinical data and medical imaging:* a computational mesh is reconstructed from computed tomography scans of a few selected patient-specific cases. The resulting mesh includes native coronary arteries and (multiple) bypass grafts. The current clinical trial investigates representative cases of different grafting procedures, grafting materials and native coronary artery disease.
2. *computational reduction techniques:* performing computational studies on patient-specific geometries is a very challenging task. Considerable computational costs are usually involved, especially when dealing with a parametric study. Reduced-order model techniques for parametrized PDEs, based in particular on proper orthogonal decomposition, allow to evaluate the haemodynamics for different flow conditions (such as Reynolds numbers) or different geometrical features (e.g. related to native coronary artery disease) in a rapid and reliable way.
3. *geometrical parametrization and reduction:* shape parametrization techniques are exploited in order to perform local changes to the reconstructed geometry in a flexible and reliable way. In fact, different choices of anastomoses are possible in the clinical practice. A local geometrical variation of patient-specific data, performed by means of a centerlines-based parametrization, is employed to perform a comparison among different cases.

Numerical results on patient-specific configurations are presented and a detailed clinical discussion is provided, enlightening relevant physical and geometrical features affecting blood flow dynamics in a wide range of bypass configurations.

Summary

Coronary artery bypass grafting (CABG) is a surgical procedure in which one or more grafts are used to create new paths to restore blood flow to the myocardium when severe *coronary artery disease (CAD)* occurs. In this case, one or several major coronary arteries are occluded; this condition undermines the perfusion of oxygen-rich blood to the heart. Due to this critical issue, although several alternative treatments exist, CABG is still one of the largest components of surgical practice worldwide. However, current clinical experience suggests that, after some years, the implanted vessel themselves tend to occlude, leading to the failure of the surgery and the need of reintervention.

Large clinical experience has been built on this subject since the early attempts on CABG in the 50s, concerning preliminary assessment of the disease, choices of the bypass grafts and anastomosis locations during the surgery, and survey of clinical outcomes after the surgery. As for the preliminary phase, it has been suggested to evaluate the necessity of the intervention taking into account the number of diseased arteries (single-, double- or triple-vessel) and the severity of the stenosis. In fact, double or triple-vessel (especially on the left coronary artery tree) involve a far more critical reduction of blood supply to the heart. Moreover, during the preparation of the surgery and during the surgery itself, the cardiac surgeon needs to choose among several possibilities, e.g. concerning grafting materials (arterial or venous grafts, or both, are usually considered), proximal anastomoses (i.e. what source of blood should provide the graft; common choices are free grafts in aorta or Y-grafts), distal anastomoses (e.g. local features of end-to-side anastomoses) and sequential procedures for complete revascularization (one graft may feature more than one side-to-side anastomosis and a distal end-to-side anastomosis in order to revascularize multiple coronary arteries). Some clinical studies have been carried out for each one of these choices; for example, it is nowadays agreed that, due to anatomical and physiological features, an internal mammary artery graft is particularly suitable to revascularize the left anterior descending branch (one of the two main branches of the left coronary tree), and that only critical stenoses should be bypassed.

Investigating global and local features of the blood flow, in particular near the anastomoses is of considerable clinical interest. In fact, some fluid dynamics indicators, such as wall shear stresses and oscillatory shear index, are strictly related to the development of intimal thickening and can be efficiently and accurately estimated by means of experimental methods and numerical simulations. However, experimental measures can be invasive and

some of these may not be routinely performed in the clinical practice. For this reason, in the last decades several computational fluid dynamics (CFD) studies of the cardiovascular system have been performed. In this thesis CFD methods are developed, focusing on complex geometries obtained from *clinical data*, with a special attention to *computational reduction techniques*, allowing for *individualized (patient-specific)* simulations.

The title of this thesis contains two keyphrases of the proposed computational framework for the study of CABGs: *reduced-order models* and *patient-specific*.

In the recent decades vast research interest has been devoted to *model order reduction techniques* for problems arising from partial differential equations in a broad variety of contexts. Reduced-order models (ROM) have been applied for example in heat conduction problems, acoustics, structural mechanics and fluid dynamics. In all these cases projection-based ROMs, such as reduced basis methods and proper orthogonal decomposition (POD), allow to obtain an accurate description of the physical behavior of the system at greatly reduced computational costs. POD-Galerkin methods are considered in this thesis.

A finite element (FE) discretization is employed in a construction stage (offline), to be performed once, possibly on high performance computing (HPC) facilities. Afterwards, few relevant basis functions are computed from a set of snapshots of the full-order model, and the PDE is projected on the reduced basis space, that is, on the space spanned by these basis functions. Therefore, the number of degrees of freedom of the evaluation stage (online) is drastically reduced, allowing for fast computations, which can be performed several times (e.g. for different physical properties of the system), possibly on a laptop. The main motivation behind the use of ROMs is that clinical interest lies not only in the simulation on a patient-specific configuration, but also in addressing the variation of the flow conditions and of the geometry for a detailed analysis of several scenarios, aiming at a possible improvement of the design of the surgical operation. The solution of a finite element simulation for *each* new physical or geometrical configuration is usually unaffordable, especially in the clinical context, and reduced-order models are employed to overcome this problem.

Moreover, a second important aspect is to be able to perform individualized and *patient-specific* studies. A collaboration with Ospedale Luigi Sacco (Divisions of Cardiac Surgery and Radiology) in Milan has been established in order to share their experience on the topic, clinical data (angiography and CT scan) of some representative cases, and feedback to analyze our computational results.

The proposed *reduced-order framework for CFD problems* on *patient-specific geometries of coronary artery bypass grafts* can be summarized in the following steps:

a) reconstruction of a mesh starting from *patient-specific clinical data*. The available clinical dataset is composed of 14 patients, who have undergone a coronary artery bypass surgery at Ospedale Luigi Sacco in Milan. They feature different characteristics concerning both the disease (different stenosed coronary arteries) and the surgical procedure (different grafting materials, anastomosis features, single or sequential grafts). The reconstruction has been carried out for fourteen patients, starting from CT scan data and implementing a *medical imaging pipeline* devised for this particular application.

b) formulation of a shape parametrization for the geometrical variation of the prosthetic devices. The capabilities of volume-based and line-based parametrizations in this context have been explored. This experience resulted in the proposal of a *centerlines-based parametrization*, which combines line-based parametrization for both local (e.g. stenosis) and global (e.g. rigid movement) variation of the coronary arteries and grafts, and a volume-based parametrization for local (e.g. angles) variations near the anastomoses.

c) *construction of a reduced-order model for the haemodynamics of patient-specific CABG configurations* that takes into account geometrical and possibly physical variations.
d) *evaluation of the reduced-order model*, for example in a sensitivity/scenarios analysis procedure.

The structure of the thesis is as follows. Chapter 1 provides an introduction to the clinical problem. The anatomy of the coronary arteries is recalled, with a focus on the four major branches where the arteriosclerotic process usually occurs. A brief review of possible causes of coronary artery disease is presented, together with a summary of clinical evidence that is usually considered when planning the surgery. A few aspects of coronary artery bypass grafting are also discussed, concerning graft choices (internal mammary artery, radial artery, saphenous vein), proximal anastomosis (free graft vs Y-graft), distal anastomosis (single vs sequential, flow vs T-shaped vs cross). Finally, possible alternative procedures are summarized.

Part I (Chapter 2) contains a review of the available clinical data and a thorough discussion of the proposed medical imaging pipeline. Angiographical data in a pre-surgical phase and CT scan data in post-surgical phase are acquired for each patient. A computational mesh is obtained for each patient by means of a medical imaging pipeline. Nine steps are required, starting from gray levels fields in the DICOM, preprocessing of the data, centerlines extraction, to three dimensional lumen surface and volume generation. Fourteen patients have been reconstructed using this pipeline. The current dataset features a broad variability of both disease (for example, different two- or three-vessels disease) and surgical intervention (for example, different combination of single or sequential grafts, Y-grafts or free grafts, radial artery or saphenous vein grafts). Alongside with the proposed medical imaging procedure, the detailed reconstruction of such clinical dataset is a main contribution of the present thesis. In fact, few studies on patient-specific numerical simulations have been published,but the present work features a larger and more complete (with respect to anastomosis features, grafting procedures, coronary artery disease) CABG dataset, and none of the previous contributions has been coupled to computational reduction techniques for parametric studies, which are the topic of the next Part.

Part II deals with the computational reduction framework.

A *POD-Galerkin reduced-order model* for steady incompressible Navier-Stokes equations is introduced in Chapter 3, which is rather technical. An enrichment procedure of the reduced spaces by means of supremizer solutions is employed in order to obtain an *inf-sup stable* reduced-order model. In fact, in contrast to other references in the literature of POD reduced-order models for incompressible flows, our aim is to provide a simultaneous online approximation of both velocity and pressure fields, and not only for the velocity. From the technical standpoint this is partially motivated by the choice of the transformation to the reference domain, which does not preserve the incompressibility constraint. Moreover, from the point of view of the CABG application, this is strongly motivated also by the possible interest to recover the pressure, because of clinical practice in the pre-operative phase to evaluate stenosis severity. The capabilities of the proposed ROM are shown by means of theoretical results and numerical examples. In particular, a theoretical result to detect the existence of online spurious pressure modes has been proved. Some numerical examples on CFD test cases are summarized in order to study the relation between the online inf-sup constant and the online dimension of the reduced spaces, characterizing in this way the minimum number of supremizer basis functions that are needed to obtain an inf-sup stable ROM. Such an analysis was not available yet in the reduced-order modeling literature, and constitutes a

contribution of the present thesis.

An extension to the *unsteady* case is provided in Chapter 4. When both parameter and time dependence are considered, a computational bottleneck may arise in the offline stage, requiring a compression of the temporal trajectory. To overcome this obstacle, a *two-level POD* technique is proposed, in which two nested PODs are exploited. The innermost provides a compression of the temporal trajectory, while the outermost accounts for the parametric dependence. It is shown that this procedure provides reduced spaces which closely resemble the ones in which the most expensive full POD (on both parametric and time trajectories) is computed. The application of such two-level POD to unsteady flows is another contribution of the current work.

Part III (Chapter 5) deals with possible shape parametrization techniques for patient-specific configurations of coronary artery bypass grafts. Volume-based parametrizations are first introduced, together with a screening procedure for the selection of the geometrical design parameters. The application of such screening procedures to shape parametrization maps is a novel contribution of this thesis. Advantages and drawbacks of this approach are discussed by means of a numerical example of flows in an idealized bypass configuration. Among the latter, we mention: need to impose additional constraints in order to ensure that no undesired variation of geometrical features (radii, in particular) happens during the deformation; no immediate physical interpretation of the design variables; a rapidly increasing number of design variables in complex geometries. For these reasons, a new idea of shape parametrization is combined to the volume-based approach, namely the *centerlines-based shape parametrization*. This technique is based on the assumption that coronary arteries and bypass grafts can be represented as a network of tubular geometries. In this framework, we manage to obtain an intuitive description of the whole network, accounting for few parameters related to the variation of relevant design variables, such as stenoses severity and anastomosis features. To the best of our knowledge, no similar parametrization, with an interface to patient-specific clinical data and coupling to reduced-order models, has been proposed in literature.

Part IV (Chapter 6) presents several results of the proposed framework on patient-specific CABG configurations. We examine variation of inlet flow rates (grafts and coronary arteries) among physical parameters; this is representative for example of different stress or rest conditions of the patient. Moreover, both disease-related (stenosis severity) and surgery-related (anastomosis features) geometrical parameters are considered.

As a first scenario, we show that inlet flow rates have a significant impact on the magnitude of wall shear stress (WSS) and the extension of the region of high oscillatory shear index (OSI). As a second scenario, we consider both variation of inlet flow rates and stenosis severity. The relation between stenosis severity and pressure drop or maximum WSS in the stenosis is explored, and local WSS patterns near the anastomosis are analyzed. As a third scenario, the variation of both stenosis and end-to-side anastomoses is considered. Different cases, namely mammary artery, saphenous vein and radial artery, are considered. Possible relations between anastomosis type and locations where intimal thickening may occur are discussed.

Finally, some conclusions and an outlook of possible future research conclude this thesis in Chapter 7.

Contents

CHAPTER 1

Introduction and motivation

Disease of the cardiovascular system currently represents the leading cause of mortality in our country. Recent data from the National Institute for Statistics (ISTAT), reported and analyzed in [198], show that, in fact, cardiovascular diseases accounts for approximately 45% of all deaths in Italy. Moreover, two out of three of the 250,000 annual deaths due to cardiovascular diseases are related to coronary artery disease. Among the patients with acute myocardial infarction, approximately 3 out of 10 men and 4 women out of 10 die within a month of onset of early symptoms, in many cases before being admitted to the hospital. Those who survive an heart attack become chronic sufferers, resulting in a lower quality of life. In Italy, according to data compiled by ISTAT, 4.4 per thousand of the population suffers from cardiovascular disability; 23.5% of Italian pharmaceutical expenses is related to drugs for the treatment of the cardiovascular system. Ischemic heart disease, ranging from angina pectoris, to heart attack and heart failure, is estimated to affect 5% of the population, with over 2,000,000 patients and 350,000 new cases a year. Therefore, a better knowledge of coronary artery disease and related clinical procedures could potentially have a strong impact on the quality of life of a relevant percentage of the Italian population.

In case of coronary artery disease, *coronary artery bypass grafting (CABG)* is a surgical procedure in which one or more blocked coronary arteries are bypassed by a blood vessel graft. New pathways are thus created in order to restore sufficient flow of oxygen-rich blood to the heart. Autologous grafts are commonly used, that is, vessels employed in the procedure are patient's own arteries or veins. The goals of the surgical procedure are to relieve symptoms of the coronary artery disease, to decrease the risk of heart attack and related heart problems, and to enable the patient to resume a normal lifestyle after the procedure. CABG surgery represents the largest component of surgical practice worldwide, with approximately three quarters of million cases performed annually worldwide [208]. We also refer to the comprehensive heart disease and stroke statistics review reported in [110], which contains the most up-to-date statistics on heart disease, stroke, and other vascular diseases.

The availability of imaging techniques, such as angiography and computed tomography scans, allows a more precise evaluation of the disease in the pre-surgical stage as well as of the surgery outcomes in the post-surgical stage. We refer to [198, 199, 246] for recent progresses and future challenges in CT-scan imaging of coronary arteries and CABGs. Moreover, once patient-specific data has been acquired and reconstructed, computational fluid dynamics methods can give a detailed description of the phenomena. We refer to [97] for an overview of mathematical methods applied to cardiovascular problems.

A detailed description of the coronary arteries, coronary artery disease and a clinical introduction to revascularization procedures can be found for instance in [74, 127, 144]; a basic introduction to these topics, adapted from the previously cited references, is reported in the next sections.

1.1 Coronary arteries

From an anatomical point of view, the coronary artery network is divided into two trees: left and right, both arising from the aorta. However, from the surgeon standpoint, four subdivisions are usually considered: the *left main coronary artery (LCA)*, the *left anterior descending coronary artery (LAD)* and its branches, the *left circumflex coronary artery (LCX)* and its branches, and the *right coronary artery (RCA)* and its branches.

To ensure a good perfusion of the whole heart, the major coronary arteries form a loop about the heart. In particular, a circle is formed by the right coronary and left circumflex arteries, as they travel across the atrioventricular sulci; the loop between the ventricles, instead, is formed by the left anterior descending coronary artery and the posterior descending coronary artery, as they circle the septum. The blood supply to the back of the left ventricle is guaranteed by a series of parallel arteries, called obtuse marginal coronary arteries, which are branches of the left circumflex artery. The blood supply to the anterior portion of the left ventricle comes from the left anterior descending artery and its branches. The left anterior descending artery is also the source of the blood supply of the ventricular septum (in the front), together with the posterior descending artery. Variability in the origin of the latter is referred to as *dominance*. A right dominant circulation is the one in which the posterior descending artery is a terminal branch of the right coronary artery; this is the most frequent case. However, a left dominant circulation occurs in approximately $10 \sim 15\%$ cases, where the posterior descending artery is a branch of the left circumflex artery.

Various reporting systems have been proposed in the past decades, in order to define a common nomenclature of the coronary arteries, possibly subdivided in more segments, and a precise denomination of their branches. We mention in particular [17, 236] and the recent proposals [165, 277]. An overview of the coronary artery system, together with the segment identification proposed in [277], is provided in Figure 1.1.

1.1.1 Left main coronary artery

The *left main coronary artery* originates from the ostium and travels to the left sinus of Valsava, where it bifurcates into the *left anterior descending artery* and the *left circumflex* branch. It is located between the pulmonary artery and the left atrial appendage; its bifurcation into two daughter branches occurs near the left atrioventricular groove. It is also possible that an additional vessel, other than left anterior descending and circumflex arteries, originates from the left main coronary artery; such additional branch is called *ramus intermedius*. As a rare variation (occurring in approximately 1% of patients) the left main coronary artery is not present, and the left anterior descending and left circumflex coronary

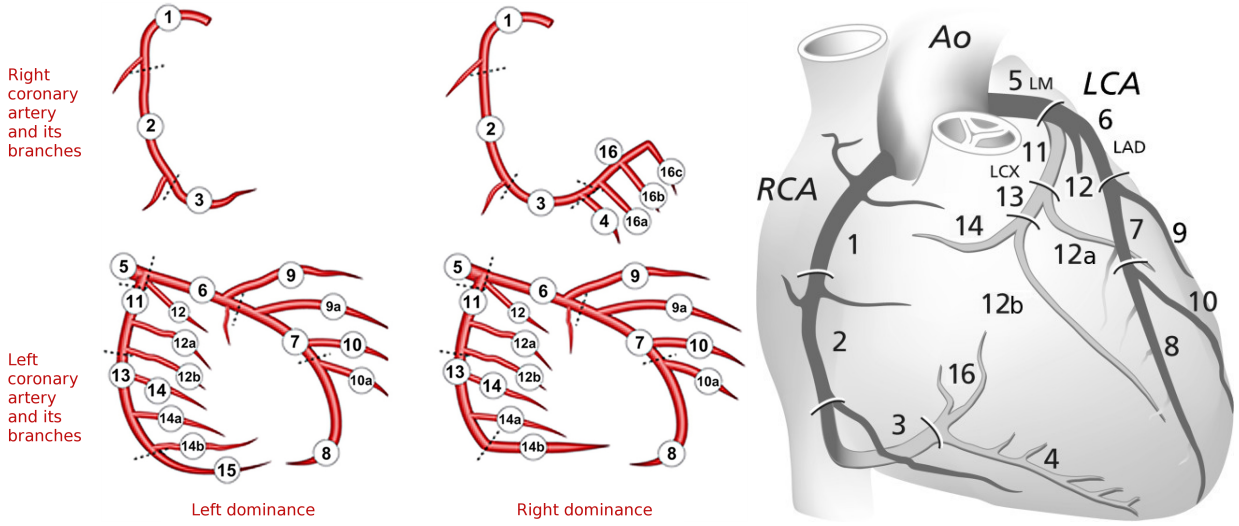

(a) *Differences between left and right dominance.*

(b) *Three-dimensional representation (right dominant).*

Figure 1.1: *Sixteen-segment-based coronary segment classification used in SYNTAX (Synergy Between PCI With Taxus and Cardiac Surgery) score. Adapted from [277] (figure (a)) and [120] (figure (b)).*

Nomenclature:
1: proximal right coronary artery;
2: mid right coronary artery;
3: distal right coronary artery;
4: posterior descending artery (right dominance only);
5: left main coronary artery;
6: proximal left anterior descending;
7: mid left anterior descending;
8: apical left anterior descending;
9, 9a: ramus intermedius, also called first diagonal branches of the left anterior descending;
10, 10a: (second) diagonal branches of the left anterior descending;
11: proximal circumflex artery;
12: intermediate/anterolateral artery;
12a, 12b: obtuse marginal;
13: distal circumflex artery;
14, 14a, 14b: left posterolateral;
15: left posterior descending (left dominance only);
16, 16a, 16b, 16c: posterolateral branch from right coronary artery (right dominance only).

arteries originate directly from the aorta.

1.1.2 Left anterior descending coronary artery

The *left anterior descending coronary artery*, which is a branch of the left main coronary artery, travels along the anterior interventricular sulcus to the apex of the heart. Its distal part may terminate before the apex or extend around the apex in the posterior interventricular sulcus, supplying blood to the apical portion of both right and left ventricles. It also supplies blood to the septum (via its *septal branches*) and to the left ventricular wall (via its *diagonal branches*).

1.1.3 Left circumflex coronary artery

The *left circumflex coronary artery* originates from the left main coronary artery at approximately a 90° angle. Its mid-distal part, also called atrial circumflex artery, courses around the left atrium near the atrioventricular groove, and supplies blood to the left atrium. Its branches, called *obtuse marginal arteries*, supply blood to the obtuse margin of the heart. Other bifurcations, named *left posterolateral* branches, occur downstream to obtuse marginal arteries; these branches provide blood to the inferior surface of the left ventricle. Only in hearts with left dominant circulation, the left circumflex artery gives rise to the *left posterior descending artery* before the crux.

1.1.4 Right coronary artery

The *right coronary artery* travels down the right atrioventricular groove. The first large branch is usually the *anterior right atrial artery*, which supplies the anterior right ventricular wall. This branch also gives origin to the sinus node artery. A second large branch of the right coronary artery arises in the region of the acute margin of the heart, which is called *acute marginal artery*, and courses to the apex of the heart. In right dominant systems, the right coronary bifurcates at the crux of the heart into the *right posterior descending coronary artery* and *right posterolateral coronary artery*. The posterior descending artery travels in the posterior interventricular sulcus; the posterolateral coronary artery, instead, supplies blood to inferior part of the left ventricle.

1.2 Coronary artery disease

Coronary artery disease (or, more precisely, stenotic arteriosclerotic coronary artery disease) is a narrowing of the coronary arteries due to atherosclerosis. Due to this condition, the blood flow to the myocardium is limited, and this may lead to ischemic heart disease. Initially, the disease affects the coronary artery circulation only in exercise conditions, decreasing the capability of the heart to increase coronary blood flow. However, when sufficiently advanced, the blood flow through the affected artery is reduced even at rest and, in its most severe form, the coronary artery may be occluded completely.

The arteriosclerotic process in the coronary arteries consists in the accumulation of lipids, carbohydrates and calcium deposits. The lipoid materials are converted into plaques of fibrous tissue; these plaques may become very thick and encroach upon the lumen of the artery. This produces a stenotic lesion. New layers slowly develop on the luminal side of the plaque, resulting in further narrowing and, possibly, complete coronary occlusion. Thrombosis may also complicate the coronary arteriosclerotic process, because of platelet aggregation within the lumen, possibly producing an acute myocardial infarction.

The arteriosclerotic process usually affects multiple coronary arteries (double- or triple-vessel disease) rather than a single vessel. The disease usually involves the proximal portion of the major coronary arteries, in particular at the sites of branching or just distally to them. Moreover, coronary artery stenoses in the main branches of the left anterior descending artery, circumflex and right coronary arteries often involve also their branches (that is, the diagonal branch for the LAD, the obtuse marginal for the LCX ad the posterior descending artery of the RCA). Disease in more distal branches is uncommon. The right coronary artery and the left anterior descending artery are more involved in the atherosclerotic process than the circumflex artery.

Myocardial necrosis occurs when myocardial blood flow is sufficiently impaired in comparison to myocardial oxygen demands. Infarctions may occur with different degrees of severity, ranging from subendocardial (where necrosis does not involve the entire thickness of the ventricular wall) to transmural (where necrosis extends to the entire thickness of the ventricular wall) infarctions. Without any medical intervention, an infarction affects the myocardial tissue, causing ventricular systolic and diastolic dysfunction, and possibly ventricular fibrillation, which together with additional factors (such as acute thrombosis, sudden increase of the severity of the stenotic lesion) may even lead to the death of the patient.

The patient with suspected coronary artery disease may undergo a coronary arteriography (angiography) study in order to assess the location and severity of the stenosis. The surgeon then evaluates the necessity of the intervention taking into account the number of diseased arteries (single, double or triple vessel) and the severity of the stenosis. When important narrowing (stenosis severity greater than 70%) is limited to one major coronary artery survival rates without surgery are high (5-year survival rate of order of 90%) [67,102,186]; however, a stenosis of the left anterior descending is more critical than the other main coronary arteries, and should be treated because it affects more deeply the correct functioning of the left ventricle. 5-year survival rates drop to $50 \sim 80\%$ when two or more coronary arteries feature critical stenoses, and again the case of a LAD stenosis is the most critical one [91,207]. Finally, especially for patient with higher life expectancy, it should also be taken into account when planning the surgery that non-critical stenoses may progress in time and eventually become critical.

1.3 Coronary artery bypass grafts

Preliminary strategies to perform myocardial revascularization were reported in 1935 by Beck [33], who used the left pectoral muscle as a graft, in 1951 by Vineberg [266], who implanted an internal thoracic artery directly into the myocardium, and in 1968 by Sen [234], who performed a transmyocardial acupuncture. Early applications of coronary artery bypass graft revascularization procedures appear in the 50s-60s, by Longmire [170] in 1958, Goetz [111] in 1961 and Kolessov [147] in 1964, employing the internal thoracic artery. Sabiston (1962) [226], Garrett (1964) [105] and Favaloro (1968) [92] performed the first revascularization surgeries using saphenous vein grafts instead. Surgery was not common in the clinical practice before this first pioneering studies. Relevant technical improvements, both related to the surgery itself (cardiopulmonary bypass, developed by Gibbon [108] in 1954, to take over the function of the heart during the surgery) and its preliminary planning (coronary arteriography, developed by Sones and Shirey [248] in 1962), contributed to a more widespread application of coronary artery bypass grafting in the clinical practice. First occurrences of sequential grafting procedures, in which a single graft is used to revascularize multiple coronary arteries, appear in the 70s (Flemma 1971 [96], Bartley 1972 [29] and Sewell 1974 [237]).

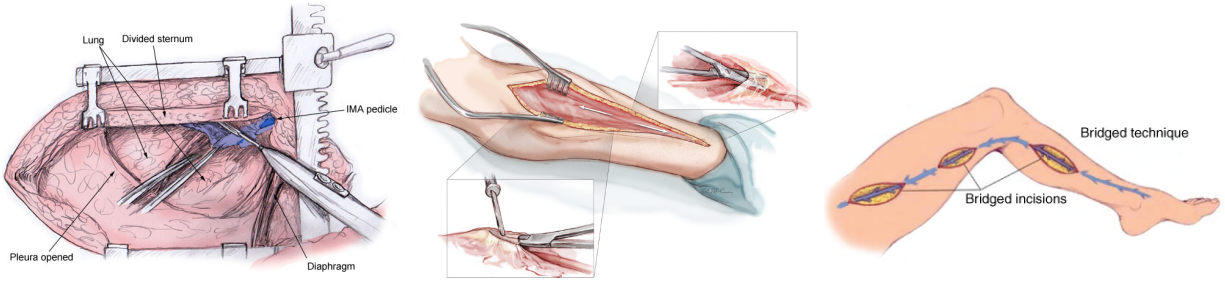

(a) *Harvesting of the internal thoracic artery. Adapted from [74].* **(b)** *Harvesting of the radial artery. Adapted from [41].* **(c)** *Harvesting of the saphenous vein. Adapted from [74].*

Figure 1.2: *Internal thoracic artery, radial artery and saphenous vein grafts harvesting.*

The strategy of the surgery aims at complete revascularization bypassing all significant stenoses, in all main coronary arterial trunks and branches. Different grafting materials may be used: internal thoracic artery (from the chest), radial artery (from the arm) and saphenous vein (from the leg), as summarized in the next sections (see also Figure 1.2). We refer to [124] for a comprehensive review and medical guideline on the topic.

1.3.1 Graft choice: internal thoracic artery

The *internal thoracic arteries (ITA)*, also known as internal mammary arteries, arise from the subclavian arteries (branches of the aorta), and can be harvested in order to be used as a bypass graft. The diameter of the ITA varies from approximately 2.5 mm at the origin from the subclavian artery to 1.5 mm just proximal to the anastomosis, [252], although remarkable variations are possible both because of graft adaptation and different harvest techniques (pedicle vs skeletonized graft). Several study have shown that the *left internal thoracic artery (LITA)* has proven to be the most effective blood vessel to be used as graft to the LAD, in terms of long-term patency and clinical outcomes [58, 76, 89, 113, 171, 235]. It is nowadays widely agreed in the clinical practice that LITA to LAD anastomosis should be performed whenever possible [208]. The internal thoracic artery shows remarkable resistance to the development of atherosclerosis, possibly because of some characteristics of its endothelium [162]. The superior patency of the LITA with respect to venous grafts has been shown in [27]. Moreover, the LITA is able to remodel over time, adapting to the demand for flow by varying its diameter, in the same way as native coronary arteries would do [117]. Superior patency and graft adaptation translate into higher survival rates when compared to other grafting materials, as shown in multiple trials: 1-year patency can be as high as 98% (compared to 87% of vein grafts) [274], 4-year patency 91% (versus 83%) [232] and 15-year patency 85% (versus 32%) [253].

1.3.2 Graft choice: radial artery

The *radial artery (RA)* originates from the brachial artery in the upper arm and courses to the wrist; it features an average length of approximately 20 cm and an average diameter of $2 \sim 3$ mm [241]. The use of the RA has been proposed for the first time in 1973 by Carpentier [63], although its extensive application in the clinical practice is more recent [1, 2, 128]. High patency rate has been reported for the RA: a 93% patency rate at 9 months has been found in [1], and 5-year patency ranges from 85 to 90% [128, 204]. However, RA should be employed only for critical stenosis, because the graft failure rate is higher when it is employed to revascularize a non critical stenosis; in fact the studies in [84, 188] shows

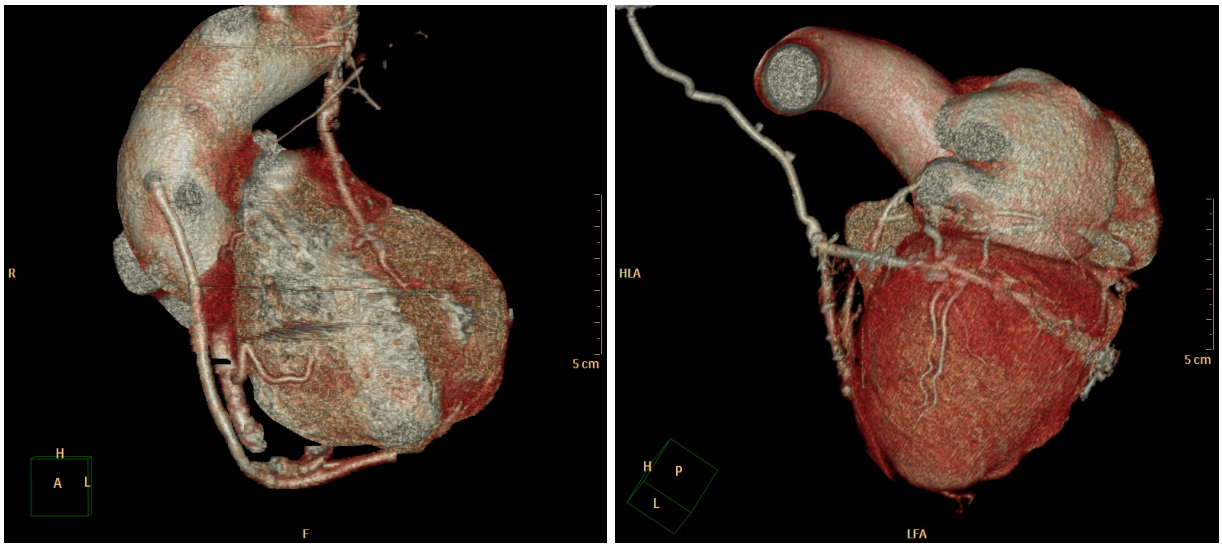

(a) *CT scan reconstruction of a free graft with proximal anastomosis to the ascending aorta.* **(b)** *CT scan reconstruction of a Y-graft.*

Figure 1.3: *Free graft versus Y-graft*

that radial artery patency increases when bypassing coronary arteries with 70%, or more, stenosis.

1.3.3 Graft choice: saphenous vein

The *greater saphenous vein (SV)* is a vein running along the entire length of the leg; segments of approximately 30 *cm* are needed for a bypass graft. Diameter is usually larger than 3 *mm* [71]. Although its use is still common, several studies suggest that arterial grafts feature better performance than SV grafts. In particular, intimal thickening occurs in SV grafts that have been in place for more than one month [25, 51, 267]; however, this process is not a progressive one, and seems to be related to graft modifications in order to match the vein lumen size to that of the coronary arteries supplied by the graft [245]. The highest rate of anastomotic closure occurs during the first few postoperative weeks [158]. 10% to 25% grafts occlude in the first year [72, 224], while additional 1% to 2% occlude each year from the first to the fifth year, and from 4% to 5% from the sixth to the tenth year [44], resulting in a 10-year patency between 45% and 60% [44, 59].

1.3.4 Proximal anastomosis: free graft or Y-graft

In contrast with the other mentioned bypass grafts, the proximal LITA is already in situ (attached to the subclavian artery) and only a distal anastomosis (to the diseased coronary artery) needs to be performed. Instead, for radial artery and saphenous vein grafts, also a proximal anastomosis is made. Common choices are a *free graft* with proximal anastomosis to the ascending aorta [3, 85] and *Y-graft* between the LITA and RA/SV (see Figures 1.3-1.5). The latter procedure involves performing an anastomosis between the LITA and RA/SV, so that the blood flow in the LITA is divided between the LITA itself and the RA/SV. This procedure was performed for the first time in the 80s by Mills [185] to avoid placing vein grafts in a atherosclerotic ascending aorta, and studied in more details in the following years [231, 255]. An advantage of this approach is that the proximal anastomosis of RA/SV grafts is closer to the heart (and, in particular, distal circumflex and right coronary artery

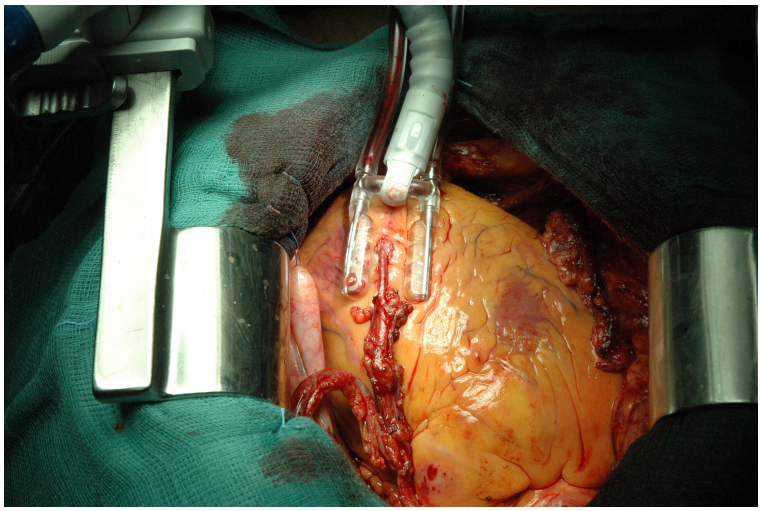

Figure 1.4: *Y-graft between left internal thoracic artery (employed to revascularize the left anterior descending artery) and left radial artery (employed to revascularize obtuse marginal branches of the left circumflex artery). Courtesy of Ospedale Luigi Sacco, Milan.*

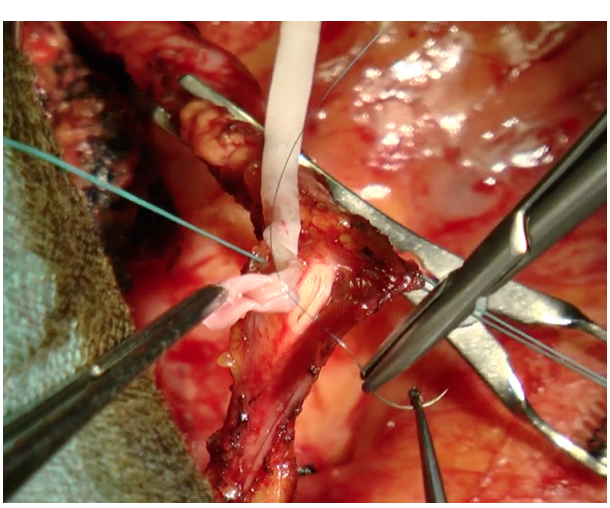

(a) *Step 1. The vein graft is anastomosed to the mammary artery. The photo shows the incision on the mammary artery and the application of the first stitch.*

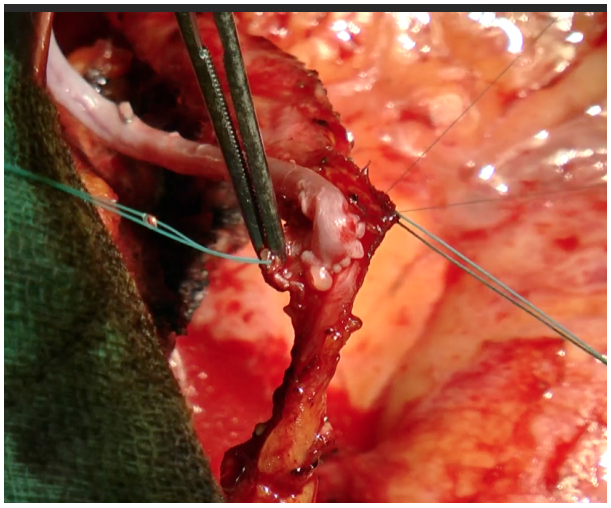

(b) *Step 2. The suture is continued and the anastomosis is completed.*

Figure 1.5: *Y-graft between left internal thoracic artery and saphenous vein. Details of two steps in the surgical procedure. Courtesy of Ospedale Luigi Sacco, Milan.*

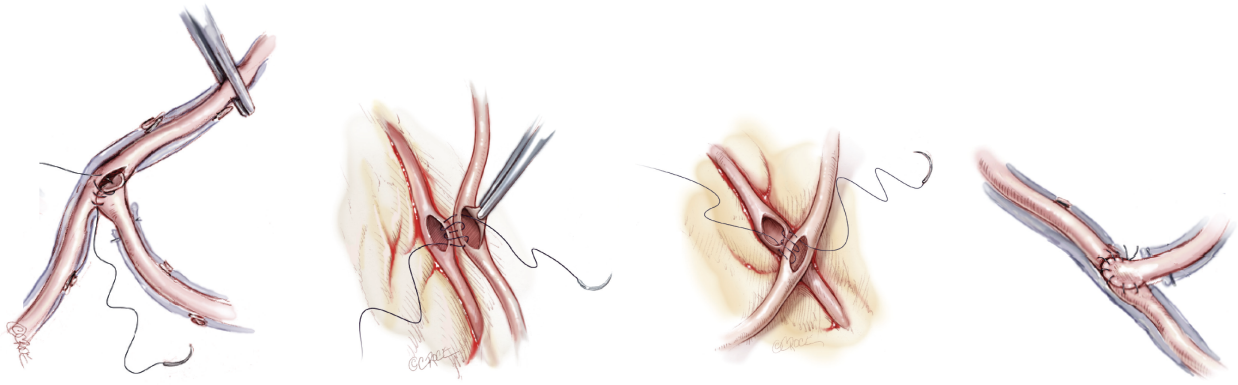

(a) *Y-graft.* **(b)** *Sequential grafting: flow-direction side-to-side anastomosis.* **(c)** *Sequential grafting: diamond-shaped cross anastomosis.* **(d)** *End-to-side anastomosis.*

Figure 1.6: *Y-graft, sequential anastomosis and end-to-side anastomosis. Adapted from [54].*

branches) than when performed to the aorta. This makes it possible to totally bypass patients with three-vessels disease more easily.

1.3.5 Distal anastomosis: single vs sequential, flow vs T-shaped vs cross

Some of the grafts may be used to bypass more than one coronary artery. In this case the procedure is called *sequential* coronary artery bypass grafting. Usually, in order to obtain a complete revascularization in case of two- or three-vessels disease, at least a graft is used in a sequential fashion. A sequential graft features some intermediate *latero-lateral* (side-to-side) anastomosis and a distal *termino-lateral* (end-to-side) anastomosis. The alternative procedure, in which a graft is employed to bypass only a single native artery, is called *single* grafting procedure.

Current clinical practice suggests that at least three possible termino-lateral (end-to-side) anastomoses are possible: *flow-direction* anastomoses (also called *antegrade*), which feature the same direction for graft flow and native vessel flow in the anastomosis, *T-shaped* (graft is perpendicular to the native vessel) and *retrograde* anastomoses (opposite directions for graft flow and native vessel flow in the anastomosis). The first two options are more common in the clinical practice than the last one.

Two possible latero-lateral (side-to-side) anastomosis are currently employed: *flow-direction* anastomoses and *diamond-shaped* (also known as *cross*) anastomoses (see Figure 1.6) In the flow-direction case, similar to the termino-lateral case which shares the same name, the flow in the graft (both proximal and distal to the anastomosis) features the same direction as the native vessel. In contrast, in the diamond case the graft is perpendicular to coronary artery (similar to a termino-lateral T-shaped anastomosis). This procedure was first introduced in [114]. Important technical differences occur between these two cases, e.g. concerning the orientation of the incision to be performed by the surgeon in the native coronary artery [136]. Current clinical practice and anatomical considerations suggest the use of flow anastomoses in the left anterior descending and diagonal branches (when aiming at a revascularization of the left anterior descending and its branches), while the cross anastomosis should be used for left circumflex and obtuse marginal arteries (when aiming at a revascularization of both the left circumflex and right coronary arterial trees).

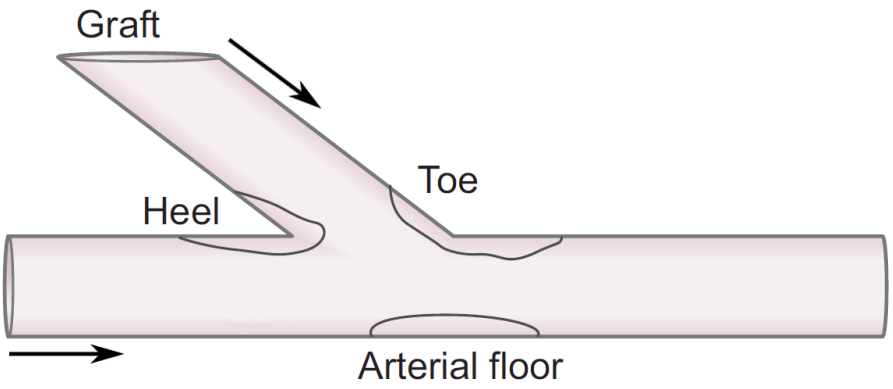

Figure 1.7: *Illustration of typical distributions of intimal thickening on an end-to-side anastomosis. Arrows denote flow direction. Adapted from [173].*

1.4 Possible alternative procedures

Several alternative treatments are possible for coronary artery disease. These include: medical therapy (prescription of drugs, such as aspirin, beta blockers and ranolazine), balloon angioplasty (non-surgical technique to widen narrowed arteries by means of the inflation of a balloon at the stenosis location), percutaneous coronary intervention (PCI) or percutaneous transluminal coronary angioplasty (PTCA) (non-surgical technique in which, after the balloon angioplasty, a stent may be placed within the coronary artery to keep the vessel open), rotablation (removal of the plaque without a surgical intervention, by means of a small drill, usually associated to PTCA), endarterectomy (surgical removal of plaque from stenosed coronary arteries, formerly associated with the first CABG interventions). Complete guidelines are reported for each of these treatments, depending on the severity, position and number of atherosclerotic vessels and clinical history of the patient. Joint studies of American College of Cardiology Foundation (ACCF) and American Heart Association (AHA) provided a series of guidelines for these procedures, in particular for both PCI [167] and CABG [124]. For high risk patients, such as the cases discussed in Section 1.2 (double- or triple-vessel disease), severe ventricular dysfunction and diabetes mellitus, CABG is the preferred treatment. We refer to [217], and the references therein, for a detailed comparison between different coronary artery disease treatments. We also remark that it is possible for these procedures to not be mutually exclusive, and that more than one of them could be needed during the patient's life depending on the evolution of the cardiovascular disease. For example, it was found in [217] that balloon angioplasty is associated with a greater need for subsequent CABG surgery.

1.5 Outline of the thesis

A deeper understanding of the fluid dynamics in CABGs can be a valuable tool in the study of such prosthetic devices, possibly contributing to a better explanation of the process of *restenosis*. *Computational fluid dynamics* can help in the assessment of unfavorable flow conditions near the anastomosis of the CABG, which can be strictly related to the onset of restenosis. Typical regions [173,249] where this process occurs are shown in Figure 1.7. Some fluid dynamics indicators, such as wall shear stresses (WSS) and oscillatory shear index (OSI), have been associated [173] to the development of intimal thickening and can be estimated by means of numerical simulations.

Several recent reviews [107, 181, 184, 196] recognize the importance of *patient-specific simulations* and *parametric studies*. On one hand it is important to perform simulations in realistic configurations, especially when dealing with a complex network of grafts (such as in sequential grafts, which, as it has been discussed in the previous section, are common in the clinical practice). On the other hand, clinical interest lies not only in the simulation on patient-specific configurations, but also in parametric studies obtained modifying the patient-specific data for different flow conditions and/or local geometrical features. For these reasons, a *reduced-order computational framework* for the simulation of the haemodynamics in three-dimensional *patient-specific* CABGs is proposed in this thesis. The first three Parts of this thesis will detail each component of this framework. The last Part will show numerical results on patient-specific CABG configurations. We summarize the main contents of each Part in the following (see also Figure 1.8). For convenience of the reader, a "focus" (either clinical or methodological, or both), is assigned to each Part.

Part I, *clinical data and medical imaging:*

Focus (and keywords): clinical (data acquisition, medical imaging pipeline, reconstructed patients).

A summary of the clinical data and of the medical imaging pipeline is provided in this Part.

Patient-specific data have been acquired for each patient; fourteen patients, who have undergone a coronary artery bypass surgery, have been enrolled in this study. The current dataset features a broad variability of both disease (for example, different two- or three-vessels disease) and surgical intervention (for example, different combination of single or sequential grafts, Y-grafts or free grafts, radial artery or saphenous vein grafts).

For each patient clinical collaborators at Ospedale Luigi Sacco in Milan acquire angiographical data in a pre-surgical phase (in order for the cardiac surgeon to understand number, location and severity of stenoses) and CT scan data in post-surgical phase (in order for the surgeon, and his collaborators at the radiology unit, to evaluate the outcomes of the coronary artery bypass graft surgery).

A clinical imaging pipeline will be introduced and discussed, and relies for the most part on CT scan data. This is motivated by the higher resolution of the data, availability of software for image processing and, nonetheless, the presence of bypass grafts (which are not included in the angiography, because it is performed in a pre-surgical stage in order to assess the disease). The reconstructions obtained for each patient will also be discussed, summarizing some details of the surgical intervention (single or sequential grafts, Y-grafts or free grafts, radial artery or saphenous vein grafts).

Part II, *computational reduction techniques:*

Focus (and keywords): methodological (reduced-order modeling (ROM), supremizer stabilization of POD-Galerkin ROMs, pressure recovery in ROMs for incompressible flows, compression of the temporal trajectory in ROMs for unsteady problems).

As we will discuss in this Part, numerical modeling has some advantages over in vivo or in vitro studies (higher resolution, minor invasivity). One of its main drawback, however, is the computational cost that is required for each simulation, especially in parametric studies. Performing a finite element simulation for *each* new physical or geometrical configuration is however usually unaffordable, and reduced-order models are employed to overcome this problem. Some additional motivation for both CFD and ROM computation are also discussed in the introduction to this Part.

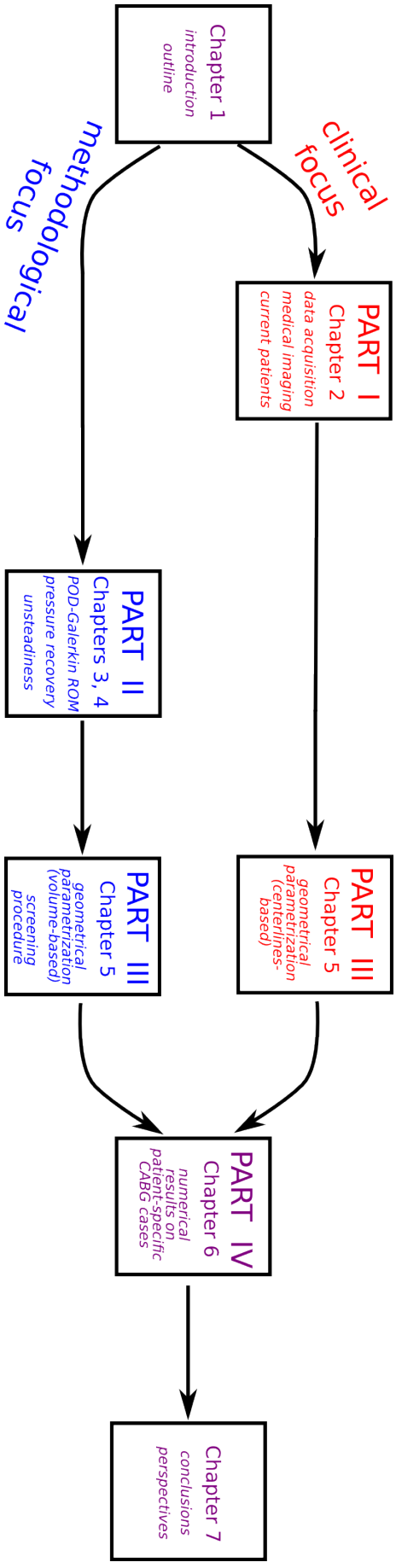

Figure 1.8: *Outline of the thesis.*

Model order reduction techniques are introduced in the this Part to cut down large computational costs. For the sake of a methodological study, these techniques will be presented on a general domain Ω, for general parameters $\boldsymbol{\mu}$, and applications to numerical test cases (instead of patient-specific geometries) will be provided. However, the same model order reduction techniques will be applied in Part III to idealized bypass configurations and in Part IV to patient-specific CABG configurations. A Proper Orthogonal Decomposition (POD)–Galerkin reduced-order model is studied in detail in this part, with focus on pressure recovery for incompressible flows, inf-sup stabilization of the resulting ROM, compression of the temporal trajectory for unsteady problems.

Part III, *geometrical parametrization and reduction:*

Focus (and keywords): methodological (volume-based parametrizations, screening procedures for design variables selection) and clinical (centerlines-based parametrization for deformation of a network of coronary arteries and bypass grafts)

Possible approaches for an efficient geometrical parametrization are discussed in this Part. Shape parametrization techniques will be employed in Part IV to perform local changes to the reconstructed geometry. A possible motivation for a parametric study has been mentioned for instance in Section 1.2, where it has been highlighted that the outcome of the surgery depends on the stenosis severity; it may be therefore of clinical interest to compare the haemodynamics for different values of stenosis. Also, different choices of anastomoses are possible in the clinical practice. We propose in this Part a shape parametrization, namely the *centerlines-based parametrization*, to deform patient-specific configurations to compare some of these choices. It is based on the assumption that coronary arteries and bypass grafts can be represented as a network of tubular geometries. The centerlines-based parametrization will provide an intuitive description of the whole network and of the desired features of clinical interest. In particular, local variation of the centerline radius accounts for stenosis severity, while local variation of the centerline reference frame (and in particular, the tangent vector) accounts for anastomosis features.

The resulting parametrization can be readily coupled to the POD-Galerkin ROM discussed in Part II, as we will show by tests on an idealized bypass configuration, considering both physical (Reynolds number, residual flow in the native artery) and geometrical (grafting angle) parameters.

Part IV, *numerical results:*

Focus (and keywords): clinical (numerical results of the proposed framework on patient-specific CABG configurations)

The proposed computational framework will finally be applied to patient-specific CABG configurations (described in Part II) in this Part. Once a patient-specific mesh has been generated, numerical simulations can be carried out and some fluid dynamics indices can be computed to better understand the clinical outcome of the surgery. We will assume pulsatile, Newtonian flow, under a rigid wall assumption. The POD-Galerkin reduced-order model introduced in Part II is employed, along with the centerlines-based parametrization (Part III). Parameters of interest in this case are a variation of inlet flow rates (grafts and coronary arteries), disease-related (stenosis severity) and surgery-related (anastomosis features) geometrical parameters.

Three cases, with increasing complexity, will be analyzed: variation of inlet flow rates only, variation of stenosis severity (and inlet flow rates), and variation of anastomosis

(and stenosis severity). In each case, results on a few patient-specific configurations will be discussed in detail, by means of fluid dynamic indices such as wall shear stress, oscillatory shear index, transversal velocity profiles, at the toe and heel of the graft, or a the arterial bed of the native coronary artery. These indices have been in fact related to critical regions of the surgical procedures, and their dependence on the considered physical and geometrical parameters will be discussed.

Finally, we will provide some conclusions and perspectives. We mention here some of the perspectives, in order for the reader to be aware of two fundamental assumptions of the present work (although common in the current literature). The first assumption is on non deformable walls. Future investigations shall be related to the extension to a *fluid-structure interaction* model, in order to take into account both myocardial motion and different rheological properties of the grafts, which are currently out of the scope of the available clinical data and proposed computational model. A second important assumption is related to the fact that only short term simulations are carried out. In fact, more complex phenomena, such as graft adaptation and flow competition, occur in the long term, but their detailed clinical understanding and mathematical modeling is not mature yet.

Part I

Medical imaging pipeline

CHAPTER 2

Clinical data and medical imaging

Available clinical data on patient-specific configurations of coronary artery bypass grafts, analyzed in collaboration with clinicians at Ospedale Luigi Sacco in Milan, are presented in this chapter, along with the description of the imaging procedures performed in order to obtain a mesh of the reconstructed patients. Section 2.1 details the current clinical data, covering also some technical details of the acquisition procedures. A presentation of the clinical imaging pipeline is given in Section 2.2. This procedure has been applied to fourteen patients in the current clinical dataset, and each one of them is presented in Section 2.3.

2.1 Clinical data

2.1.1 Pre-surgery angiography

A pre-surgery angiographic study is carried out by means of a coronary angiography. A Thosiba angiography system is employed. The study allows to visualize the morphology of the coronary arteries, and to detect the location and severity of stenoses. It is necessary for the patient to fast (avoid food and drinks) for several hours prior the angiographic study.

The examination is divided in three phases: in the first phase the medical team proceed the introduction of a catheter into the radial or femoral artery. This phase is performed under local anesthesia. The catheter is then moved to the coronary arteries. In the second phase of the medical examination a contrast agent is injected through the catheter. This allows to capture X-ray images of the distribution of the radioactive tracer in the coronary tree. The third, and final, step is the extraction of the catheter; compression around the area of introduction is also performed to allow the hemostasis of the radial or femoral artery.

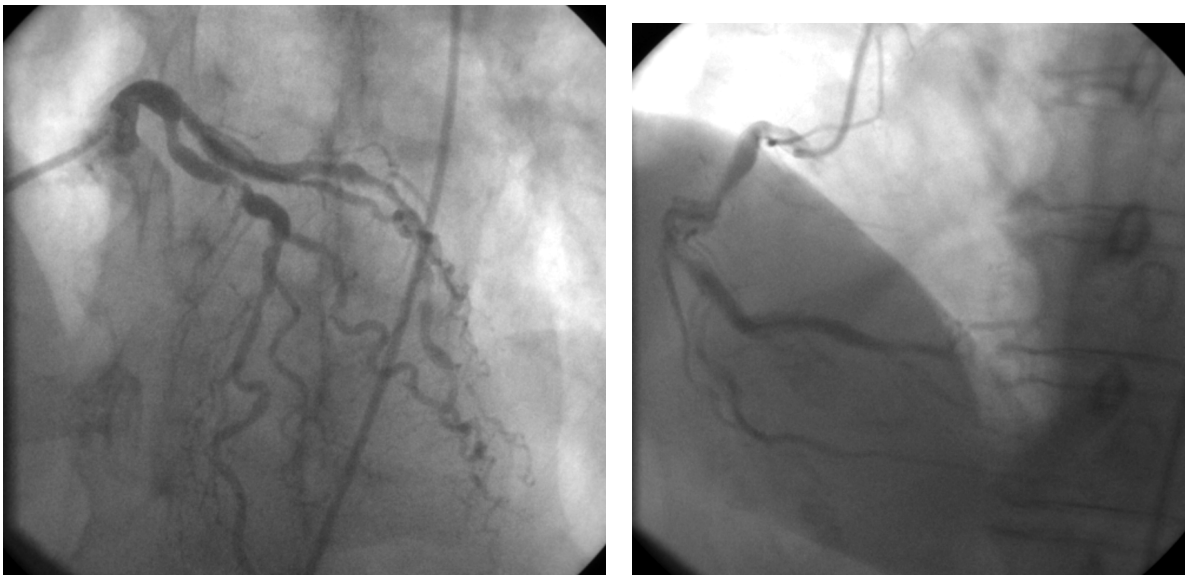

(a) *Left coronary tree.* **(b)** *Right coronary tree.*

Figure 2.1: *Pre-surgery angiography image. Courtesy of Ospedale Luigi Sacco, Milan.*

2.1.2 Post-surgery computed tomography scan

Computed tomography (CT) is an imaging technique that allows to perform a reconstruction of the anatomical structure evaluating the attenuation of a ionizing radiation (in particular, X-rays). Since each tissue features different capabilities to capture radiation, the attenuation level can be used to obtain a detailed representation of the anatomy. The resulting image contains the attenuation data expressed in HU (Hounsfield unit), which is usually rendered in a gray-scale for visualization purposes. The air assumes values around -1000 (black), the water and soft tissues around 0 (gray), and bones and solid structures around 1000 (white). To increase the contrast of vascular structures a contrast agent is usually injected in the patient: in the resulting image vascular structures are bright. A Philips Brilliance CT 64-slice system is employed to perform a post-surgery contrast enhanced CT-scan study. This system allows the acquisition of 64 submillimeter slices per rotation. An optimal image quality is obtained by combining an isotropic spatial resolution ($0.4\ mm^3$) and a rotation speed of about $0.33s$ [55]. Coronary artery bypass graft study is carried out by a volumetric retrospective gating scan of the chest; image acquisition is performed in the interval between 45% and $75 - 80\%$ of the cardiac cycle (systole and meso-telediastole). If the heart rate is less than $65bpm$, then native coronary arteries are studied by a step & shoot cardiac acquisition mode; otherwise a volumetric retrospective scan is carried out also for native coronary arteries.

Technical parameters of the CT system include: collimation: $64 \times 0.625\ mm$, maximum voltage: $120\ kVp$, maximum current intensity: $1000\ mAs$, rotation time: $0.4\ s$, pitch: 0.15, field of view: $250\ mm$, reconstruction matrix: 512×512, slice thickness: $0.67\ mm$, reconstruction thickness: $2.2\ mm$, Xres standard filter (XCB), acquisition time: $7\ s$. In particular, each slice in the final image will be a structured grid of size 512×512 (size of the reconstruction matrix); each cell in this grid is denoted by voxel. The resulting resolution is of the order of $0.3 \sim 0.4\ mm \times 0.3 \sim 0.4\ mm \times 0.3 \sim 0.4\ mm$.

The examination allows to assess the outcome of the coronary revascularization surgery. The contrast agent injection protocol involves the administration of approximately 95 ml of contrast agent (in particular, Iopamiro 370 mgI/ml) as follows:

1. 15 ml in the first dose of a bolus injection, at $3ml/s$;

2. $50 - 60$ ml in the second dose of a bolus injection, at $6ml/s$;

3. 20 ml in the third dose of a bolus injection, at $3ml/s$;

4. a fourth injection of 20 ml of physiologic solution, at $3ml/s$.

Also for the cardiac CT it is necessary for the patient to fast, at least starting from six hours before the exam. A short treatment with an oral beta-blocker, starting three days prior to the examination until the morning of the examination, is also required to optimize the patient's heart rate.

The tomographic examination starts with the preliminary acquisition of image (scout-view). The scout-view is necessary to define lower and upper bounds of the CT scan – defining the anatomical region of interest (ROI) – and to evaluate the inclination angle.

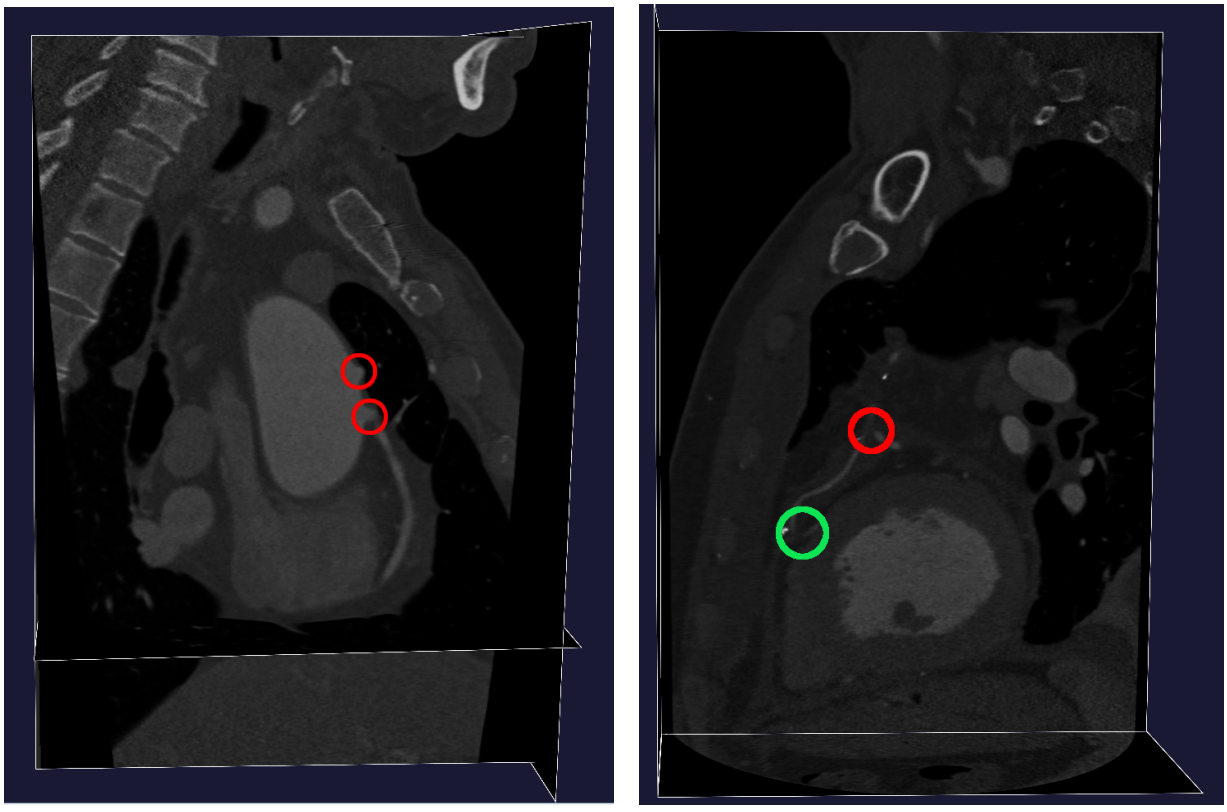

(a) *CT scan of a patient with two free grafts in aorta. Anastomosis locations are denoted by red circles. One of the two grafts is also clearly visible.*

(b) *CT scan of a patient featuring a surgery with LITA to LAD and Radial artery Y-graft on obtuse marginal branches. Red circle: Y-graft. Green circle: LITA to LAD anastomosis.*

Figure 2.2: *Post-surgery CT-scan slices. Courtesy of Ospedale Luigi Sacco, Milan.*

2.2 Medical imaging

In this section we detail the procedure to obtain a mesh starting from patient-specific CT-scan data. The Vascular Modelling Toolkit `vmtk` [11] and `3DSlicer` [93] are employed.

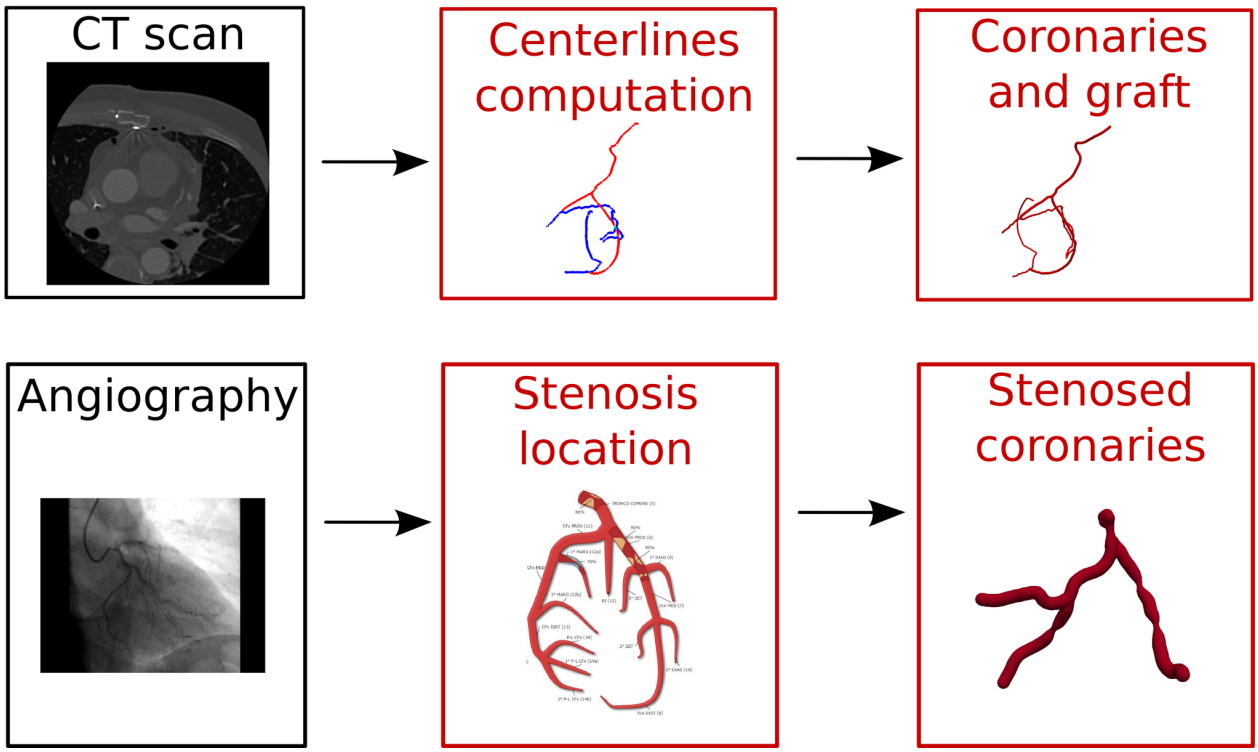

Figure 2.3: *Summary of the medical imaging pipeline*

2.2.1 Preprocessing steps

2.2.1.1 Step 1. DICOM image extraction

The Digital Imaging and Communications in Medicine (DICOM) format is a widely used format for handling and storing medical images, first developed by American College of Radiology and National Electrical Manufacturers Association in 1985. CT-scan data at different phases of the cardiac cycle are saved in DICOM image format. The following procedure could be applied to all stored phases, possibly providing a reconstruction of the coronary arteries and bypass grafts for each phase of the cardiac cycle; however, since the proposed procedure is not fully automated and highly time consuming we perform the extraction of the CT data only at a particular phase, at approximately 75% of the cardiac cycle, during which the heart is in the diastolic phase. This choice is motivated by the fact that in this phase coronary arteries (which lie on the myocardium and are therefore subject to the heart deformation) are, in general, less stretched and more perfused by blood than in the systolic phase. For practical convenience the CT-scan is saved in a different format, namely the MetaImage format. Moreover, it is also possible to extract a subvolume containing the region of interest (coronary arteries and bypass grafts) and discarding unnecessary data. This step is performed in `3DSlicer`. In the following we will denote by $\widehat{I} : C \subset \mathbb{R}^3 \to \mathbb{R}$ the scalar field of gray levels discretized by each image voxel.

2.2.1.2 Step 2. Anisotropic diffusion filter

The second preprocessing step concerns the application of gradient anisotropic diffusion to the image gray scale intensity function $\widehat{I}$. Anisotropic diffusion methods [200] are devised to reduce noise in images, still preserving specific image features (in particular edges of the

vessels). In general, diffusion methods are based on the following partial differential equation

$$\frac{\partial I}{\partial t} = \mathrm{div}(c(\boldsymbol{x},t)\nabla I) = c(\boldsymbol{x},t)\Delta I + \nabla c(\boldsymbol{x},t)\cdot\nabla I, \quad (\boldsymbol{x},t)\in B\times[0,T],$$

coupled with suitable boundary conditions and the initial condition $I|_{t=0} = \widehat{I}$. Isotropic diffusion methods employ a constant value for $c(\boldsymbol{x},t)$; however, with this choice, the image is blurred disregarding edges. A smoother image is obtained for large intervals $[0,T]$; for isotropic diffusion, the fictitious time t can also be interpreted as the variance of a Gaussian kernel $G(\boldsymbol{x},t)$, for which $I(\boldsymbol{x},t) = \widehat{I}(\boldsymbol{x}) * G(\boldsymbol{x},t)$.

Anisotropic diffusion filters, instead, are able to preserve the boundaries of the vessels by featuring high values of c inside (and outside) the vessels (say, $c\approx 1$), where smoothing should occur, and low values of c on the edges (say, $c\approx 0$). A possible function c, employed in [200], is

$$c(\boldsymbol{x},t) = \frac{1}{1+\left(\frac{\|\nabla I(\boldsymbol{x},t)\|}{k}\right)^2}. \tag{2.1}$$

This choice is based on the observation that large spatial variation of the gray scale intensity occur mostly at the edges, where the diffusion coefficient should be low. The parameter k can be tuned by the user.

The module `GradientAnisotropicDiffusion` of `3DSlicer` has been employed in practice to apply the filter. After the application of the diffusion filter a smoother image, featuring also sharper edges, is obtained as the final solution $I(\boldsymbol{x},T)$. For simplicity, the preprocessed image will be still denoted in the following by $\widehat{I}(\boldsymbol{x})$.

2.2.1.3 Step 3. Vessel enhancement filter

The purpose of this vessel enhancement filters is to enhance vessel structures with the eventual goal of vessel segmentation. A widely used filter has been introduced by A. Frangi in [99]. Most vessel enhancement filters are based on the analysis of the eigenvalues of the Hessian matrix of image intensity. In fact, the magnitude of eigenvalues is helpful to detect the the shape of the underlying object. In particular, locally isotropic structures feature three negative[1] eigenvalues, while tubular structures present only two negative eigenvalues and one null eigenvalue [99]. Denoting by λ_i the eigenvalues of the Hessian matrix, sorted such that $|\lambda_1|\le|\lambda_2|\le|\lambda_3|$, a *vesselness* function can be defined as[2]

$$\mathscr{V}_s(\lambda_1,\lambda_2,\lambda_3) = \begin{cases} \left(1-\exp\left(-\frac{R_a^2}{2\alpha^2}\right)\right)\exp\left(-\frac{R_b^2}{2\beta^2}\right)\left(1-\exp\left(-\frac{S^2}{2\gamma^2}\right)\right), & \text{if } \lambda_2<0 \text{ and } \lambda_3<0,\\ 0, & \text{otherwise,}\end{cases}$$

where

$$R_a(\lambda_1,\lambda_2,\lambda_3) = |\lambda_2|/|\lambda_3|, \quad R_b(\lambda_1,\lambda_2,\lambda_3) = |\lambda_1|/\sqrt{|\lambda_2\lambda_3|}, \quad S(\lambda_1,\lambda_2,\lambda_3) = \sqrt{\lambda_1^2+\lambda_2^2+\lambda_3^2}$$

and α, β and γ are user-defined parameters. In our case α and β were set equal to 0.5, while γ was assumed equal to 7.0.

Tubular structures are associated with high values of $\mathscr{V}_s(\lambda_1,\lambda_2,\lambda_3)$. In fact:

1. the ratio $R_b(\lambda_1,\lambda_2,\lambda_3)$ accounts for deviation from a bob-like structure. Indeed, $R_b(\lambda_1,\lambda_2,\lambda_3)$ attains its maximum for blob-like structures (where λ_1 is non-zero) and its minimum for tubular structures (where λ_1 is small).

[1] The negative sign is taken according to the fact that the background is dark, while vascular structures are bright.
[2] Positive values of λ_2 or λ_3 are discarded because correspond to the background.

2. the ratio $R_a(\lambda_1, \lambda_2, \lambda_3)$ accounts for the aspect ratio of the structure. Indeed, $R_a(\lambda_1, \lambda_2, \lambda_3)$ is approximately zero in the line-like case, while is approximately unity in the plane-like case.

3. the term $S(\lambda_1, \lambda_2, \lambda_3)$ distinguish between the background, in which all the eigenvalues are approximately zero because no structure is present (and therefore no variation induced), and the vascular structures, in which at least an eigenvalues is non-null.

The footer s in $\mathscr{V}_s(\lambda_1, \lambda_2, \lambda_3)$ indicates that vesselness is not computed on the image intensity function $\widehat{I}$, but rather on a smoothed version of it which takes into account spatial variation at the scale s. A Gaussian smoothing with variance s is for example suitable in this context. The eigenvalues $\lambda_i = \lambda_i(\boldsymbol{x}, s)$ of the Hessian of the smoothed intensity function are thus computed, for each point $\boldsymbol{x} \in B$, in practice. Finally, a multiscale vesselness measure can be defined computing the vesselness functions for each scale in the interval $[s_{\min}, s_{\max}]$ and setting

$$\mathscr{V}(\boldsymbol{x}) = \max_{s \in [s_{\min}, s_{\max}]} \mathscr{V}_s(\lambda_1(\boldsymbol{x}, s), \lambda_2(\boldsymbol{x}, s), \lambda_3(\boldsymbol{x}, s)).$$

In the coronary artery case we set $s_{\min} = 0.7\ mm$ and $s_{\max} = 3\ mm$, since it is representative of the radius range for coronary arteries and grafts. The implementation provided by `vmtk` in the script `vmtkimagevesselenhancement` has been used.

2.2.2 Segmentation

2.2.2.1 Step 4. Level sets segmentation

A *level sets* technique is employed during the segmentation. The idea behind this technique is that the surface of interest can be represented as the isosurface of level k of a scalar function. In particular, a surface evolving in time

$$S : \mathbb{R}^2 \times \mathbb{R} \to \mathbb{R}^3,$$

can be represented as an isosurface of level k of a time dependent scalar function

$$\Phi(\boldsymbol{x}, t) : \mathbb{R}^3 \times \mathbb{R} \to \mathbb{R}.$$

so that

$$S(t) := \left\{ \boldsymbol{x} \in \mathbb{R}^3 | \ \Phi(\boldsymbol{x}, t) = k \right\}. \tag{2.2}$$

is the k *level set* of $\Phi(\boldsymbol{x}, t)$. In particular we choose $k = 0$.

Following [9], the following evolution equation should be solved:

$$\begin{cases} \dfrac{\partial \Phi}{\partial t}(\boldsymbol{x}, t) = -w_1 G(\boldsymbol{x}) \left\| \nabla \Phi \right\| + 2 w_2 H(\boldsymbol{x}) \left\| \nabla \Phi \right\| + w_3 \nabla P(\boldsymbol{x}) \cdot \nabla \Phi, & (\boldsymbol{x}, t) \in B \times [0, T], \\ \Phi(\boldsymbol{x}, 0) = \Phi_0(\boldsymbol{x}), & \boldsymbol{x} \in B, \end{cases} \tag{2.3}$$

coupled with suitable boundary conditions and the initial condition defined employing the *signed distance function*

$$\Phi_0(\boldsymbol{x}) = \begin{cases} -D_0(\boldsymbol{x}) & \text{if } \boldsymbol{x} \text{ is inside } S(0), \\ +D_0(\boldsymbol{x}) & \text{if } \boldsymbol{x} \text{ is outside } S(0), \\ 0 & \text{if } \boldsymbol{x} \in S(0), \end{cases}$$

where $D_0(\boldsymbol{x}) = \min_{\boldsymbol{y} \in S(0)} \{ \| \boldsymbol{x} - \boldsymbol{y} \| \}$. In particular:

- w_1, w_2, w_3 are user-defined weights;
- the function $G(\boldsymbol{x})$ is defined as:

$$G(\boldsymbol{x}) = \frac{1}{1 + \left\|\nabla \widehat{I}(\boldsymbol{x})\right\|}.$$

  and is called *inflation speed*. The term $-w_1 G(\boldsymbol{x}) \|\nabla \Phi\|$ is an inflation term. The surface expands along $\|\nabla \Phi(\boldsymbol{x})\|$, which is the direction normal to the zero level of Φ, with velocity proportional to $G(\boldsymbol{x})$. The inflation speed is lower when image gradient is higher, so that it is approximately equal to one (maximum value) inside the vessel and negligible near the edges.

- the function $H(\boldsymbol{x})$ is defined as:

$$H(\boldsymbol{x}) = \nabla \cdot \left(\frac{\nabla \Phi}{\|\nabla \Phi\|} \right),$$

  and is equal to the curvature of the zero level set of $\Phi(\boldsymbol{x})$. The term $2w_2 H(\boldsymbol{x}) \|\nabla \Phi\|$ is a penalization term to guarantee the smoothness of the surface, penalizing high curvatures.

- the function $P(\boldsymbol{x})$ is defined as:

$$P(\boldsymbol{x}) = -\left\|\nabla \widehat{I}(\boldsymbol{x})\right\|$$

  and is called *attraction potential*. The term $w_3 \nabla P(\boldsymbol{x}) \cdot \nabla \Phi$ defines a convective term that drives the surface towards the edges.

The solution of this problem in `vmtk` is performed by the script `vmtklevelsetsegmentation`.

A critical aspect is the choice of the initial level set function Φ_0. A possible initialization is based on the *colliding front* method [11], where it is necessary to manually select two seeds $\boldsymbol{P}_i$, $i = 1, 2$, on the image at the far ends of the vessel of interest. The selection of the seeds *cannot* be fully automated for the coronary artery network, and accounts for the most critical part in which user-defined input and experience is required. The extraction of the portion of vessel between these seeds is then computed as propagation of two independent wave fronts, starting respectively from each seeds, with speed proportional to local image intensity. The Eikonal equation [11], which is a nonlinear hyperbolic equation, is employed for this purpose

$$\|\nabla T_i(\boldsymbol{x})\| = \frac{1}{1 + \widehat{I}(\boldsymbol{x})}, \quad T_i(\boldsymbol{P}_i) = 0$$

where T_1 and T_2 are arrival time for the two wave fronts, travelling with velocity $\widehat{I}(\boldsymbol{x})$ (i.e. faster where image is brighter, as is typically the case of the lumen), at each point of the domain.

The initial condition is defined as

$$\Phi_0(\boldsymbol{x}) := \nabla T_1 \cdot \nabla T_2.$$

This choice is motivated by the fact that the scalar product is negative if the two fronts are colliding (and positive if they move in the same direction), so that Φ_0 is negative in the region connected by the two initial seeds and positive otherwise. This allows to obtain an approximation of the desired segment of the vessel, also excluding other branches and the background.

Generally, segmentation is an iterative process; we usually started from the main trunk of the left coronary artery, proximal right coronary artery, and mammary artery at its origin from the subclavian artery, and afterwards incrementally added the remaining branches of the left and right coronary trees and possibly additional bypass grafts.

2.2.3 Intermediate surface generation

2.2.3.1 Step 5. Marching cubes surface generation

Once the level set segmentation step is completed, a marching cubes algorithm [172] is employed to generate a polygonal surface, as implemented in the script `vmtkmarchingcubes`. However, the generated surface should be post-processed before being used to generate a three-dimensional mesh of the coronary arteries. In fact, the generated surface may contain artefacts either arising from CT scan data or our reconstruction procedure. Overall, the surface may contain incorrect blob-like structures (that would alter the values computed for important fluid dynamics quantities, such as wall shear stress) or an incorrect reconstruction of the stenoses (possibly due the precision of CT-scan data or due to the filters applied in the preprocessing steps). For these reasons we adopt a simplifying assumption and take advantage of the fact that both coronary arteries and bypass grafts are vessels of a network of tubular structures, and use the reconstructed geometry to extract the axes (centerlines) of these tubular structures.

2.2.4 Centerlines generation

2.2.4.1 Step 6. Centerlines generation

Centerlines computation is a fundamental step in our framework and, as shown in Chapter 5, it will be the basic concept in the description of shape deformation maps tailored specifically for this clinical application. The last part of the medical imaging pipeline details how to construct the network of tubular structures, or more in general $2\frac{1}{2}$D geometries; we refer to $2\frac{1}{2}$D as to volumes which can be obtained by sweeping a bidimensional section (possibly, of variable shape) along a monodimensional path (the centerline). Although being a simplification (in particular, the full Voronoi diagram may be considered instead of the centerlines), we believe nonetheless that the main features of the problem are still captured. This assumption is fundamental in our parametrized framework, is the main motivation for the shape parametrization proposed in Chapter 5. We refer however to [95] for additional studies, still carried out in the framework of the collaboration with Ospedale Sacco, in which this assumption has been weakened.

We refer to centerline as the curve drawn from the two outermost sections of a tubular structure which locally maximizes the distance from the vessel boundary. Concepts related to centerlines are the medial axis and the Voronoi diagram [9–11]. The medial axis $MA(\Omega)$ of an object Ω is defined as the locus of centers of maximal spheres into Ω. A sphere is maximal if it is not strictly contained in any other inscribed sphere. Denoting by $\mathcal{P}$ a scattered dataset of points on $\partial\Omega$, an approximation of $MA(\Omega)$ is the computation of the Voronoi diagram $\mathrm{Vor}(\mathcal{P})$ of $\mathcal{P}$, defined as

$$\mathrm{Vor}(\mathcal{P}) = \bigcup_{\boldsymbol{x}\in\mathcal{P}} \mathrm{V}(\boldsymbol{x}),$$

where the Voronoi region $\mathrm{V}(\boldsymbol{x})$,

$$\mathrm{V}(\boldsymbol{x}) = \{\boldsymbol{y} \in \mathbb{R}^3 : \|\boldsymbol{x}-\boldsymbol{y}\| \leq \min_{\boldsymbol{z}\in\mathcal{P}} \|\boldsymbol{z}-\boldsymbol{y}\|\},$$

is the region of the euclidean space closer to $\boldsymbol{x}$ than to any other point $\boldsymbol{z}$ in $\mathcal{P}$. We refer to [9–11] for more details on the topic and their practical computation.

Once the medial axis has been computed, the centerline is sought as the path on the Voronoi diagram between a source point A and a target point B which maximizes the distance

from the boundary or, equivalently, the solution of the following optimization problem

$$\min_{\gamma \in \Gamma_{(A,B)}(MA(\Omega))} \int_{\gamma^{-1}(A)}^{\gamma^{-1}(B)} F(\gamma(t))\, \mathrm{d}t$$

where $\Gamma_{(A,B)}(MA(\Omega))$ is the set of all paths from A to B on $MA(\Omega)$, and the cost functional $F(\boldsymbol{x}) = 1/R(\boldsymbol{x})$ is the inverse of maximal inscribed sphere radius. As in step 4, the practical computation of the centerline requires the solution of a Eikonal equation

$$\|\nabla T(\boldsymbol{x})\| = F(\boldsymbol{x}), \quad \boldsymbol{x} \in MA(\Omega).$$

The Eikonal equation on the Voronoi diagram is solved by the script `vmtkcenterlines`.

Finally, the value of the maximal inscribed sphere radius is associated to each centerline point. A smoothing procedure (both on the curve coordinates and on the radius) may also be performed; in particular, we have performed a running average smoothing on the coordinates and a linearization (with respect to the curvilinear abscissa) on the radius of the vessels (stenosis are added back in step 9). A reference coordinate frame (tangent, normal and binormal vector) for each point on the centerlines may also be computed; more details on this will be given in Chapter 5. A complete monodimensional description (with additional radius information) can be computed in this way, for each branch of the network.

2.2.5 Canal surface generation

2.2.5.1 Step 7. Canal surface generation and volume meshing

The $2\frac{1}{2}$D geometry of the coronary artery and bypass grafts network can then be obtained sweeping a circular section of variable radius (stored in the centerline itself) along each centerline. The resulting surface, which is envelope of maximal inscribed spheres along the centerlines, produces a canal surface, or tube. The resulting surface can be described as a generalized cylinder as follows,

$$\boldsymbol{C}(\rho, \theta, s) = \boldsymbol{\gamma}(s) + \rho r(s) \left[\cos\theta\, \boldsymbol{n}_1(s) + \sin\theta\, \boldsymbol{n}_2(s)\right]$$

being $\boldsymbol{\gamma}(s)$ the centerline, (ρ, θ, s) "cylindrical" coordinates of the vessel (local radius, angle, curvilinear abscissa, respectively) and $(\boldsymbol{t}(s(\boldsymbol{x}), \boldsymbol{n}_1(s(\boldsymbol{x}), \boldsymbol{n}_2(s(\boldsymbol{x}))$ a reference coordinate frame on the centerline. Once the surface has been obtained, its interior is filled with volumetric elements in order to obtain a volume mesh. Tetrahedral mesh generation is performed in `vmtk`, using the script `vmtkmeshgenerator`, which internally uses TetGen for the tetrahedralization. In particular, a radius adaptive mesh is generated, in order to properly take into account the variation of the radius along each centerline.

2.2.5.2 Step 8. Canal surface splitting

It is necessary, as a last step in the generation of the canal surface network, to partition the generated mesh among each branch, taking advantage of the underlying monodimensional structure. Each point $\boldsymbol{x}$ in the mesh is projected on every centerline i, and the distance $d_i(\boldsymbol{x})$ between the point $\boldsymbol{x}$ and the centerline i is computed. If $d_i(\boldsymbol{x})$ is less than the local radius $r_i(\boldsymbol{x})$ (possibly scaled by a multiplicative factor) for only one index i, then $\boldsymbol{x}$ is a point in the i-th vessel; if multiple indices $i_1, i_2, \ldots, i_N$ have been found, than $\boldsymbol{x}$ is in the intersection (e.g. bifurcation or anastomosis) between those vessels. Figures in the next section show the partitioned domains, where different colors denotes different branches. Gray color is associated to bifurcation/anastomosis.

2.2.5.3 Step 9. Stenosis insertion

Finally, a manual editing of the mesh should be performed in order to insert the stenosis; this can be performed at step 7 considering a local variation of the radius stored in $r(s)$ for curvilinear abscissa in the neighborhood of $s = \mu$, for example by the relation

$$r(s)\sqrt{1 - \alpha \exp\left(-\frac{(s-\mu)^2}{\sigma^2}\right)}$$

in order to represent a stenosis at the point located at curvilinear abscissa μ, where the factor α is the surface reduction and the standard deviation σ controls the "extension" of the stenotic region. In view of the parametrization introduced in Chapter 5, however, we prefer to generate meshes without stenoses. The shape parametrization will then handle the insertion of the stenosis, performing the required local variation of the radius. When available, the location and entity of the stenoses may also be taken from the medical report of the angiography.

2.3 Reconstructed CABG patients

The medical imaging pipeline described in the previous section has been applied to fourteen patients, who have undergone coronary artery bypass surgery at Ospedale Luigi Sacco in Milan. The following color legend is employed in the presentation of the fourteen cases. We refer to Section 1.1 for a clinical explanation and location of the native coronary arteries, and to Sections 1.3.1-1.3.3 for a clinical comparison of the different grafts.

Figure 2.4: *Color legend for patient-specific cases. Each branch is denoted by a different color. The right coronary tree is denoted by blue colors; the left coronary tree by red/yellow colors; grafts are colored with green tonalities.*
Acronyms – right coronary tree:
RCA: right coronary artery;
PDA: posterior descending artery;
PL: postero-lateral artery;
Acronyms – left coronary tree:
LCA: main trunk of the left coronary artery;
LAD: left anterior descending artery;
Diag.: diagonal branch of the left anterior descending artery;
LCX: left circumflex artery;
OM: obtuse marginal artery;
Acronyms – grafts:
Mamm. (LITA): left mammary artery (left internal thoracic artery) bypass graft;
Rad.: radial artery bypass graft;
Saph. (SVG): saphenous vein bypass graft.

In particular:

0. one patient with no relevant coronary artery disease (and, therefore, no grafts) is included in the study;

1. one patient with a single bypass is available;

2. four patients with double bypass surgery are being studied. They feature different surgery and different disease;

3. three patients with triple bypass surgery are being studied. They feature different surgical procedures and different disease;

4. four patients with quadruple bypass surgery are being studied.

5. one patient with a quintuple bypass is available in the current study.

Table 2.1 gives an overview of the CABG surgery, reporting the graft type (LITA, Radial, SVG), either single or sequential. More details, concerning also the bypassed native coronary arteries and the anastomoses features, are also provided in Tables 2.2-2.14, for each patient. An explanation of the headers single/sequential, Y-graft/aorta, T-shaped/flow/cross has been discussed in Sections 1.3.4-1.3.5.

Patient	**LITA**		**Radial**		**SVG**	
	single	*sequential*	*single*	*sequential*	*single*	*sequential*
1	×			×		
2	×		×		×	
3		×	×			
4		×				
6	×				×	
7	×					×
8						
9		×	×			
10		×				×
11		×			×	
12	×				×	
13		×				×
14	×			×		
15	×					

Table 2.1: *Overview of the CABG surgery performed for each patient.*

Patient 1

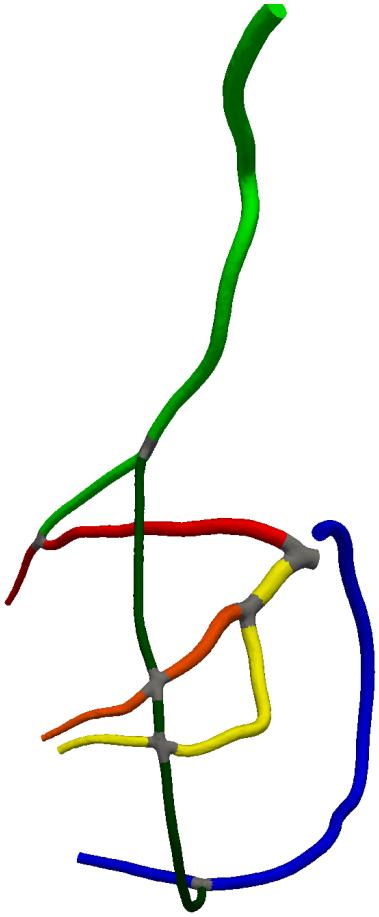

(a) *Three-dimensional reconstruction (coronary arteries, bypass grafts) obtained employing the medical imaging pipeline detailed in Section 2.2.*

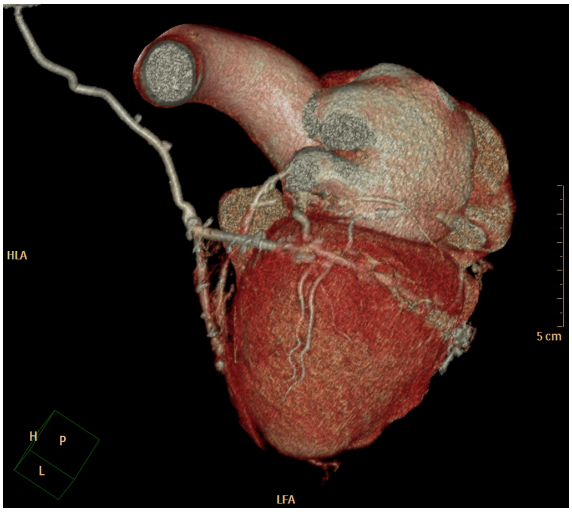

(b) *Reference three-dimensional reconstruction (coronary arteries, bypass grafts, aorta, heart) provided by the radiology department.*

Figure 2.5: ***Patient 1****: three-dimensional reconstruction.*

Patient 1 reconstruction features:

- *Coronary arteries:* LCA, LAD, LCX-OM; RCA, PDA.
- *Bypass grafts:* LITA-Diag-LAD; Radial Y-graft on LITA-OM-LCX-PDA.

	LITA	**Radial**		**SVG**		**Anastomosis**		
		Y-graft	*Aorta*	*Y-graft*	*Aorta*	*T-shaped*	*flow*	*cross*
LAD	×						×	
Diag.								
LCX		×						×
OM		×						×
PDA		×				×		
PL								

Table 2.2: ***Patient 1****: detailed report of the CABG surgery.*

Patient 2

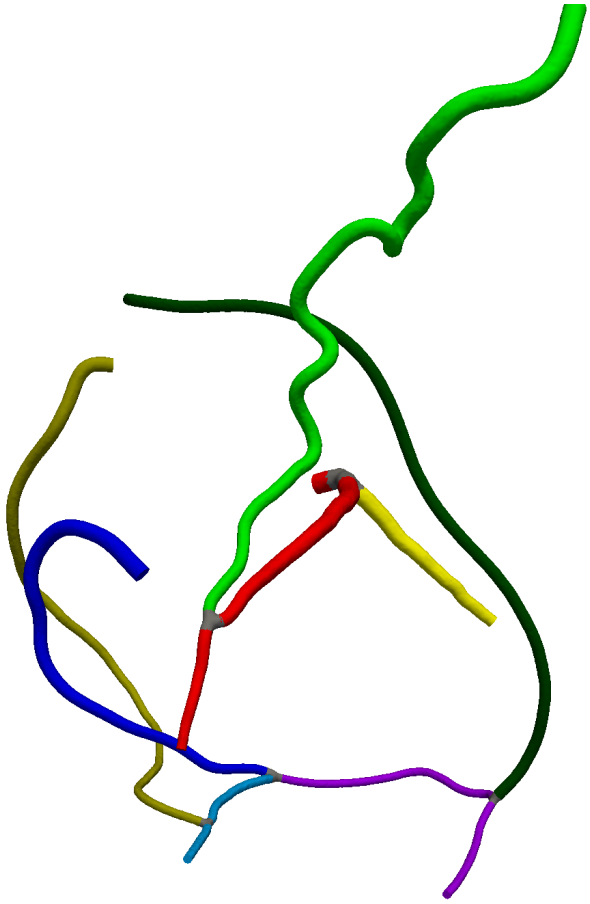

(a) *Three-dimensional reconstruction (coronary arteries, bypass grafts) obtained employing the medical imaging pipeline detailed in Section 2.2.*

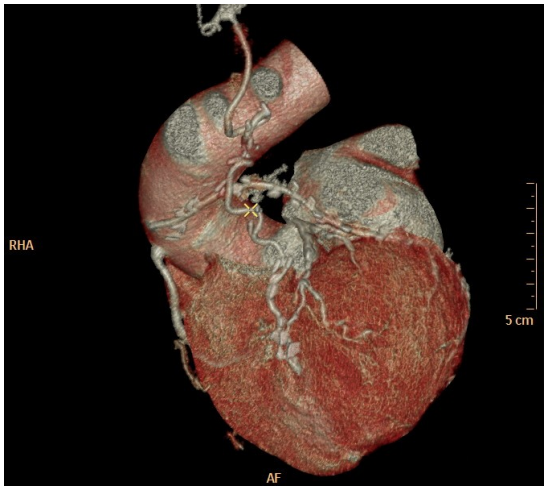

(b) *Reference three-dimensional reconstruction (coronary arteries, bypass grafts, aorta, heart) provided by the radiology department.*

Figure 2.6: ***Patient 2****: three-dimensional reconstruction.*

Patient 2 reconstruction features:

- *Coronary arteries:* LCA, LAD, LCX; RCA, PDA, PL.
- *Bypass grafts:* LITA to LAD; Aorta-SVG-PDA; Aorta-Radial-PL.

	LITA	**Radial**		**SVG**		**Anastomosis**		
		Y-graft	*Aorta*	*Y-graft*	*Aorta*	*T-shaped*	*flow*	*cross*
LAD	×						×	
Diag.								
LCX								
OM								
PDA					×	×		
PL			×			×		

Table 2.3: ***Patient 2****: detailed report of the CABG surgery.*

Patient 3

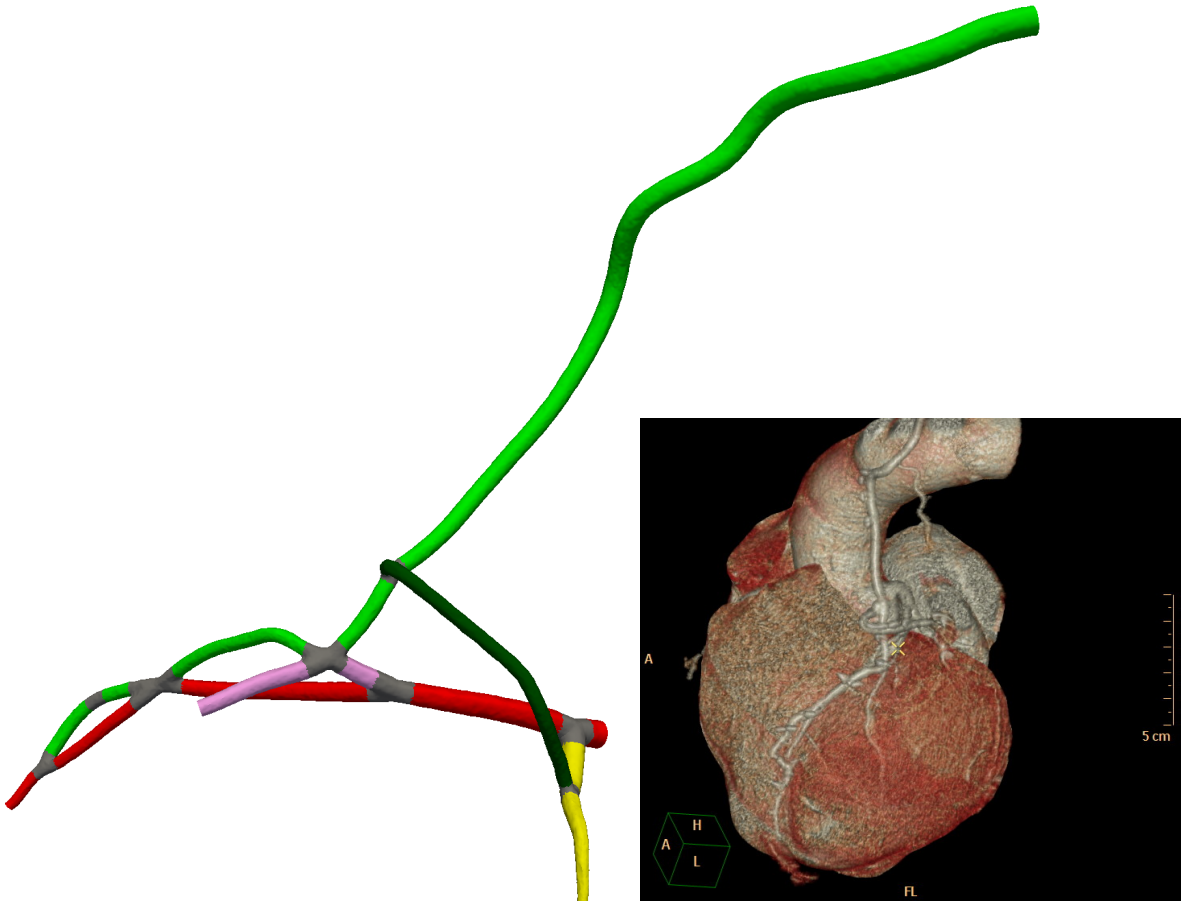

(a) *Three-dimensional reconstruction (coronary arteries, bypass grafts) obtained employing the medical imaging pipeline detailed in Section 2.2.*

(b) *Reference three-dimensional reconstruction (coronary arteries, bypass grafts, aorta, heart) provided by the radiology department.*

Figure 2.7: ***Patient 3****: three-dimensional reconstruction.*

Patient 3 reconstruction features:

- *Coronary arteries:* LCA, LAD-Diag, LCX.
- *Bypass grafts:* LITA-Diag-LAD-LAD; Radial Y-graft on LITA-LCX.

	LITA	**Radial**		**SVG**		**Anastomosis**		
		Y-graft	*Aorta*	*Y-graft*	*Aorta*	*T-shaped*	*flow*	*cross*
LAD	× ×						× ×	
Diag.	×						×	
LCX		×					×	
OM								
PDA								
PL								

Table 2.4: ***Patient 3****: detailed report of the CABG surgery.*

Patient 4

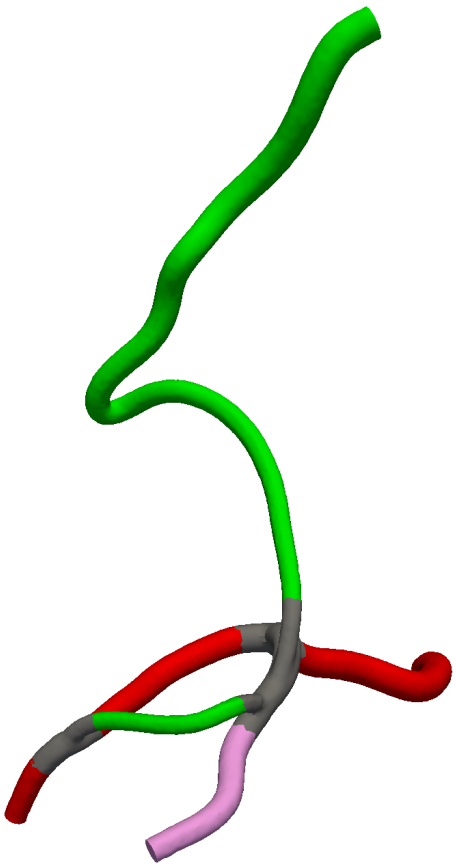

(a) *Three-dimensional reconstruction (coronary arteries, bypass grafts) obtained employing the medical imaging pipeline detailed in Section 2.2.*

(b) *Reference three-dimensional reconstruction (coronary arteries, bypass grafts, aorta, heart) provided by the radiology department.*

Figure 2.8: ***Patient 4****: three-dimensional reconstruction.*

Patient 4 reconstruction features:

- *Coronary arteries:* LCA, LAD-Diag.
- *Bypass grafts:* LITA-Diag-LAD.

	LITA	**Radial**		**SVG**		**Anastomosis**		
		Y-graft	*Aorta*	*Y-graft*	*Aorta*	*T-shaped*	*flow*	*cross*
LAD	×						×	
Diag.	×						×	
LCX								
OM								
PDA								
PL								

Table 2.5: ***Patient 4****: detailed report of the CABG surgery.*

Patient 6

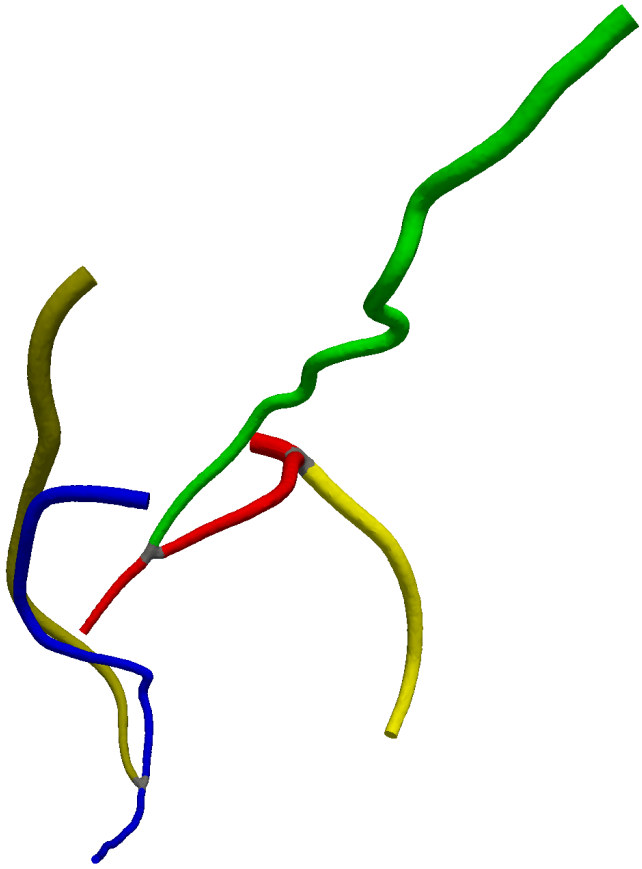

(a) *Three-dimensional reconstruction (coronary arteries, bypass grafts) obtained employing the medical imaging pipeline detailed in Section 2.2.*

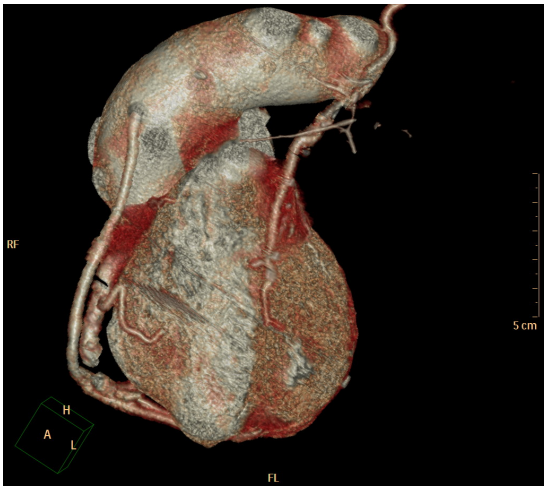

(b) *Reference three-dimensional reconstruction (coronary arteries, bypass grafts, aorta, heart) provided by the radiology department.*

Figure 2.9: ***Patient 6****: three-dimensional reconstruction.*

Patient 6 reconstruction features[3]:

- *Coronary arteries:* LCA, LAD, LCX; RCA, PDA.
- *Bypass grafts:* LITA to LAD; Aorta-SVG-PDA.

	LITA	**Radial**		**SVG**		**Anastomosis**		
		Y-graft	*Aorta*	*Y-graft*	*Aorta*	*T-shaped*	*flow*	*cross*
LAD	×						×	
Diag.								
LCX								
OM								
PDA					×		×	
PL								

Table 2.6: ***Patient 6****: detailed report of the CABG surgery.*

[3]Patient 5 has been excluded from the study due to several artefacts in the CT scan.

Patient 7

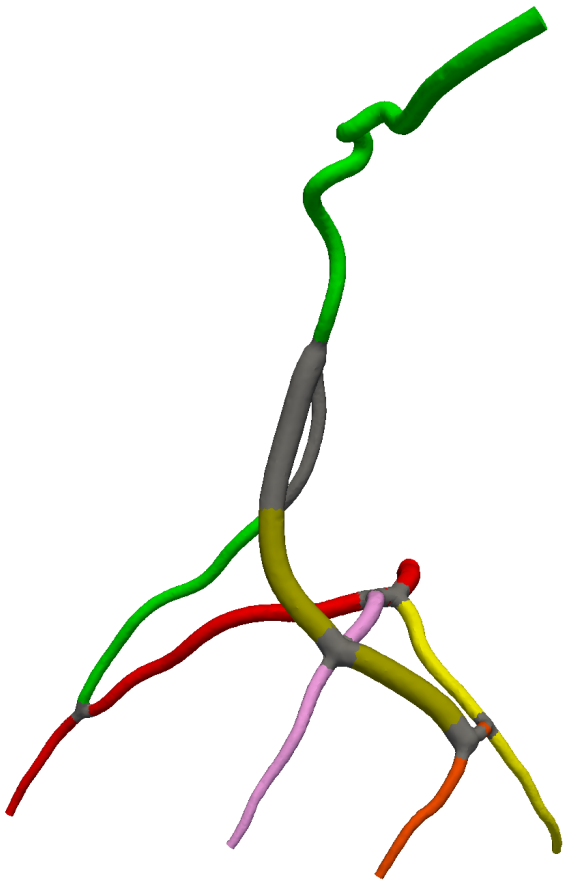

(a) *Three-dimensional reconstruction (coronary arteries, bypass grafts) obtained employing the medical imaging pipeline detailed in Section 2.2.*

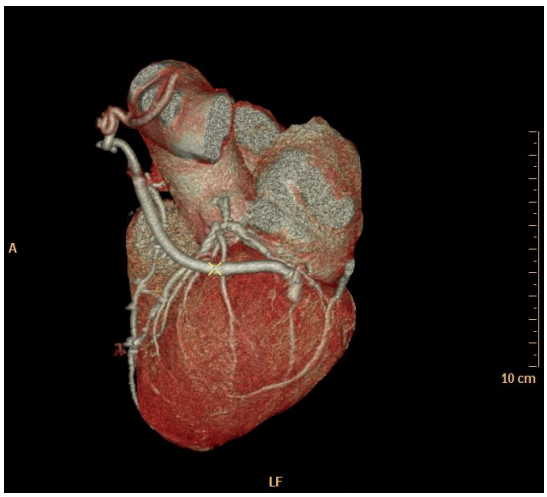

(b) *Reference three-dimensional reconstruction (coronary arteries, bypass grafts, aorta, heart) provided by the radiology department.*

Figure 2.10: ***Patient 7****: three-dimensional reconstruction.*

Patient 7 reconstruction features:

- *Coronary arteries:* LCA, LAD-Diag, LCX-OM.
- *Bypass grafts:* LITA to LAD; SVG Y-graft on LITA-Diag-OM.

	LITA	**Radial**		**SVG**		**Anastomosis**		
		Y-graft	*Aorta*	*Y-graft*	*Aorta*	*T-shaped*	*flow*	*cross*
LAD	×						×	
Diag.				×				×
LCX								
OM				×		×		
PDA								
PL								

Table 2.7: ***Patient 7****: detailed report of the CABG surgery.*

Patient 8

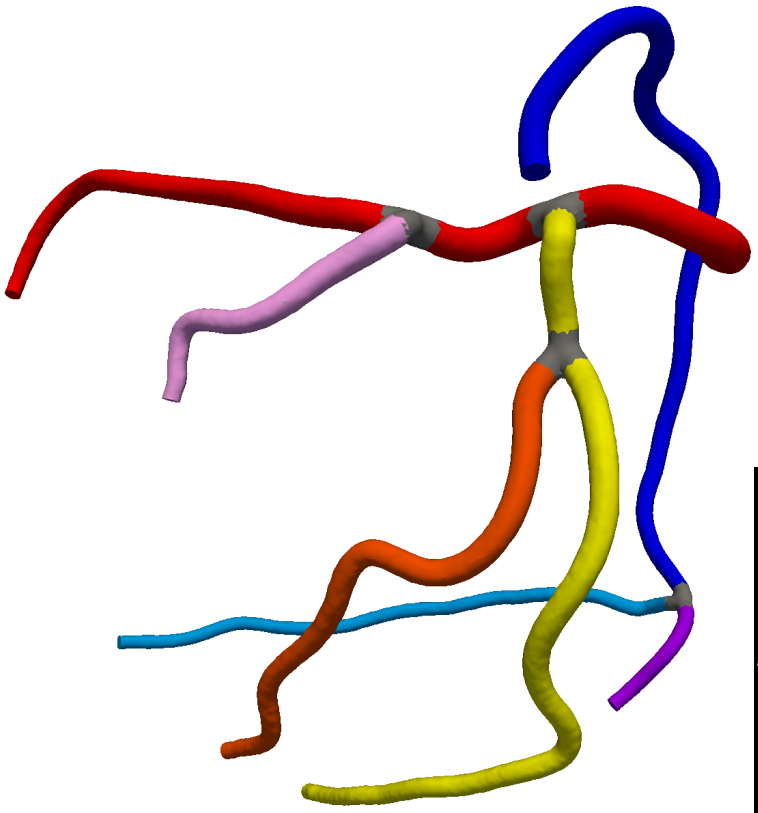

(a) *Three-dimensional reconstruction (coronary arteries) obtained employing the medical imaging pipeline detailed in Section 2.2.*

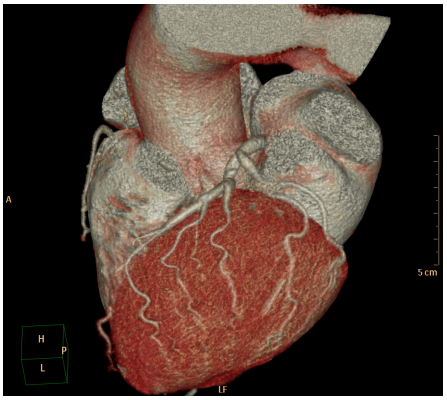

(b) *Reference three-dimensional reconstruction (coronary arteries, aorta, heart) provided by the radiology department.*

Figure 2.11: ***Patient 8****: three-dimensional reconstruction.*

Patient 8 reconstruction features:

- *Coronary arteries:* LCA, LAD-Diag, LCX-OM; RCA, PDA, PL.

Patient 9

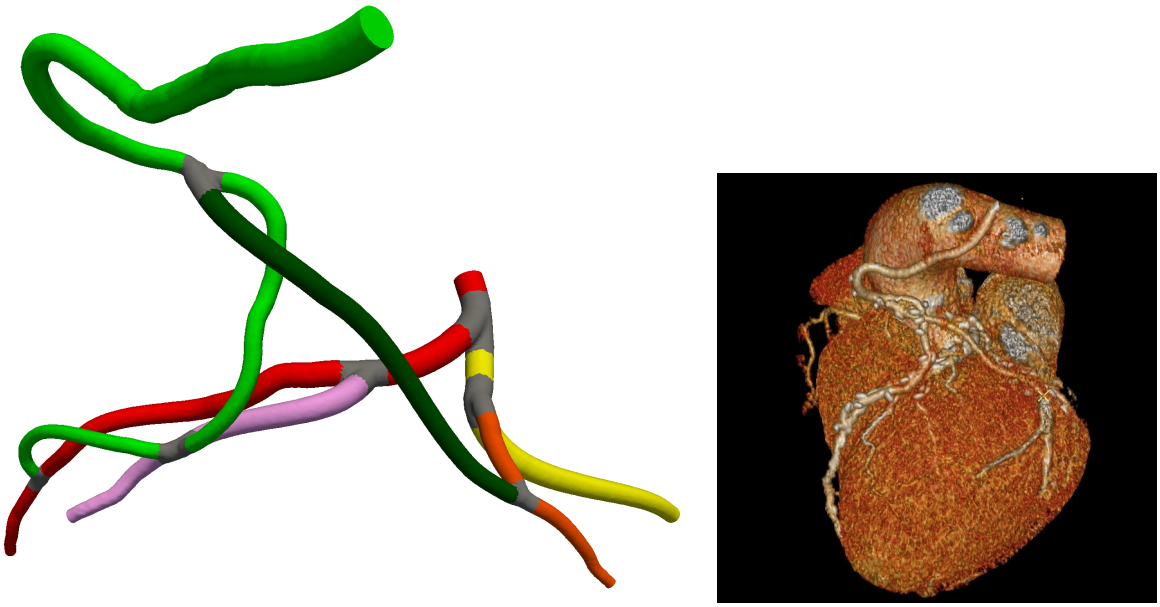

(a) *Three-dimensional reconstruction (coronary arteries, bypass grafts) obtained employing the medical imaging pipeline detailed in Section 2.2.*

(b) *Reference three-dimensional reconstruction (coronary arteries, bypass grafts, aorta, heart) provided by the radiology department.*

Figure 2.12: ***Patient 9****: three-dimensional reconstruction.*

Patient 9 reconstruction features[4]:

- *Coronary arteries:* LCA, LAD-Diag, LCX-OM.
- *Bypass grafts:* LITA-Diag-LAD; Radial Y-graft on LITA to OM.

	LITA	**Radial**		**SVG**		**Anastomosis**		
		Y-graft	*Aorta*	*Y-graft*	*Aorta*	*T-shaped*	*flow*	*cross*
LAD	×						×	
Diag.	×						×	
LCX								
OM		×					×	
PDA								
PL								

Table 2.8: ***Patient 9****: detailed report of the CABG surgery.*

[4]The collaboration of Riccardo Ferrero [95] in the segmentation of this patient is gratefully acknowledged.

Patient 10

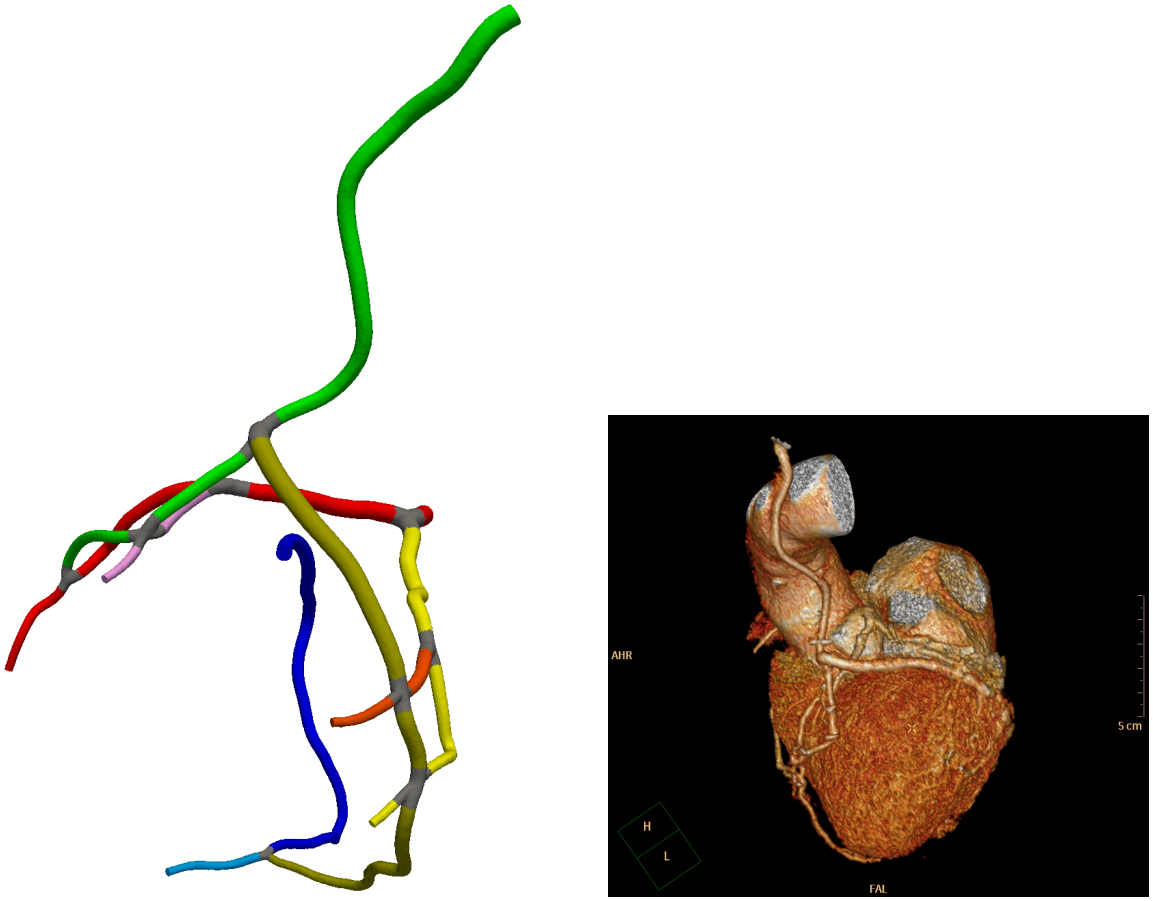

(a) *Three-dimensional reconstruction (coronary arteries, bypass grafts) obtained employing the medical imaging pipeline detailed in Section 2.2.*

(b) *Reference three-dimensional reconstruction (coronary arteries, bypass grafts, aorta, heart) provided by the radiology department.*

Figure 2.13: ***Patient 10****: three-dimensional reconstruction.*

Patient 10 reconstruction features:

- *Coronary arteries:* LCA, LAD-Diag, LCX-OM, RCA, PDA.
- *Bypass grafts:* LITA-Diag-LAD; SVG Y-graft on LITA-OM-LCX-PDA.

	LITA	**Radial**		**SVG**		**Anastomosis**		
		Y-graft	*Aorta*	*Y-graft*	*Aorta*	*T-shaped*	*flow*	*cross*
LAD	×						×	
Diag.	×						×	
LCX				×				×
OM				×				×
PDA				×		×		
PL								

Table 2.9: ***Patient 10****: detailed report of the CABG surgery.*

Patient 11

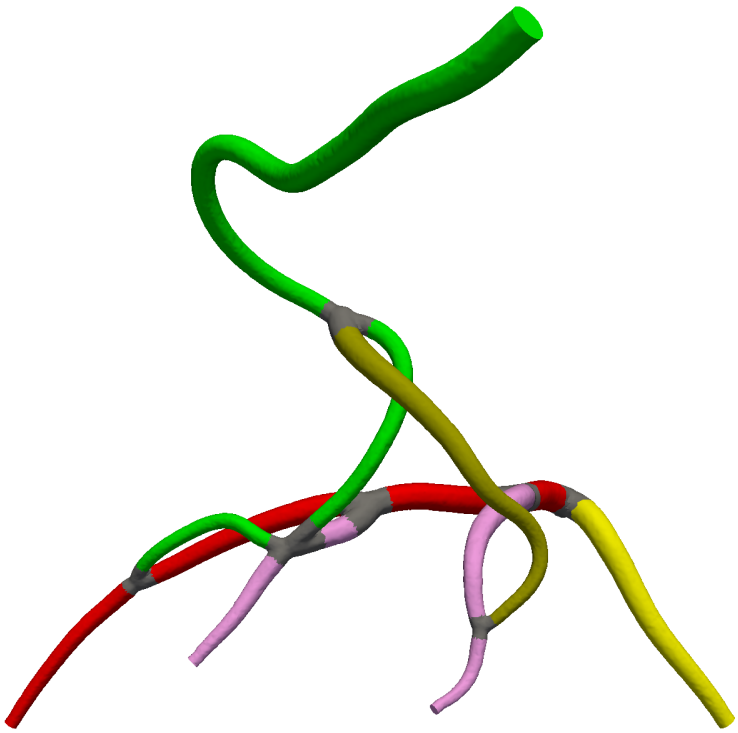

(a) *Three-dimensional reconstruction (coronary arteries, bypass grafts) obtained employing the medical imaging pipeline detailed in Section 2.2.*

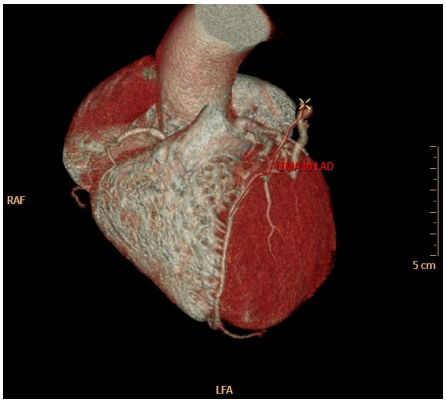

(b) *Reference three-dimensional reconstruction (coronary arteries, bypass grafts, aorta, heart) provided by the radiology department.*

Figure 2.14: ***Patient 11****: three-dimensional reconstruction.*

Patient 11 reconstruction features[5]:

- *Coronary arteries:* LCA, LAD-Diag 1-Diag 2, LCX.
- *Bypass grafts:* LITA-Diag 2-LAD; SVG Y-graft on LITA-Diag 1.

	LITA	**Radial**		**SVG**		**Anastomosis**		
		Y-graft	*Aorta*	*Y-graft*	*Aorta*	*T-shaped*	*flow*	*cross*
LAD	×						×	
Diag. 1				×			×	
Diag. 2	×						×	
LCX								
OM								
PDA								
PL								

Table 2.10: ***Patient 11****: detailed report of the CABG surgery.*

[5]The collaboration of Riccardo Ferrero [95] in the segmentation of this patient is gratefully acknowledged.

Patient 12

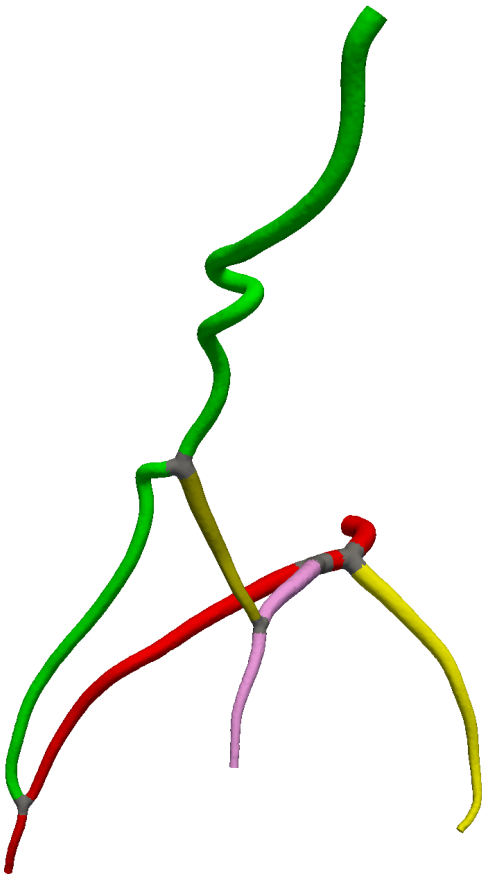

(a) *Three-dimensional reconstruction (coronary arteries, bypass grafts) obtained employing the medical imaging pipeline detailed in Section 2.2.*

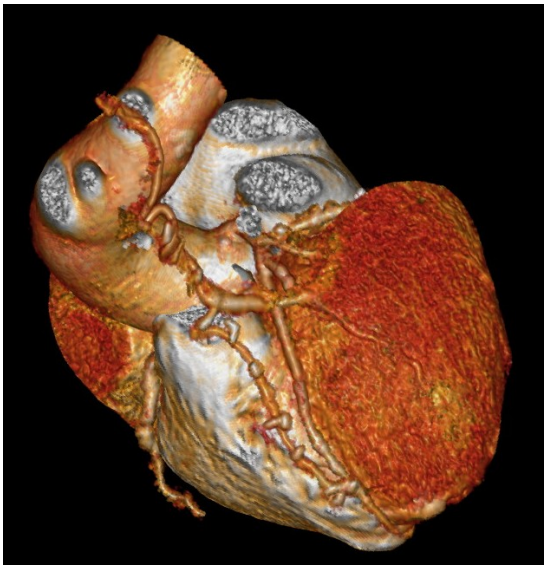

(b) *Reference three-dimensional reconstruction (coronary arteries, bypass grafts, aorta, heart) provided by the radiology department.*

Figure 2.15: ***Patient 12****: three-dimensional reconstruction.*

Patient 12 reconstruction features:

- *Coronary arteries:* LCA, LAD-Diag, LCX.
- *Bypass grafts:* LITA to LAD; SVG Y-graft on LITA to Diag.

	LITA	**Radial**		**SVG**		**Anastomosis**		
		Y-graft	*Aorta*	*Y-graft*	*Aorta*	*T-shaped*	*flow*	*cross*
LAD	×						×	
Diag.				×			×	
LCX								
OM								
PDA								
PL								

Table 2.11: ***Patient 12****: detailed report of the CABG surgery.*

Patient 13

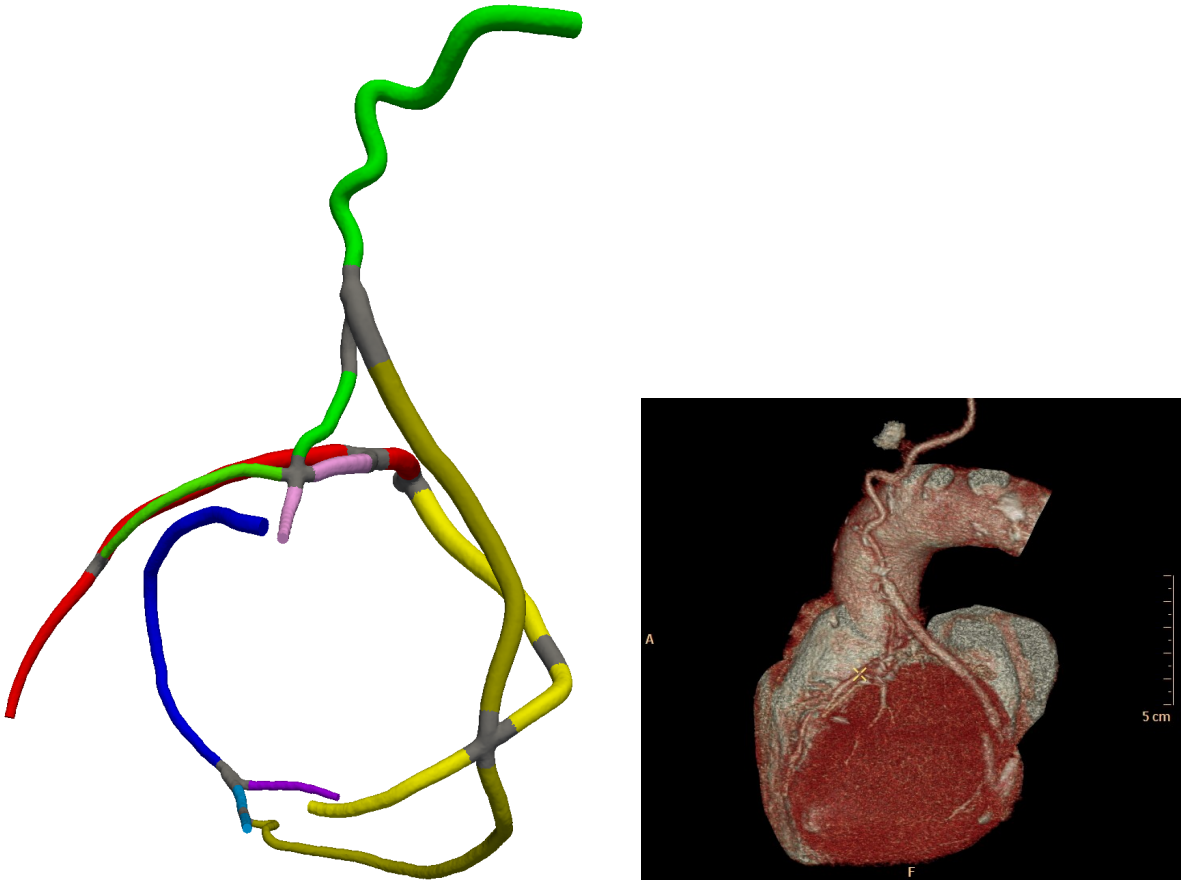

(a) *Three-dimensional reconstruction (coronary arteries, bypass grafts) obtained employing the medical imaging pipeline detailed in Section 2.2.*

(b) *Reference three-dimensional reconstruction (coronary arteries, bypass grafts, aorta, heart) provided by the radiology department.*

Figure 2.16: ***Patient 13****: three-dimensional reconstruction.*

Patient 13 reconstruction features[6]:

- *Coronary arteries:* LCA, LAD-Diag, LCX; RCA, PDA, PL.
- *Bypass grafts:* LITA-Diag-LAD; SVG Y-graft on LITA-LCX-PDA.

	LITA	**Radial**		**SVG**		**Anastomosis**		
		Y-graft	*Aorta*	*Y-graft*	*Aorta*	*T-shaped*	*flow*	*cross*
LAD	×						×	
Diag.	×						×	
LCX				×				×
OM								
PDA				×		×		
PL								

Table 2.12: ***Patient 13****: detailed report of the CABG surgery.*

[6]The collaboration of Riccardo Ferrero [95] in the segmentation of this patient is gratefully acknowledged.

Patient 14

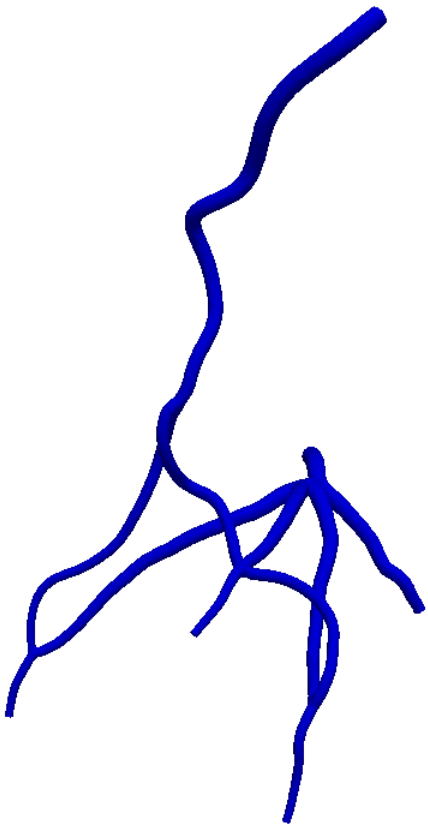

(a) *Three-dimensional reconstruction (coronary arteries, bypass grafts) obtained employing the medical imaging pipeline detailed in Section 2.2.*

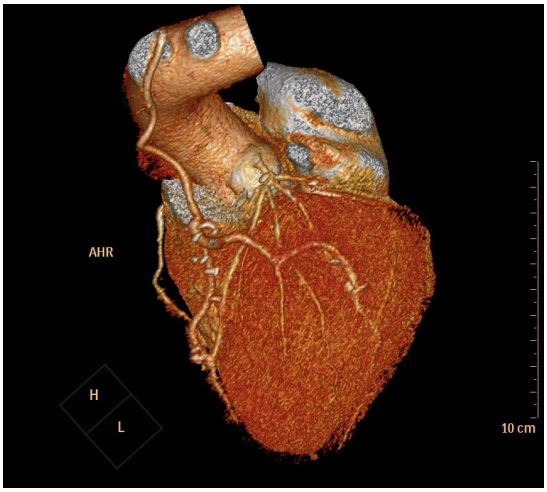

(b) *Reference three-dimensional reconstruction (coronary arteries, bypass grafts, aorta, heart) provided by the radiology department.*

Figure 2.17: ***Patient 14****: three-dimensional reconstruction.*

Patient 14 reconstruction features:

- *Coronary arteries:* LCA, LAD-Diag, ramus intermedius, LCX.
- *Bypass grafts:* LITA to LAD; Radial Y-graft on LITA-Diag-intermedius.

	LITA	**Radial**		**SVG**		**Anastomosis**		
		Y-graft	*Aorta*	*Y-graft*	*Aorta*	*T-shaped*	*flow*	*cross*
LAD	×						×	
Diag.		×					×	
Intermedius		×					×	
LCX								
OM								
PDA								
PL								

Table 2.13: ***Patient 14****: detailed report of the CABG surgery.*

Patient 15

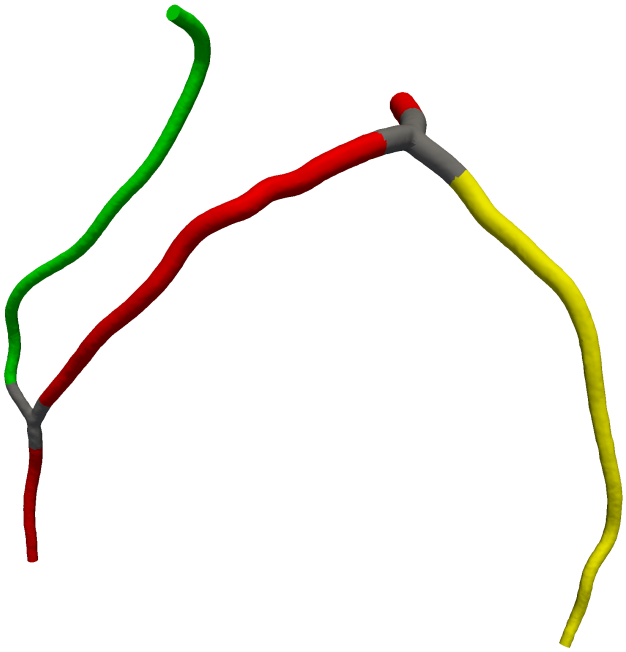

(a) *Three-dimensional reconstruction (coronary arteries, bypass grafts) obtained employing the medical imaging pipeline detailed in Section 2.2.*

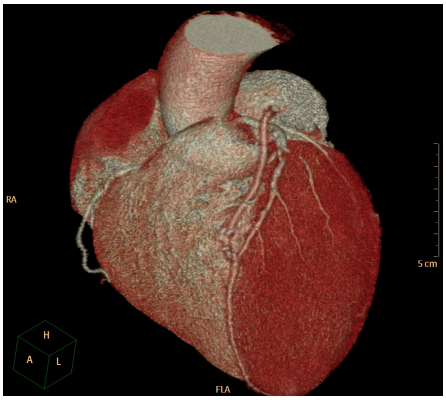

(b) *Reference three-dimensional reconstruction (coronary arteries, bypass grafts, aorta, heart) provided by the radiology department.*

Figure 2.18: ***Patient 15****: three-dimensional reconstruction.*

Patient 15 reconstruction features:

- *Coronary arteries:* LCA, LAD, LCX.
- *Bypass grafts:* LITA to LAD.

	LITA	**Radial**		**SVG**		**Anastomosis**		
		Y-graft	*Aorta*	*Y-graft*	*Aorta*	*T-shaped*	*flow*	*cross*
LAD	×						×	
Diag.								
LCX								
OM								
PDA								
PL								

Table 2.14: ***Patient 15****: detailed report of the CABG surgery.*

Part II

Computational reduction framework

Introduction to Part II

Motivation for CFD computations and quantities of clinical interest

Clinical experience suggests that coronary artery bypass grafts tend to fail some years after the surgery due to the development of intimal thickening (restenosis). In fact, even though early graft failure (within thirty days) might be related to possible surgical technical errors and thrombosis, late graft failures are caused by progression of atherosclerosis and intimal hyperplasia [53].

Altered, unfavorable or unnatural flow conditions near the anastomosis are believed to be important in the genesis and development of intimal thickening [30, 125]. Typical locations of intimal thickening are the distal anastomosis and the coronary artery bed near the anastomosis [173, 249]. The quantification of fluid dynamics conditions by means of haemodynamic indices can be therefore a useful tool. Relevant computational indices in this context are velocity profiles, transversal velocity profiles, helicity, wall shear stress and oscillatory shear index [173]:

- recirculation regions may be detected by means of velocity profiles (streamlines) and helicity indices. In particular, the local normalized helicity [189], defined as the normalized scalar product between the velocity $\boldsymbol{u}$ and the vorticity $\nabla \times \boldsymbol{u}$,

  $$LNH = \frac{\boldsymbol{u} \cdot (\nabla \times \boldsymbol{u})}{|\boldsymbol{u}|\,|\nabla \times \boldsymbol{u}|}, \qquad -1 \leq LNH \leq 1$$

  is a scalar quantity which describes the occurrence spiral patterns into the flow. A purely axial motion associated to $LNH = 0$, while a purely helicoidal flow to $|LNH| = 1$. Positive (negative) LNH values are related to left-handed (right-handed, respectively) rotating structures;

- the formation of Dean vortices in the region distal to the anastomosis is detected thanks to transversal velocity profiles. In fact, secondary flow structures (i.e. perpendicular to the flow direction) are usually not negligible at the anastomosis, and the formation of a pair of vortical structures has been observed many times [238];

- the existence of a safe bandwidth of wall shear stress (WSS) has been suggested in [145], highlighting that both low WSS and high WSS may favor the restenosis process. In fact, high WSS may lead to endothelial injury and cause the development of a lesion. Instead, low WSS and long particle residence time in flow recirculation zones favors the deposit

of fatty materials and cholesterol on the surface of the lumen, causing the growth of the atheroma;

- a correlation between plaque location and oscillating shear stress has been described in [148], showing that oscillations in the direction of wall shear may cause atherogenesis. To recognize oscillatory nature of WSS, the oscillatory shear index (OSI), defined as

$$OSI = \frac{1}{2}\left[1 - \frac{\left|\int_0^T \boldsymbol{WSS}(t)dt\right|}{\int_0^T |\boldsymbol{WSS}(t)|\,dt}\right] \qquad 0 \leq OSI \leq 0.5,$$

has been introduced, being T the period of the cardiac cycle. OSI ranges from a minimum value of 0, which corresponds to region experiencing no reverse flow, to a maximum value of 0.5, which corresponds to regions with fully oscillatory flow.

We refer to [161] for a comparison and a study of correlation among these haemodynamic indices.

Some studies on the correlation between haemodynamics indices and intimal thickening have been conducted in vivo or in in vitro. We refer in particular to [254] for an overview on experimental methods in cardiovascular fluid mechanics. Experimental methods, such as Magnetic Resonance Imaging (MRI) and Doppler ultrasound techniques, can be used to provide a noninvasive quantification of the blood flow. The computation of the haemodynamic indices is then carried out to evaluate the disease and the outcome of the medical procedure. Critical regions highlighted by haemodynamic indices are located near the heel and toe of the graft, and on the arterial bed near to the anastomosis. In the last decades, moreover, an increasing interest has been devoted to the development of computational methods for cardiovascular applications (see [97] and references therein), coupled to medical imaging techniques to obtain patient-specific geometrical configurations. Although experimental and computational methods for the simulation of blood flows can be used together (for example, to provide patient-specific boundary conditions, to validate the results of the numerical simulation, etc.), in this thesis we will focus only on the latter.

Throughout this thesis we assume to deal with pulsatile, Newtonian flow in patient-specific coronary arteries, under a rigid wall assumption. More complex models have also been studied, such as non-Newtonian fluid and fluid-structure interaction models, concerning the motion due to both vessel compliance (in order to characterize, for example, the different rheological properties of arterial and venous grafts) and due to the underlying myocardial motion. The former effects have been found to be negligible in some studies [264, 265]. As noted in [270], including the latter is significantly more challenging (both in terms of required clinical data and adopted mathematical models) and, although cyclic curvature deformation of coronary arteries do have strong effect on the local distribution of wall shear stress [187, 206, 273], the deformation affects the magnitude rather than the macroscopic characteristics of the flow.

Our focus is, instead, to couple patient-specific clinical data to model order reduction techniques. In fact, a considerable advantage of computational methods is the possibility to explore cases that are not (easily) available in vivo, depending on different *parameters* of the problem, discussed in detail in the next section. In fact, clinical interest lies not only in the simulation on a given configuration, possibly patient-specific, but also in addressing the variation of the flow conditions and of the geometrical configuration for comparison among different scenarios, aiming at a possible improvement of the design of the surgical procedure. However, the solution of a finite element problem for *each* new physical or geometrical configuration is usually unaffordable, especially if the aim is to provide, eventually, a fast

computational toolbox for the surgeon to visualize in real-time the outcome of different surgical procedures or flow conditions. Reduced-order models (ROM) [213] are applied to be able to do that *efficiently* and, possibly, on deployed platforms (such as on standard personal computers available at the hospital, instead of high performance computing facilities).

Motivation for ROM computations

Several recent reviews [107, 181, 184, 196] recognize the importance of a physical and geometrical parametrization in the study of coronary artery bypass grafts. Among relevant parameters, we mention:

- *inlet flow rates*: different rest or stress conditions are taken into account by means of a variation of inlet flow rates. In fact, an increased blood flow to the heart is required under stress conditions, and, since coronary arteries are the only source of blood supply to the heart, flow across them is increased in response to this need. Moreover, the effect of graft adaptation [195,197,223,225,251] should be also considered for the internal thoracic artery, which causes the flow to adapt depending on the native coronary stenosis. In our model we consider a parametrization on inlet flow rates by means of multiplicative factors on a reference flow profile available from literature (see Section 6.2);

- *stenosis severity*: as discussed in Section 1.2, graft patency rates are related to proximal stenosis severity [124, 218, 224, 225]. A specialized geometrical parametrization has been devised to change the severity, by performing local variation to the radius of the vessel (see Section 5.2.2.1);

- *local anastomosis configuration*: tissue remodeling and intimal hyperplasia are highly sensitive to the graft configuration near the anastomosis [94, 101, 135, 141, 249]. To investigate different possible termino-lateral (end-to-side) anastomosis, we introduce in our parametrized formulation a variation of the angle between the graft and the native vessel (see Section 5.2.3).

The proposed computational and geometrical reduction framework is able to consider these aspects by means of few relevant parameters.

Another important aspect that is considered by our computational model, but currently not by our parametrized formulation (i.e. this property is equal to the one of patient-specific data and is not parametrized), is

- *grafting materials, and related graft-to-host diameter ratio*: as discussed in Section 1.3, the computational model should take into account the different grafting materials (artery vs vein). A possible relevant distinction between these two cases is related to the different graft-to-host diameter ratio. In fact it has been observed that larger ratios have better performance than smaller ones [42, 209], and that the small caliber of vein grafts is a risk factor for graft failure [131, 259]. In this thesis the main difference between arterial and vein grafts is the graft-to-host diameter ratio.

Once a set of relevant parameters has been introduced, model order reduction techniques can be applied to obtain an efficient evaluation of the parametrized flows. In fact, the main advantage over classical methods (finite element, finite volume, etc.) is that faster evaluations are possible thanks to a database a representative solutions, previously computed. Early results on the coupling between ROM, parametrization techniques and idealized bypass configurations have been proposed in [4, 5, 154, 180, 211, 219, 220]. An increasing interest has

been devoted in recent years to model order reduction techniques and a broad range of biomedical applications:

- a Proper Orthogonal Decomposition(POD)-based ROM coupled with an atlas-based shape parametrization has been applied in [115, 183] to Tetralogy of Fallot patients;
- POD ROMs have also been applied to cardiac electrophysiology problems in [43];
- a real time approximation of deformable models of non-linear tissues in the human cornea has been sought in [192, 193] by a proper generalized decomposition (PGD) formulation; the same authors applied PGD also to a liver palpation problem in [194];
- applications to fluid structure interaction problems have been addressed in [37, 75].

Moreover, we refer the interested reader to the recent review [77] on real-time simulations for computational surgery.

Overview

In this Part of the thesis we describe a computational framework to deal with efficient simulation of parametrized nonlinear unsteady flows, based on POD-Galerkin reduced-order models (ROMs). We thus focus on the following problem: given $\boldsymbol{\mu} \in \mathcal{D} \subset \mathbb{R}^P$, solve

$$\begin{cases} \frac{\partial}{\partial t}\boldsymbol{u}_o(t;\boldsymbol{\mu}) - \nu(\boldsymbol{\mu}_p)\Delta\boldsymbol{u}_o(\boldsymbol{\mu}) + \boldsymbol{u}_o(t;\boldsymbol{\mu})\cdot\nabla\boldsymbol{u}_o(t;\boldsymbol{\mu}) & \\ \quad +\nabla p_o(t;\boldsymbol{\mu}) = \boldsymbol{f}(t;\boldsymbol{\mu}_p) & \text{in } \Omega_o(\boldsymbol{\mu}_g)\times(0,T), \\ \operatorname{div}\boldsymbol{u}_o(t;\boldsymbol{\mu}) = 0 & \text{in } \Omega_o(\boldsymbol{\mu}_g)\times(0,T), \\ \boldsymbol{u}_o(t;\boldsymbol{\mu}) = \boldsymbol{g}_D(t;\boldsymbol{\mu}_p) & \text{on } \Gamma_D\times(0,T), \\ \boldsymbol{u}_o(t;\boldsymbol{\mu}) = \boldsymbol{0}, & \text{on } \Gamma_{o,W}(\boldsymbol{\mu}_g)\times(0,T), \\ \nu(\boldsymbol{\mu}_p)\dfrac{\partial\boldsymbol{u}_o(t;\boldsymbol{\mu})}{\partial\boldsymbol{n}} - p_o(t;\boldsymbol{\mu})\boldsymbol{n} = \boldsymbol{g}_N(t;\boldsymbol{\mu}_p), & \text{on } \Gamma_N, \\ \boldsymbol{u}_o(t;\boldsymbol{\mu})|_{t=0} = \boldsymbol{g}_0(\boldsymbol{\mu}), & \text{in } \Omega_o(\boldsymbol{\mu}_g), \end{cases}$$

In Chapter 6 we will apply the ROM to some of the patient-specific configurations shown in Section 2.3. The domain $\Omega_o(\boldsymbol{\mu}_g)$ is going to be the mesh obtained from the reconstructed geometries, and the boundaries Γ_D, $\Gamma_{o,W}(\boldsymbol{\mu}_g)$ and Γ_N are respectively inlet boundaries (LCA and RCA inlets from the aorta, LITA inlet from the subclavian artery, and possibly inflow sections of other free grafts from the aorta), lateral surfaces of the coronary arteries and grafts, and outlet sections (e.g. LAD, LCX, PDA outlet sections, or also outlet sections of their branches). However in Chapters 3 and 4 we will employ two-dimensional test cases and simplified configurations to setup and assess the methodology.

In general, reduced-order models are devised to deliver an accurate solution to parametrized PDEs at lower computational costs. Based on modal analysis and singular value decomposition [13, 14, 36, 64, 216, 269], POD has been initially applied to provide efficient model order reduction in turbulent viscous flow computations, with the aim of preserving the most important energetic flow features. In the same period Reduced Basis methods were also proposed for nonlinear viscous flows [201].

For nonlinear PDEs, several issues need however to be faced when using ROMs in order to guarantee efficiency, accuracy and reliability. These include the efficient exploration of the parameters space to build reduced basis spaces that, ideally, should: *(i)* have low dimension

but also the capability to capture fine physical features on the whole temporal interval; *(ii)* be stable also for noncoercive problems as in the case of saddle-point problems; *(iii)* allow accurate and fast estimation of stability factors. Optimal sampling procedures [151, 271], different POD methods such as weighted POD and predefined POD [73], window POD [112] or a sensitivity analysis enriched POD [122] have been proposed to deal with issue *(i)*. Such choices allow to obtain a correct representation of the long term behavior of the resulting ROM in the case of limit cycles and periodic flow solutions [6, 243]. Issue *(ii)* arises if the simultaneous approximation of both velocity and pressure is sought online. Although early proposal of model order reduction techniques for computational fluid dynamics problems contemplated only an approximation of the velocity, this is a topic of growing research interest in the last decades, and several ways to address it have been proposed. Among these, a first class of methods relies either on pressure Poisson approaches [6,271], possibly combined with suitable closure terms based on variation multiscale methods and residual-based stabilizations [35,271], closely related velocity-pressure ROMs based on SUPG-PSPG residual-based online stabilizations [18, 57], or an explicit formulation of the ROM [19, 20]. A second class of methods relies instead on an enrichment of the velocity space [212,221,222], to obtain an inf-sup stable ROM. Estimation of stability factors (issue *(iii)*) has been in fact closely developed in conjunction with this second class [82, 106, 178, 221, 262]; we also refer to [68, 69, 150] for additional insights on error estimates.

Chapter 3 introduces the proposed POD-Galerkin ROM in the steady case and focus on issues *(ii)* and *(iii)*, considering an inf-sup stabilization procedure by means of *supremizer enrichment* of the reduced velocity space. This model order reduction framework is extended to the unsteady case in Chapter 4, focusing on issue *(i)*, by means of a *two-level POD* to efficiently handle the increased dimensionality of the SVD, to face the time-dependence.

CHAPTER 3

POD-Galerkin ROM for parametrized steady Navier-Stokes equations: supremizer inf-sup stabilization for velocity-pressure approximation

A reduced-order model for parametrized steady incompressible Navier-Stokes (NS) equations, based on a Proper Orthogonal Decomposition and Galerkin projection, is introduced in this chapter[1]. In particular, parametrized steady incompressible Navier-Stokes problems and their full-order approximation are introduced in Section 3.1, considering both physical and geometrical parameters. In Section 3.2 a POD-Galerkin ROM is presented, featuring a POD for the construction of both pressure and velocity spaces. In the offline stage of the resulting strategy, several Navier-Stokes truth solutions are computed, and a POD is performed to extract a low dimensional representation of both velocity and pressure spaces. A key point which is investigated in Sections 3.3-3.4 is related to *possible sources of pressure instabilities*, in order to avoid *spurious pressure modes* in the POD approximation of parametrized flows. A *supremizer stabilization* technique, and a stability analysis based on the introduction of an inf-sup condition at the reduced level, will be employed to deal with this problem. The stability analysis is also carried out by means of some numerical tests (Section 3.5).

3.1 Formulation and full-order approximation of parametrized steady Navier-Stokes equations

3.1.1 Continuous formulation

In the steady case, on a spatial domain $\Omega_o(\boldsymbol{\mu}_g) \subset \mathbb{R}^d$, $d = 2, 3$, NS equations read as follows:

[1] This chapter is a re-adaptation of the following publication:
[23] F. Ballarin, A. Manzoni, A. Quarteroni, and G. Rozza. Supremizer stabilization of POD–Galerkin approximation of parametrized steady incompressible Navier–Stokes equations. International Journal for Numerical Methods in Engineering (in press, published online at `http://onlinelibrary.wiley.com/doi/10.1002/nme.4772/abstract`), 2014.

$$\begin{cases} -\nu(\boldsymbol{\mu}_p)\Delta \boldsymbol{u}_o + (\boldsymbol{u}_o \cdot \nabla)\boldsymbol{u}_o + \nabla p_o = \boldsymbol{f}(\boldsymbol{\mu}_p) & \text{in } \Omega(\boldsymbol{\mu}_g), \\ \operatorname{div} \boldsymbol{u}_o = 0 & \text{in } \Omega_o(\boldsymbol{\mu}_g), \\ \boldsymbol{u}_o = \boldsymbol{g}_D(\boldsymbol{\mu}_p) & \text{on } \Gamma_D, \\ \boldsymbol{u}_o = \boldsymbol{0}, & \text{on } \Gamma_{o,W}(\boldsymbol{\mu}_g), \\ \nu(\boldsymbol{\mu}_p)\dfrac{\partial \boldsymbol{u}_o}{\partial \boldsymbol{n}} - p_o \boldsymbol{n} = \boldsymbol{g}_N(\boldsymbol{\mu}_p), & \text{on } \Gamma_N, \end{cases} \tag{3.1}$$

for some given distributed force term $\boldsymbol{f}$, Dirichlet data $\boldsymbol{g}_D$ and Neumann fluxes $\boldsymbol{g}_N$. Here we denote by $\boldsymbol{\mu} = (\boldsymbol{\mu}_g, \boldsymbol{\mu}_p)^T \in \mathcal{D} \subset \mathbb{R}^P$ a vector of parameters which may characterize either the geometrical configuration $\Omega_o(\boldsymbol{\mu}_g)$ or physical properties of our system, such as kinematic viscosity $\nu = \nu(\boldsymbol{\mu}_p)$, boundary data $\boldsymbol{g}_D = \boldsymbol{g}_D(\boldsymbol{\mu}_p)$, $\boldsymbol{g}_N = \boldsymbol{g}_N(\boldsymbol{\mu}_p)$ or source terms $\boldsymbol{f} = \boldsymbol{f}(\boldsymbol{\mu}_p)$. For the sake of notation, we shall distinguish between n_p physical parameters $\boldsymbol{\mu}_p \in \mathcal{D}_p \subset \mathbb{R}^{n_p}$ and $n_g = P - n_p$ geometrical parameters $\boldsymbol{\mu}_g \in \mathcal{D}_g \subset \mathbb{R}^{n_g}$. We thus denote by $(\boldsymbol{u}_o, p_o) = (\boldsymbol{u}_o(\boldsymbol{\mu}), p_o(\boldsymbol{\mu}))$ the velocity and pressure fields, by omitting the dependence on $\boldsymbol{\mu}$ for the sake of notation.

We denote by Γ_W and Γ_D the portion of $\partial\Omega_o$ where we impose homogeneous (resp., inhomogeneous) Dirichlet conditions, whereas we assign on $\Gamma_N = \partial\Omega \backslash (\Gamma_W \cup \Gamma_D)$ the Neumann conditions; here $\boldsymbol{n}$ denotes the normal unit vector to the boundary. Hereafter we assume that Γ_D and Γ_N are not affected by the geometrical parametrization of the domain: this simplifies our problem, by avoiding the use of Piola transformation even in presence of geometrical parametrizations [130]. Indeed, this is not a limitation in view of the clinical application since, for instance, the position of the inlet sections of LCA and RCA is fixed, as they arise from the aorta, and cannot be changed by the surgeon. The same is also true for the LITA, being a branch of the subclavian artery.[2] For the sake of simplicity, we consider the case $\boldsymbol{f} = \boldsymbol{g}_N = \boldsymbol{0}$; the extension to other cases is straightforward. We also define the Reynolds number as $Re = L|\bar{\boldsymbol{u}}|/\nu$, being L a characteristic length of the domain, $\bar{\boldsymbol{u}}$ a typical velocity of the flow and ν the kinematic viscosity; in the numerical test cases presented in this chapter (and also in the clinical application, since we are dealing with small vessels and low velocities) we will consider flows with $Re \in [1, 10^3]$.

To derive the algebraic formulation of (3.1), we first need to write this problem under weak form. To do this, we introduce a reference, $\boldsymbol{\mu}_g$-independent configuration Ω, by assuming that each parametrized domain $\Omega_o(\boldsymbol{\mu}_g)$ can be obtained as the image of Ω through a parametrized map $\boldsymbol{T}(\cdot; \boldsymbol{\mu}_g) : \mathbb{R}^d \to \mathbb{R}^d$, i.e. $\Omega_o(\boldsymbol{\mu}_g) = \boldsymbol{T}(\Omega; \boldsymbol{\mu}_g)$. The choice of the map $\boldsymbol{T}$ is a central issue in the current clinical application, to which Chapter 5 will be devoted. Moreover, we denote by $\boldsymbol{V}, Q$ the velocity and the pressure space, respectively, defined over Ω; here

$$\boldsymbol{V} = \boldsymbol{H}^1_{0,\Gamma_E}(\Omega), \qquad Q = L^2(\Omega)$$

being $\Gamma_E = \Gamma_D \cup \Gamma_W$. We equip $\boldsymbol{V}$ and Q with the (vector) H^1-seminorm and the L^2-norm, the former being equivalent to the H^1-norm since $\Gamma_E \neq \varnothing$. Bold symbols denote vectorial functions in the velocity space. The weak formulation can be obtained by multiplying (3.1) by test functions $(\boldsymbol{v}, q)$ and integrating by parts; then, by tracing everything back onto the reference domain Ω, we end up with the following weak parametrized formulation of (3.1): find $(\boldsymbol{u}, p) \in \boldsymbol{V} \times Q$ such that

$$\begin{cases} a(\boldsymbol{u}, \boldsymbol{v}; \boldsymbol{\mu}) + b(\boldsymbol{v}, p; \boldsymbol{\mu}) + c(\boldsymbol{u}, \boldsymbol{u}, \boldsymbol{v}; \boldsymbol{\mu}) + d(\boldsymbol{u}, \boldsymbol{v}; \boldsymbol{\mu}) = F(\boldsymbol{v}; \boldsymbol{\mu}) & \forall \boldsymbol{v} \in \boldsymbol{V} \\ b(\boldsymbol{u}, q; \boldsymbol{\mu}) = G(q; \boldsymbol{\mu}) & \forall q \in Q \end{cases} \tag{3.2}$$

[2] This is not true however for free grafts anastomized to the aorta, where the surgeon is free to choose where to place the anastomosis. However, we do not take into account this additional source of complexity. In fact, as we will see in Chapter 6, all inlet boundary conditions are taken from literature and *not* from a simulation of the blood flow in the aorta.

where

$$a(\boldsymbol{u},\boldsymbol{v};\boldsymbol{\mu})=\int_\Omega \nabla\boldsymbol{u}\,\boldsymbol{\kappa}(\boldsymbol{x};\boldsymbol{\mu}):\nabla\boldsymbol{v}\,d\boldsymbol{x},\qquad b(\boldsymbol{v},q;\boldsymbol{\mu})=-\int_\Omega q\,\mathrm{tr}(\boldsymbol{\chi}(\boldsymbol{x},t;\boldsymbol{\mu})\,\nabla\boldsymbol{v})\,d\boldsymbol{x} \tag{3.3}$$

are the bilinear forms[3] related to diffusion and pressure/divergence operators, respectively, whereas

$$c(\boldsymbol{u},\boldsymbol{v},\boldsymbol{z};\boldsymbol{\mu})=\int_\Omega(\nabla\boldsymbol{v}\,\boldsymbol{\chi}(\boldsymbol{x},t;\boldsymbol{\mu}))\boldsymbol{u}\cdot\boldsymbol{z}\,d\boldsymbol{x} \tag{3.4}$$

is the trilinear form related to the convective term. Here we denote by

$$\begin{aligned}\boldsymbol{\kappa}(\boldsymbol{x};\boldsymbol{\mu})&=\nu(\boldsymbol{\mu}_p)(J_{\boldsymbol{T}}(\boldsymbol{x};\boldsymbol{\mu}_g))^{-1}(J_{\boldsymbol{T}}(\boldsymbol{x};\boldsymbol{\mu}_g))^{-T}|J_{\boldsymbol{T}}(\boldsymbol{x};\boldsymbol{\mu}_g)|\\ \boldsymbol{\chi}(\boldsymbol{x};\boldsymbol{\mu})&=(J_{\boldsymbol{T}}(\boldsymbol{x};\boldsymbol{\mu}_g))^{-1}|J_{\boldsymbol{T}}(\boldsymbol{x};\boldsymbol{\mu}_g)|,\end{aligned} \tag{3.5}$$

the tensors encoding both physical and geometrical parametrizations in the NS operators, obtained with the change of variable from $\Omega_o(\boldsymbol{\mu}_g)$ to Ω; $J_{\boldsymbol{T}}\in\mathbb{R}^{d\times d}$ is the Jacobian matrix of the map $\boldsymbol{T}(\cdot;\boldsymbol{\mu}_g)$, and $|J_{\boldsymbol{T}}|$ its determinant.

Other terms are yielded by the lifting of the Dirichlet boundary conditions: denoting by $\boldsymbol{l}(\boldsymbol{\mu}_p)\in\boldsymbol{H}^1(\Omega)$ a parametrized lifting function such that $\boldsymbol{l}(\boldsymbol{\mu}_p)|_{\Gamma_D}=\boldsymbol{g}_D(\boldsymbol{\mu}_p)$, $\boldsymbol{l}(\boldsymbol{\mu}_p)|_{\Gamma_W}=\boldsymbol{0}$, we have that

$$\begin{aligned}d(\boldsymbol{u},\boldsymbol{v};\boldsymbol{\mu})&=c(\boldsymbol{l}(\boldsymbol{\mu}_p),\boldsymbol{u},\boldsymbol{v};\boldsymbol{\mu})+c(\boldsymbol{u},\boldsymbol{l}(\boldsymbol{\mu}_p),\boldsymbol{v};\boldsymbol{\mu})\\ F(\boldsymbol{v};\boldsymbol{\mu})&=-a(\boldsymbol{l}(\boldsymbol{\mu}_p),\boldsymbol{v};\boldsymbol{\mu})-c(\boldsymbol{l}(\boldsymbol{\mu}_p),\boldsymbol{l}(\boldsymbol{\mu}_p),\boldsymbol{v};\boldsymbol{\mu}),\qquad G(q;\boldsymbol{\mu})=-b(\boldsymbol{l}(\boldsymbol{\mu}_p),q;\boldsymbol{\mu}).\end{aligned}$$

In particular, we consider parametrized Dirichlet data $\boldsymbol{g}_D(\boldsymbol{\mu}_p)=\Theta_D(\boldsymbol{\mu}_p)\tilde{\boldsymbol{g}}$, for a given scalar function $\Theta_D(\boldsymbol{\mu}_p)$ and a suitable inlet profile $\tilde{\boldsymbol{g}}$. Thus, a parameter independent lifting function $\tilde{\boldsymbol{l}}$ is actually computed in practice, and $\boldsymbol{l}(\boldsymbol{\mu}_p)=\Theta_D(\boldsymbol{\mu}_p)\tilde{\boldsymbol{l}}$. Without loss of generality, we can assume that $\tilde{\boldsymbol{l}}$ is divergence-free, given e.g. by a suitably scaled solution of an auxiliary Stokes flow, so that $G(q;\boldsymbol{\mu})=0$.

3.1.2 The full-order model and its algebraic formulation

To formulate the full-order model (FOM), we introduce two finite-dimensional subspaces $\boldsymbol{V}_h\subset\boldsymbol{V}$, $Q_h\subset Q$ of dimension $N^h_{\mathbf{u}}$ and N^h_p, respectively, being $h>0$ related to the computational mesh size. We consider a Galerkin-Finite Element (FE) approximation, and denote by $\{\boldsymbol{\varphi}^h_i\}_{i=1,\dots,N^h_{\mathbf{u}}}$ and $\{\zeta^h_k\}_{k=1,\dots,N^h_p}$ two (Lagrangian) basis of $\boldsymbol{V}_h$ and Q_h, respectively. The Galerkin-FE approximation of the parametrized problem (3.2) reads as follows: given $\boldsymbol{\mu}\in\mathcal{D}$, we seek for (the full-order solution) $(\boldsymbol{u}_h(\boldsymbol{\mu}),p_h(\boldsymbol{\mu}))\in\boldsymbol{V}_h\times Q_h$ such that

$$\begin{cases} a(\boldsymbol{u}_h(\boldsymbol{\mu}),\boldsymbol{v}_h;\boldsymbol{\mu})+d(\boldsymbol{u}_h(\boldsymbol{\mu}),\boldsymbol{v}_h;\boldsymbol{\mu})+b(\boldsymbol{v}_h,p_h(\boldsymbol{\mu});\boldsymbol{\mu}) & \\ \qquad +c(\boldsymbol{u}_h(\boldsymbol{\mu}),\boldsymbol{u}_h(\boldsymbol{\mu}),\boldsymbol{v}_h;\boldsymbol{\mu}) &= F(\boldsymbol{v}_h;\boldsymbol{\mu}) \quad \forall\boldsymbol{v}_h\in\boldsymbol{V}_h \\ b(\boldsymbol{u}_h(\boldsymbol{\mu}),q_h;\boldsymbol{\mu}) &= G(q_h;\boldsymbol{\mu}) \quad \forall q_h\in Q_h. \end{cases} \tag{3.6}$$

For algebraic purposes, we state the following bijection between $\mathbb{R}^{N^h_{\mathbf{u}}}$ and $\boldsymbol{V}_h$ (resp. $\mathbb{R}^{N^h_p}$ and Q_h):

$$\begin{cases} \underline{\mathbf{v}}=(v_h^{(1)},\dots,v_h^{(N^h_{\mathbf{u}})})^T\in\mathbb{R}^{N^h_{\mathbf{u}}} \quad\leftrightarrow\quad \boldsymbol{v}_h=\displaystyle\sum_{r=1}^{N^h_{\mathbf{u}}}v_h^{(r)}\boldsymbol{\varphi}^h_r\in\boldsymbol{V}_h, \\ \underline{\mathbf{q}}=(q_h^{(1)},\dots,q_h^{(N^h_p)})^T\in\mathbb{R}^{N^h_p} \quad\leftrightarrow\quad q_h=\displaystyle\sum_{r=1}^{N^h_p}q_h^{(r)}\zeta^h_r\in Q_h. \end{cases} \tag{3.7}$$

[3] tr denotes the trace of a matrix, and $A:B=\mathrm{tr}(A^TB)$.

Thanks to this identification, (3.6) is equivalent to the following (nonlinear) system:

$$\begin{bmatrix} A(\boldsymbol{\mu}) + C(\underline{\mathbf{u}}(\boldsymbol{\mu}); \boldsymbol{\mu}) & B^T(\boldsymbol{\mu}) \\ B(\boldsymbol{\mu}) & 0 \end{bmatrix} \begin{bmatrix} \underline{\mathbf{u}}(\boldsymbol{\mu}) \\ \underline{\mathbf{p}}(\boldsymbol{\mu}) \end{bmatrix} = \begin{bmatrix} \underline{\mathbf{f}}(\boldsymbol{\mu}) \\ \underline{\mathbf{g}}(\boldsymbol{\mu}) \end{bmatrix} \tag{3.8}$$

for the vectors of coefficients $\underline{\mathbf{u}} = (u_h^{(1)}, \ldots, u_h^{(N_{\mathbf{u}}^h)})^T$, $\underline{\mathbf{p}} = (p_h^{(1)}, \ldots, p_h^{(N_p^h)})^T$ where, for $1 \leq i, j \leq N_{\mathbf{u}}^h$ and $1 \leq k \leq N_p^h$:

$$\begin{aligned} (A(\boldsymbol{\mu}))_{ij} &= a(\boldsymbol{\varphi}_j^h, \boldsymbol{\varphi}_i^h; \boldsymbol{\mu}) + d(\boldsymbol{\varphi}_j^h, \boldsymbol{\varphi}_i^h; \boldsymbol{\mu}), \qquad (B(\boldsymbol{\mu}))_{ki} = b(\boldsymbol{\varphi}_i^h, \zeta_k^h; \boldsymbol{\mu}), \\ (C(\underline{\mathbf{u}}(\boldsymbol{\mu}); \boldsymbol{\mu}))_{ij} &= \sum_{m=1}^{N_{\mathbf{u}}^h} u_h^{(m)}(\boldsymbol{\mu}) c\left(\boldsymbol{\varphi}_m^h, \boldsymbol{\varphi}_j^h, \boldsymbol{\varphi}_i^h; \boldsymbol{\mu}\right), \end{aligned} \tag{3.9}$$

$$(\underline{\mathbf{g}}(\boldsymbol{\mu}))_k = -b(\boldsymbol{l}_h, \zeta_k^h; \boldsymbol{\mu}), \quad (\underline{\mathbf{f}}(\boldsymbol{\mu}))_i = -a(\boldsymbol{l}_h, \boldsymbol{\varphi}_i^h; \boldsymbol{\mu}) - c(\boldsymbol{l}_h, \boldsymbol{l}_h, \boldsymbol{\varphi}_i^h; \boldsymbol{\mu}) \tag{3.10}$$

and $\boldsymbol{l}_h = \boldsymbol{l}_h(\boldsymbol{\mu}_p) \in \boldsymbol{V}_h$ is a FE interpolant of the lifting function. Moreover, let us introduce the mass matrices $X_{\mathbf{u}}$, X_p for the velocity and pressure spaces, respectively, whose elements are given by

$$(X_{\mathbf{u}})_{ij} = (\boldsymbol{\varphi}_j^h, \boldsymbol{\varphi}_i^h)_{\boldsymbol{V}} \qquad (X_p)_{kl} = (\zeta_l^h, \zeta_k^h)_Q$$

for $1 \leq i, j \leq N_{\mathbf{u}}^h$ and $1 \leq k, l \leq N_p^h$, being $(\cdot, \cdot)_{\boldsymbol{V}}$ and $(\cdot, \cdot)_Q$ the (discrete) inner products defined over the two spaces. We denote (with a little abuse of notation) by

$$(\underline{\mathbf{v}}, \underline{\mathbf{w}})_{\boldsymbol{V}} = (X_{\mathbf{u}} \underline{\mathbf{v}}, \underline{\mathbf{w}}), \qquad (\underline{\mathbf{p}}, \underline{\mathbf{q}})_Q = (X_p \underline{\mathbf{p}}, \underline{\mathbf{q}})$$

the corresponding vector inner products for velocity and pressure fields, respectively; here $(\cdot, \cdot)$ denotes the usual Euclidean inner product in $\mathbb{R}^{N_h}$ ($N_h = N_{\mathbf{u}}^h, N_p^h$ depending on the case).

Solving the NS system (3.8) requires a nonlinear iteration with a linearized problem (involving nonsymmetric, indefinite matrix) being solved at each step; Newton and fixed-point (or Picard) iterations are the most common strategies, employed in this thesis.

3.1.3 A key assumption for efficient ROMs: affine parametric dependence

We need to ensure a further assumption on the operators appearing in (3.9)-(3.10), already at the full-order level. In fact, a key requirement for an efficient ROM evaluation is the capability to decouple the construction stage of the reduced-order space (offline) from the evaluation stage (online), thus featuring the so-called offline-online decomposition. To meet this goal, we require that matrices and vectors appearing in (3.9)-(3.10) can be written as

$$A(\boldsymbol{\mu}) = \sum_{q=1}^{Q_A} \Theta_q^A(\boldsymbol{\mu}) A^q, \qquad C(\underline{\mathbf{w}}; \boldsymbol{\mu}) = \sum_{q=1}^{Q_C} \Theta_q^C(\boldsymbol{\mu}) C^q(\underline{\mathbf{w}}), \qquad \underline{\mathbf{f}}(\boldsymbol{\mu}) = \sum_{q=1}^{Q_f} \Theta_q^f(\boldsymbol{\mu}) \underline{\mathbf{f}}^q,$$

and in a similar way for the other terms. When it is possible to express operators in such a way, we say that they fulfill the assumption of affine parametric dependence. This expression is straightforward to be obtained in case of (both physical and geometrical) affine parametrizations. Instead, when dealing with more general nonaffine parametrizations, an approximate affine expansion can be recovered by means of the empirical interpolation method (EIM) [28]. See e.g. [212] for further details. EIM will be required in the application of clinical interest when dealing with the geometrical parametrizations introduced in Chapter 5.

3.2 A POD-Galerkin ROM for parametrized Navier-Stokes equations

In this section we present a reduced-order model (ROM) for parametrized NS equations based on a Proper Orthogonal Decomposition technique and a Galerkin projection. In the context of parametrized PDEs, ROMs are usually based upon a suitable (and stable) combination of "snapshot" FE solutions, thus aiming at building reduced spaces $\boldsymbol{V}_N \subset \boldsymbol{V}_h$, $Q_N \subset Q_h$ of global approximation functions for velocity and pressure, respectively. At least two approaches in the construction stage of the reduced basis can be pursued: greedy algorithms and Proper Orthogonal Decomposition [156]. In this thesis we consider the latter [52, 57, 73, 116].

In the context of (possibly, unsteady) incompressible flows depending on physical parameters, POD-based ROMs usually aim at approximating just the velocity fields. This is motivated by the fact that each snapshot is already divergence free, and so all the pressure terms in the momentum equation drop out, that is, the continuity equation is automatically fulfilled. However, we are interested to get a reduced approximation of the pressure field too, either because of the application at hand (for example, it is of interest to recover the pressure field in the coronary artery applications because some clinical assessments of the stenosis severity in the pre-surgical stage are based on pressure measurements), or since the divergence-free assumption fails to hold due to the geometrical variation/parametrization. In this case, the reduced-order model will benefit of a standard Galerkin projection with orthonormal global approximation basis functions for both velocity and pressure, provided a suitable stabilization is introduced to fulfill an equivalent inf-sup condition and then recover correctly the pressure field.

3.2.1 A POD-Galerkin ROM for simultaneous approximation of velocity and pressure

We will first derive the formulation of our POD-Galerkin ROM, leaving the inf-sup stabilization issue to the following section. In particular, we adopt an algebraic standpoint, by considering the following bijection between the spaces $\mathbb{R}^{N_\mathbf{u}}$ and $\boldsymbol{V}_N$ (resp. $\mathbb{R}^{N_p}$ and Q_N):

$$\begin{cases} \underline{\mathbf{v}}_N = (v_N^{(1)}, \dots, v_N^{(N_\mathbf{u})})^T \in \mathbb{R}^{N_\mathbf{u}} \quad \leftrightarrow \quad \boldsymbol{v}_N = \displaystyle\sum_{n=1}^{N_\mathbf{u}} v_N^{(n)} \boldsymbol{\varphi}_n \in \boldsymbol{V}_N, \\ \underline{\mathbf{q}}_N = (q_N^{(1)}, \dots, q_N^{(N_p)})^T \in \mathbb{R}^{N_p} \quad \leftrightarrow \quad q_N = \displaystyle\sum_{n=1}^{N_p} q_N^{(n)} \zeta_n \in Q_N. \end{cases} \tag{3.11}$$

Let us denote by $\Xi_{\text{train}} = \{\boldsymbol{\mu}^1, \dots, \boldsymbol{\mu}^{N_{\text{train}}}\} \subset \mathcal{D}$ a (large) training sample of N_{train} points chosen randomly over $\mathcal{D}$, and consider the *snapshot matrices*

$$S_\mathbf{u} = [\underline{\mathbf{u}}(\boldsymbol{\mu}^1) \mid \dots \mid \underline{\mathbf{u}}(\boldsymbol{\mu}^{N_{\text{train}}})] \in \mathbb{R}^{N_\mathbf{u}^h \times N_{\text{train}}}, \qquad S_p = [\underline{\mathbf{p}}(\boldsymbol{\mu}^1) \mid \dots \mid \underline{\mathbf{p}}(\boldsymbol{\mu}^{N_{\text{train}}})] \in \mathbb{R}^{N_p^h \times N_{\text{train}}}.$$

Here we take $N_{\text{train}} < N_p^h$ since we assume to deal with a very fine FE discretization, where $N_\mathbf{u}^h > N_p^h \gg 1$. A POD basis for the velocity and pressure spaces can be obtained by considering the singular value decomposition (SVD) of the following matrices

$$X_\mathbf{u}^{1/2} S_\mathbf{u} = U_\mathbf{u} \Sigma_\mathbf{u} W_\mathbf{u}^T, \qquad X_p^{1/2} S_p = U_p \Sigma_p W_p^T$$

where

- $U_\mathbf{u} \in \mathbb{R}^{N_\mathbf{u}^h \times N_{\text{train}}}$ and $U_p \in \mathbb{R}^{N_p^h \times N_{\text{train}}}$ are two matrices containing the first N_{train} left singular vectors;

- $W_{\mathbf{u}} \in \mathbb{R}^{N_{\text{train}} \times N_{\text{train}}}$ and $W_p \in \mathbb{R}^{N_{\text{train}} \times N_{\text{train}}}$ are two orthogonal matrices of right singular vectors;
- $\Sigma_{\mathbf{u}} \in \mathbb{R}^{N_{\text{train}} \times N_{\text{train}}}$ and $\Sigma_p \in \mathbb{R}^{N_{\text{train}} \times N_{\text{train}}}$ are two diagonal matrices, made by the *singular values* of $S_{\mathbf{u}}$ and S_p, so that $(\Sigma_{\mathbf{u}})_{ii} = \sigma_i^{\mathbf{u}}$ with $\sigma_1^{\mathbf{u}} \geq \ldots \geq \sigma_{N_{\text{train}}}^{\mathbf{u}} \geq 0$, $(\Sigma_p)_{ii} = \sigma_i^p$ with $\sigma_1^p \geq \ldots \geq \sigma_{N_{\text{train}}}^p \geq 0$.

In fact, for any $N_{\mathbf{u}}, N_p < N_{\text{train}}$, the POD basis (of dimension $N_{\mathbf{u}}$, N_p) is given by the first $N_{\mathbf{u}}, N_p$ columns of $U_{\mathbf{u}}, U_p$, respectively (left singular vectors). In this way, we can define

$$Z_{\mathbf{u}} = [\underline{\boldsymbol{\varphi}}_1 \mid \ldots \mid \underline{\boldsymbol{\varphi}}_{N_{\mathbf{u}}}] \in \mathbb{R}^{N_{\mathbf{u}}^h \times N_{\mathbf{u}}}, \qquad Z_p = [\underline{\zeta}_1 \mid \ldots \mid \underline{\zeta}_{N_p}] \in \mathbb{R}^{N_p^h \times N_p}$$

as the basis matrices for velocity and pressure, respectively. Thus, the basis functions of spaces $\boldsymbol{V}_N$ and Q_N are FE solutions, expressed w.r.t. a Lagrangian FE basis by the components of the columns of $Z_{\mathbf{u}}$, Z_p, respectively. A slightly different option, which however might be affected by worse conditioning, relies on the solution of the so-called *method of snapshots* [244]. In this case, we shall solve two eigenproblems for the correlation matrices

$$C_{\mathbf{u}} = S_{\mathbf{u}}^T X_{\mathbf{u}} S_{\mathbf{u}} \in \mathbb{R}^{N_{\text{train}} \times N_{\text{train}}}, \qquad C_p = S_p^T X_p S_p \in \mathbb{R}^{N_{\text{train}} \times N_{\text{train}}}$$

and defines the POD bases for velocity and pressure spaces as their first $N_{\mathbf{u}}$ (resp. N_p) eigenvectors:

$$\underline{\boldsymbol{\varphi}}_j = \frac{1}{\sqrt{\lambda_j^{\mathbf{u}}}} S_{\mathbf{u}} \underline{\boldsymbol{\psi}}_j^{\mathbf{u}}, \qquad \underline{\zeta}_l = \frac{1}{\sqrt{\lambda_l^p}} S_p \underline{\psi}_l^p, \qquad j = 1, \ldots, N_{\mathbf{u}},\ l = 1, \ldots, N_p,$$

being

$$C_{\mathbf{u}} \underline{\boldsymbol{\psi}}_j^{\mathbf{u}} = \lambda_j^{\mathbf{u}} \underline{\boldsymbol{\psi}}_j^{\mathbf{u}}, \qquad C_p \underline{\psi}_l^p = \lambda_l^p \underline{\psi}_l^p, \qquad j = 1, \ldots, N_{\mathbf{u}},\ l = 1, \ldots, N_p$$

and $\lambda_j^{\mathbf{u}} = (\sigma_j^{\mathbf{u}})^2$, $\lambda_l^p = (\sigma_l^p)^2$, respectively. Basis functions are automatically orthonormal, since

$$(\underline{\boldsymbol{\varphi}}_i, \underline{\boldsymbol{\varphi}}_j)_{\boldsymbol{V}} = \frac{1}{\sqrt{\lambda_i^{\mathbf{u}} \lambda_j^{\mathbf{u}}}} (\underline{\boldsymbol{\psi}}_i^{\mathbf{u}}, S_{\mathbf{u}}^T X_{\mathbf{u}} S_{\mathbf{u}} \underline{\boldsymbol{\psi}}_j^{\mathbf{u}}) = \frac{1}{\sqrt{\lambda_i^{\mathbf{u}} \lambda_j^{\mathbf{u}}}} (\underline{\boldsymbol{\psi}}_i^{\mathbf{u}}, \lambda_j^{\mathbf{u}} \underline{\boldsymbol{\psi}}_j^{\mathbf{u}}) = \sqrt{\frac{\lambda_j^{\mathbf{u}}}{\lambda_i^{\mathbf{u}}}} \delta_{ij}, \tag{3.12}$$

$$(\underline{\zeta}_k, \underline{\zeta}_l)_Q = \frac{1}{\sqrt{\lambda_k^p \lambda_l^p}} (\underline{\psi}_k^p, S_p^T X_p S_p \underline{\psi}_l^p) = \frac{1}{\sqrt{\lambda_k^p \lambda_l^p}} (\underline{\psi}_k^p, \lambda_l^p \underline{\psi}_l^p) = \sqrt{\frac{\lambda_l^p}{\lambda_k^p}} \delta_{kl}. \tag{3.13}$$

We remark that the reduced spaces dimensions $N_{\mathbf{u}}$, N_p can be chosen as the smallest integers for which the "energy" of the retained modes

$$E^{\mathbf{u}}(\boldsymbol{\varphi}_1, \ldots, \boldsymbol{\varphi}_{N_{\mathbf{u}}}) = \frac{\sum_{j=1}^{N_{\mathbf{u}}} (\sigma_j^{\mathbf{u}})^2}{\sum_{j=1}^{N_{\text{train}}} (\sigma_j^{\mathbf{u}})^2}, \qquad E^p(\zeta_1, \ldots, \zeta_{N_p}) = \frac{\sum_{l=1}^{N_p} (\sigma_l^p)^2}{\sum_{l=1}^{N_{\text{train}}} (\sigma_l^p)^2}$$

is greater than $1 - \varepsilon_{tol}^*$, for some prescribed (small) tolerance ε_{tol}^*.

3.2.2 Algebraic formulation of the POD-Galerkin ROM

Once we have obtained two orthonormal sets of basis functions for the spaces $\boldsymbol{V}_N$ and Q_N, we seek for a reduced-order approximation of both velocity and pressure field under the form

$$\underline{\mathbf{u}}(\boldsymbol{\mu}) \approx Z_{\mathbf{u}} \underline{\mathbf{u}}_N(\boldsymbol{\mu}), \qquad \underline{\mathbf{p}}(\boldsymbol{\mu}) \approx Z_p \underline{\mathbf{p}}_N(\boldsymbol{\mu}). \tag{3.14}$$

In our case, for any $\boldsymbol{\mu} \in \mathcal{D}$, $\underline{\mathbf{u}}_N(\boldsymbol{\mu}) \in \mathbb{R}^{N_\mathbf{u}}$, $\underline{\mathbf{p}}_N(\boldsymbol{\mu}) \in \mathbb{R}^{N_p}$ are determined through a Galerkin projection, that is, we impose that the residual (obtained by inserting (3.14) in (3.8)) is orthogonal to the columns of $Z_\mathbf{u}$, Z_p:

$$\begin{bmatrix} Z_\mathbf{u}^T & O \\ O & Z_p^T \end{bmatrix} \begin{bmatrix} \underline{\mathbf{f}}(\boldsymbol{\mu}) - (A(\boldsymbol{\mu}) + C(Z_\mathbf{u}\underline{\mathbf{u}}_N(\boldsymbol{\mu}); \boldsymbol{\mu}))Z_\mathbf{u}\underline{\mathbf{u}}_N(\boldsymbol{\mu}) - B^T(\boldsymbol{\mu})Z_\mathbf{u}\underline{\mathbf{p}}_N(\boldsymbol{\mu}) \\ \underline{\mathbf{g}}(\boldsymbol{\mu}) - B(\boldsymbol{\mu})Z_\mathbf{u}\underline{\mathbf{u}}_N(\boldsymbol{\mu}) \end{bmatrix} = \begin{bmatrix} \underline{\mathbf{0}} \\ \underline{\mathbf{0}} \end{bmatrix}.$$

Thus, once we have built the reduced basis for both velocity and pressure fields (during the offline stage), for any new parameter value $\boldsymbol{\mu} \in \mathcal{D}$ the following reduced-order problem has to be solved (at the online stage) to find the NS reduced-order approximation:

$$\begin{bmatrix} A_N(\boldsymbol{\mu}) + C_N(\underline{\mathbf{u}}_N(\boldsymbol{\mu}); \boldsymbol{\mu}) & B_N^T(\boldsymbol{\mu}) \\ B_N(\boldsymbol{\mu}) & 0 \end{bmatrix} \begin{bmatrix} \underline{\mathbf{u}}_N(\boldsymbol{\mu}) \\ \underline{\mathbf{p}}_N(\boldsymbol{\mu}) \end{bmatrix} = \begin{bmatrix} \underline{\mathbf{f}}_N(\boldsymbol{\mu}) \\ \underline{\mathbf{g}}_N(\boldsymbol{\mu}) \end{bmatrix}. \tag{3.15}$$

Similarly to what shown in [178], [210, Chapter 19],

$$A_N(\boldsymbol{\mu}) = Z_\mathbf{u}^T\ A(\boldsymbol{\mu})\ Z_\mathbf{u}, \qquad B_N(\boldsymbol{\mu}) = Z_p^T\ B(\boldsymbol{\mu})\ Z_\mathbf{u}, \qquad C_N(\ \cdot\ ; \boldsymbol{\mu}) = Z_\mathbf{u}^T C(\ \cdot\ ; \boldsymbol{\mu}) Z_\mathbf{u}; \tag{3.16}$$

in the same way, for the right-hand sides we have

$$\underline{\mathbf{f}}_N(\boldsymbol{\mu}) = Z_\mathbf{u}^T\ \underline{\mathbf{f}}(\boldsymbol{\mu}), \qquad \underline{\mathbf{g}}_N(\boldsymbol{\mu}) = Z_p^T\ \underline{\mathbf{g}}(\boldsymbol{\mu}).$$

We point out that this offline-online decomposition is made possible thanks to the assumption of affine parametric dependence (see Section 3.1.3).Nevertheless, this features some extra difficulties in order to handle nonlinear terms in an efficient way. Our current approach is to store the third order tensor

$$C_N(\boldsymbol{\varphi}_j; \boldsymbol{\mu}) = Z_\mathbf{u}^T C(\boldsymbol{\varphi}_j; \boldsymbol{\mu}) Z_\mathbf{u}, \quad \forall j = 1, \dots, N_\mathbf{u}$$

in order to compute, at each fixed point iteration, the nonlinear term as

$$C_N(\underline{\mathbf{u}}_N(\boldsymbol{\mu}); \boldsymbol{\mu}) = \sum_{j=1}^{N_\mathbf{u}} u_N^{(j)} C_N(\boldsymbol{\varphi}_j; \boldsymbol{\mu})$$

and preserve the offline-online decomposition. We remark however that such (dense) third order tensor may entail high storage costs; recent alternative approaches make use of a discrete empirical interpolation method [275] or hyper-reduction techniques, such as *gappy POD* [62], or again compressive tensor approximations [61] to alleviate this problem.

3.3 Stability analysis and supremizer enrichment

In this Section we show how to obtain, starting from the POD modes, a couple of reduced spaces for velocity and pressure which fulfill a (reduced version of the) Ladyzhenskaya-Babuška-Brezzi (LBB) inf-sup condition. To this goal, we provide a detailed stability analysis of the POD-Galerkin ROM we have previously derived.

3.3.1 Stability of the full-order approximation and characterization of the stability factor $\beta_h(\boldsymbol{\mu})$

In view of the analysis of the POD-Galerkin ROM, let us briefly recall the conditions ensuring the full-order problem (3.8) to be solvable and stable. A deeper analysis can be found e.g. in [47,48], whereas we refer to [178] for further details about the analysis in the parametrized case.

For any $\boldsymbol{\mu} \in \mathcal{D}$, at each step $k = 1, 2, \dots$ of the fixed point iteration we need to solve the linear system obtained from (3.8) by replacing $C(\underline{\mathbf{u}}(\boldsymbol{\mu}); \boldsymbol{\mu})$ with $C(\underline{\mathbf{z}}(\boldsymbol{\mu}); \boldsymbol{\mu})$, being at each

step $\underline{\mathbf{z}}(\boldsymbol{\mu}) = \underline{\mathbf{u}}^{(k)}(\boldsymbol{\mu})$. In order to avoid pressure instability, we require that the spaces $\boldsymbol{V}_h$ and Q_h are chosen in such a way that there exists $\tilde{\beta}_h > 0$ such that

$$\beta_h(\boldsymbol{\mu}) = \inf_{\underline{\mathbf{q}} \neq \underline{\mathbf{0}}} \sup_{\underline{\mathbf{v}} \neq \underline{\mathbf{0}}} \frac{\underline{\mathbf{q}}^T B(\boldsymbol{\mu}) \underline{\mathbf{v}}}{\|\underline{\mathbf{v}}\|_{\boldsymbol{V}} \|\underline{\mathbf{q}}\|_Q} \geq \tilde{\beta}_h > 0 \qquad \forall \boldsymbol{\mu} \in \mathcal{D}. \tag{LBB$_h$}$$

This relation is nothing but the parametrized version of the LBB condition, and guarantees the unique solvability of (3.8) with respect to the pressure – that is, it prevents (3.8) from being indefinite. This requirement is met if, e.g., the Taylor-Hood ($\mathbb{P}_2$-$\mathbb{P}_1$) FE spaces are chosen. In particular, condition (LBB$_h$) implies that $\dim(\ker(B^T(\boldsymbol{\mu}))) = 0$, so that no *spurious pressure modes* appear at the numerical level. Moreover, we must have $N_{\mathbf{u}}^h \geq N_p^h$; as we will detail later on, it is mandatory to ensure a similar condition at the reduced-order level, too, and to provide a suitable criterion to check its validity.

In order to evaluate the stability factor $\beta_h(\boldsymbol{\mu})$ numerically, we can express it (see [23, Section 4.1] and references therein) as

$$\beta_h(\boldsymbol{\mu}) = \sqrt{\lambda_1(\boldsymbol{\mu})}, \tag{3.17}$$

where $\lambda_1(\boldsymbol{\mu})$ denotes the minimum eigenvalue solution of the following generalized eigenvalue problem:

$$\begin{bmatrix} X_{\mathbf{u}} & B^T(\boldsymbol{\mu}) \\ B(\boldsymbol{\mu}) & O \end{bmatrix} \begin{bmatrix} \underline{\mathbf{v}} \\ \underline{\mathbf{q}} \end{bmatrix} = -\lambda(\boldsymbol{\mu}) \begin{bmatrix} O & O \\ O & X_p \end{bmatrix} \begin{bmatrix} \underline{\mathbf{v}} \\ \underline{\mathbf{q}} \end{bmatrix}. \tag{3.18}$$

Moreover, for any $\underline{\mathbf{q}} \neq \underline{\mathbf{0}}$, the corresponding *supremizer* is defined as the solution $\underline{\mathbf{s}}^{\boldsymbol{\mu}} = \underline{\mathbf{s}}^{\boldsymbol{\mu}}(\underline{\mathbf{q}})$ of the following problem

$$X_{\mathbf{u}} \underline{\mathbf{s}}^{\boldsymbol{\mu}}(\underline{\mathbf{q}}) = B^T(\boldsymbol{\mu}) \underline{\mathbf{q}}. \tag{3.19}$$

The name *supremizer* derives from the fact that $\underline{\mathbf{s}}^{\boldsymbol{\mu}}(\underline{\mathbf{q}})$ is the element which, given $\underline{\mathbf{q}} \in Q$, realizes the supremum in (LBB$_h$), that is,

$$\underline{\mathbf{s}}^{\boldsymbol{\mu}}(\underline{\mathbf{q}}) = \arg\sup_{\underline{\mathbf{v}} \neq \underline{\mathbf{0}}} \frac{(\underline{\mathbf{q}}, B(\boldsymbol{\mu}) \underline{\mathbf{v}})}{\|\underline{\mathbf{v}}\|_{\boldsymbol{V}}}. \tag{3.20}$$

We refer to [23, Proposition 1] for a proof of this statement.

3.3.2 Stability of the POD approximation and supremizer enrichment of the reduced velocity space

Great care is required in order to build compatible reduced approximation spaces for velocity and pressure so that an equivalent LBB condition holds at the reduced-order level, thus ensuring the stability of the pressure field approximated through our POD-Galerkin ROM (3.15). We point out that our effort is made in order to avoid spurious pressure modes, and not to cure the stability loss due to higher Reynolds numbers – the latter issue will not be addressed in this thesis, since the application we focus on are associated with moderate Reynolds numbers, not yielding to strong convection dominated problems.

Following Section 3.3.1, let us now discuss under which conditions the POD-Galerkin ROM (3.15) leads to a stable pressure approximation. For any $\boldsymbol{\mu} \in \mathcal{D}$, at each step $k = 1, 2, \ldots$ of the *online* fixed point iteration, we need to solve the linear system obtained from (3.15) by replacing $C_N(\underline{\mathbf{u}}_N(\boldsymbol{\mu}); \boldsymbol{\mu})$ with $C_N(\underline{\mathbf{z}}_N(\boldsymbol{\mu}); \boldsymbol{\mu})$, being at each step $\underline{\mathbf{z}}_N(\boldsymbol{\mu}) = \underline{\mathbf{u}}_N^{(k)}(\boldsymbol{\mu})$. In order to avoid pressure instability, we require that there exists $\tilde{\beta}_N > 0$ such that

$$\beta_N(\boldsymbol{\mu}) = \inf_{\underline{\mathbf{q}}_N \neq \underline{\mathbf{0}}} \sup_{\underline{\mathbf{v}}_N \neq \underline{\mathbf{0}}} \frac{\underline{\mathbf{q}}_N^T B_N(\boldsymbol{\mu}) \underline{\mathbf{v}}_N}{\|\underline{\mathbf{v}}_N\|_{\boldsymbol{V}_N} \|\underline{\mathbf{q}}_N\|_{Q_N}} \geq \tilde{\beta}_N > 0 \qquad \forall \boldsymbol{\mu} \in \mathcal{D}. \tag{LBB$_N$}$$

A key point is that, even though the velocity basis functions are obtained through a stable full-order model, a Galerkin projection over the reduced spaces built as in (3.15) does not guarantee the fulfillment of the reduced LBB condition (LBB_N).

For this reason, we need to enrich the velocity space in a suitable way, so that (LBB_N) can be satisfied. Inspired by the current state of the art in the greedy-RB setting (see e.g. [106, 221, 222] and different approaches therein) we propose to enrich the velocity space $\boldsymbol{V}_N$ with properly chosen *supremizer solutions*. We have described in detail in [23] two possible strategies (*exact supremizer enrichment* and *approximate supremizer enrichment*) for generating $N_{\mathbf{s}}$ supremizer basis functions, resulting in a less or more efficient offline-online algorithm. In both cases, the enrichment algorithm provides a supremizer basis functions matrix

$$Z_{\mathbf{s}} = [\underline{\boldsymbol{\eta}}_1 \mid \ldots \mid \underline{\boldsymbol{\eta}}_{N_{\mathbf{s}}}] \in \mathbb{R}^{N_{\mathbf{u}}^h \times N_{\mathbf{s}}}.$$

Note that $Z_{\mathbf{s}}$ may depend on $\boldsymbol{\mu}$ and N_p, but this dependence is omitted hereon. Then, we define a velocity space $\tilde{\boldsymbol{V}}_N$ of dimension $N_{\mathbf{u}}+N_{\mathbf{s}}$, as the direct sum of velocity and supremizer basis functions, where

$$\underline{\mathbf{v}}_N = (v_N^{(1)}, \ldots, v_N^{(N_{\mathbf{u}})}, s_N^{(1)}, \ldots, s_N^{(N_{\mathbf{s}})})^T \in \mathbb{R}^{N_{\mathbf{u}}+N_{\mathbf{s}}} \quad \leftrightarrow \quad \boldsymbol{v}_N = \sum_{n=1}^{N_{\mathbf{u}}} v_N^{(n)} \boldsymbol{\varphi}_n + \sum_{m=1}^{N_{\mathbf{s}}} s_N^{(m)} \boldsymbol{\eta}_m \in \tilde{\boldsymbol{V}}_N$$

replaces $(3.11)_1$. From now on, we will omit the superscript $\sim$ for the enriched velocity space, and still denote it by $\boldsymbol{V}_N$. Moreover, let us define by

$$(\underline{\mathbf{v}}_N, \underline{\mathbf{w}}_N)_{\boldsymbol{V}_N} = (X_{\mathbf{u}}^N \underline{\mathbf{v}}_N, \underline{\mathbf{w}}_N), \qquad (\underline{\mathbf{p}}_N, \underline{\mathbf{q}}_N)_{Q_N} = (X_p^N \underline{\mathbf{p}}_N, \underline{\mathbf{q}}_N) \tag{3.21}$$

the inner products in the reduced spaces, where $X_{\mathbf{u}}^N$ and X_p^N are the reduced mass matrices for velocity and pressure fields, respectively, defined as

$$X_{\mathbf{u}}^N = \begin{bmatrix} X_{\mathbf{u}}^{N,\mathbf{uu}} & X_{\mathbf{u}}^{N,\mathbf{us}} \\ X_{\mathbf{u}}^{N,\mathbf{su}} & X_{\mathbf{u}}^{N,\mathbf{ss}} \end{bmatrix} = \begin{bmatrix} Z_{\mathbf{u}}^T X_{\mathbf{u}} Z_{\mathbf{u}} & Z_{\mathbf{u}}^T X_{\mathbf{u}} Z_{\mathbf{s}} \\ Z_{\mathbf{s}}^T X_{\mathbf{u}} Z_{\mathbf{u}} & Z_{\mathbf{s}}^T X_{\mathbf{u}} Z_{\mathbf{s}} \end{bmatrix}, \qquad X_p^N = Z_p^T X_p Z_p. \tag{3.22}$$

In particular, owing to the orthonormality of basis functions in $Z_{\mathbf{u}}$ (see (3.12)), $Z_{\mathbf{s}}$ and Z_p (see (3.13)), $X_{\mathbf{u}}^{N,\mathbf{uu}}$, $X_{\mathbf{u}}^{N,\mathbf{ss}}$ and X_p^N are identity matrices; this property enhances the algebraic stability of the resulting ROM. However, we remark that the extra diagonal blocks $X_{\mathbf{u}}^{N,\mathbf{us}}$ and $X_{\mathbf{u}}^{N,\mathbf{su}}$ do not vanish because velocity and supremizer basis functions are not mutually orthogonal. The other reduced data structures ($A_N(\boldsymbol{\mu})$, $B_N(\boldsymbol{\mu})$, etc.) can be redefined in a similar way.

The first option, to which we refer as *exact* supremizer enrichment, is to enrich the velocity space is to consider, for any pressure basis function, the solution of problem (3.19), according to the following algorithm:

Algorithm 3.1 Exact supremizer enrichment.

STAGE: online
INPUT: current parameter $\boldsymbol{\mu}$ (online query), N_p, Z_p;
OUTPUT: supremizer basis functions matrix $Z_{\mathbf{s}}$, $N_{\mathbf{s}}$;
for $k = 1, \ldots, N_p$ **do**
  solve (3.19) to obtain the supremizer $\underline{\mathbf{s}}^{\boldsymbol{\mu}}(\underline{\zeta}_k)$ corresponding to the k-th basis function $\underline{\zeta}_k$;
end for
orthonormalize the set $\{\underline{\mathbf{s}}^{\boldsymbol{\mu}}(\underline{\zeta}_k)\}_{k=1}^{N_p}$ (Gram-Schmidt procedure or POD);
store the corresponding basis functions in the matrix $Z_{\mathbf{s}} = Z_{\mathbf{s}}(\boldsymbol{\mu}, N_p)$;
define $N_{\mathbf{s}} := N_p$;

Similarly to the greedy-RB case, this option, which we have described in detail in [23, Section 4.2.2], guarantees that enriching the velocity space with $N_{\mathbf{s}} = N_p$ supremizers ensures

the fulfillment of the reduced inf-sup condition (LBB_N) and, moreover, also that

$$\beta_N(\boldsymbol{\mu}) \geq \beta_h(\boldsymbol{\mu}) > 0 \qquad \forall \boldsymbol{\mu} \in \mathcal{D}, \tag{3.23}$$

where, similarly to (3.18), $\beta_N(\boldsymbol{\mu})$ is the square root of the minimum eigenvalue of the following reduced-order eigenproblem:

$$\begin{bmatrix} X_{\mathbf{u}}^N & B_N(\boldsymbol{\mu})^T \\ B_N(\boldsymbol{\mu}) & O \end{bmatrix} \begin{bmatrix} \underline{\mathbf{v}}_N(\boldsymbol{\mu}) \\ \underline{\mathbf{q}}_N(\boldsymbol{\mu}) \end{bmatrix} = -\lambda(\boldsymbol{\mu}) \begin{bmatrix} O & O \\ O & X_p^N \end{bmatrix} \begin{bmatrix} \underline{\mathbf{v}}_N(\boldsymbol{\mu}) \\ \underline{\mathbf{q}}_N(\boldsymbol{\mu}) \end{bmatrix}. \tag{3.24}$$

However, this strategy to enrich the velocity space is hard to be employed in practice. In fact, the evaluation of the *exact* supremizers $\underline{\mathbf{s}}^{\boldsymbol{\mu}}(\cdot)$ would lead to a $\boldsymbol{\mu}$-dependent velocity space because of the dependence on $B^T(\boldsymbol{\mu})$ in (3.19), and thus would deteriorate the offline-online efficiency. Not only, condition (3.23) might be in some cases too restrictive, that is, it is enough to have $\beta_N(\boldsymbol{\mu}) > 0$ without necessarily require that $\beta_N(\boldsymbol{\mu}) \geq \beta_h(\boldsymbol{\mu})$. For this reason, in the same spirit of the RB methods (see e.g. [106, 221, 222]) an *approximate* supremizer enrichment is rather preferred.

The *approximate* supremizer enrichment algorithm, instead, is based on the solution of (3.19) for each pressure snapshot (rather than for each pressure basis function), at the corresponding value of the parameters, and thus can be entirely performed during the offline stage, thus allowing a very efficient online evaluation of the NS solution, as follows:

Algorithm 3.2 Approximate supremizer enrichment.

STAGE: offline
INPUT: training sample $\Xi_{\text{train}} = \{\boldsymbol{\mu}^1, \dots, \boldsymbol{\mu}^{N_{\text{train}}}\}$.
OUTPUT: supremizer basis functions matrix $Z_{\mathbf{s}}$, $N_{\mathbf{s}}$;
for $j = 1, \dots, N_{\text{train}}$ **do**
  solve (3.19) to obtain the supremizer $\underline{\mathbf{s}}^{\boldsymbol{\mu}^j}(\underline{\mathbf{p}}(\boldsymbol{\mu}^j))$ corresponding to the j-th pressure snapshot;
end for
define $S_{\mathbf{s}} = [\underline{\mathbf{s}}^{\boldsymbol{\mu}^1}(\underline{\mathbf{p}}(\boldsymbol{\mu}^1)) \mid \dots \mid \underline{\mathbf{s}}^{\boldsymbol{\mu}^{N_{\text{train}}}}(\underline{\mathbf{p}}(\boldsymbol{\mu}^{N_{\text{train}}}))]$;
compute a POD basis of $\{\underline{\mathbf{s}}^{\boldsymbol{\mu}^j}(\underline{\mathbf{p}}(\boldsymbol{\mu}^j))\}_{j=1}^{N_{\text{train}}}$ by performing the SVD of $X_{\mathbf{u}}^{1/2} S_{\mathbf{s}}$;
store $N_{\mathbf{s}} < N_{\text{train}}$ supremizer modes in the matrix $Z_{\mathbf{s}}$;

Compared to the exact enrichment, this algorithm allows to get a strong reduction of online computational costs, because the matrix $Z_{\mathbf{s}}$ does *not* depend on $\boldsymbol{\mu}$ and N_p anymore. Moreover, $N_{\mathbf{s}}$ can be chosen different from N_p. However, by relying on *approximate* supremizers, it is not possible to rigorously show that (3.23) holds. Instead, we can provide some heuristic criteria to ensure (or, possibly, to check in a post-processing stage) that $\beta_N(\boldsymbol{\mu}) > 0$, thus yielding pressure stability in the sense of (LBB_N)). This is the goal of the following sections. We refer to [23, Section 4.2.3] for additional details and comments on this procedure.

3.4 Heuristic criteria for online supremizer enrichment

In this Section we give further insights on the stability of the POD-Galerkin ROM, and provide some practical criteria for the online supremizer enrichment.

The aim of this Section, as well as of the numerical results presented in the next Section, is to investigate pressure stability by providing an answer to the following questions:

Q1. for which values of $(N_{\mathbf{u}}, N_{\mathbf{s}}, N_p)$ is the online system (3.15) stable, i.e. when does it satisfy the condition (LBB_N) ?

Q2. which values of $(N_{\mathbf{u}}, N_{\mathbf{s}}, N_p)$ prevent an online locking phenomenon to occur?

Q3. for which values of $(N_{\mathbf{u}}, N_{\mathbf{s}}, N_p)$ does the POD-Galerkin ROM satisfy the inf-sup condition in the sense of relation (3.23) (that is, provided that condition (LBB_h) is satisfied at the full-order level)?

As shown in Section 3.2, a computation of the inf-sup constant can be carried out in order to check the online stability of the reduced-order model. Question Q1 is thus related to the dimension of $\ker(B_N(\boldsymbol{\mu})^T)$, that is, to the possible occurrence of spurious pressure modes for the reduced-order model. As of question Q2, locking phenomena occur if $\beta_N(\boldsymbol{\mu}) \to 0$ as N "increases". Finally, question Q3 is equivalent to check whether the inequality $\beta_N(\boldsymbol{\mu}) \geq \beta_h(\boldsymbol{\mu})$ holds. An a priori practical criterion for online supremizer enrichment is detail in the following subsections and is inspired by question Q1. More insights on questions Q2 and Q3 have been discussed in [23, Section 6] through several numerical results. Section 3.5 report a brief summary of these results.

3.4.1 Case I: physical parametrization only

In the case of parametrized problems involving only physical parameters, a criterion for choosing the number $N_{\mathbf{s}}$ of supremizer is to assume that $N_{\mathbf{s}} \geq N_p$. As a matter of fact, let us consider the matrix

$$B_N(\boldsymbol{\mu})^T = \begin{bmatrix} B_{N,p\mathbf{u}}(\boldsymbol{\mu})^T \\ B_{N,p\mathbf{s}}(\boldsymbol{\mu})^T \end{bmatrix} \in \mathbb{R}^{(N_{\mathbf{u}}+N_{\mathbf{s}})\times N_p}$$

where $B_{N,p\mathbf{s}}(\boldsymbol{\mu})^T \in \mathbb{R}^{N_{\mathbf{s}}\times N_p}$, $B_{N,p\mathbf{u}}(\boldsymbol{\mu})^T \in \mathbb{R}^{N_{\mathbf{u}}\times N_p}$. The block $B_{N,p\mathbf{u}}(\boldsymbol{\mu})^T$ is identically zero because each velocity basis function is divergence free. Then, a necessary condition for $B_N(\boldsymbol{\mu})^T$ to be full-rank is that $N_{\mathbf{s}} \geq N_p$. More insights on the practical convenience entailed by choosing $N_{\mathbf{s}} = N_p$ or $N_{\mathbf{s}} > N_p$ will be given in the next section.

3.4.2 Case II: physical and geometrical parametrization

In the case of both physical and geometrical parameters, a possible criterion for the online supremizer enrichment is based on the following result:

Proposition 3.1. *Let $\lambda_N^k(\boldsymbol{\mu}) > 0$, $k = k(N_{\mathbf{u}}, N_{\mathbf{s}}, N_p; \boldsymbol{\mu}) \in \mathbb{N}$, be the first non-null eigenvalue of the generalized eigenvalue problem* (3.24)*. The following relation holds:*

$$k_{pm} = k - 1 + N_p - N_{\mathbf{u}} - N_{\mathbf{s}} > 0 \quad \Longrightarrow \quad \dim(\ker\, B_N(\boldsymbol{\mu})^T) > 0.$$

Proof. Equivalently, we shall prove the following:

$$\dim(\ker\, B_N(\boldsymbol{\mu})^T) = 0 \quad \Longrightarrow \quad k_{\mathrm{pm}} = k - 1 + N_p - N_{\mathbf{u}} - N_{\mathbf{s}} \leq 0.$$

For the sake of brevity the dependence on $\boldsymbol{\mu}$ is omitted. Let

$$M_N = \begin{bmatrix} X_{\mathbf{u}}^N & B_N^T \\ B_N & O \end{bmatrix}, \qquad S_N = B_N\, (X_{\mathbf{u}}^N)^{-1}\, B_N^T.$$

1. From (3.24), it follows that $\dim(\ker\, M_N) = k - 1$. Moreover, from the Guttman rank additivity formula
$$\mathrm{rank}\, M_N = \mathrm{rank}\, X_{\mathbf{u}}^N + \mathrm{rank}\, S_N,$$
it follows that
$$\dim(\ker\, S_N) = N_p - \mathrm{rank}\, M_N + \mathrm{rank}\, X_{\mathbf{u}}^N = k - 1.$$

Case	**Case I**	**Case II**
Physical parameters	2: ν, u_{in}	2: ν, u_{in}
Range ν	[0.05, 2]	[0.05, 2]
Range u_{in}	[0.5, 5]	[0.5, 5]
Resulting range of Reynolds number	[0.75, 300]	[0.75, 300]
Geometrical parameters	0	1: H_o
Range H_o/H	–	[0.5, 1.5]
N_{train}	300	300
POD offline CPU time	3 $h \times 6$ processors	5 $h \times 6$ processors
$N_{\max}$	100	100

Table 3.1: *Computational details of the offline stage of the test cases.*

2. Furthermore, we have

$$\dim(\ker B_N^T) = N_p - \text{rank } B_N^T = N_p - \text{rank } B_N = N_p - N_{\mathbf{u}} - N_{\mathbf{s}} + \dim(\ker B_N).$$

3. Finally, owing to the hypothesis $\dim(\ker B_N(\boldsymbol{\mu})^T) = 0$ and the invertibility of $X_{\mathbf{u}}^N$,

$$k - 1 = \dim(\ker S_N) = \dim[((X_{\mathbf{u}}^N)^{-1} B_N^T)^{-1}(\ker B_N)] \leq$$
$$\leq \dim[\ker((X_{\mathbf{u}}^N)^{-1} B_N^T)] + \dim(\ker B_N) = N_{\mathbf{u}} + N_{\mathbf{s}} - N_p.$$

□

The previous proposition is an extension to the ROM framework of a similar result holding for the full-order model (see e.g. [31]). We rely on this criterion in the numerical results in Section 3.5 to detect the existence of spurious pressure modes; in practice this criterion is able to discard the choice $N_{\mathbf{s}} = 0$.

3.5 Numerical results and analysis of the ROM

3.5.1 Case I: physical parameters only

In this section an analysis of the ROM is performed for the case of physical parametrization. A bidimensional configuration of a backward facing step is considered in this section, with parametrization of Reynolds number in the interval $[0.75, 300]$. A Taylor-Hood $\mathbb{P}_2 - \mathbb{P}_1$ FE discretization has been considered for the full-order model, in order to compare stability factors between the FOM and ROM. Computational details of the offline stage are summarized in Table 3.1 (left column). We refer to [23, Section 6] for additional details on both the offline and online stages and some representative solutions.

Figures 3.1 and 3.2 report stability factors $\beta_N(\boldsymbol{\mu})$ and relative errors for some representative values of the Reynolds number and different choices $N_{\mathbf{s}}$ and $N_{\mathbf{u}} = N_p$. These results provide a useful insight, showing that, in the case of physical parameters only, it is sufficient to consider $N_{\mathbf{s}} \geq N_p$ supremizers to obtain both a stable ROM and to provide numerical evidence that $\beta_N(\boldsymbol{\mu}) \geq \beta_h(\boldsymbol{\mu})$. Instead, if $N_{\mathbf{s}} < N_p$, the ROM is not stable in the sense of (LBB_N), as $\beta_N(\boldsymbol{\mu}) = 0$. We underline again that the supremizers are subject to a POD procedure, too: with respect to the most expensive *exact* supremizer options with online parametric dependence, the less expensive *approximate* option is successfully exploited.

We also remark that, although necessary to obtain a stable system, ROM solution components corresponding to supremizer basis functions are actually smaller than the smallest component related to (divergence-free) velocity basis functions.

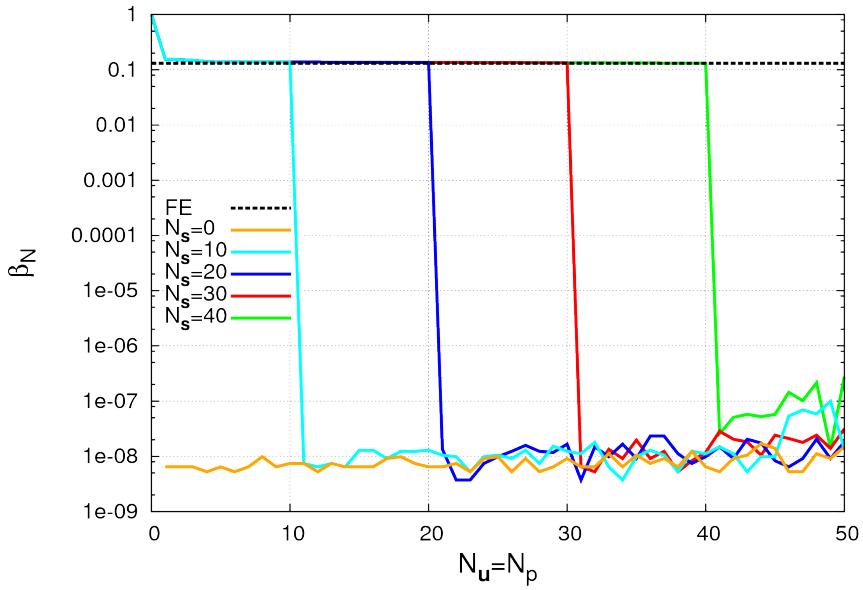

Figure 3.1: *Case I – physical parameters only: analysis of the stability factor* $\beta_N(\boldsymbol{\mu})$.

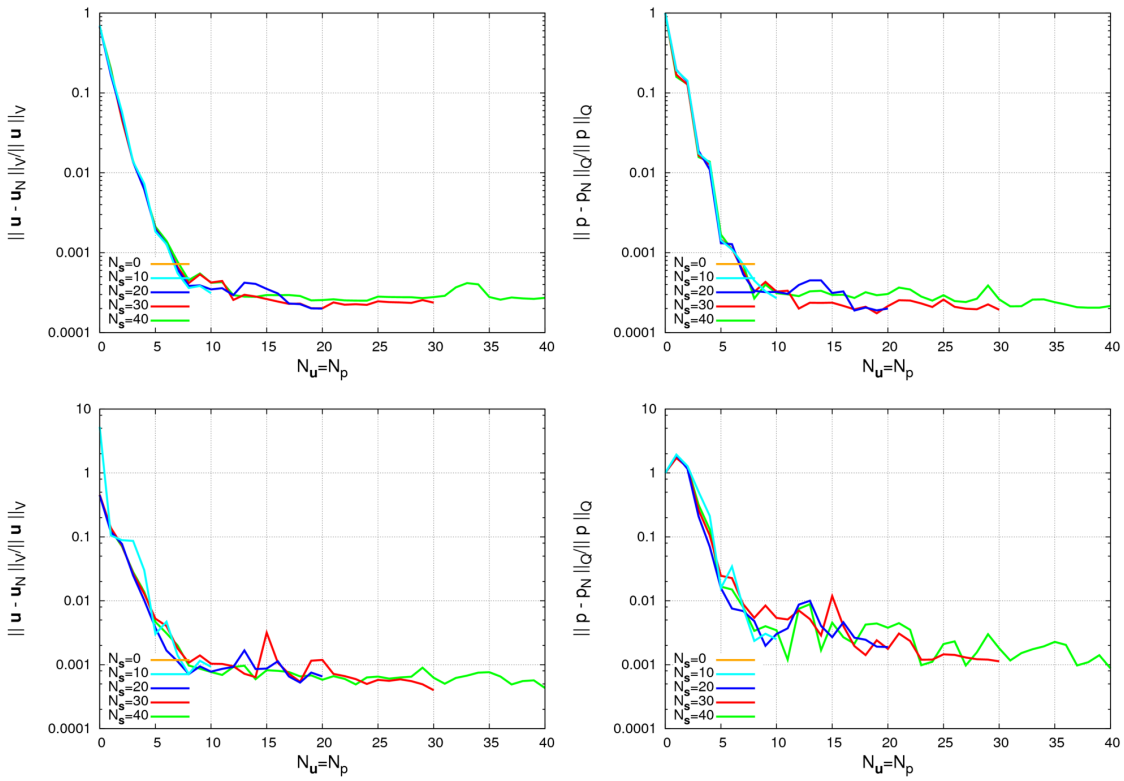

Figure 3.2: *Case I – physical parameters only: error analysis on velocity (left) and pressure (right); top:* $Re = 30$*, bottom:* $Re = 90$*. Error analysis is not performed for* $N_{\mathbf{s}} < N_p$ *because in these cases the reduced-order system* (3.15) *would be singular.*

$N_{\mathbf{s}}$	k	k_{pm}	spurious pressure modes	$\beta_N(\boldsymbol{\mu})^2$	$\left\|\underline{\mathbf{p}}_N\right\|_2$
0	5	4	yes	$<$ tol	1.1653e+09
1	4	2	yes	$<$ tol	7.5223e+06
5	1	-5	no	1.8201e-09	4.3631e+02
7	1	-7	no	3.3185e-08	2.6174e+01
10	1	-10	no	1.0258e-06	1.1228e+01
15	1	-15	no	1.6581e-05	1.1078e+01
30	1	-30	no	1.7305e-02	1.1061e+01
FOM	–	–	no	1.7312e-02	–

Table 3.2: *Case II – physical and geometrical parameters: stability analysis of the reduced problem ($Re = 150, H_o/H = 1$, $N_{\mathbf{u}} = N_p = 30$).*

3.5.2 Case II: physical and geometrical parameters

We now turn to the second case, dealing with both physical and geometrical parameters. A bidimensional configuration of a backward facing step is considered in this section, with parametrization of Reynolds number in the interval $[0.75, 300]$ and geometrical variation of the step height H_o. Also in this case a Taylor-Hood $\mathbb{P}_2 - \mathbb{P}_1$ FE discretization has been considered for the full-order model. Computational details of the offline stage are summarized in Table 3.1 (right column), and we refer to [23, Section 6] for additional details.

Compared to the former, this case requires a more detailed analysis. Figures 3.3 and 3.4 show a plot of stability factors $\beta_N(\boldsymbol{\mu})$ and relative errors for representative values of the parameters and for different choices $N_{\mathbf{s}}$ and $N_{\mathbf{u}} = N_p$. Moreover, we report in Table 3.2 the evaluation of the quantities introduced in Proposition 3.1 (namely, the computed values of $k = k(N_{\mathbf{u}}, N_{\mathbf{s}}, N_p; \boldsymbol{\mu})$ and $k_{\text{pm}} = k_{\text{pm}}(N_{\mathbf{u}}, N_{\mathbf{s}}, N_p; \boldsymbol{\mu})$, together with the value of $\beta_N(\boldsymbol{\mu})$ and the norm of the reduced pressure $\|\underline{\mathbf{p}}_N\|_{Q_N}$), for increasing values of $N_{\mathbf{s}}$ and $N_{\mathbf{u}} = N_p = 30$.

We also remark that similar considerations can be made on a wider class of computational domains and geometrical variations, and they are thus not limited to the two-dimensional domain and affine shape parametrization considered in the case at hand. For instance, Figure 3.6 shows a similar analysis on the stability factor $\beta_N(\boldsymbol{\mu})$ in the three-dimensional idealized bypass configuration of Section 5.1.4, featuring a non-affine shape deformation, and no noticeable difference in the behavior of $\beta_N(\boldsymbol{\mu})$ can be observed when compared to the case reported in Figure 3.3.
Thanks to these results, we can answer the questions highlighted in Section 3.4 as follows:

Q1. In order to ensure $\dim(\ker B_N(\boldsymbol{\mu})^T) = 0$, it is necessary to enrich the velocity space by adding at least a few supremizers. In fact, when $N_{\mathbf{s}} = 0$ or $N_{\mathbf{s}} = 1$, Table 3.2 (first and second rows, respectively) shows that $k_{\text{pm}} > 0$. Then, from Proposition 3.1, it follows that spurious pressure modes occur. Numerically, this is confirmed by the large value of $\|\underline{\mathbf{p}}_N\|_{Q_N}$ (see also Figure 3.5, first and second rows). Moreover, an incorrect approximation of the velocity would be provided by the ROM in these cases (see Figure 3.5, first row, image on the left).

Q2. An online locking phenomenon ($\beta_N(\boldsymbol{\mu}) \to 0$) may occur if too few supremizers are considered, say $0 < N_{\mathbf{s}} < N_p/2$ (see Figure 3.3). Table 3.2 (rows 3 and 4) shows that for $N_{\mathbf{s}} = 5$ or $N_{\mathbf{s}} = 7$, even though the ROM is inf-sup stable and the velocity is correctly approximated, yet the pressure is not recovered accurately (see also Figure 3.5, rows 3 and 4). However, if enough supremizers are considered (say, $N_{\mathbf{s}} > N_p/2$), the ROM is not only inf-sup stable, but also allows to get a better qualitative agreement with the truth FE solutions. The correct order of magnitude for the solution is recovered

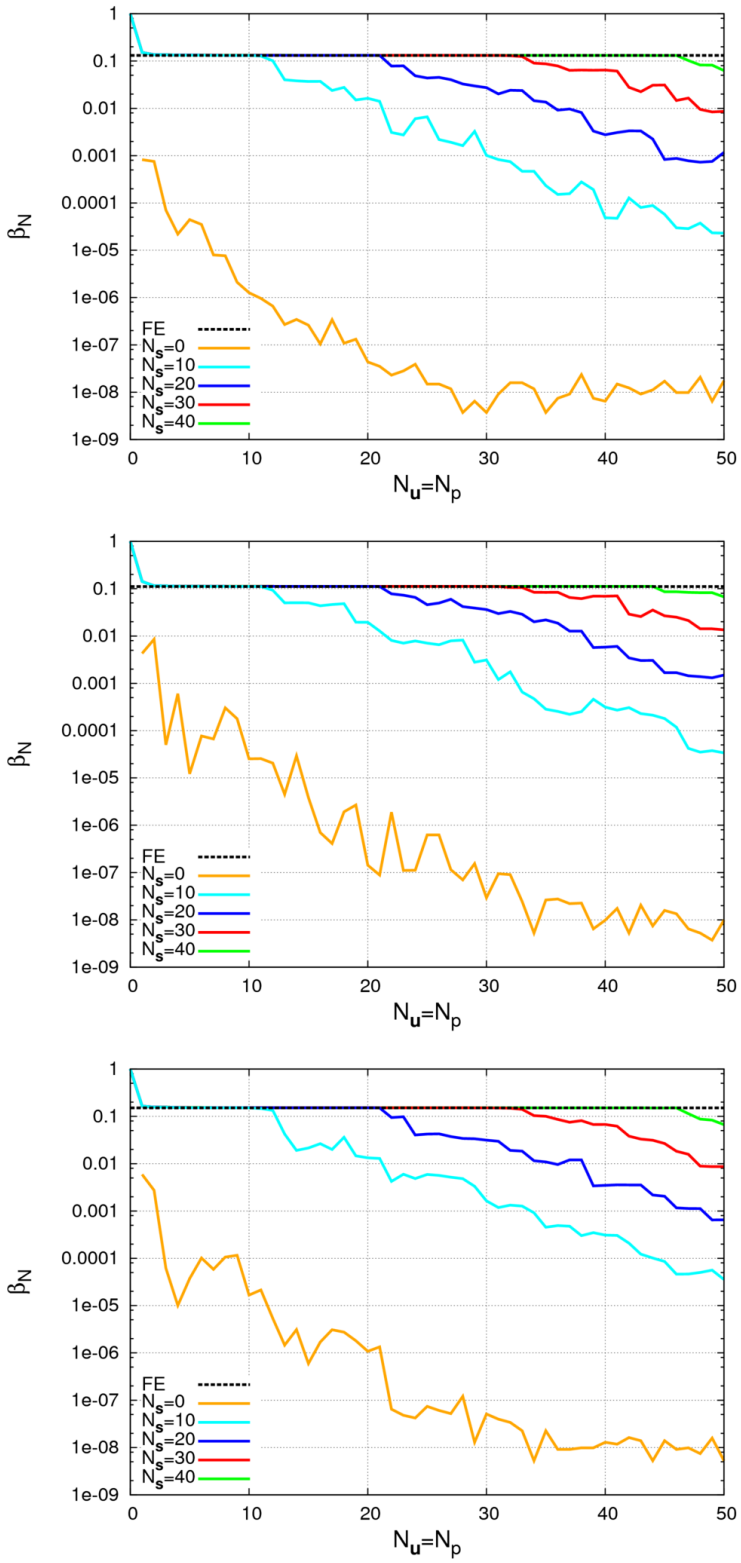

Figure 3.3: *Case II – physical and geometrical parameters: analysis of the stability factor* $\beta_N(\boldsymbol{\mu})$. *Top:* $H_o/H = 1$*; center:* $H_o/H = 0.5$*; bottom:* $H_o/H = 1.5$.

Figure 3.4: *Case II – physical and geometrical parameters: error analysis on velocity (left) and pressure (right). From top to bottom: ($Re = 90$, $H_o/H = 1$), ($Re = 150$, $H_o/H = 1$), ($Re = 150$, $H_o/H = 0.5$), ($Re = 150$, $H_o/H = 1.5$).*

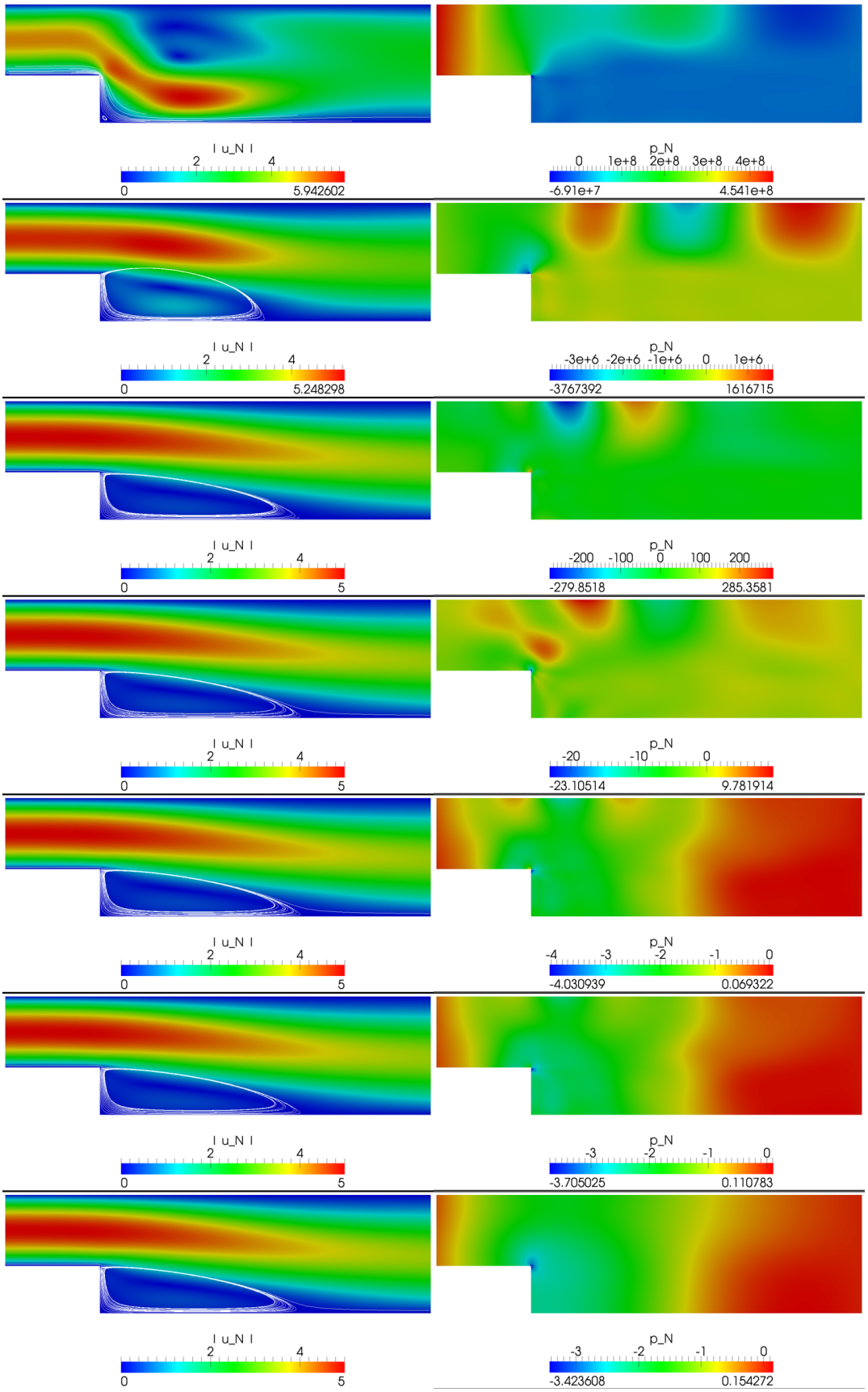

Figure 3.5: *Case II – physical and geometrical parameters: POD solutions at* $Re = 150, H_o/H = 1$*, for* $N_{\mathbf{u}} = N_p = 30$ *(left: velocity, right: pressure). From top to bottom:* $N_{\mathbf{s}} = \{0, 1, 5, 7, 10, 15, 30\}$.

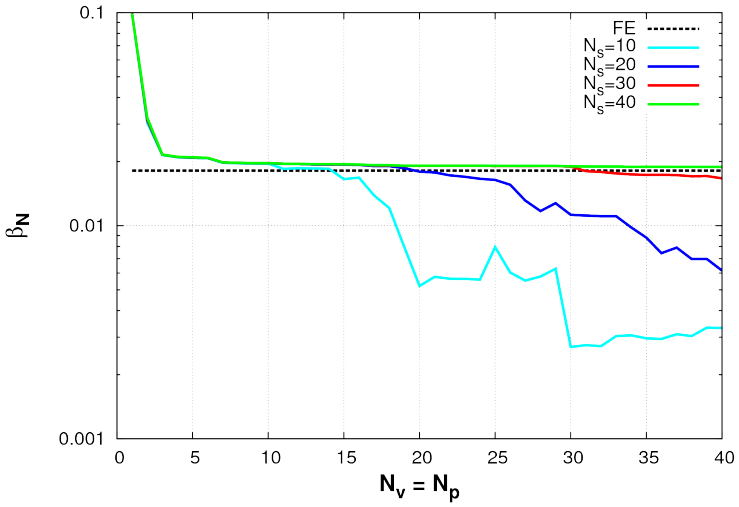

Figure 3.6: *Case II (bis) – physical and geometrical parameters: analysis of the stability factor $\beta_N(\boldsymbol{\mu})$ in an idealized bypass configuration with non-affine shape parametrization (see Section 5.1.4).*

(see Table 3.2, rows 5 and 6, $N_{\mathbf{s}} = 10, 15$, respectively, and Figure 3.5, rows 5 and 6). Moreover, stability factors increase (and errors decrease) as long as $N_{\mathbf{s}}$ increases (see Figure 3.4).

Q3. As in the case of the previous subsection, we obtain that $\beta_N(\boldsymbol{\mu}) \geq \beta_h(\boldsymbol{\mu})$ if $N_{\mathbf{s}} \geq N_p$ (see Figure 3.3). Moreover, $N_{\mathbf{s}}$ should not be taken strictly greater than $N_p = N_{\mathbf{u}}$ because *(i)* the online system dimension would increase and *(ii)* the algebraic stability of the system deteriorates, so that more iterations of the nonlinear solver would be needed to converge. The latter drawback is due to the fact that supremizers and velocities basis functions are orthonormal separately into two different sets.

3.6 Outlook

Key concepts introduced in this chapter (POD-Galerkin ROM, supremizer stabilization, shape parametrization) are going to be employed throughout the rest of the thesis. However, before turning to patient-specific simulations (Chapter 6), further attention needs to be devoted to the extension of the (stabilized) ROM to *time dependent* parametrized problems, since pulsatility is an important feature in the modelling of the cardiovascular system. A possible computational bottleneck may arise in the offline stage, because the dimension of the correlation matrices may depend on the number of subintervals of the time discretization e.g. when considering the whole time evolution in the snapshot matrices. A methodological focus of the next chapter will therefore be related to a compression strategy of the temporal trajectory.

CHAPTER 4

POD-Galerkin ROM for parametrized unsteady Navier-Stokes equations: a two-level POD

In this chapter we extend the POD-Galerkin ROM introduced in Chapter 3 to the case of unsteady flows. Some relevant topics in order to deal with the time-dependent case are summarized in Section 4.1. The parametrized formulation is introduced in Section 4.2, and full-order approximation is described in Section 4.3. The reduced-order approximation is detailed in Section 4.4, along with the two main ingredients of the unsteady POD-Galerkin ROM, namely the *two-level POD* and the *residual-based greedy algorithm*. Some numerical examples are provided in Section 4.5 for all cases.

4.1 Accounting for unsteadiness in the ROM

Unsteadiness, and in particular pulsatility, is an important feature for the description of many complex phenomena, among which is the cardiovascular problem of interest in this thesis. We will detail in this chapter a POD-Galerkin reduced-order model for *non-stationary* parametrized Navier-Stokes equations.

The reduced-order framework introduced in the previous chapter can be extended to deal with the time-dependent case by considering time as an additional parameter. In this case, computing a POD basis is more challenging, since a single snapshot consists in a sequence of several solutions, one for each time step. The inclusion of all time steps renders the basis computation infeasible for temporal discretizations with a small time-step. A compression of the temporal trajectory is therefore needed; POD has been employed for this task in POD-greedy algorithms (see e.g. [118, 119, 191]) in the context of reduced basis methods. A similar idea can be exploited in the POD-Galerkin context, thus performing two nested PODs, the innermost on the temporal trajectory and the outermost on the parametric space (not including time); a closely related method has been proposed in [15, 16] to construct spatial and temporal basis functions of a parabolic problem, where it has been called *two-level POD*.

Other relevant questions for unsteady problems are formulated below:

- should the snapshot temporal difference quotients be used in the POD or not? Both cases have been considered in literature with similar outcomes, and no agreement has been reached yet; in particular [69, 175, 242] do not use difference quotients, while [70, 150] do use them. See also [81, 132] for a recent comparison. In this work we *do not* use difference quotients;
- computation of global-in-time versus local-in-time basis functions (see e.g. [215]). This is particularly useful for instance in problems with transient phenomena, for which the long term behavior might be different from the short term one. Therefore, local-in-time basis functions should be computed, to be able to correctly approximate the truth solution in a small time span of the transient phenomena. The same basis functions may not be accurate enough on a larger time interval, and therefore a recomputation of the ROM may be needed. However, since the cardiovascular system exhibits a near-periodic behavior (at least for short period observations), we believe that global-in-time basis functions, computed over a period, are sufficient for our problem. In fact in this chapter we will discuss also the converse idea, that is, we employ POD basis functions generated on a small time interval and perform a time extrapolation over the global interval. Although possibly limited to periodic systems and not applicable in general, time extrapolation of projection-based ROM have also been discussed e.g. in [174, 176];
- optimal snapshot location (see e.g. [151]), to reduce the computational cost of the offline stage by a careful selection of the training parameters; this may be especially prohibitive in non-stationary problems because, for each training parameter, several finite element systems need to be solved, one for each time step. For this purpose a residual-based greedy algorithm is employed in this chapter;
- stability of the reduced-order solution: in this work the approximate supremizer enrichment, proposed in the previous chapter, has been tested with success, also for the time-dependent case. See also [19, 20, 160] for alternative stabilization procedures.

Both the cases of physical and geometrical parametrizations are considered; due to time-dependence, three cases are indeed possible:

I. physical parameters only (possibly time-dependent);

II. physical and geometrical parameters;

III. physical and *time-dependent* geometrical parameters.

The presentation of this chapter will focus on case III, which is the most general. Moreover, few references in literature for ROM for non-stationary problems consider geometrical parameters (see [260]), and most of those consider *time-invariant* geometrical parameters (thus, case II).

4.2 Problem formulation

For the sake of generality, we present the whole formulation on the case involving both physical and time-dependent geometrical parameters (case III); in fact, if geometrical parameters are not time-dependent, then the parametrized tensors encoding the geometrical variation are constant in time and the formulation is equivalent to case II. If no geometrical parameters are considered, then the weak form is already written on the reference domain, and it is equivalent to case I.

4.2.1 Parameters dependence

Let $\Omega \subset \mathbb{R}^d$, $d = 2, 3$, be a (reference) configuration, and assume that the current configuration $\Omega_o(\widetilde{\boldsymbol{\mu}}_g(t))$ can be obtained as the image of a map $\boldsymbol{T}(\cdot; \widetilde{\boldsymbol{\mu}}_g(t)) : \mathbb{R}^d \to \mathbb{R}^d$, i.e. $\boldsymbol{x}_o = \boldsymbol{T}(\boldsymbol{x}; \widetilde{\boldsymbol{\mu}}_g(t))$ and $\Omega_o(\widetilde{\boldsymbol{\mu}}_g(t)) = \boldsymbol{T}(\Omega; \widetilde{\boldsymbol{\mu}}_g(t))$. Note that the map $\boldsymbol{T}$ depends on time only through $\widetilde{\boldsymbol{\mu}}_g(t) \in \mathbb{R}^{n_g}$. The main assumption of the current framework is that each component of $\widetilde{\boldsymbol{\mu}}_g(t)$ can be expressed as

$$[\widetilde{\boldsymbol{\mu}}_g(t)]_i = [\boldsymbol{\mu}_g]_i d_{g,i}(t), \quad \forall i = 1, \dots, n_g, \tag{4.1}$$

for some smooth, given, parameter-independent, *time-dependent functions* $d_{g,i}(t)$ and some *time-independent geometrical parameters* $\boldsymbol{\mu}_g$. As we will see in the following, this assumption is crucial to obtain an efficient offline/online decomposition. Physical properties are encoded by a vector $\boldsymbol{\mu}_p \in \mathbb{R}^{n_p}$ of *physical parameters*. We assume to express time-dependent physical parameters (e.g. inlet boundary conditions) in a similar way to (4.1). As in the previous chapter, we will refer to $\boldsymbol{\mu} = (\boldsymbol{\mu}_g, \boldsymbol{\mu}_p)^T \in \mathcal{D} \subset \mathbb{R}^P$, $P = n_g + n_p$ as parameters.

4.2.2 An ALE formulation

Let $v_o(\boldsymbol{x}_o, t)$ be a function defined on the current configuration $\Omega_o(\widetilde{\boldsymbol{\mu}}_g(t))$ at time t, and let $v(\boldsymbol{x}, t)$ be the function obtained by tracing back onto the reference domain Ω, that is, $v(\boldsymbol{x}, t) = v_o(\boldsymbol{T}(\boldsymbol{x}; \widetilde{\boldsymbol{\mu}}_g(t)), t)$. The symbol $\frac{D}{Dt}$ will denote the time derivative in the reference frame:

$$\frac{D}{Dt} v_o(\boldsymbol{x}_o, t) = \frac{d}{dt} v(\boldsymbol{T}^{-1}(\boldsymbol{x}_o; \widetilde{\boldsymbol{\mu}}_g(t)), t),$$

and, in particular, the domain velocity $\boldsymbol{w}_o$ is defined as $\boldsymbol{w}_o = \frac{D}{Dt}\boldsymbol{x}_o = \frac{D}{Dt}\boldsymbol{T}(\boldsymbol{x}; \widetilde{\boldsymbol{\mu}}_g(t))$. The unsteady Navier-Stokes equations, in Arbitrary Lagrangian Eulerian (ALE) formulation in order to consider case III, reads as follows:

$$\begin{cases} \frac{D}{Dt}\boldsymbol{u}_o(t;\boldsymbol{\mu}) - \nu(\boldsymbol{\mu}_p)\Delta\boldsymbol{u}_o(\boldsymbol{\mu}) + ((\boldsymbol{u}_o(t;\boldsymbol{\mu}) - \boldsymbol{w}_o(\boldsymbol{\mu})) \cdot \nabla)\boldsymbol{u}_o(t;\boldsymbol{\mu}) & \\ \quad + \nabla p_o(t;\boldsymbol{\mu}) = \boldsymbol{f}(t;\boldsymbol{\mu}_p) & \text{in } \Omega_o(\widetilde{\boldsymbol{\mu}}_g(t)) \times (0,T), \\ \operatorname{div} \boldsymbol{u}_o(t;\boldsymbol{\mu}) = 0 & \text{in } \Omega_o(\widetilde{\boldsymbol{\mu}}_g(t)) \times (0,T), \\ \boldsymbol{u}_o(t;\boldsymbol{\mu}) = \boldsymbol{g}_D(t;\boldsymbol{\mu}_p) & \text{on } \Gamma_D \times (0,T), \\ \boldsymbol{u}_o(t;\boldsymbol{\mu}) = \boldsymbol{w}_o(t;\boldsymbol{\mu}), & \text{on } \Gamma_{o,W}(\widetilde{\boldsymbol{\mu}}_g(t)) \times (0,T), \\ \nu(\boldsymbol{\mu}_p)\dfrac{\partial \boldsymbol{u}_o(t;\boldsymbol{\mu})}{\partial \boldsymbol{n}} - p_o(t;\boldsymbol{\mu})\boldsymbol{n} = \boldsymbol{g}_N(t;\boldsymbol{\mu}_p), & \text{on } \Gamma_N, \\ \boldsymbol{u}_o(t;\boldsymbol{\mu})|_{t=0} = \boldsymbol{g}_0(\boldsymbol{\mu}), & \text{in } \Omega_o(\boldsymbol{\mu}_g(0)), \end{cases} \tag{4.2}$$

for some given distributed force term $\boldsymbol{f}(t;\boldsymbol{\mu})$, Dirichlet data $\boldsymbol{g}_D(t;\boldsymbol{\mu})$, Neumann flux $\boldsymbol{g}_N(t;\boldsymbol{\mu})$ and initial condition $\boldsymbol{g}_0(\boldsymbol{\mu})$. We thus denote by $(\boldsymbol{u}_o(t;\boldsymbol{\mu}), p_o(t;\boldsymbol{\mu}))$ the velocity and pressure fields on the current configuration.

Inhomogeneous Dirichlet boundary conditions are imposed on $\Gamma_D \subset \partial\Omega$. The boundary Γ_D is assumed to be fixed. Also $\Gamma_N \subset \partial\Omega$, over which Neumann conditions are prescribed, is fixed[1]; here $\boldsymbol{n}$ denotes the normal unit vector to Γ_N. Finally, the boundary $\Gamma_{o,W}(\widetilde{\boldsymbol{\mu}}_g(t))$ is the image of the reference boundary Γ_W under the map $\boldsymbol{T}(\cdot; \widetilde{\boldsymbol{\mu}}_g(t))$. The continuity of the velocity on $\Gamma_{o,W}(\widetilde{\boldsymbol{\mu}}_g(t))$ is imposed. The initial condition is assumed to be the solution of the steady-state problem, for the same parameters, in the current configuration $\Omega_o(\widetilde{\boldsymbol{\mu}}_g(0))$ at the initial time.

[1] ... although this assumption can be weakened e.g. if $\boldsymbol{g}_N = \boldsymbol{0}$.

4.2.3 Weak form

Let us introduce the pressure and velocity spaces on the reference domain

$$Q = L^2(\Omega), \qquad \boldsymbol{V} = \boldsymbol{H}^1_{0,\Gamma_E}(\Omega), \qquad \Gamma_E = \Gamma_D \cup \Gamma_W$$

equipped respectively with the (vector) H^1-seminorm and the L^2-norm. By multiplying (4.2) for suitable test functions, integrating by parts, and tracing everything back onto the reference domain Ω, we obtain the following weak parametrized formulation:

$$\begin{aligned}
&\text{given } \boldsymbol{\mu} \in \mathcal{D}, \text{ find } (\boldsymbol{u}(t;\boldsymbol{\mu}), p(t;\boldsymbol{\mu})),\\
&\quad \boldsymbol{u}(\cdot;\boldsymbol{\mu}) \in L^2(0,T;\boldsymbol{H}^1(\Omega)) \cap C([0,T];\boldsymbol{L}^2(\Omega)), \quad \tfrac{\partial}{\partial t}\boldsymbol{u}(\cdot;\boldsymbol{\mu}) \in L^2(0,T;\boldsymbol{V}'),\\
&\quad \boldsymbol{u}(\cdot;\boldsymbol{\mu})|_{\Gamma_D\times(0,T)} = \boldsymbol{g}_D(\cdot;\boldsymbol{\mu}_p), \quad \boldsymbol{u}(\cdot;\boldsymbol{\mu})|_{\Gamma_W\times(0,T)} = \tfrac{\partial}{\partial t}\boldsymbol{T}(\boldsymbol{x};\widetilde{\boldsymbol{\mu}}_g(\cdot))|_{\Gamma_W\times(0,T)},\\
&\quad p(\cdot;\boldsymbol{\mu}) \in L^2(0,T;Q), \text{s.t.}\\
&\begin{cases}
m(\frac{\partial}{\partial t}\boldsymbol{u},\boldsymbol{v};t;\boldsymbol{\mu}) + a(\boldsymbol{u},\boldsymbol{v};t;\boldsymbol{\mu}) + b(\boldsymbol{v},p;t;\boldsymbol{\mu}) & \\
\qquad +c(\boldsymbol{u},\boldsymbol{u},\boldsymbol{v};t;\boldsymbol{\mu}) + c_{ALE}(\boldsymbol{u},\boldsymbol{v};t;\boldsymbol{\mu}) = F(\boldsymbol{v};t;\boldsymbol{\mu}), & \forall \boldsymbol{v} \in \boldsymbol{V},\ t>0,\\
b(\boldsymbol{u},q;t;\boldsymbol{\mu}) = G(q;t;\boldsymbol{\mu}), & \forall q \in Q,\ t>0,\\
\boldsymbol{u}|_{t=0} = \boldsymbol{g}_0(\boldsymbol{\mu}), &
\end{cases}
\end{aligned} \tag{4.3}$$

where

$$\begin{aligned}
a(\boldsymbol{u},\boldsymbol{v};t;\boldsymbol{\mu}) &= \int_\Omega \nabla\boldsymbol{u}\,\boldsymbol{\kappa}(\boldsymbol{x},t;\boldsymbol{\mu}) : \nabla\boldsymbol{v}\,d\boldsymbol{x}, \qquad & b(\boldsymbol{v},q;t;\boldsymbol{\mu}) &= -\int_\Omega q\,\mathrm{tr}(\boldsymbol{\chi}(\boldsymbol{x},t;\boldsymbol{\mu})\,\nabla\boldsymbol{v})\,d\boldsymbol{x}\\
m(\boldsymbol{u},\boldsymbol{v};t;\boldsymbol{\mu}) &= \int_\Omega \pi(\boldsymbol{x},t;\boldsymbol{\mu})\,\boldsymbol{u}\cdot\boldsymbol{v}\,d\boldsymbol{x}, \qquad & c_{ALE}(\boldsymbol{u},\boldsymbol{v};t;\boldsymbol{\mu}) &= -\int_\Omega \nabla\boldsymbol{u}\,\boldsymbol{\sigma}(\boldsymbol{x},t;\boldsymbol{\mu})\cdot\boldsymbol{v}\,d\boldsymbol{x}
\end{aligned} \tag{4.4}$$

are the bilinear forms related to diffusion, pressure/divergence, mass and ALE operators, respectively, and

$$c(\boldsymbol{u},\boldsymbol{v},\boldsymbol{z};t;\boldsymbol{\mu}) = \int_\Omega (\nabla\boldsymbol{v}\,\boldsymbol{\chi}(\boldsymbol{x},t;\boldsymbol{\mu}))\boldsymbol{u}\cdot\boldsymbol{z}\,d\boldsymbol{x} \tag{4.5}$$

is the trilinear form associated to the convective term. As for steady problems, we assume for simplicity that $\boldsymbol{f} = \boldsymbol{g}_N = \boldsymbol{0}$, so that the right-hand sides $F(\boldsymbol{v};t;\boldsymbol{\mu})$ and $G(q;t;\boldsymbol{\mu})$ vanish.

Here we denote by

$$\begin{aligned}
\boldsymbol{\kappa}(\boldsymbol{x},t;\boldsymbol{\mu}) &= \nu(\boldsymbol{\mu}_p)(J_{\boldsymbol{T}}(\boldsymbol{x};\widetilde{\boldsymbol{\mu}}_g(t)))^{-1}(J_{\boldsymbol{T}}(\boldsymbol{x};\widetilde{\boldsymbol{\mu}}_g(t)))^{-T}|J_{\boldsymbol{T}}(\boldsymbol{x};\widetilde{\boldsymbol{\mu}}_g(t))|\\
\boldsymbol{\chi}(\boldsymbol{x},t;\boldsymbol{\mu}) &= (J_{\boldsymbol{T}}(\boldsymbol{x};\widetilde{\boldsymbol{\mu}}_g(t)))^{-1}|J_{\boldsymbol{T}}(\boldsymbol{x};\widetilde{\boldsymbol{\mu}}_g(t))|,\\
\pi(\boldsymbol{x},t;\boldsymbol{\mu}) &= |J_{\boldsymbol{T}}(\boldsymbol{x};\widetilde{\boldsymbol{\mu}}_g(t))|,\\
\boldsymbol{\sigma}(\boldsymbol{x},t;\boldsymbol{\mu}) &= (J_{\boldsymbol{T}}(\boldsymbol{x};\widetilde{\boldsymbol{\mu}}_g(t)))^{-1}\tfrac{\partial}{\partial t}\boldsymbol{T}(\boldsymbol{x};\widetilde{\boldsymbol{\mu}}_g(t))|J_{\boldsymbol{T}}(\boldsymbol{x};\widetilde{\boldsymbol{\mu}}_g(t))|,
\end{aligned} \tag{4.6}$$

the tensors $\boldsymbol{\kappa},\boldsymbol{\chi}$, the vector $\boldsymbol{\sigma}$ and the scalar π encoding both physical and geometrical parametrization; we recall that $J_{\boldsymbol{T}} \in \mathbb{R}^{d\times d}$ is the Jacobian matrix of the map $\boldsymbol{T}(\cdot;\widetilde{\boldsymbol{\mu}}_g(t))$, and $|J_{\boldsymbol{T}}|$ denotes its determinant.

4.3 Full-order approximation of parametrized unsteady Navier-Stokes equations

As in the previous chapter, let us introduce two finite-dimensional subspaces $\boldsymbol{V}_h \subset \boldsymbol{V}$, $Q_h \subset Q$ of dimension $N^h_{\mathbf{u}}$ and N^h_p, respectively, based on a Finite Element (FE) discretization of mesh size h. Denote by $\{\boldsymbol{\varphi}^h_i\}_{i=1,\dots,N^h_{\mathbf{u}}}$ and $\{\zeta^h_k\}_{k=1,\dots,N^h_p}$ two bases of the FE velocity and pressure spaces, respectively.

4.3.1 The semi-discrete problem

The semi-discrete Galerkin-FE approximation of the parametrized problem (4.3) reads as follows:

given $\boldsymbol{\mu} \in \mathcal{D}$, find $(\boldsymbol{u}_h(t;\boldsymbol{\mu}), p_h(t;\boldsymbol{\mu}))$,
$\boldsymbol{u}_h(\cdot;\boldsymbol{\mu}) \in L^2(0,T_h;\boldsymbol{H}^1(\Omega)) \cap C([0,T_h];\boldsymbol{L}^2(\Omega))$, $\frac{\partial}{\partial t}\boldsymbol{u}_h(\cdot;\boldsymbol{\mu}) \in L^2(0,T_h;\boldsymbol{V}')$,
$\boldsymbol{u}_h(\cdot;\boldsymbol{\mu})|_{\Gamma_D\times(0,T)} = \boldsymbol{g}_D(\cdot;\boldsymbol{\mu}_p)$, $\boldsymbol{u}_h(\cdot;\boldsymbol{\mu})|_{\Gamma_W\times(0,T)} = \frac{\partial}{\partial t}\boldsymbol{T}(\boldsymbol{x};\widetilde{\boldsymbol{\mu}}_g(\cdot))|_{\Gamma_W\times(0,T)}$,
$p_h(\cdot;\boldsymbol{\mu}) \in L^2(0,T_h;Q)$, s.t.

$$\begin{cases} m(\frac{\partial}{\partial t}\boldsymbol{u}_h,\boldsymbol{v}_h;t;\boldsymbol{\mu}) + a(\boldsymbol{u}_h,\boldsymbol{v}_h;t;\boldsymbol{\mu}) + b(\boldsymbol{v}_h,p_h;t;\boldsymbol{\mu}) + \\ \quad c(\boldsymbol{u}_h,\boldsymbol{u}_h,\boldsymbol{v}_h;t;\boldsymbol{\mu}) + c_{ALE}(\boldsymbol{u}_h,\boldsymbol{v}_h;t;\boldsymbol{\mu}) = F(\boldsymbol{v}_h;t;\boldsymbol{\mu}) & \forall \boldsymbol{v}_h \in \boldsymbol{V}_h,\ t>0, \\ b(\boldsymbol{u}_h,q_h;t;\boldsymbol{\mu}) = G(q_h;t;\boldsymbol{\mu}) & \forall q_h \in Q_h,\ t>0, \\ \boldsymbol{u}|_{t=0} = \boldsymbol{g}_{0,h}(\boldsymbol{\mu}). \end{cases}$$

4.3.2 Time discretization

Consider a partition of the interval $[0,T_h]$ into M_h equally spaced time intervals of size Δt. Applying an Implicit Euler time discretization we obtain the following discrete problem:

given $\boldsymbol{\mu} \in \mathcal{D}$ and $(\boldsymbol{u}_h^n(\boldsymbol{\mu}), p_h^n(\boldsymbol{\mu}))$, find $(\boldsymbol{u}_h^{n+1}(\boldsymbol{\mu}), p_h^{n+1}(\boldsymbol{\mu}))$, s.t.
$\boldsymbol{u}_h^{n+1}(\boldsymbol{\mu})|_{\Gamma_D} = \boldsymbol{g}_D(\boldsymbol{\mu}_p)|t=t^{n+1}$, $\boldsymbol{u}_h^{n+1}(\boldsymbol{\mu})|_{\Gamma_W} = \frac{\partial}{\partial t}\boldsymbol{T}(\boldsymbol{x};\widetilde{\boldsymbol{\mu}}_g(t^{n+1}))|_{\Gamma_W}$,

$$\begin{cases} \frac{1}{\Delta t}m(\boldsymbol{u}_h^{n+1},\boldsymbol{v}_h;t^{n+1};\boldsymbol{\mu}) + a(\boldsymbol{u}_h^{n+1},\boldsymbol{v}_h;t^{n+1};\boldsymbol{\mu}) + b(\boldsymbol{v}_h,p_h^{n+1};t^{n+1};\boldsymbol{\mu}) + \\ \quad c(\boldsymbol{u}_h^{n+1},\boldsymbol{u}_h^{n+1},\boldsymbol{v}_h;t^{n+1};\boldsymbol{\mu}) + c_{ALE}(\boldsymbol{u}_h^{n+1},\boldsymbol{v}_h;t^{n+1};\boldsymbol{\mu}) = \\ \quad \frac{1}{\Delta t}m(\boldsymbol{u}_h^n,\boldsymbol{v};t^n;\boldsymbol{\mu}) + F(\boldsymbol{v}_h;t^{n+1};\boldsymbol{\mu}) & \forall \boldsymbol{v}_h \in \boldsymbol{V}_h,\ n=0,\dots,M_h-1, \\ b(\boldsymbol{u}_h^{n+1},q_h;t^{n+1};\boldsymbol{\mu}) = G(q_h;t^{n+1};\boldsymbol{\mu}) & \forall q_h \in Q_h,\ n=0,\dots,M_h-1, \\ \boldsymbol{u}_h^0 = \boldsymbol{g}_{0,h}(\boldsymbol{\mu}). \end{cases}$$

4.3.3 Algebraic formulation

Similarly to what we have done in the steady case, we can provide and algebraic formulation of the semi-discrete problem. The resulting nonlinear ODEs system is as follows:

$$\begin{bmatrix} M(t;\boldsymbol{\mu}) & 0 \\ 0 & 0 \end{bmatrix} \begin{bmatrix} \dot{\underline{\mathbf{u}}}(t;\boldsymbol{\mu}) \\ \dot{\underline{\mathbf{p}}}(t;\boldsymbol{\mu}) \end{bmatrix} + \begin{bmatrix} L(t;\boldsymbol{\mu}) + C(\underline{\mathbf{u}}(t;\boldsymbol{\mu});t;\boldsymbol{\mu}) & B^T(t;\boldsymbol{\mu}) \\ B(t;\boldsymbol{\mu}) & 0 \end{bmatrix} \begin{bmatrix} \underline{\mathbf{u}}(t;\boldsymbol{\mu}) \\ \underline{\mathbf{p}}(t;\boldsymbol{\mu}) \end{bmatrix} = \begin{bmatrix} \underline{\mathbf{f}}(t;\boldsymbol{\mu}) \\ \underline{\mathbf{g}}(t;\boldsymbol{\mu}) \end{bmatrix}$$

for the vector of coefficients $\underline{\mathbf{u}} = (u_h^{(1)},\dots,u_h^{(N_{\mathbf{u}}^h)})^T$, $\underline{\mathbf{p}} = (p_h^{(1)},\dots,p_h^{(N_p^h)})^T$ where, for $1 \le i,j \le N_{\mathbf{u}}^h$ and $1 \le k \le N_p^h$:

$$\begin{gathered} (M(t;\boldsymbol{\mu}))_{ij} = m(\boldsymbol{\varphi}_j^h,\boldsymbol{\varphi}_i^h;t;\boldsymbol{\mu}), \qquad (A(t;\boldsymbol{\mu}))_{ij} = a(\boldsymbol{\varphi}_j^h,\boldsymbol{\varphi}_i^h;t;\boldsymbol{\mu}), \\ (B(t;\boldsymbol{\mu}))_{ki} = b(\boldsymbol{\varphi}_i^h,\zeta_k^h;t;\boldsymbol{\mu}), \qquad (C_{ALE}(t;\boldsymbol{\mu}))_{ij} = c_{ALE}(\boldsymbol{\varphi}_j^h,\boldsymbol{\varphi}_i^h;t;\boldsymbol{\mu}) \\ (C(\underline{\mathbf{u}}(\boldsymbol{\mu});t;\boldsymbol{\mu}))_{ij} = \textstyle\sum_{m=1}^{N_{\mathbf{u}}^h} u_h^{(m)}(t;\boldsymbol{\mu}) c\left(\boldsymbol{\varphi}_m^h,\boldsymbol{\varphi}_j^h,\boldsymbol{\varphi}_i^h;t;\boldsymbol{\mu}\right), \\ (\underline{\mathbf{f}}(t;\boldsymbol{\mu}))_i = F(\boldsymbol{\varphi}_i^h;t;\boldsymbol{\mu}), \qquad (\underline{\mathbf{g}}(t;\boldsymbol{\mu}))_k = G(\zeta_k^h;t;\boldsymbol{\mu}) \end{gathered} \tag{4.7}$$

and $L(t;\boldsymbol{\mu}) = A(t;\boldsymbol{\mu}) + C_{ALE}(t;\boldsymbol{\mu})$.

The resulting nonlinear system after a time discretization with the Implicit Euler scheme is

$$\begin{bmatrix} \frac{M(t^{n+1};\boldsymbol{\mu})}{\Delta t} + L(t^{n+1};\boldsymbol{\mu}) + C(\underline{\mathbf{u}}(t^{n+1};\boldsymbol{\mu});t^{n+1};\boldsymbol{\mu}) & B^T(t^{n+1};\boldsymbol{\mu}) \\ B(t^{n+1};\boldsymbol{\mu}) & 0 \end{bmatrix} \begin{bmatrix} \underline{\mathbf{u}}(t^{n+1};\boldsymbol{\mu}) \\ \underline{\mathbf{p}}(t^{n+1};\boldsymbol{\mu}) \end{bmatrix} = \begin{bmatrix} \underline{\mathbf{f}}(t^{n+1};\boldsymbol{\mu}) \\ \underline{\mathbf{g}}(t^{n+1};\boldsymbol{\mu}) \end{bmatrix} + \begin{bmatrix} \frac{M(t^{n};\boldsymbol{\mu})}{\Delta t} & 0 \\ 0 & 0 \end{bmatrix} \begin{bmatrix} \underline{\mathbf{u}}(t^{n};\boldsymbol{\mu}) \\ \underline{\mathbf{p}}(t^{n};\boldsymbol{\mu}) \end{bmatrix} \tag{4.8}$$

Note that the matrices appearing in (4.8) have to be, in principle, reassembled at every time-step because of the time-dependence of the domain; see also the next section. Non-homogeneous Dirichlet boundary conditions are imposed by introducing a suitable lifting function, in a similar way as in steady state problems shown in the previous chapter. At each time step, the nonlinear system is solved by means of Picard or Newton iterations.

4.3.4 Affine parametric dependence

An affine parametric dependence assumption on (4.7) is made, i.e.

$$A(t;\boldsymbol{\mu}) = \sum_{q=1}^{Q_A} \Theta_q^A(t;\boldsymbol{\mu}) A^q, \qquad C_{ALE}(t;\boldsymbol{\mu}) = \sum_{q=1}^{Q_{C_{ALE}}} \Theta_q^{C_{ALE}}(t;\boldsymbol{\mu}) C_{ALE}^q, \qquad \underline{\mathbf{f}}(\boldsymbol{\mu}) = \sum_{q=1}^{Q_f} \Theta_q^f(t;\boldsymbol{\mu}) \underline{\mathbf{f}}^q,$$

$$\boldsymbol{g}_D(t;\boldsymbol{\mu}_p) = \sum_{q=1}^{Q_D} \Theta_q^D(t;\boldsymbol{\mu}) \boldsymbol{g}_D^q, \qquad \frac{\partial}{\partial t}\boldsymbol{T}(\cdot;\widetilde{\boldsymbol{\mu}}_g(t)) = \sum_{q=1}^{Q_w} \Theta_q^w(t;\boldsymbol{\mu}) \boldsymbol{w}^q, \tag{4.9}$$

and in a similar way for the other terms. As in the previous chapter, this expression is usually recovered by means of the so-called empirical interpolation method (EIM) [28]. Note that, thanks to this assumption, the temporal dependence is stored in the coefficients $\Theta_q^*(t;\boldsymbol{\mu})$, the data structures A^q, C_{ALE}^q, etc. being instead independent on both $\boldsymbol{\mu}$ and t. As we will see in the next section this will be a key point in the offline-online decomposition of the reduced-order model. Moreover, the term $\Theta_q^D(t;\boldsymbol{\mu})$ is actually the only one with an explicit time dependence; for the other terms, $\Theta_q^*(t;\boldsymbol{\mu}) = \widetilde{\Theta}_q^*(\boldsymbol{\mu}_p, \boldsymbol{\mu}_g(t))$, since the parametrized NS operators do not depend explicitly on time, but only through $\boldsymbol{\mu}_g(t)$.

4.4 A POD-Galerkin ROM for parametrized unsteady Navier-Stokes equations

We present a POD-Galerkin ROM for solving parametrized unsteady NS equations. The supremizer solutions enrichment described in the previous chapter is applied to enhance the stability of the resulting reduced-order model.

Let

$$N_{\mathbf{u},\mathbf{s}} = Q_D + Q_w + N_{\mathbf{u}} + N_{\mathbf{s}}, \quad N_p$$

be the dimensions of the reduced spaces for velocity $\boldsymbol{V}_N$ and pressure Q_N, respectively. Here, $N_{\mathbf{u}}, N_{\mathbf{s}}, N_p$ are the dimension of the online degrees of freedom for the reduced-order model for velocity, supremizers and pressure, respectively. Q_D and Q_w are, instead, fixed by the affine expansion (4.9). As for the full-order model, consider the following bijection between

the spaces $\mathbb{R}^{N_{\mathbf{u},\mathbf{s}}}$ and $\boldsymbol{V}_N$ (resp. $\mathbb{R}^{N_p}$ and Q_N):

$$\begin{cases} \underline{\mathbf{v}}_N = (d_N^{(1)}, \dots, d_N^{(Q_D)}, w_N^{(1)}, \dots, w_N^{(Q_w)}, v_N^{(1)}, \dots, v_N^{(N_\mathbf{u})}, s_N^{(1)}, \dots, s_N^{(N_\mathbf{s})})^T \in \mathbb{R}^{N_{\mathbf{u},\mathbf{s}}} \\ \leftrightarrow \quad \boldsymbol{v}_N = \sum_{q=1}^{Q_D} d_N^{(q)} \widetilde{\boldsymbol{g}}_D^q + \sum_{q=1}^{Q_w} w_N^{(q)} \widetilde{\boldsymbol{w}}^q + \sum_{n=1}^{N_\mathbf{u}} v_N^{(n)} \boldsymbol{\varphi}_n + \sum_{n=1}^{N_\mathbf{s}} s_N^{(n)} \boldsymbol{\eta}_n \in \boldsymbol{V}_N, \\ \underline{\mathbf{q}}_N = (q_N^{(1)}, \dots, q_N^{(N_p)})^T \in \mathbb{R}^{N_p} \quad \leftrightarrow \quad q_N = \sum_{n=1}^{N_p} q_N^{(n)} \zeta_n \in Q_N. \end{cases}, \tag{4.10}$$

where $\widetilde{\boldsymbol{g}}_D^q$ and $\widetilde{\boldsymbol{w}}^q$ are (divergence-free) extensions of the non-homogeneous Dirichlet boundary data $\boldsymbol{g}_D^q$ and $\boldsymbol{w}^q$ in (4.9), respectively.

4.4.1 A two-level Proper Orthogonal Decomposition

Let us denote by $\Xi_{\text{train}} = \{\boldsymbol{\mu}^1, \dots, \boldsymbol{\mu}^{N_{\text{train}}}\} \subset \mathcal{D}$ a (large) training sample of N_{train} points chosen randomly over $\mathcal{D}$. For each point ($i = 1, \dots, N_{\text{train}}$) in the training sample a truth solve is performed and the temporal evolution of the full-order solutions is stored in the following *snapshot matrices on the temporal trajectory*

$$\begin{aligned} S_\mathbf{u}^i &= [\underline{\widehat{\mathbf{u}}}(t^0; \boldsymbol{\mu}^i) \mid \dots \mid \underline{\widehat{\mathbf{u}}}(t^{M_h-1}; \boldsymbol{\mu}^i)] \in \mathbb{R}^{N_\mathbf{u}^h \times M_h}, \quad \forall i = 1, \dots, N_{\text{train}}, \\ S_p^i &= [\underline{\mathbf{p}}(t^0; \boldsymbol{\mu}^i) \mid \dots \mid \underline{\mathbf{p}}(t^{M_h-1}; \boldsymbol{\mu}^i)] \in \mathbb{R}^{N_p^h \times M_h}, \quad \forall i = 1, \dots, N_{\text{train}}, \\ S_\mathbf{s}^i &= [\underline{\mathbf{s}}^{\boldsymbol{\mu}}(\underline{\mathbf{p}}(t^0; \boldsymbol{\mu}^i)) \mid \dots \mid \underline{\mathbf{s}}^{\boldsymbol{\mu}}(\underline{\mathbf{p}}(t^{M_h-1}; \boldsymbol{\mu}^i))] \in \mathbb{R}^{N_\mathbf{u}^h \times M_h}, \quad \forall i = 1, \dots, N_{\text{train}}. \end{aligned}$$

The notation $\underline{\widehat{\mathbf{u}}}(t^n; \boldsymbol{\mu}^i)$ refers to the difference between the full-order solution $\underline{\mathbf{u}}(t^n; \boldsymbol{\mu}^i)$ and the lifting functions at $t = t^n$ and $\boldsymbol{\mu} = \boldsymbol{\mu}^i$. At each time step, the following elliptic problem

$$X_\mathbf{u} \underline{\mathbf{s}}^{\boldsymbol{\mu}}(\underline{\mathbf{p}}(t^n; \boldsymbol{\mu}^i)) = B^T(\boldsymbol{\mu}) \underline{\mathbf{p}}(t^n; \boldsymbol{\mu}^i) \tag{4.11}$$

is solved to obtain the supremizer solution $\underline{\mathbf{s}}^{\boldsymbol{\mu}}(\underline{\mathbf{p}}(t^n; \boldsymbol{\mu}^i))$, where $X_\mathbf{u}$ is the FE matrix of the inner product on V_h.

Two strategies have been employed to obtain a POD basis:

1. *standard (full) POD*: the following *snapshot matrices on the temporal trajectory and parameter space* are assembled, that is, we store

$$\begin{aligned} S_\mathbf{u} &= [S_\mathbf{u}^1 | \dots | S_\mathbf{u}^{N_{\text{train}}}] \in \mathbb{R}^{N_\mathbf{u}^h \times (M_h \cdot N_{\text{train}})}, \\ S_p &= [S_p^1 | \dots | S_p^{N_{\text{train}}}] \in \mathbb{R}^{N_p^h \times (M_h \cdot N_{\text{train}})}, \\ S_\mathbf{s} &= [S_\mathbf{s}^1 | \dots | S_\mathbf{s}^{N_{\text{train}}}] \in \mathbb{R}^{N_\mathbf{u}^h \times (M_h \cdot N_{\text{train}})}. \end{aligned}$$

   Then, a POD is performed for each matrix and the first $N_\mathbf{u}, N_p, N_\mathbf{s}$ (respectively) left singular vectors are considered as basis functions $\{\boldsymbol{\varphi}_n\}_{n=1}^{N_\mathbf{u}}, \{\zeta_n\}_{n=1}^{N_p}, \{\boldsymbol{\eta}_n\}_{n=1}^{N_\mathbf{s}}$.

2. *two-level POD*: in the previous case, a POD basis for (e.g.) the velocity can be obtained either by a singular value decomposition of $X_\mathbf{u}^{1/2} S_\mathbf{u}$ or by the so-called *method of snapshots*, which entails the solution of an eigenvalue problem for the correlation matrix $S_\mathbf{u}^T X_\mathbf{u} S_\mathbf{u}$. Although possibly less well numerically conditioned, the latter is usually preferred because it allows a considerable dimensionality reduction in the computations. In fact, the size of the matrix $X_\mathbf{u}^{1/2} S_\mathbf{u}$ is $N_\mathbf{u}^h \times (M_h \cdot N_{\text{train}})$, while the size of the correlation matrix $S_\mathbf{u}^T X_\mathbf{u} S_\mathbf{u}$ is $(M_h \cdot N_{\text{train}}) \times (M_h \cdot N_{\text{train}})$. Therefore, in steady-state problems ($M_h = 1$), the cost of the computation of the POD basis is independent on the FE grid size. For unsteady problems, however, the resulting eigenvalue problem is still dependent

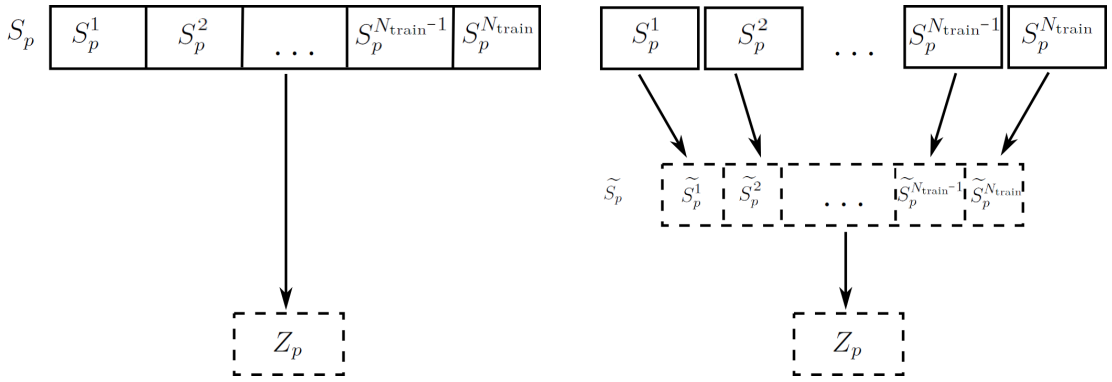

(a) *Standard POD.* **(b)** *Two-level POD.*

Figure 4.1: *Summary of the standard (full) POD and two-level POD strategies. Box represent data storage; solid boxes require the FE solution for all time steps, dashed box require a POD. Each arrow represents the computation of a POD. For the sake of exposition the summary is provided only for the computation of the pressure basis functions, since the scheme for velocity and supremizer basis functions is similar.*

on the temporal discretization, entailing high costs for the storage of all the $M_h \cdot N_{\text{train}}$ snapshots and the spectrum computation can thus be very expensive if $M_h \to \infty$.

Following the approach presented in [16], an alternative strategy can be employed to overcome this drawback:

(i) *POD on the temporal dynamics*: for any $\boldsymbol{\mu}^i \in \Xi_{\text{train}}$, $i = 1, \dots, N_{\text{train}}$, compute the FE solution for all time-steps and perform a POD on $S^i_{\mathbf{u}}$ (S^i_p, $S^i_{\mathbf{s}}$, respectively). Then, extract the first M_{2-POD} modes and build a "compressed" matrix $\widetilde{S}^i_{\mathbf{u}} \in \mathbb{R}^{N^h_{\mathbf{u}} \times M_{2-POD}}$ ($\widetilde{S}^i_p \in \mathbb{R}^{N^h_p \times M_{2-POD}}$,$\widetilde{S}^i_{\mathbf{s}} \in \mathbb{R}^{N^h_{\mathbf{s}} \times M_{2-POD}}$, respectively) containing those modes (*non-weighted* version), possibly scaled by the respective singular values $\{\sigma^{(i)}_j\}_{j=1,\dots,M_{2-POD}}$ (*weighted* version). A similar weighting is proposed also in [215]. The most important features of the temporal dynamics should be captured as long as M_{2-POD} is large enough. Computational savings are possible if $M_{2-POD} \ll M_h$. The value of M_{2-POD} may depend on i and on the singular values $\sigma^{(i)}_j$, based on the same energetic considerations as in Section 3.2.1.

(ii) *POD on the parameter space*: at the end of the training phase, assemble the following *compressed snapshot matrices on the temporal trajectory and parameter space*

$$\widetilde{S}_{\mathbf{u}} = [\widetilde{S}^1_{\mathbf{u}}, \dots, \widetilde{S}^{N_{\text{train}}}_{\mathbf{u}}] \in \mathbb{R}^{N^h_{\mathbf{u}} \times (M_{2-POD} \cdot N_{\text{train}})},$$
$$\widetilde{S}_p = [\widetilde{S}^1_p, \dots, \widetilde{S}^{N_{\text{train}}}_p] \in \mathbb{R}^{N^h_p \times (M_{2-POD} \cdot N_{\text{train}})},$$
$$\widetilde{S}_{\mathbf{s}} = [\widetilde{S}^1_{\mathbf{s}}, \dots, \widetilde{S}^{N_{\text{train}}}_{\mathbf{s}}] \in \mathbb{R}^{N^h_{\mathbf{s}} \times (M_{2-POD} \cdot N_{\text{train}})},$$

perform a second POD (in this case, the spectrum of a matrix of smaller size $M_{2-POD} \cdot N_{\text{train}} \ll M_h \cdot N_{\text{train}}$ needs to be computed), and store the first $N_{\mathbf{u}}$ (N_p, $N_{\mathbf{s}}$, respectively) left singular vectors as basis functions $\boldsymbol{\varphi}_n$ (ζ_n, $\boldsymbol{\eta}_n$, respectively).

A summary of the standard and two-level POD strategies is provided in Figure 4.1. Let

$$Z_{\mathbf{u},\mathbf{s}} = [\underline{\widetilde{\mathbf{g}}}^1_D \mid \dots \mid \underline{\widetilde{\mathbf{g}}}^{Q_D}_D \mid \underline{\widetilde{\mathbf{w}}}^1 \mid \dots \mid \underline{\widetilde{\mathbf{w}}}^{Q_w} \mid \underline{\boldsymbol{\varphi}}_1 \mid \dots \mid \underline{\boldsymbol{\varphi}}_{N_{\mathbf{u}}} | \underline{\boldsymbol{\eta}}_1 \mid \dots \mid \underline{\boldsymbol{\eta}}_{N_{\mathbf{s}}}] \in \mathbb{R}^{N^h_{\mathbf{u}} \times N_{\mathbf{u},\mathbf{s}}},$$
$$Z_p = [\underline{\zeta}_1 \mid \dots \mid \underline{\zeta}_{N_p}] \in \mathbb{R}^{N^h_p \times N_p}$$

denote matrices whose columns are provided by the offline bases for reduced velocity and pressure spaces, respectively.

4.4.2 A greedy algorithm for parameters selection

It is well known that the training space Ξ_{train} should be carefully chosen in order to have a good reduced-order model. In fact, on one hand the space should be large enough in order to well capture the parametric variation of the phenomena; however, on the other hand, especially when dealing with complex geometrical configurations and unsteady problems, one would like to be able to perform as little as possible truth solves during the offline stage. In the same spirit of standard greedy-RB methods [214], a residual-based greedy algorithm can be considered for the selection of the parameters in the training sample.

Algorithm 4.1 A residual-based greedy algorithm for parameters selection.

INPUT: $\Xi_{test} \subset \mathcal{D}$, $W \in \mathbb{N}$, $N_{\mathbf{u}}^{\text{int}}, N_{\mathbf{s}}^{\text{int}}, N_p^{\text{int}}$, $\varepsilon \in \mathbb{R}$.
OUTPUT: $\Xi_{test} \subset \mathcal{D}$, $\Xi_{train} \subset \mathcal{D}$.
for $M = 1, \dots, |\Xi_{test}|/W$ **do**
  if $M = 1$ **then**
    Update ROM data structures A_N, B_N, etc., assuming $N_{\mathbf{u}}^{\text{int}} = N_{\mathbf{s}}^{\text{int}} = N_p^{\text{int}} = 0$.
  else
    Update ROM data structures A_N, B_N, etc.
  end if
  for all $\boldsymbol{\mu} \in \Xi_{test}$ **do**
    Compute the reduced-order solution;
    Compute and store the full-order residual of the reduced-order solution.
  end for
  Sort the parameters in Ξ_{test} by decreasing values of residual;
  if all residuals are less than ε **then**
    break
  end if
  Move the first W parameters of Ξ_{test} to Ξ_{train};
  $\Xi_{test} = \Xi_{test} \setminus \Xi_{train}$;
  Perform truth solves for the last W points in Ξ_{train};
  Perform a two-level POD to compute $N_{\mathbf{u}}^{\text{int}}, N_{\mathbf{s}}^{\text{int}}, N_p^{\text{int}}$ basis functions.
end for

Let us remark that W should be chosen strictly greater than 1. In fact, the evaluation of the residual involves computations on the full-order FE grid. Moreover, also the update of ROM data structures associated to the nonlinear term is expensive, because *(i)* it requires the computation of (possibly more than one, depending on the complexity of the shape variation) dense third-order tensors and *(ii)* the reduced-order spaces at iteration M and $M+1$ are not hierarchical, because of the addition of new snapshots.

4.4.3 Algebraic formulation of the POD-Galerkin ROM

A reduced-order approximation of both velocity and pressure field is obtained by means of a Galerkin projection on the reduced spaces $\boldsymbol{V}_N$ and Q_N. In particular, we seek an approximation of the form

$$\underline{\mathbf{u}}(t;\boldsymbol{\mu}) \approx Z_{\mathbf{u},\mathbf{s}}\underline{\mathbf{u}}_N(t;\boldsymbol{\mu}), \qquad \underline{\mathbf{p}}(t;\boldsymbol{\mu}) \approx Z_p\underline{\mathbf{p}}_N(t;\boldsymbol{\mu}), \tag{4.12}$$

In the online stage, the resulting reduced-order approximation for any $\boldsymbol{\mu} \in \mathcal{D}$ is as follows:

$$\begin{bmatrix} \frac{M_N(t^{n+1};\boldsymbol{\mu})}{\Delta t} + L(t^{n+1};\boldsymbol{\mu}) + C_N(\underline{\mathbf{u}}_N(t^{n+1};\boldsymbol{\mu});t^{n+1};\boldsymbol{\mu}) & B_N^T(t^{n+1};\boldsymbol{\mu}) \\ B_N(t^{n+1};\boldsymbol{\mu}) & 0 \end{bmatrix} \begin{bmatrix} \underline{\mathbf{u}}_N(t^{n+1};\boldsymbol{\mu}) \\ \underline{\mathbf{p}}_N(t^{n+1};\boldsymbol{\mu}) \end{bmatrix} = \begin{bmatrix} \underline{\mathbf{f}}_N(t^{n+1};\boldsymbol{\mu}) \\ \underline{\mathbf{g}}_N(t^{n+1};\boldsymbol{\mu}) \end{bmatrix} + \begin{bmatrix} \frac{M_N(t^n;\boldsymbol{\mu})}{\Delta t} & 0 \\ 0 & 0 \end{bmatrix} \begin{bmatrix} \underline{\mathbf{u}}_N(t^n;\boldsymbol{\mu}) \\ \underline{\mathbf{p}}_N(t^n;\boldsymbol{\mu}) \end{bmatrix}, \tag{4.13}$$

where, similarly to what we did in the previous chapter,

$$A_N(t;\boldsymbol{\mu}) = Z_{\mathbf{u},\mathbf{s}}^T\, A(t;\boldsymbol{\mu})\, Z_{\mathbf{u},\mathbf{s}}, \qquad B_N(t;\boldsymbol{\mu}) = Z_p^T\, B(t;\boldsymbol{\mu})\, Z_{\mathbf{u},\mathbf{s}}, \qquad C_N(\,\cdot\,;t;\boldsymbol{\mu}) = Z_{\mathbf{u},\mathbf{s}}^T C(\,\cdot\,;t;\boldsymbol{\mu}) Z_{\mathbf{u},\mathbf{s}},$$

$$\underline{\mathbf{f}}_N(t;\boldsymbol{\mu}) = Z_{\mathbf{u},\mathbf{s}}^T\, \underline{\mathbf{f}}(t;\boldsymbol{\mu}), \qquad \underline{\mathbf{g}}_N(\boldsymbol{\mu}) = Z_p^T\, \underline{\mathbf{g}}(t;\boldsymbol{\mu}).$$

The remaining terms can be obtained in the same way. Moreover, thanks to the affine parametric dependence, only the matrices and vectors

$$A_N^q = Z_{\mathbf{u},\mathbf{s}}^T\, A^q\, Z_{\mathbf{u},\mathbf{s}}, \qquad B_N^q = Z_p^T\, B^q\, Z_{\mathbf{u},\mathbf{s}}, \qquad C_N(\,\cdot\,;t;\boldsymbol{\mu}) = Z_{\mathbf{u},\mathbf{s}}^T C^q(\,\cdot\,) Z_{\mathbf{u},\mathbf{s}},$$

$$\underline{\mathbf{f}}_N^q = Z_{\mathbf{u},\mathbf{s}}^T\, \underline{\mathbf{f}}^q, \qquad \underline{\mathbf{g}}_N^q = Z_p^T\, \underline{\mathbf{g}}^q.$$

need to be stored. We remark that, thanks to the affine parametric dependence assumption (see section 4.3.4), the stored data structures do not depend explicitly on time because the temporal dependence is stored in the multiplicative factors $\Theta_q^*(t;\boldsymbol{\mu})$, thus yielding to storage costs comparable to the steady case. This gives the chance to perform a temporal extrapolation, i.e. to consider $k = 0, \ldots, M_N - 1$ with $M_N \gg M_h$.

At each time, the nonlinear system is solved by means of Picard or Newton iterations. Dirichlet boundary conditions are imposed modifying the first Q_D+Q_w rows of the online system, so that the only non-null term appears on the main diagonal, and the first Q_D+Q_w terms of the right-hand side to store the corresponding values of $\Theta_q^D(t^{n+1};\boldsymbol{\mu})$ and $\Theta_q^w(t^{n+1};\boldsymbol{\mu})$.

4.5 Test cases

4.5.1 Case I: backward facing step

In this Section the same backward facing step flow problem of Section 3.5.1 is considered, with a parametrization with respect to the Reynolds number. This first example compares the standard POD approach and the two-level POD approach; moreover the possibility of an online time extrapolation is explored. Finally, a comparison with an offline stage performed on a *stationary* problem is carried out.

Details of the offline stage, FE discretization and temporal discretization are summarized in Table 4.1. Two physical parameters $\boldsymbol{\mu}_p = (\nu, u_{in})$ are considered (viscosity ν and magnitude of the normal velocity u_{in} at the inlet section), yielding a Reynolds number in the range $[0.75, 300]$. Dirichlet boundary conditions on the inlet feature $Q_D = 1$, $\Theta_q^1(t;\boldsymbol{\mu}) = u_{in}(1 + 0.5\sin(2\pi t))$, and $\boldsymbol{g}_D^1$ is a parabolic profile. The offline stage is performed only in the interval $[0, 0.5]$ (half-period of the inlet profile), while the online phase is performed over the whole period $[0, 1]$. Homogeneous Dirichlet boundary conditions are imposed on the walls, and homogeneous Neumann boundary conditions are imposed on the outlet.

Physical parameters	2: ν, u_{in}
Range ν	[0.05, 2]
Range u_{in}	[0.5, 5]
Resulting range of Reynolds number	[0.75, 300]
FE velocity order	2
FE pressure order	1
Total number of FE dofs	116,136
Final time T_h	0.5
Time step Δt	0.01
Snapshots for each parameter	50 (all time steps, standard POD) or 5 (90% reduction, two-level POD)
N_{train}	75
$N_{\max}$	75

Table 4.1: *Computational details of the offline stage.*

Comparison between standard POD and two-level POD

Figure 4.2 shows a comparison between standard POD (50 time steps $\times$ 75 training samples, resulting in snapshot matrices of dimension 3750) and two-level POD (5 modes out of 50 are extracted within the innermost POD $\times$ 75 training samples, resulting in snapshot matrices of dimension 375). The comparison of the POD singular values and retained energy shows that, in both cases, few basis functions are needed in order to capture the most relevant features of the problem. A comparison of the retained energy shows that the weighted version of the two-level POD performs sensibly better than the non-weighted one; a proper weighting in the innermost POD is therefore important to preserve the most relevant energetic features of the phenomenon. In fact, even though there is a consistent dimensional reduction (90%) in the innermost POD, the singular values decay of the weighted two-level POD is comparable to the one of the standard POD.

Reduced-order solutions for $Re = 30, 90, 150$, $t = 0, 0.25, 0.5$ are reported in Figures 4.3, 4.4, 4.5, subfigures (a),(b),(c),(f),(g), images on top and center. We do not notice any strong difference between standard POD and two-level POD in terms of online accuracy.

Time extrapolation

Reduced-order solutions for $Re = 30, 90, 150$, $t = 0.75, 0.9$ are illustrated in Figures 4.3, 4.4, 4.5, subfigures (d),(e),(h),(i), images on top and center. Even though the offline stage was run for $t \in [0, 0.5]$ (when the Dirichlet datum $\Theta_q^1(t; \boldsymbol{\mu}) \geq 1$), the reduced-order model is able to correctly extrapolate for $t \in (0.5, 1]$ (when the Dirichlet datum $\Theta_q^1(t; \boldsymbol{\mu}) < 1$), although the errors slightly increase (Figures 4.6, 4.7, 4.8).

Comparison with the stationary case

Figures 4.3, 4.4, 4.5, images on the bottom, show that physical features of the unsteady phenomena are *not* correctly captured by basis functions generated from stationary flows, especially for the velocity at $t = 0.75$ and the pressure at $t = 0.25$ and $t = 0.75$.

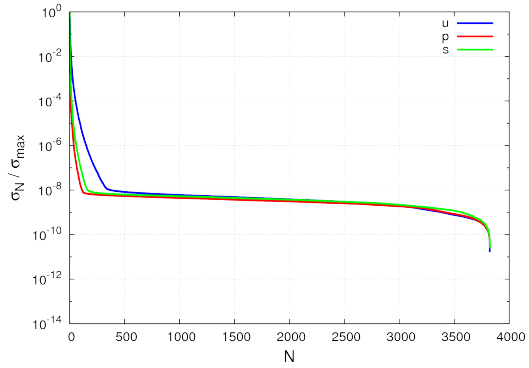

(a) *POD singular values: standard POD.*

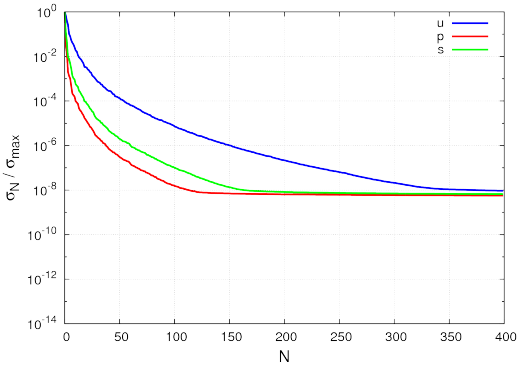

(b) *POD singular values: standard POD – zoom in the interval* $N \in [0, 400]$.

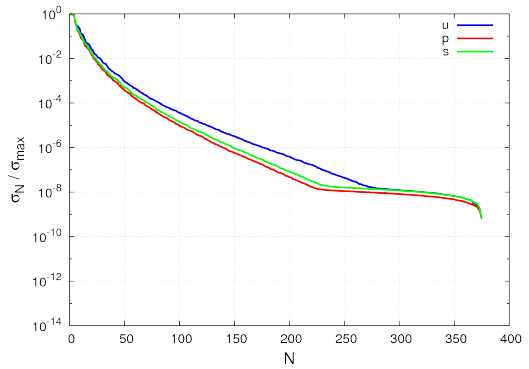

(c) *POD singular values: two-level POD.*

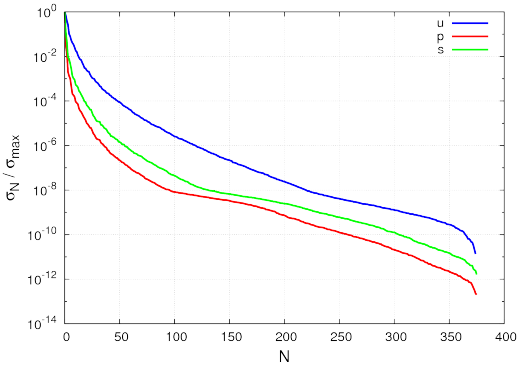

(d) *POD singular values: weighted two-level POD.*

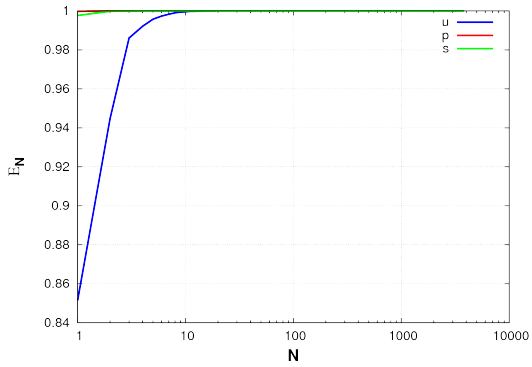

(e) *POD retained energy: standard POD.*

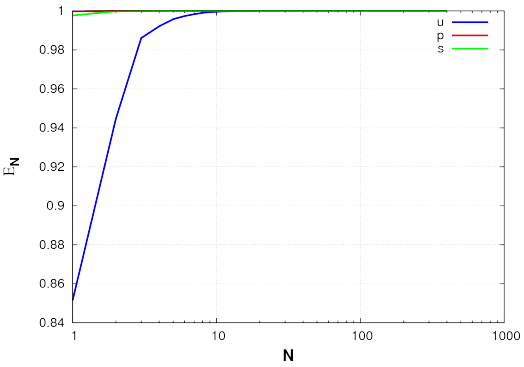

(f) *POD retained energy: standard POD – zoom in the interval* $N \in [0, 400]$.

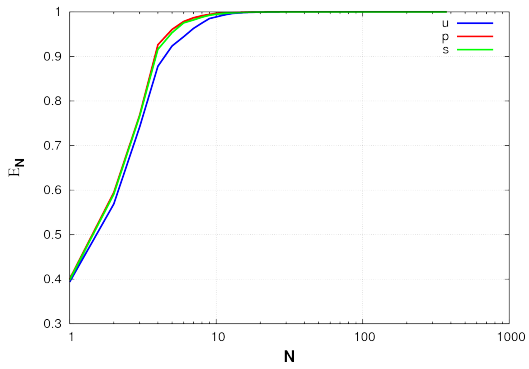

(g) *POD retained energy: two-level POD.*

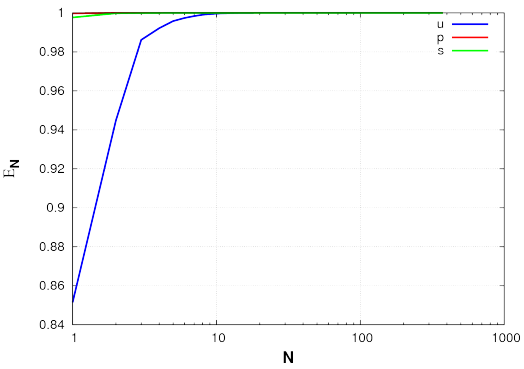

(h) *POD retained energy: weighted two-level POD.*

Figure 4.2: *Results of the offline stage: POD singular values and retained energy for velocity, pressure and supremizers.*

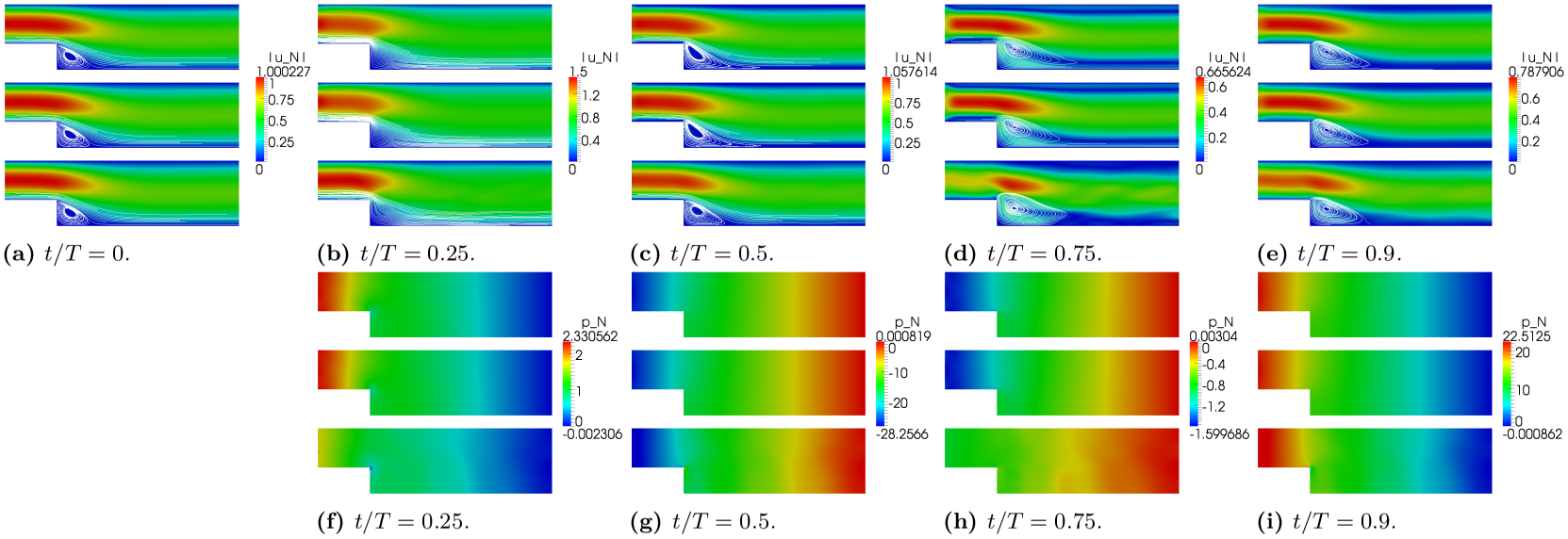

(a) $t/T = 0$. **(b)** $t/T = 0.25$. **(c)** $t/T = 0.5$. **(d)** $t/T = 0.75$. **(e)** $t/T = 0.9$.

(f) $t/T = 0.25$. **(g)** $t/T = 0.5$. **(h)** $t/T = 0.75$. **(i)** $t/T = 0.9$.

Figure 4.3: *Reduced-order solutions, for* $N_{\mathbf{u}} = N_p = N_{\mathbf{s}} = 25$*, at* $Re = 30$*. From top to bottom: standard POD, two-level POD, stationary basis.*

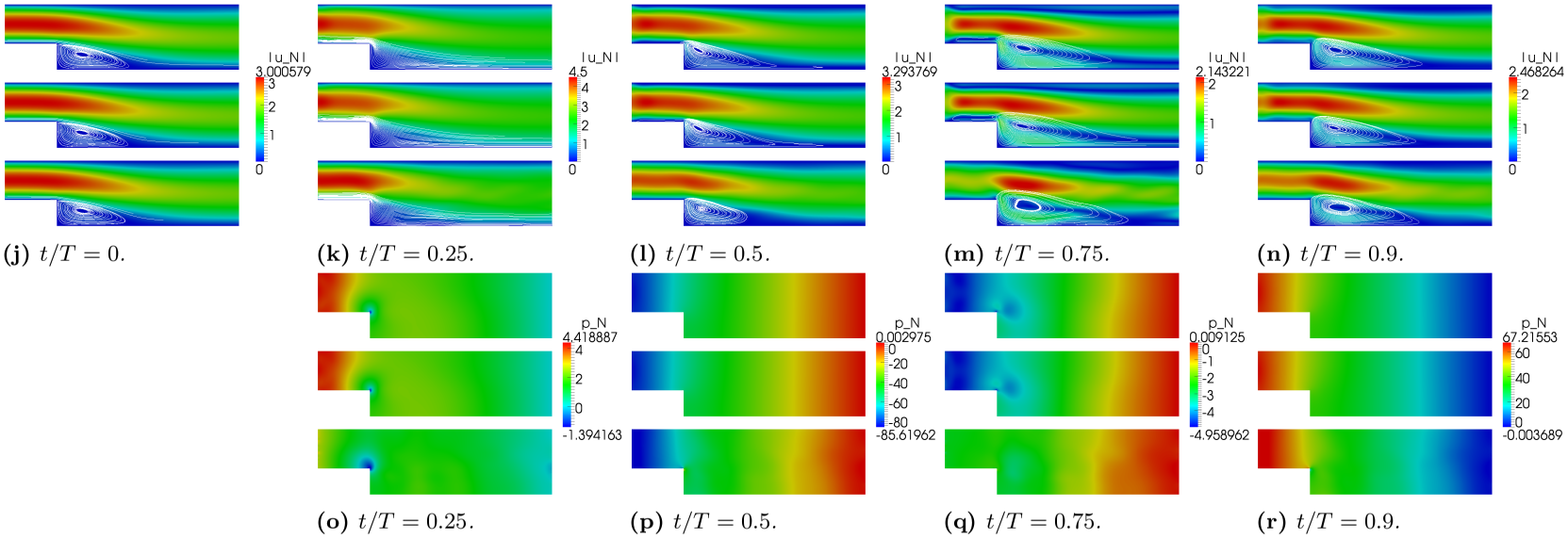

(j) $t/T = 0$. **(k)** $t/T = 0.25$. **(l)** $t/T = 0.5$. **(m)** $t/T = 0.75$. **(n)** $t/T = 0.9$.

(o) $t/T = 0.25$. **(p)** $t/T = 0.5$. **(q)** $t/T = 0.75$. **(r)** $t/T = 0.9$.

Figure 4.4: *Reduced-order solutions, for* $N_{\mathbf{u}} = N_p = N_{\mathbf{s}} = 25$*, at* $Re = 90$*. From top to bottom: standard POD, two-level POD, stationary basis.*

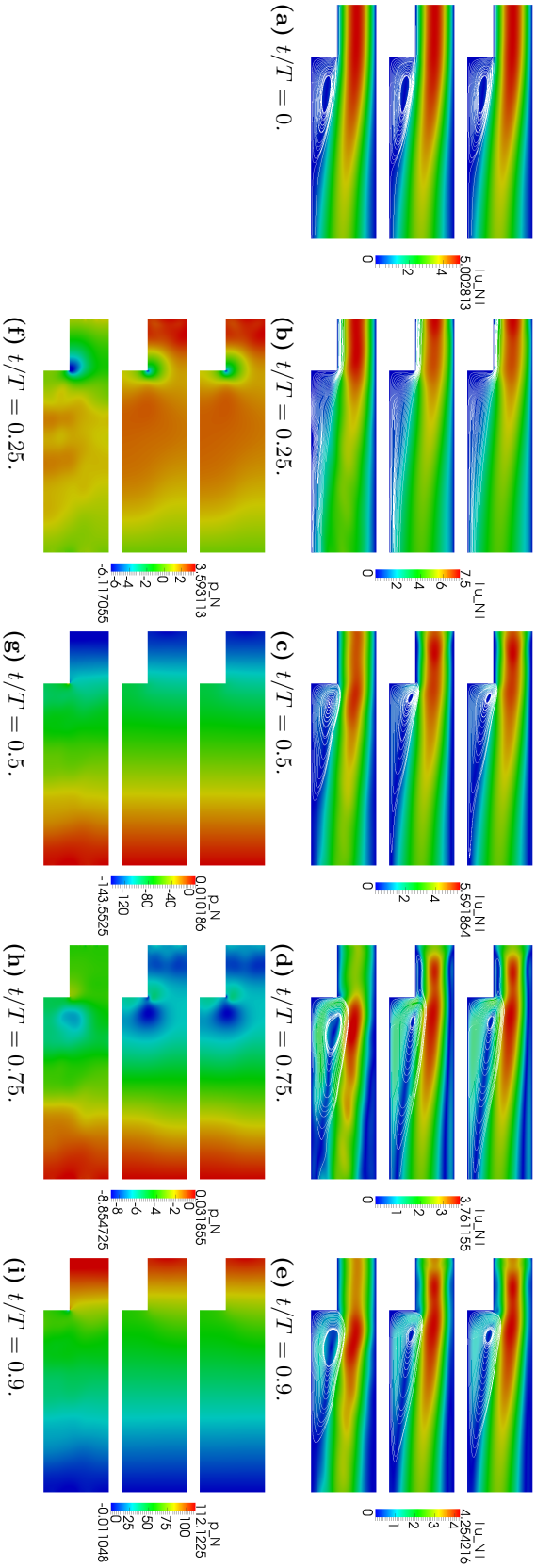

Figure 4.5: *Reduced-order solutions, for* $N_{\mathbf{u}} = N_p = N_{\mathbf{s}} = 25$*, at* $Re = 150$*. From top to bottom: standard POD, two-level POD, stationary basis.*

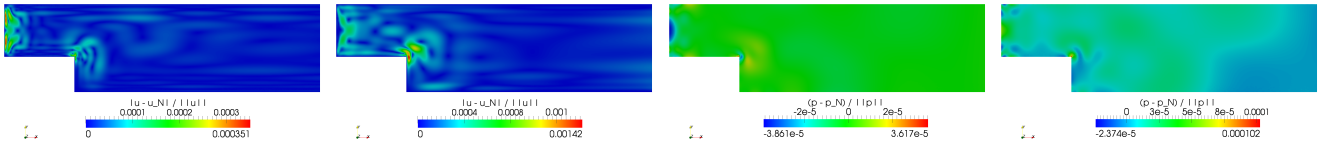

(a) $t/T = 0.5$. **(b)** $t/T = 1$. **(c)** $t/T = 0.5$. **(d)** $t/T = 1$.

Figure 4.6: *Relative errors between truth and reduced-order solutions (standard POD), for* $N_{\mathbf{u}} = N_p = N_{\mathbf{s}} = 25$*, at* $Re = 30$.

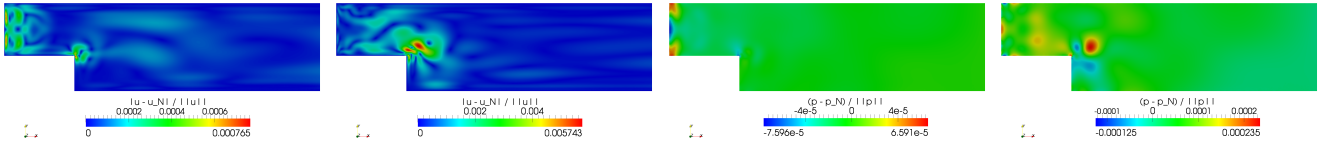

(e) $t/T = 0.5$. **(f)** $t/T = 1$. **(g)** $t/T = 0.5$. **(h)** $t/T = 1$.

Figure 4.7: *Relative errors between truth and reduced-order solutions (standard POD), for* $N_{\mathbf{u}} = N_p = N_{\mathbf{s}} = 25$*, at* $Re = 90$.

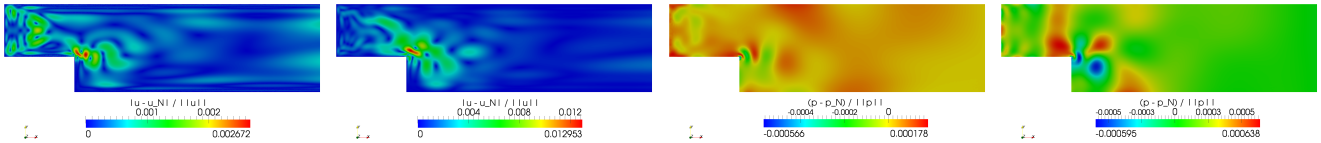

(a) $t/T = 0.5$. **(b)** $t/T = 1$. **(c)** $t/T = 0.5$. **(d)** $t/T = 1$.

Figure 4.8: *Relative errors between truth and reduced-order solutions (standard POD), for* $N_{\mathbf{u}} = N_p = N_{\mathbf{s}} = 25$*, at* $Re = 150$.

4.5.2 Case II: a double elbow geometry

In this section a parametrized flow in a double elbow geometry is considered, similar to the one analyzed in [178]. Both physical and geometrical parameters are considered. Two physical parameters $\boldsymbol{\mu}_p = (\nu, u_{in})$ are examined (viscosity ν and magnitude of the normal velocity u_{in} at the inlet section); the resulting range of Reynolds number is $[0.5, 200]$. A single geometrical parameter μ_g is considered, equal to the length of the vertical section of the domain. Dirichlet boundary conditions on the inlet feature $Q_D = 1$, $\Theta_q^1(t; \boldsymbol{\mu}) = u_{in}(1 + 0.5\sin(2\pi t))$, and $\boldsymbol{g}_D^1$ is a parabolic profile. Homogeneous Dirichlet boundary conditions are imposed on the wall, and homogeneous Neumann boundary conditions are imposed at the outlet. Details of the offline stage, FE discretization and temporal discretization are summarized in Table 4.2. A slower decay of the singular values (Figure 4.9), when compared to the previous example, is obtained in this case, because of the additional geometrical parameter.

The velocity field for increasing Reynolds numbers and different values of the geometrical parameter is shown in Figures 4.10, 4.11, 4.12. Recirculation zones appear close to the channel corners, especially at $t = 0.75$ (minimum of the inlet profile over the period $T = 1$).

Physical parameters	2: ν, u_{in}
Range ν	[0.05, 2]
Range u_{in}	[0.5, 10]
Resulting range of Reynolds number	[0.25, 200]
Geometrical parameters	1: μ_g
Range μ_g	[2, 5]
FE velocity order	2
FE pressure order	1
Total number of FE dofs	34,635
Final time T_h	1.0
Time step Δt	0.01
Snapshots for each parameter	10 (90% reduction, two-level POD)
N_{train}	75
$N_{\max}$	75

Table 4.2: *Computational details of the offline stage.*

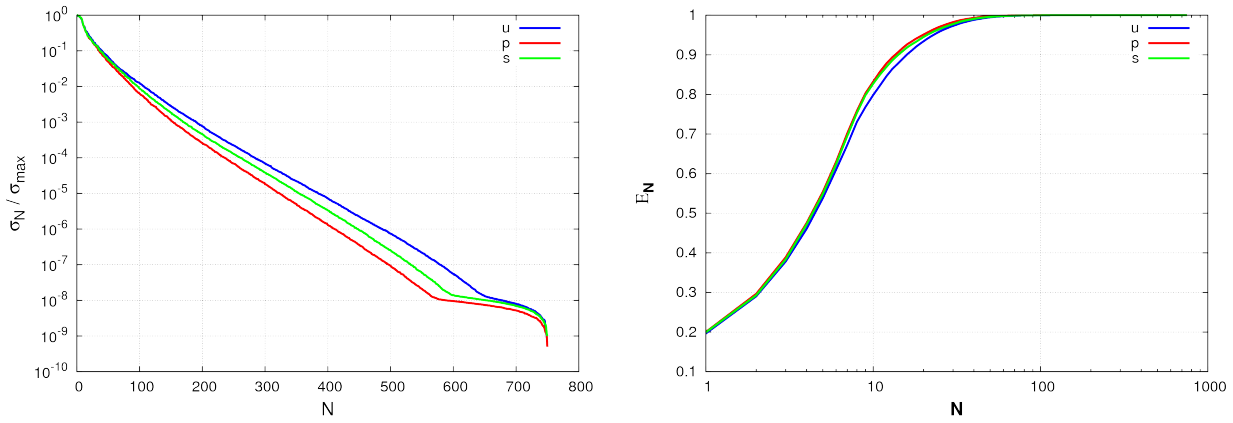

(a) *POD singular values: two-level POD.* **(b)** *POD retained energy: two-level POD.*

Figure 4.9: *Results of the offline stage: POD singular values and retained energy for velocity, supremizers, pressure.*

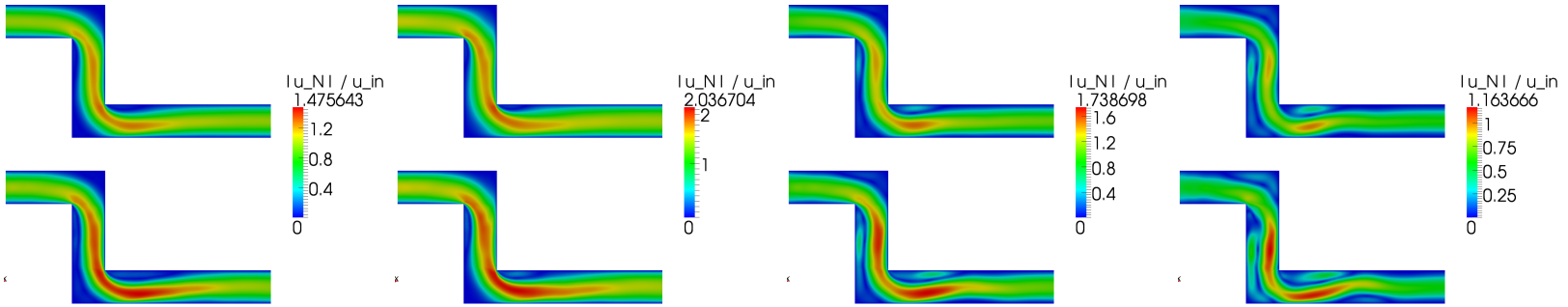

(a) $t/T = 0.$ **(b)** $t/T = 0.25.$ **(c)** $t/T = 0.5.$ **(d)** $t/T = 0.75.$

Figure 4.10: *Reduced-order solutions, for* $N_{\mathbf{u}} = N_p = N_{\mathbf{s}} = 75$*, at* $\mu_g = 2$*. From top to bottom:* $Re = 100$*,* $Re = 150$*.*

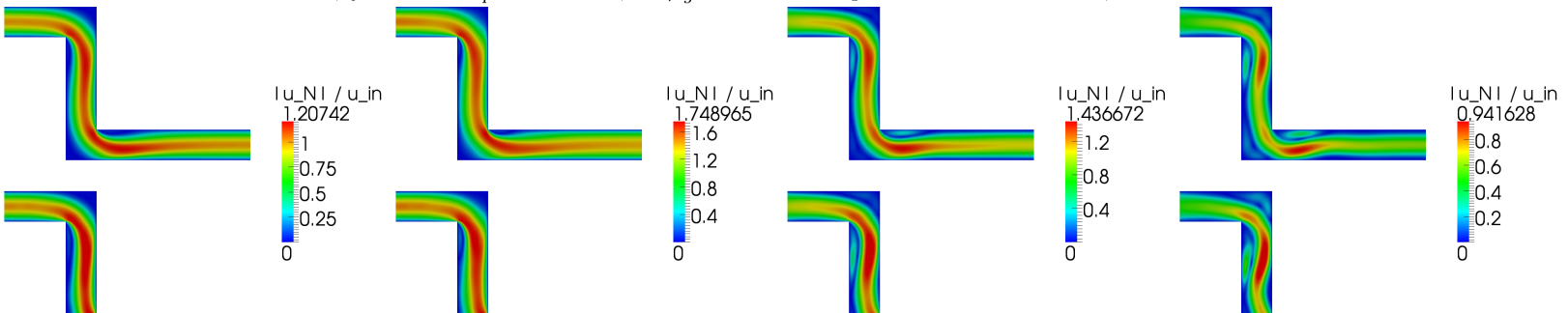

(e) $t/T = 0.$ **(f)** $t/T = 0.25.$ **(g)** $t/T = 0.5.$ **(h)** $t/T = 0.75.$

Figure 4.11: *Reduced-order solutions, for* $N_{\mathbf{u}} = N_p = N_{\mathbf{s}} = 75$*, at* $\mu_g = 3$*. From top to bottom:* $Re = 100$*,* $Re = 150$*.*

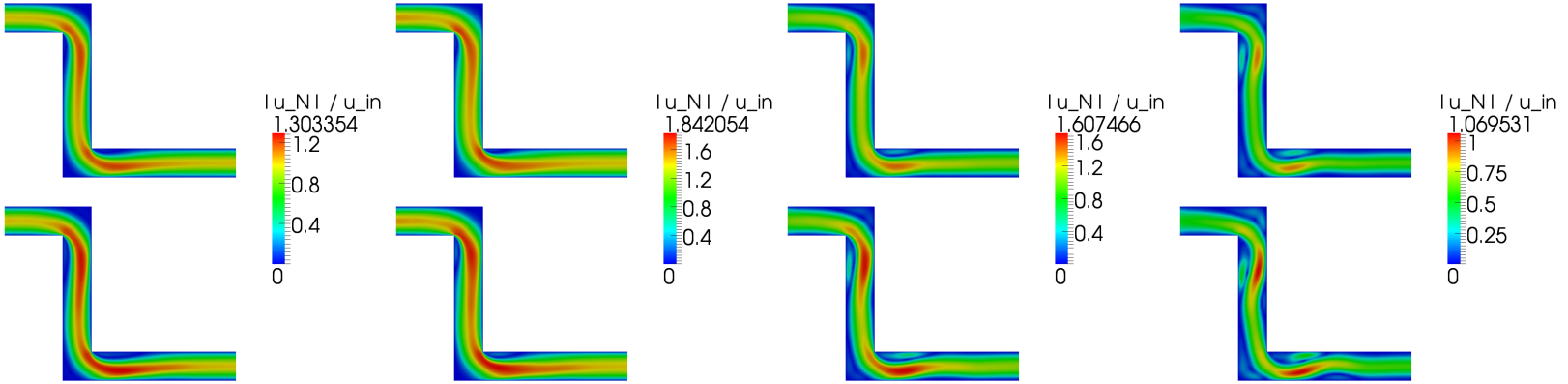

(a) $t/T = 0.$ **(b)** $t/T = 0.25.$ **(c)** $t/T = 0.5.$ **(d)** $t/T = 0.75.$

Figure 4.12: *Reduced-order solutions, for* $N_{\mathbf{u}} = N_p = N_{\mathbf{s}} = 75$*, at* $\mu_g = 4$*. From top to bottom:* $Re = 100$*,* $Re = 150$*.*

4.5.3 Case III: a moving domain test case

In this section a test case for the ALE formulation is carried out [240,247,250]. Two physical parameters $\boldsymbol{\mu}_p = (\nu, u_{in})$ are considered (viscosity ν and magnitude of the normal velocity u_{in} at the inlet section). The resulting range of Reynolds number is $[285, 800]$. Details of the offline stage, FE discretization and temporal discretization are summarized in Table 4.3. Figure 4.13 shows that, as in the example for case I, the weighted version of the two-level POD is able to preserve the most relevant features of the phenomenon with fewer basis functions.

Physical parameters	2: ν, u_{in}
Range ν	[0.0025, 0.0035]
Range u_{in}	[2, 4]
Resulting range of Reynolds number	[285, 800]
Geometrical parameters	1: μ_g
Range μ_g	[0.5, 1.5]
FE velocity order	2
FE pressure order	1
Total number of FE dofs	35,934
Final time T_h	1.0
Time step Δt	0.01
Snapshots for each parameter	10 (90% reduction, two-level POD)
N_{train}	75
$N_{\max}$	75

Table 4.3: *Computational details of the offline stage.*

The reference domain is $\Omega = (0,5) \times (0,0.5)$. A single geometrical parameter μ_g defines the current configuration as $\boldsymbol{x}_o = \boldsymbol{T}(\boldsymbol{x}; \widetilde{\mu}_g(t))$, where

$$\begin{cases} x_{1,o} &= x_1 \\ x_{2,o} &= \begin{cases} x_2, & x_1 \leq 1 \text{ or } x_1 \geq 2, \\ x_2 - 0.2\widetilde{\mu}_g(t)\sin[2\pi(x_1 - 1)], & 1 < x_1 < 2, \end{cases} \end{cases}$$

and

$$\widetilde{\mu}_g(t) = \mu_g \sin(\pi t), \qquad \mu_g \in [0.5, 1.5]$$

Dirichlet boundary conditions on the inlet feature $Q_D = 1$, $\Theta_q^1(t; \boldsymbol{\mu}) = u_{in}$, and $\boldsymbol{g}_D^1$ is a parabolic profile. The continuity of the velocity is imposed on the walls, and Neumann boundary conditions are imposed on the outlet.

Figures 4.14, 4.15 and 4.16 show some reduced-order solutions, at different time steps, Reynolds numbers and geometrical parameters. The complexity of the flow patterns increases with both Reynolds number and the magnitude of the geometrical parameter μ_g.

Streamlines intersect the boundary in the deformable region $\Gamma_{o,W}(\widetilde{\boldsymbol{\mu}}_g(t))$. This is because of the boundary condition $\boldsymbol{u}_o(t; \boldsymbol{\mu}) = \boldsymbol{w}_o(t; \boldsymbol{\mu})$, on $\Gamma_{o,W}(\widetilde{\boldsymbol{\mu}}_g(t)) \times (0, T)$, which is non-homogeneous in the deformable boundary.

During the expansion phase ($t \in [0, 0.5]$) three vortices appear: vortex 1 at $x_1 = 1.5$, vortex 2 at $x_1 = 1.75$ and vortex 3 at $x_1 = 2.25$. At $t = 0.25$ (mid-expansion), vortex 1 and 2 are not present for low Reynolds numbers ($Re = 400$), and the dimension of vortex 3 increases both with Reynolds number and μ_g. The region between vortices 1 and 2 features an high pressure gradient, with a mild dependence on μ_g. At $t = 0.5$ (maximum expansion) all three vortices are present. The size of vortices 1 and 2 depends only on the geometrical parameter, but not on the Reynolds number. A region of low pressure appears in vortex 3,

with size increasing both with Re and μ_g. A shear jet of high velocity appears in the region above vortex 3; the velocity is increased of 15% ($Re = 400$), 80% ($Re = 600$) and 150% ($Re = 800$) with respect to the inflow boundary condition.

During the contraction phase ($t \in [0.5, 1]$) vortices 1 and 2 disappear, for all μ_g and all Re. The high velocity jet moves downstream, featuring a smaller peak velocity. For small μ_g ($\mu_g = 0.5$), vortex 3 is almost dissipated. For higher μ_g ($\mu_g = 1, 1.5$), also vortex 3 moves downstream; in these cases a fourth vortex appears on the top of the channel ($x_1 = 3$), with size increasing with Re. Moreover, for large Re and large μ_g, a fifth vortex appears, downstream to vortex 4, on the bottom of the channel at $x_1 = 4$.

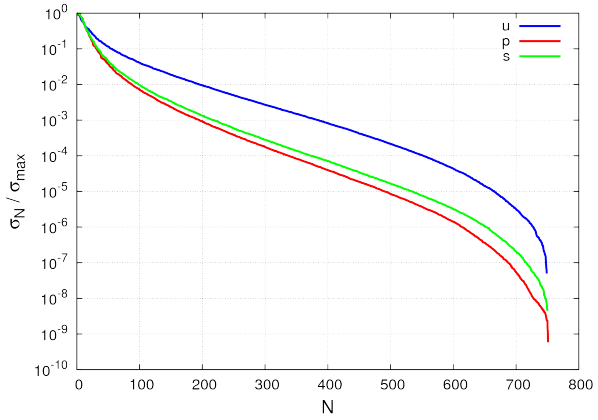

(a) *POD singular values: two-level POD.*

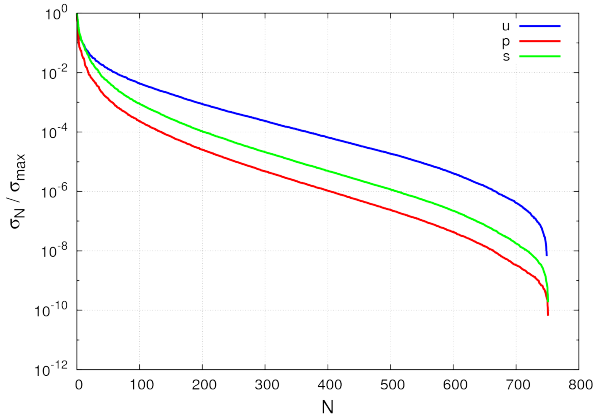

(b) *POD singular values: weighted two-level POD.*

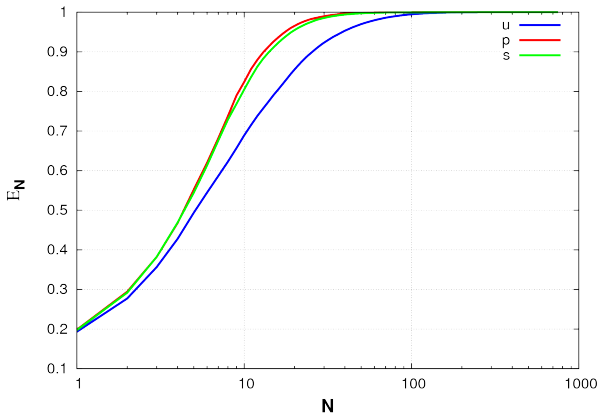

(c) *POD retained energy: two-level POD.*

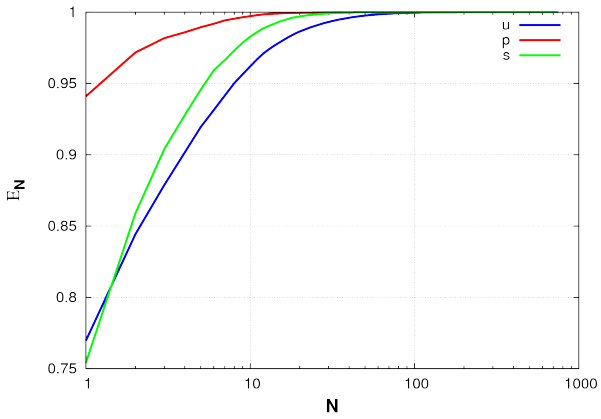

(d) *POD retained energy: weighted two-level POD.*

Figure 4.13: *Results of the offline stage: POD singular values and retained energy for velocity, supremizers, pressure.*

4.6 Outlook

Although being introduced in a general setting, model order reduction techniques introduced in this Part, will be applied on coronary artery bypass configurations in the remainder of this thesis. For the purpose of the clinical application the domain Ω will be the geometrical configuration obtained from the reconstructed geometries of Section 2.3, and a shape parametrization technique tailored for the specific application is going to be introduced in the next Chapter 5. Idealized bypass configurations will be used in the next Chapter to motivate the particular choice of the shape parametrization map $\boldsymbol{T}$.

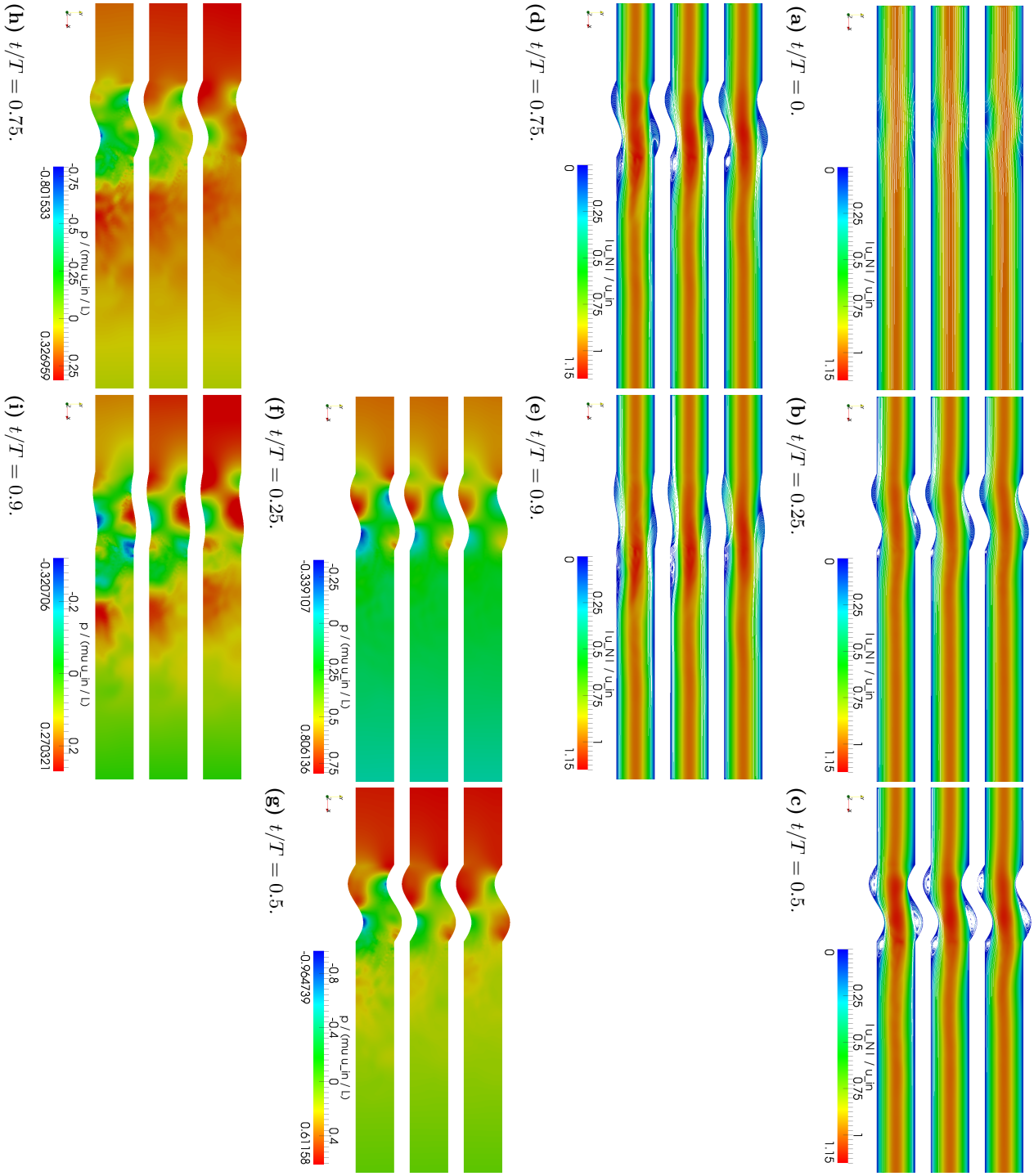

Figure 4.14: *Reduced-order solutions, for* $N_{\mathbf{u}} = N_p = N_{\mathbf{s}} = 75$*, at* $\mu_g = 0.5$*. From top to bottom:* $Re = 400$*,* $Re = 600$*,* $Re = 800$*.*

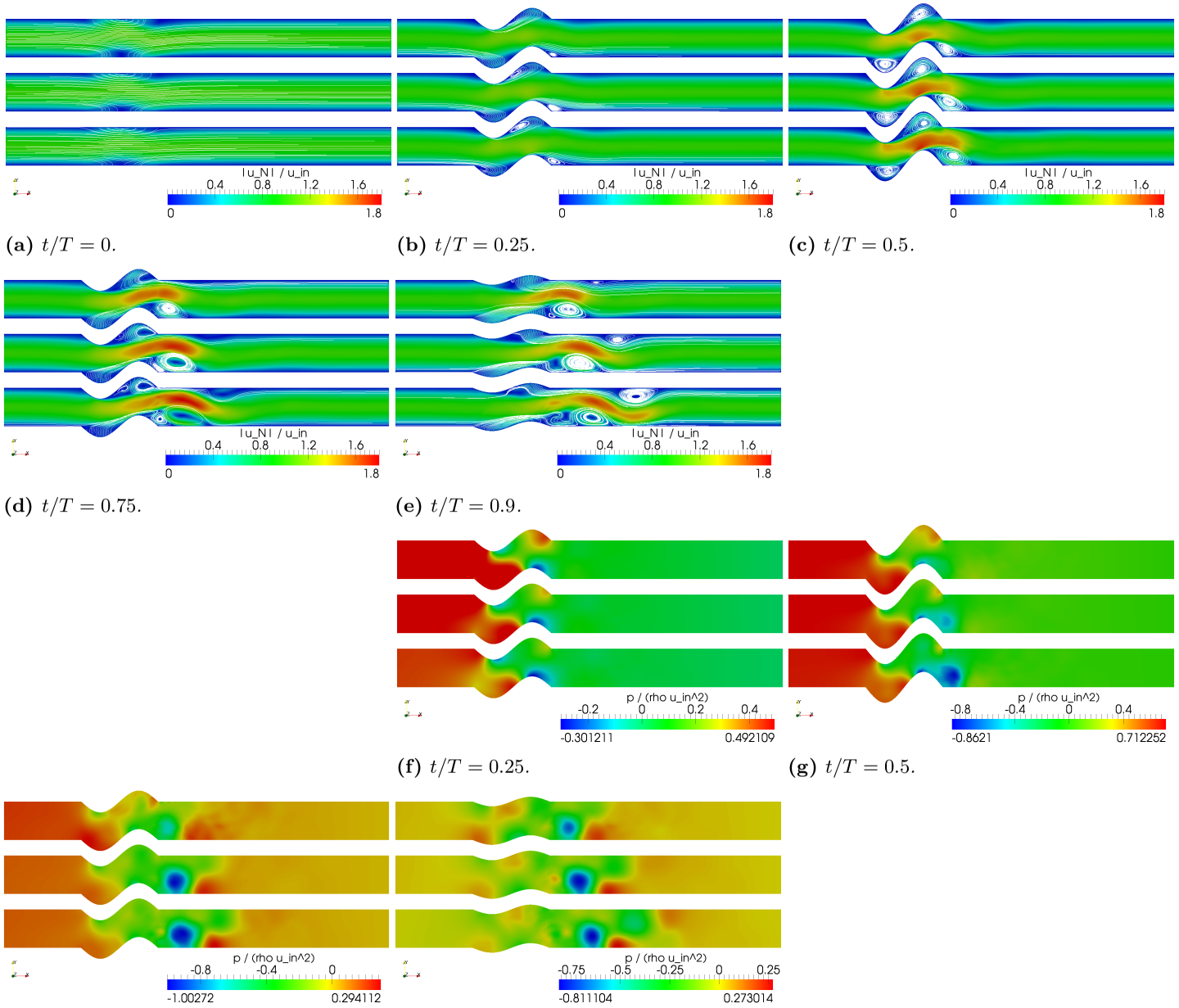

(a) $t/T = 0$. **(b)** $t/T = 0.25$. **(c)** $t/T = 0.5$.

(d) $t/T = 0.75$. **(e)** $t/T = 0.9$.

(f) $t/T = 0.25$. **(g)** $t/T = 0.5$.

(h) $t/T = 0.75$. **(i)** $t/T = 0.9$.

Figure 4.15: *Reduced-order solutions, for* $N_{\mathbf{u}} = N_p = N_{\mathbf{s}} = 75$, *at* $\mu_g = 1$. *From top to bottom:* $Re = 400$, $Re = 600$, $Re = 800$.

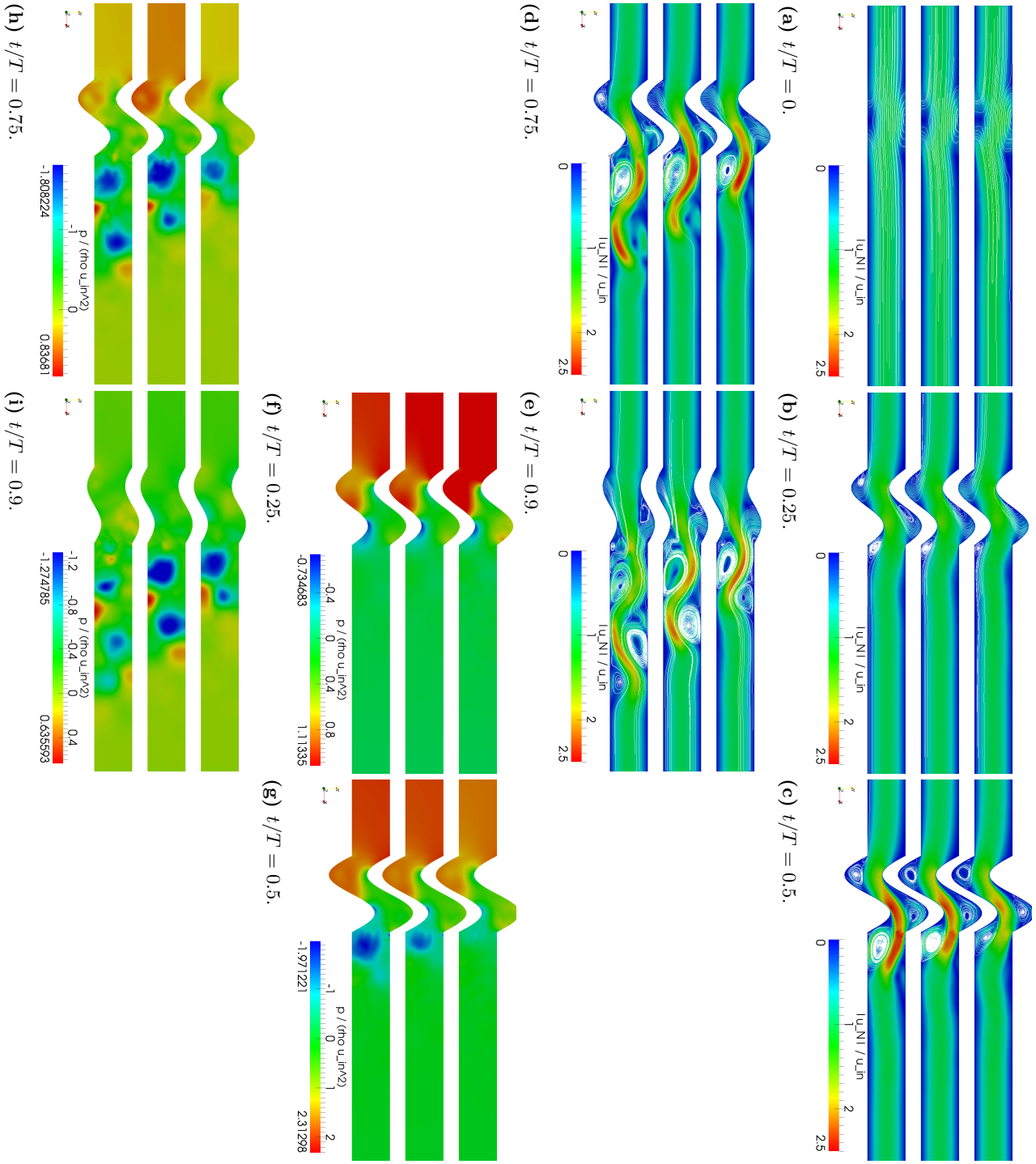

(a) $t/T = 0.$ **(b)** $t/T = 0.25.$ **(c)** $t/T = 0.5.$

(d) $t/T = 0.75.$ **(e)** $t/T = 0.9.$

(f) $t/T = 0.25.$ **(g)** $t/T = 0.5.$

(h) $t/T = 0.75.$ **(i)** $t/T = 0.9.$

Figure 4.16: *Reduced-order solutions, for* $N_{\mathbf{u}} = N_p = N_{\mathbf{s}} = 75$*, at* $\mu_g = 1.5$*. From top to bottom:* $Re = 400$*,* $Re = 600$*,* $Re = 800$*.*

Part III

Geometrical parametrization and reduction

CHAPTER 5

A centerlines-based parametrization for patient-specific coronary artery bypass grafts

Once patient-specific data have been processed and a computational domain has been generated, we aim to compute blood flows not only in the patient-specific configuration, but also in a perturbed one. The aim is either to perform a sensitivity analysis or answer to query of clinical interest related both to native coronary arteries disease (e.g. stenoses severity) and surgical intervention (e.g. anastomosis features). Relying on a suitable technique for shape representation and deformation is a key issue in the current reduction framework [157, 177, 180]. To meet this goals, in this chapter we propose a shape parametrization specifically tailored for coronary arteries and bypass grafts or, more in general, tubular structures. Two volume-based parametrizations are introduced in Section 5.1; these are general tools for deformation of an arbitrary object by displacing a set of few control points. Volume-based parametrizations will be employed for a *local* description of the deformation and coupled to a curve-based parametrization (Section 5.2) for a *global* description of the coronary artery network. Local modifications of the curve, as well as variation of the radius, are easily described within this framework. A test case, reported in Section 5.3, shows the application of the full computational reduction framework (POD-Galerkin ROM and centerlines-based parametrization) on a preliminary application to an idealized anastomosis. The same framework will then be applied to patient-specific cases in the next chapter.

5.1 Volume-based shape parametrizations

In this section we introduce two possible *volume-based representations* [103] to obtain admissible shapes by mapping a reference shape through a parametric map defined in the global space. The common assumption is that we can operate on a control volume (regardless of the object to be deformed, which is then embedded in the volume) and define parametric maps by introducing a set of control points over the control volume. Their displacements, which actually induce a shape deformation, can be considered as geometrical parameters. In

this way, shifting a control point causes a deformation of the embedding space and thereby induces a global modification of each shape located inside this volume.

5.1.1 The *free-form deformation* map

The *free-form deformation* (FFD) map[1], originally introduced in [233] is a possible example of volume-based parametrization. A reference (undeformed) domain $\Omega \subset \mathbb{R}^3$ is embedded in a control volume $D \supset \Omega$; then, a grid of control points is defined over D, and the deformed domain is obtained by a composition of the displacements of each control point (see Fig. 5.1). The parameters of the map are the displacements of a suitably chosen subset of control points. The map is named *free-form* because it is independent of the underlying shape to be deformed: this ensures that, unlike boundary parametrizations, it can be applied to arbitrarily complex domains, still keeping a small number of degrees of freedom.

Let us denote by $D = [x_1^{min}, x_1^{max}] \times [x_2^{min}, x_2^{max}] \times [x_3^{min}, x_3^{max}] \subset \mathbb{R}^3$ the control volume and by $\Omega \subset D$ the fixed reference domain. Moreover, by introducing an affine map $\boldsymbol{\psi} : D \to \widehat{D} \equiv [0,1]^3$, $\boldsymbol{x} \mapsto \widehat{\boldsymbol{x}} = \boldsymbol{\psi}(\boldsymbol{x})$:

$$\boldsymbol{\psi}(x_1, x_2, x_3) = \begin{bmatrix} \frac{x_1 - x_1^{min}}{x_1^{max} - x_1^{min}} \\ \frac{x_2 - x_2^{min}}{x_2^{max} - x_2^{min}} \\ \frac{x_3 - x_3^{min}}{x_3^{max} - x_3^{min}} \end{bmatrix},$$

let us define the FFD with respect to a system of coordinates $\boldsymbol{\psi}(x_1, x_2, x_3) \in [0,1]^3$. We denote a grid of $(K+1) \times (L+1) \times (M+1)$ control points over $\widehat{D}$ by

$$\widehat{\boldsymbol{p}}_{k,l,m} = \begin{bmatrix} k/K \\ l/L \\ m/M \end{bmatrix}, \qquad k = 0, \dots, K, \quad l = 0, \dots L, \quad m = 0, \dots, M,$$

and the displacement vector $\widehat{\boldsymbol{\mu}}_{k,l,m} \in \mathbb{R}^3$ of each control point (k,l,m). The deformed position of the control point (k,l,m) is thus given by

$$\widehat{\boldsymbol{p}}_{k,l,m} + \widehat{\boldsymbol{\mu}}_{k,l,m}.$$

Furthermore, since it is possible for some control points to be fixed or to be allowed to move only in some coordinate directions, we denote by $\boldsymbol{\mu} = [\mu_1, \dots, \mu_p]^T \in \mathcal{D} \subset \mathbb{R}^p$ the vector of the p enabled displacements, to which we refer as *degrees of freedom* of the FFD, defined as follows:

$$\mu_q = (\widehat{\boldsymbol{\mu}}_{k,l,m})_i \neq 0, \quad \text{if } \widehat{\boldsymbol{p}}_{k,l,m} \text{ is enabled to move in the } i\text{-th direction}, \tag{5.1}$$

where q is a compact notation for (i,k,l,m).

The deformation of the unitary cube $\widehat{D}$ is thus obtained by a composition of the deformed position of each control point through the map $\widehat{\boldsymbol{T}}_{FFD}(\cdot;\boldsymbol{\mu}) : \widehat{D} \to \widehat{D}_o(\boldsymbol{\mu})$, $\widehat{\boldsymbol{x}} \mapsto \widehat{\boldsymbol{x}}_o(\boldsymbol{\mu})$, defined as

$$\widehat{\boldsymbol{x}}_o(\boldsymbol{\mu}) = \widehat{\boldsymbol{T}}_{FFD}(\widehat{\boldsymbol{x}};\boldsymbol{\mu}) = \sum_{k=0}^{K} \sum_{l=0}^{L} \sum_{m=0}^{M} b_{k,l,m}^{K,L,M}(\widehat{\boldsymbol{x}}) \, [\widehat{\boldsymbol{p}}_{k,l,m} + \widehat{\boldsymbol{\mu}}_{k,l,m}], \tag{5.2}$$

[1] This section is a re-adaptation of Section 2 of the following publication:
[24] F. Ballarin, A. Manzoni, G. Rozza, and S. Salsa. Shape optimization by Free-Form Deformation: existence results and numerical solution for Stokes flows. *Journal of Scientific Computing*, 60(3):537–563, 2014.

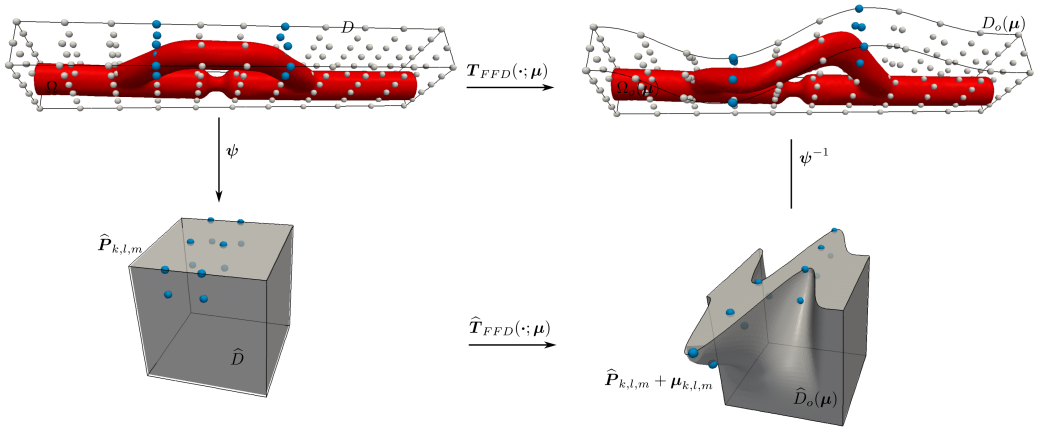

Figure 5.1: *Sketch of the Free-Form Deformation map.*

where $b_{k,l,m}^{K,L,M}(\widehat{\boldsymbol{x}}) = b_{k,l,m}^{K,L,M}(\widehat{x}_1, \widehat{x}_2, \widehat{x}_3)$ is the tensor product of one-dimensional Bernstein polynomials

$$b_{k,l,m}^{K,L,M}(\widehat{x}_1, \widehat{x}_2, \widehat{x}_3) = b_k^K(\widehat{x}_1) b_l^L(\widehat{x}_2) b_m^M(\widehat{x}_3), \qquad b_j^J(\widehat{z}) = \binom{J}{j}(1-\widehat{z})^{J-j}\widehat{z}^j.$$

Finally, the *Free-Form Deformation* is defined as the map

$$\boldsymbol{T}_{FFD}(\cdot;\boldsymbol{\mu}) : D \to \mathbb{R}^3, \quad \boldsymbol{x} \mapsto \boldsymbol{x}_o(\boldsymbol{\mu})$$

defined as the composition

$$\boldsymbol{x}_o(\boldsymbol{\mu}) = \boldsymbol{T}_{FFD}(\boldsymbol{x};\boldsymbol{\mu}) = \boldsymbol{\psi}^{-1}(\widehat{\boldsymbol{T}}(\boldsymbol{\psi}(\boldsymbol{x});\boldsymbol{\mu})); \tag{5.3}$$

a deformed domain is thus obtained as $\Omega_o(\boldsymbol{\mu}) = \boldsymbol{T}_{FFD}(\Omega;\boldsymbol{\mu})$, i.e. by applying the FFD to the reference domain Ω, with degrees of freedom $\boldsymbol{\mu}$. A summary of the construction of the map is sketched in Fig. 5.1.

Extensions of FFD to Non-Uniform Rational B-Splines (NURBS) basis functions, instead of a d-variate tensor product of Bernstein polynomials, allow a non-uniform distribution of the control points [7, 153, 230].

5.1.2 A *radial basis functions* parametrization

One of the main drawbacks of the FFD parametrization is the fact that it is not interpolatory, and therefore the physical interpretation of displacement values may not be trivial. An interpolatory shape parametrization can be defined thanks to radial basis functions (RBF) [49, 50]. RBF parametrizations have been employed e.g. in [34, 78–80, 98] for an efficient solution of FSI problems, and coupled to the reduced basis method for the solution of inverse problems in haemodynamics in [155, 177, 179].

Given a reference domain $\Omega \subset \mathbb{R}^3$, the RBF parametrization aims at describing the deformation of Ω by means of an interpolation of the deformed positions $\{\boldsymbol{p}_i + \boldsymbol{\mu}_i\}_{i=1,\dots,N}$ of a small number N of *control points* (or *centers*) originally located at $\{\boldsymbol{p}_i\}_{i=1,\dots,N}$. Note that, in contrast to the FFD definition, the control points need not to be on a lattice. In other words, the definition of a RBF-based map is reduced to a scattered data interpolation by means of three scalar functions $\tau^k : \mathbb{R}^3 \to \mathbb{R}$, $k = 1, \dots, 3$, of the form

$$\tau^k(\boldsymbol{x}) = \pi^k(\boldsymbol{x}) + \sum_{i=0}^{N} w_i^k \sigma(\varepsilon \left\|\boldsymbol{x} - \boldsymbol{x}_i\right\|_2), \quad \pi^k(\boldsymbol{x}) = c^k + \boldsymbol{a}^k \cdot \boldsymbol{x}, \qquad \boldsymbol{a}^k = [a_1^k, \dots, a_3^k]^T, \tag{5.4}$$

Gaussian	$\sigma(r) = e^{-r^2}$
Inverse Multiquadric	$\sigma(r) = (1+r^2)^{-1/2}$
Multiquadric	$\sigma(r) = (1+r^2)^{1/2}$
Polyharmonic spline	$\sigma(r) = r^k$, k odd $\sigma(r) = r^k \log r$, k even
Wendland	$\sigma(r) = (1-r)_+^4(1+4r)$

Table 5.1: *Some common functions $\sigma(r)$*

where $\varepsilon > 0$ is a shape factor, and $\sigma : \mathbb{R} \to \mathbb{R}$ is a fixed basis function, radial with respect to the Euclidean distance (the most common choices are reported in Table 5.1). The coefficients w_i^k of the radial term and the polynomial π^k are determined so that τ^k interpolates the control points deformed positions (*interpolation constraints*):

$$\tau^k(\boldsymbol{p}_i) = [\boldsymbol{p}_i + \boldsymbol{\mu}_i]^k, \forall i = 1, \dots, N$$

and satisfies (*side constraints*)

$$\sum_i w_i^k \phi(\boldsymbol{p}_i) = 0 \qquad \forall \text{ polynomials } \phi(\boldsymbol{x}) \text{ of degree one.}$$

Equivalently, the coefficients $W(\boldsymbol{\mu}) = [w_i^k]_{i,k} = [\boldsymbol{w}_1|\boldsymbol{w}_2|\dots|\boldsymbol{w}_N]^T \in \mathbb{R}^{N\times 3}, \boldsymbol{c}(\boldsymbol{\mu}) = [c^k]_k \in \mathbb{R}^3, A(\boldsymbol{\mu}) = [a_h^k]_{h,k} = [\boldsymbol{a}^1|\boldsymbol{a}^2|\dots|\boldsymbol{a}^3] \in \mathbb{R}^{3\times 3}$ are the solution of the following linear system

$$\underbrace{\begin{bmatrix} S & \mathbf{1}_N & P \\ \mathbf{1}_N^T & 0 & \mathbf{0}_3^T \\ P^T & \mathbf{0}_3 & O_{3\times 3} \end{bmatrix}}_{J} \underbrace{\begin{bmatrix} W(\boldsymbol{\mu}) \\ \boldsymbol{c}^T(\boldsymbol{\mu}) \\ A^T(\boldsymbol{\mu}) \end{bmatrix}}_{U(\boldsymbol{\mu})} = \underbrace{\begin{bmatrix} P + [\boldsymbol{\mu}] \\ \mathbf{0}_3^T \\ O_{3\times 3} \end{bmatrix}}_{B(\boldsymbol{\mu})}$$

for

$$\boldsymbol{s}(\boldsymbol{x}) = \begin{bmatrix} \sigma(\varepsilon \|\boldsymbol{x} - \boldsymbol{p}_1\|) \\ \vdots \\ \sigma(\varepsilon \|\boldsymbol{x} - \boldsymbol{p}_N\|) \end{bmatrix}, \qquad P = [\boldsymbol{p}_1|\boldsymbol{p}_2|\dots|\boldsymbol{p}_N]^T \in \mathbb{R}^{N\times 3}, \qquad [\boldsymbol{\mu}] = [\boldsymbol{\mu}_1|\boldsymbol{\mu}_2|\dots|\boldsymbol{\mu}_N]^T \in \mathbb{R}^{N\times 3}.$$

5.1.3 A screening procedure for the design parameters selection

In this section[2] we propose a screening procedure in order to select a small number of active control points – and, ultimately, the degrees of freedom $\mu_1, \dots, \mu_p$ – yet ensuring the possibility to represent a large variety of admissible shapes. In fact, *(i)* considering only a small number of enabled degrees of freedom contributes in preserving the regularity of the mesh and avoiding self-intersections [104] and *(ii)* it is difficult to obtain a good sampling of high dimensional parameter spaces (curse of dimensionality), a poor training sample will negatively affect the performance of the reduced-order model.

In order to implement a simple screening procedure in the volume-based context, we start with a large number of free parameters, say P, and attempt to find their most effective subset in representing the shapes of interest while discarding all the other parameters. For this purpose, we take advantage of the so-called Morris' randomized *one-at-a-time* design [60,190].

[2]This section is a re-adaptation of Section 6.2 of the following publication:
[24] F. Ballarin, A. Manzoni, G. Rozza, and S. Salsa. Shape optimization by Free-Form Deformation: existence results and numerical solution for Stokes flows. *Journal of Scientific Computing*, 60(3):537–563, 2014.

Through this screening procedure, we add to the retained set of parameters those with the largest observed *sensitivities* (related to a prescribed output j), by considering the so-called *elementary effects*

$$\delta_i(\boldsymbol{\mu}) = \frac{1}{\delta}(j(\mu_1, \dots, \mu_{i-1}, \mu_i + \delta, \mu_{i+1}, \dots, \mu_P) - j(\mu_1, \dots, \mu_{i-1}, \mu_i, \mu_{i+1}, \dots, \mu_P))$$

obtained by varying one parameter at a time while keeping the others fixed. In order to account also for interactions among the parameters, Morris' design requires the evaluation of a random sample of N elementary effects for each of the P parameters – giving a total cost of $\mathcal{O}(NP)$ input/output evaluations – in order to estimate the mean and the standard deviation of the distribution of elementary effects associated with each input parameter[3].

In particular, for volume-based parametrizations it is possible to compute directly the sensitivities of the output $j(\boldsymbol{\mu})$ w.r.t. each displacement μ_i, that is

$$-\frac{\partial j}{\partial \mu_i}(\boldsymbol{\mu}), \qquad \boldsymbol{\mu} \in \mathcal{C} \subset \mathbb{R}^P, \quad i = 1, \dots, P.$$

See [24] for more details on the FFD case; a possible choice for j, employed in [24] and in the following, is the computation of the viscous energy dissipation.

Therefore it is possible, for each parameter component $i = 1, \dots, P$, to evaluate the mean

$$E_i = \int_{\mathcal{C}} \left(-\frac{\partial j}{\partial \mu_i}(\boldsymbol{\mu}) \right) d\boldsymbol{\mu} \approx \frac{1}{N} \sum_{n=1}^{N} \left(-\frac{\partial j}{\partial \mu_i}(\boldsymbol{\mu}_n) \right)$$

and the standard deviation

$$S_i = \sqrt{\int_{\mathcal{C}} \left(-\frac{\partial j}{\partial \mu_i}(\boldsymbol{\mu}) - E_i \right)^2 d\boldsymbol{\mu}} \approx \sqrt{\frac{1}{N} \sum_{n=1}^{N} \left(-\frac{\partial j}{\partial \mu_i}(\boldsymbol{\mu}_n) - E_i \right)^2}$$

by Monte Carlo integration, using a (uniform) sample $\{\boldsymbol{\mu}_n\}_{n=1}^N \subset \mathcal{C}$ of size N. This can be seen as a *continuous* version of the Morris' design.

5.1.4 Discussion: strengths and weaknesses of volume-based parametrizations for the current application

In this section we consider the idealized bypass geometry in Figure 5.2 and:

- we perform the screening procedure introduced in the previous section to detect the most relevant design variables;
- retaining only the relevant design variables, we compare the flow dynamics in the idealized bypass shape based on the variation of Reynolds number and FFD parametrization.

[3] A large absolute value for the mean E_i implies that μ_i has an important *overall* effect on the output, whereas a high standard deviation S_i indicates that the effect of μ_i is not constant, which may be implied by a parameter interacting with other parameters.

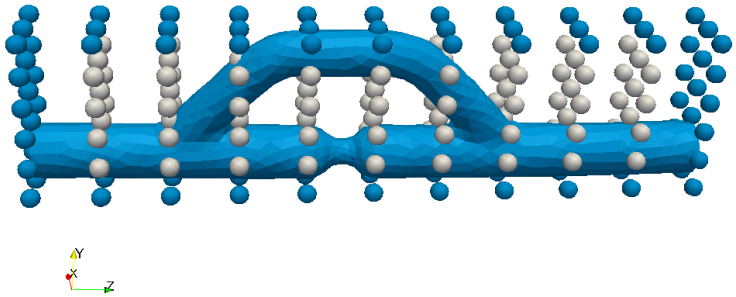

Figure 5.2: *FFD control volume (in gray), reference domain $\Omega = D \setminus B$ and (image into D of the) FFD control points grid is represented by small spherical markers.*

5.1.4.1 Screening procedure

A screening procedure is performed for all control points denoted by a gray marker in Figure 5.2. We allow control points displacements in the range $[-1, 1]$ to avoid large variations. We thus compute the means E_i and the standard deviations S_i related to $\mu_i, i = 1, \ldots, P$, by considering a sample of size $N = 200$. The solution of a PDE is required for each sample. No computational reduction is pursued in this stage since the parameter space shall be reduced in the following. Results of the analysis are shown in Figures 5.3 and 5.4.

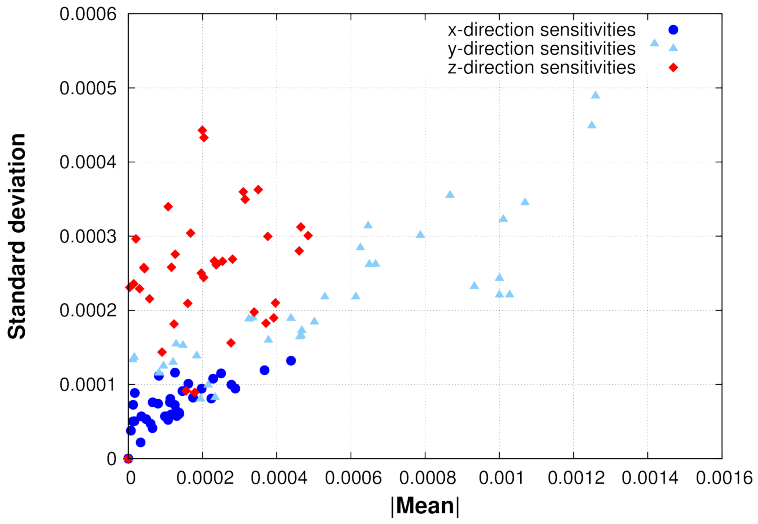

Figure 5.3: *Screening procedure: absolute value of the mean vs standard deviation, for each component of the gradient of the parametrized output $j(\boldsymbol{\mu})$.*

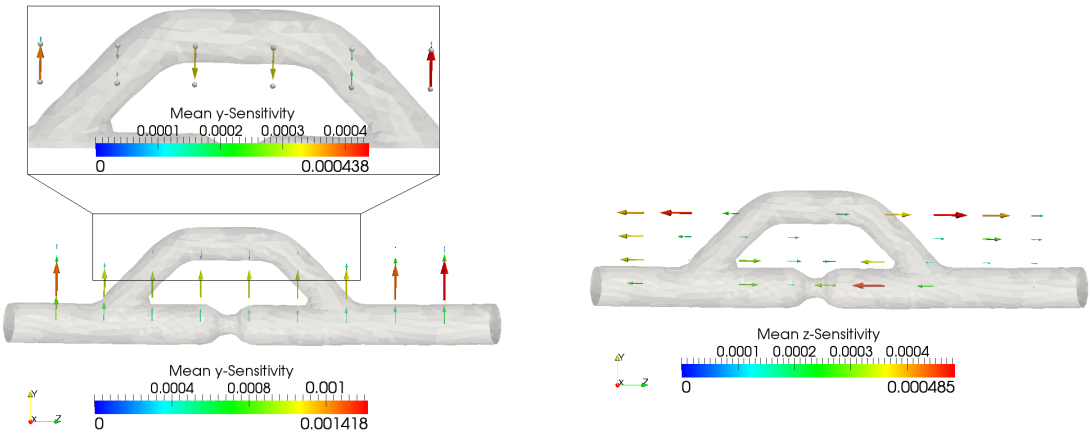

Figure 5.4: *Screening procedure: mean values in the y (left) and z (right) directions.*

5.1.4.2 Flow comparison

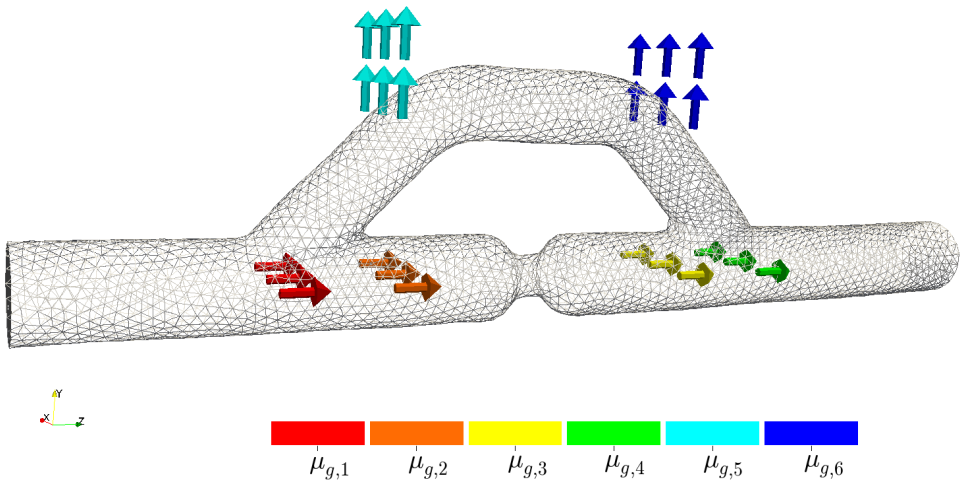

Figure 5.5: *Enabled displacements of the FFD map. Control points of the same color are moved by the same displacement.*

The POD-Galerkin ROM has been applied to the idealized bypass geometry, considering two physical parametrized quantities (viscosity and magnitude of the inlet velocity) and the six geometrical degrees of freedom shown in Figure 5.5. Table 5.2 shows some details of the computational times and results of the offline stage; over 1,000 hours of CPU time on multiple 2 GHz cores of an Intel Xeon cluster are required for the offline preparation phase, 20% of time being spent in the EIM and remaining time in the POD training and basis construction. Table 5.3 shows computational details of the online stage.

Number of physical parameters	2
Number of geometrical parameters	6
Reynolds number range	[90, 140]
Geometrical parameters range	[-2.5, 2.5]
FE velocity order	2
FE pressure order	1
Total number of FE dofs	314,954
$N_{\text{train,EIM}}$	150
EIM offline CPU time	5 $h \times 48$ processors
Affine expansions components for a, b, c	40, 10, 10
$N_{\text{train,POD}}$	150
POD-Galerkin offline CPU time	13 $h \times 72$ processors
$N_{\max}$	40

Table 5.2: *Computational details of the offline stage.*

Number of velocity basis functions	40 + 1 lifting
Number of supremizer basis functions	40
Number of pressure basis functions	40
Online CPU time for each evaluation	≈ 15 $s \times 1$ processor

Table 5.3: *Computational details of the online stage.*

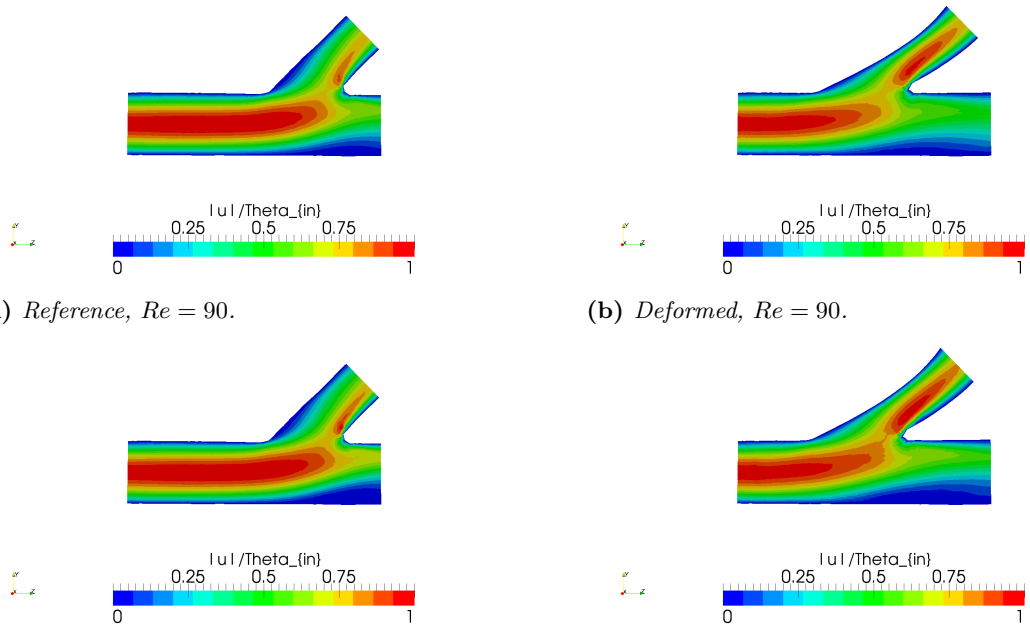

(a) *Reference,* $Re = 90$.

(b) *Deformed,* $Re = 90$.

(c) *Reference,* $Re = 140$.

(d) *Deformed,* $Re = 140$.

Figure 5.6: *Proximal anastomosis: comparison of the velocity in the reference and the deformed configuration.*

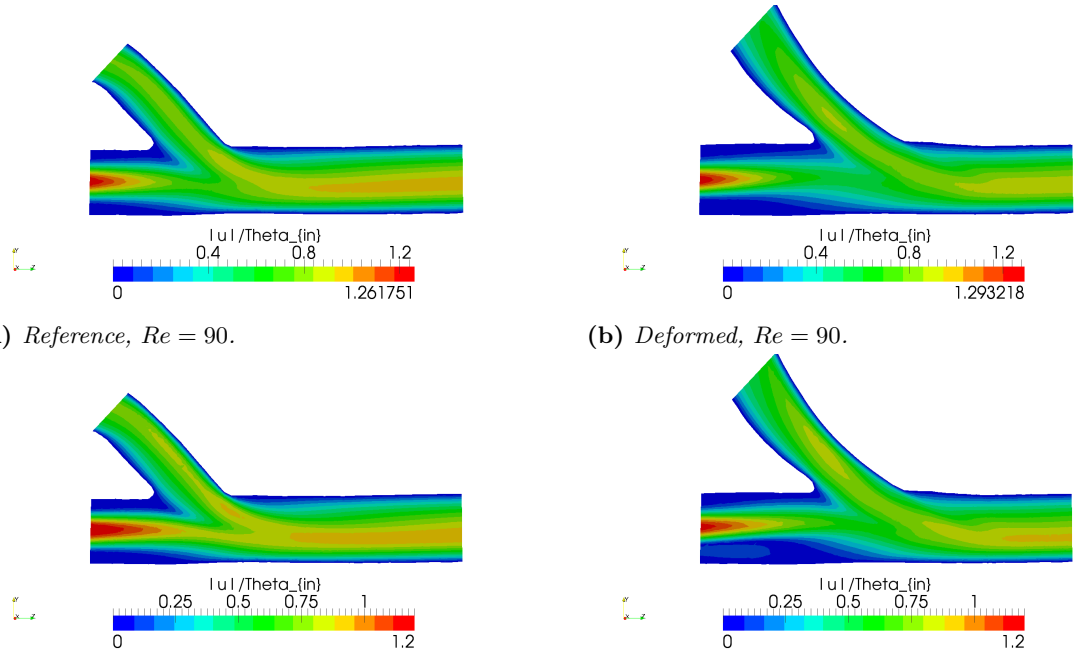

(a) *Reference,* $Re = 90$.

(b) *Deformed,* $Re = 90$.

(c) *Reference,* $Re = 140$.

(d) *Deformed,* $Re = 140$.

Figure 5.7: *Distal anastomosis: comparison of the velocity in the reference and the deformed configuration.*

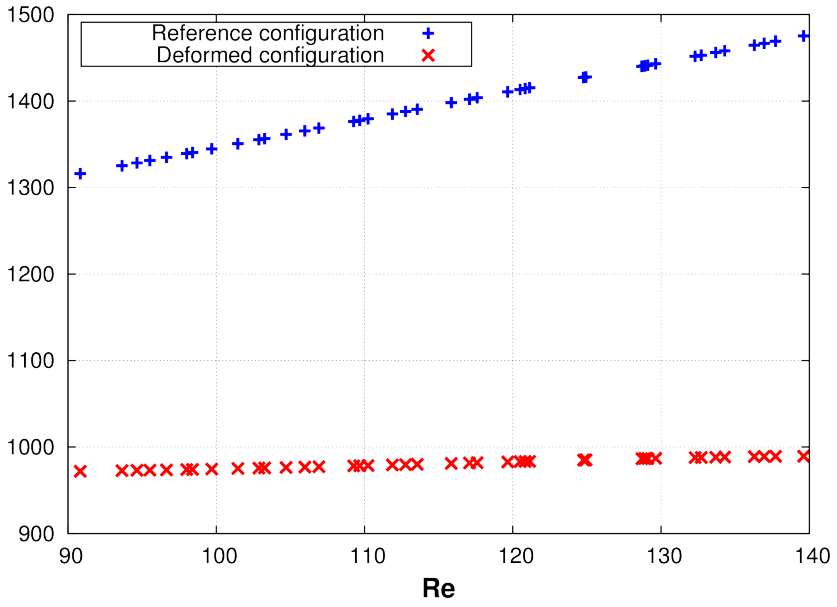

Figure 5.8: *Comparison between the energy dissipation functional in the reference (angle* $\approx 45°$*) and deformed (angle* $\approx 30°$*) for different Reynolds number.*

5.1.4.3 Discussion

The scatter plot of $|E_i|$ vs. S_i reported in Figure 5.3 shows that the most significant displacements are in the y and z directions. This allows to discard displacements in the x direction, which is transversal to plane of the vessel and the graft.

Mean values reported in Figure 5.4 show a complex pattern for the sensitivities. Control points on the boundary of the native vessel feature the highest mean sensitivities in the y direction; those displacements should be however discarded because the native vessel is *not* subject to variation. High mean sensitivities both in the y and z direction are also computed near the terminal region of the graft; translation of this control points allows for variation of anastomosis angles and anastomosis-to-vessel diameter ratio.

These results are employed in the choice of design variables for a comparison of the flow profiles for different physical and geometrical properties (see Figure 5.5). A total of six parameters is chosen in this test: parameters $\mu_{g,3}$ and $\mu_{g,4}$ have been selected by the screening procedure in order to possibly change the diameter ratio; for symmetry, parameters $\mu_{g,1}$ and $\mu_{g,2}$ are also chosen; parameters $\mu_{g,5}$ and $\mu_{g,6}$ are chosen to control anastomosis angles, as suggested by the screening procedure. To improve the quality of the deformation the same displacement is assigned for each of three longitudinal sections. Moreover, with the aim of avoiding large radius variations of the graft, displacements $\mu_{g,5}$ and $\mu_{g,6}$ are assigned for two consecutive rows of control points in the y-direction, for a total of 24 enabled displacements. A first weakness of volume-based parametrizations is apparent in the latter choice: complex constraints are needed in order to ensure that the radius of the vessel and/or graft should be constant away from the anastomosis.

The dependence of the flow patterns on the parameters $\mu_{g,1}, \mu_{g,2}$ and $\mu_{g,5}$ (proximal anastomosis) and on the Reynolds number is shown in Figure 5.6, which features a comparison between the reference configuration (angle approximately 45°) and a possible deformed configuration (approximately 30°). The effect of a similar deformation on the distal anastomosis is shown in Figure 5.7. A second drawback can be noticed here: no clear physical interpretation of the parameters is provided by volume-based parametrizations, since clinically relevant geometrical quantities (such as grafting angles, in this case) are obtained as a post-processing rather than being directly associated to a component of $\boldsymbol{\mu}_g$. Putting this limitation aside, however, volume-based parametrization are indeed able to perform meaningful local modifications to the reference geometry such as, in this case, anastomosis angle variation or anastomosis area variation.

A comparison, in terms of the same energy dissipation functional employed in the screening procedure, is performed in Figure 5.8 for the reference and deformed configurations. These clearly show that, once the proper constraints are imposed, volume based parametrizations (coupled to the POD-Galerkin ROM for a fast evaluation of the input-output relation) are able to produce a sensible variation of the energy dissipation functional[4].

To summarize, we have shown in this section that volume-based parametrizations are suitable for small *local* perturbations of an idealized bypass configuration. However, some weaknesses have arisen in this discussion:

- a screening procedure must be performed in order to detect the most relevant design variables; this procedure may be computationally expensive;
- additional constraints may be needed in order to ensure that no undesired variation of geometrical features (radii, in particular) happens during the deformation;

[4]... which, in this example, is a decrease of the energy functional of approximately $25 - 30\%$ for all Reynolds numbers, since, for the sake of comparison, geometrical parameters have been chosen in the descent direction provided by the results of the screening procedure.

- no immediate physical interpretation of the design variables is usually available;
- a rapidly increasing number of control points may be needed in more complex geometries. In particular, in this example 24 displacements were needed to perform a variation of two angles; a similar drawback applies to the parametrization an axisymmetric stenosis, where a minimum of four control points (12 displacements) may be needed to perform a local variation of (a scalar quantity such as) the radius.

In the remaining part of this chapter we combine volume-based representations with a different parametrization to overcome these limitations.

5.2 A centerlines-based shape parametrization

In this section a shape parametrization tailored for the current application is introduced. It is based on the assumption that coronary arteries and bypass grafts can be represented as a network of tubular geometries and that an efficient variation of geometrical quantities of clinical interest (such as stenoses entities and anastomosis type) is required. A better representation of the deformation can be obtained by considering a curve-based parametrization. Other curve-based approaches have been proposed in literature [139, 159, 168, 278], although none of them has been coupled to model order reduction techniques; see also [12] for an application in a biomedical context. The reliability of volume-based parametrizations on small local perturbations, as discussed in the previous section, will be exploited near the intersections (bifurcations, anastomoses), to provide suitable interface conditions across different vessels of the network.

5.2.1 Differential geometry of space curves

Let $\boldsymbol{\gamma} : [a, b] \to \mathbb{R}^3$ be a curve in $\mathbb{R}^3$ (in particular, the centerline of one of the vessels in the network). The first goal is to define a moving coordinate frame attached to $\boldsymbol{\gamma}(s)$. We refer to [121] for a short introduction on this topic; see also [202] for a biomedical application.

5.2.1.1 Frenet frame

If $\boldsymbol{\gamma}(s) \in C^3([a, b]; \mathbb{R}^3)$ with non vanishing first and second derivative for all $s \in [a, b]$ the classical Frenet frame $(\boldsymbol{t}(s), \boldsymbol{n}(s), \boldsymbol{b}(s))$ can be defined as:

$$\boldsymbol{t}(s) = \frac{\boldsymbol{\gamma}'(s)}{\|\boldsymbol{\gamma}'(s)\|}, \quad \boldsymbol{b}(s) = \frac{\boldsymbol{\gamma}'(s) \times \boldsymbol{\gamma}''(s)}{\|\boldsymbol{\gamma}'(s) \times \boldsymbol{\gamma}''(s)\|}, \quad \boldsymbol{n}(s) = \boldsymbol{b}(s) \times \boldsymbol{t}(s).$$

Moreover, $(\boldsymbol{t}(s), \boldsymbol{n}(s), \boldsymbol{b}(s))$ are the solution of the following system of differential equations (also known as Frenet-Serret formulae):

$$\begin{bmatrix} \boldsymbol{t}'(s) \\ \boldsymbol{n}'(s) \\ \boldsymbol{b}'(s) \end{bmatrix} = \|\boldsymbol{\gamma}'(s)\| \begin{bmatrix} 0 & \kappa(s) & 0 \\ -\kappa(s) & 0 & \tau(s) \\ 0 & -\tau(s) & 0 \end{bmatrix} \begin{bmatrix} \boldsymbol{t}(s) \\ \boldsymbol{n}(s) \\ \boldsymbol{b}(s) \end{bmatrix}$$

where the curvature $\kappa(s)$ and the torsion $\tau(s)$ are given by

$$\kappa(s) = \frac{\|\boldsymbol{\gamma}'(s) \times \boldsymbol{\gamma}''(s)\|}{\|\boldsymbol{\gamma}'(s)\|^3}, \quad \tau(s) = \frac{\boldsymbol{\gamma}'(s) \times \boldsymbol{\gamma}''(s) \cdot \boldsymbol{\gamma}'''(s)}{\|\boldsymbol{\gamma}'(s) \times \boldsymbol{\gamma}''(s)\|^2}.$$

The main drawback of this representation is the fact that *(i)* normal and binormal vectors are not defined if the curvature vanishes e.g. $\boldsymbol{\gamma}(s)$ is (locally) a straight line, and *(ii)* the normal vector always points towards the center of the osculating circle, and this implies discontinuities around inflection points (see e.g. [268] or [121]).

5.2.1.2 Bishop (or parallel transport) frame

Alternative moving coordinate frames can be defined, see e.g. [268] for a rotation minimizing moving coordinate frame. In this work we employ the so-called Bishop (or parallel transport) frame; originally introduced in [40], this frames relies on a different choice of the basis for the plane spanned by $(\boldsymbol{n}(s), \boldsymbol{b}(s))$.

Given the space curve $\boldsymbol{\gamma}(s)$, a vector field $\boldsymbol{v}(s)$ is said to be *normal* if it is perpendicular to the curve's tangent $\boldsymbol{t}(s)$ for all $s \in [a, b]$; a *normal* vector field $\boldsymbol{v}(s)$ is said to be parallel if its derivative is parallel to the curve's tangent $\boldsymbol{t}(s)$, $\boldsymbol{v}'(s) \parallel \boldsymbol{t}(s)$. Moreover (see [121, Section 2.2]), if $\boldsymbol{v}_1(s), \boldsymbol{v}_2(s)$ are two parallel vector fields, it holds $\boldsymbol{v}_1(s) \cdot \boldsymbol{v}_2(s) = \boldsymbol{v}_1(s_0) \cdot \boldsymbol{v}_2(s_0)$ for some $s_0 \in [a, b]$; thus, if two fields are orthogonal at $s = s_0$, their orthogonality is preserved. This property suggests the following ("Frenet-Serret" formulae) definition for an alternative moving coordinate frame: given the coordinate frame $(\boldsymbol{t}(a), \boldsymbol{n}_1(a), \boldsymbol{n}_2(a))$, solve

$$\begin{bmatrix} \boldsymbol{t}'(s) \\ \boldsymbol{n}_1'(s) \\ \boldsymbol{n}_2'(s) \end{bmatrix} = \|\boldsymbol{\gamma}'(s)\| \begin{bmatrix} 0 & k_1(s) & k_2(s) \\ -k_1(s) & 0 & 0 \\ -k_2(s) & 0 & 0 \end{bmatrix} \begin{bmatrix} \boldsymbol{t}(s) \\ \boldsymbol{n}_1(s) \\ \boldsymbol{n}_2(s) \end{bmatrix} \tag{5.5}$$

It has been shown (see [40]), that the Bishop curvatures $k_1(s)$ and $k_2(s)$ are linked to $\kappa(s)$ and $\tau(s)$ by

$$k_1(s) = \kappa(s)\cos(\phi(s)), \quad k_1(s) = \kappa(s)\sin(\phi(s)), \quad \phi'(s) = \tau(s).$$

In practice, given a partition $\{s_i\}_{i=0,\dots,N}$ of the interval $[a, b]$, the Bishop frame can be approximated by means of the following numerical procedure: the tangent at s_i is approximated by

$$\boldsymbol{t}(s_i) = \frac{\boldsymbol{\gamma}(s_{i+1}) - \boldsymbol{\gamma}(s_i)}{\|\boldsymbol{\gamma}(s_{i+1}) - \boldsymbol{\gamma}(s_i)\|}, \quad \boldsymbol{t}(s_N) = \boldsymbol{t}(s_{N-1}).$$

The idea to obtain an approximation of $\boldsymbol{n}_1(s)$ and $\boldsymbol{n}_2(s)$ is to find the rotation that has occurred between $\boldsymbol{t}(s_i)$ and $\boldsymbol{t}(s_{i+1})$, and rotate $\boldsymbol{n}_1(s_i)$ and $\boldsymbol{n}_2(s_i)$ in the same way to obtain $\boldsymbol{n}_1(s_{i+1})$ and $\boldsymbol{n}_2(s_{i+1})$; orthogonality between $\boldsymbol{n}_1(s_{i+1})$ and $\boldsymbol{n}_2(s_{i+1})$ is preserved by the parallel transport properties. In practice, given $\boldsymbol{n}_1(s_0)$ and $\boldsymbol{n}_2(s_0)$ such that $(\boldsymbol{t}(s_0), \boldsymbol{n}_1(s_0), \boldsymbol{n}_2(s_0))$ is a frame at $s = s_0$, the following procedure is performed[5]

Algorithm 5.1 Numerical computation of the Bishop frame.

INPUT: partition $\{s_i\}_{i=0,\dots,N}$ of the interval $[a, b]$, tangent vectors $\{\boldsymbol{t}(s_i)\}_{i=0,\dots,N}$, reference frame $(\boldsymbol{t}(a), \boldsymbol{n}_1(a), \boldsymbol{n}_2(a))$ at $s = s_0 = a$;
OUTPUT: $\{\boldsymbol{n}_1(s_i)\}_{i=1,\dots,N}$, $\{\boldsymbol{n}_2(s_i)\}_{i=1,\dots,N}$;
for $i = 0, \dots, N-1$ **do**
  Rotate the frame at $(\boldsymbol{n}_1(s_i), \boldsymbol{n}_2(s_i))$ of the angle $\arccos(\boldsymbol{t}(s_i) \cdot \boldsymbol{t}(s_{i+1}))$, around the normal direction to the plane $(\boldsymbol{t}(s_i), \boldsymbol{t}(s_{i+1}))$, to obtain $(\boldsymbol{n}_1(s_{i+1}), \boldsymbol{n}_2(s_{i+1}))$, i.e.
  for $j = 1, 2$ **do**
    $\boldsymbol{n}_j(s_{i+1}) = \boldsymbol{t}(s_i) \cdot \boldsymbol{t}(s_{i+1})\, \boldsymbol{n}_j(s_i) + \boldsymbol{t}(s_i) \times \boldsymbol{t}(s_{i+1}) \times \boldsymbol{n}_j(s_i) + \boldsymbol{t}(s_i) \times \boldsymbol{t}(s_{i+1}) \frac{\boldsymbol{t}(s_i) \times \boldsymbol{t}(s_{i+1}) \cdot \boldsymbol{n}_j(s_i)}{(1 + \boldsymbol{t}(s_i) \cdot \boldsymbol{t}(s_{i+1}))}$
  end for
end for

The result of this numerical procedure is shown to converge to the Bishop frame in [121] as $N \to +\infty$. This procedure is performed for each curve of the network, and an approximation of the reference frame $(\boldsymbol{t}(s), \boldsymbol{n}_1(s), \boldsymbol{n}_2(s))$ attached to each centerline is thus obtained.

[5] Recall the Rodrigues' rotation formula: the rotation of the vector $\boldsymbol{v}$ around the unit vector $\boldsymbol{k}$ (axis) of an angle θ is given by

$$\boldsymbol{v}_{\text{rot}} = \boldsymbol{v}\cos\theta + \boldsymbol{k} \times \boldsymbol{v}\sin\theta + \boldsymbol{k}\,\boldsymbol{k} \cdot \boldsymbol{v}(1 - \cos\theta) = \boldsymbol{v}\cos\theta + (\boldsymbol{k}\sin\theta) \times \boldsymbol{v} + (\boldsymbol{k}\sin\theta)\,(\boldsymbol{k}\sin\theta) \cdot \boldsymbol{v}\frac{1}{1 + \cos\theta}$$

In the present case $\theta = \arccos(\boldsymbol{t}(s_i) \cdot \boldsymbol{t}(s_{i+1}))$ and $\boldsymbol{k}\sin(\theta) = \boldsymbol{t}(s_i) \times \boldsymbol{t}(s_{i+1})$.

5.2.2 Centerline-based parametrization of a single vessel

Let $\boldsymbol{\gamma} : [a, b] \to \mathbb{R}^3$ be a C^2 curve in $\mathbb{R}^3$, which represents the centerline of a branch of coronary artery or bypass graft. The main idea behind the proposed shape parametrization is to be able to deform the vessel by displacing and/or rotating few points on the centerline, or possibly varying the local radius. This way to obtain a shape parametrization has been developed because of the straightforward interpretation of its parameters (radius, angles) and higher quality deformed meshes.

The parametrization and deformation of the vessel is split in three steps, summarized in the following Figure 5.9.

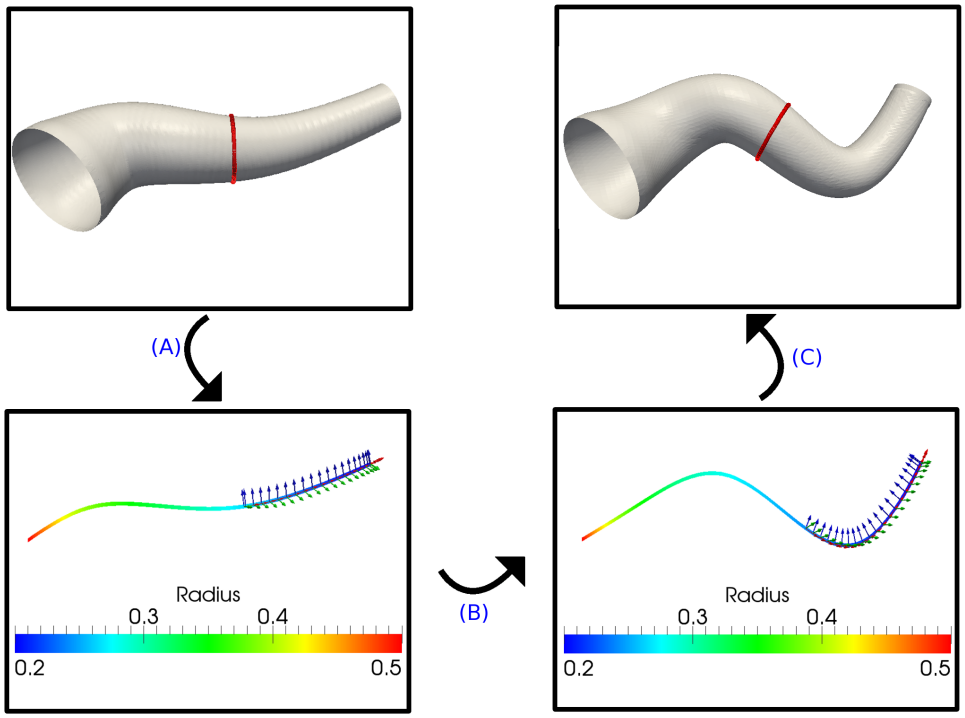

Figure 5.9: *A centerline based parametrization*

(A) in a preprocessing step, the curve $\boldsymbol{\gamma}(s)$ is computed as the medial axis of the vessel, along with a local radius $r(s)$. Moreover, a moving coordinate frame $(\boldsymbol{t}(s), \boldsymbol{n}_1(s), \boldsymbol{n}_2(s))$ attached to $\boldsymbol{\gamma}(s)$ is defined, by means of the parallel transport procedure (Bishop frame) described previously. Finally, "cylindrical" coordinates $\rho(\boldsymbol{x}) \in [0, 1], \theta(\boldsymbol{x}) \in [0, 2\pi), s(\boldsymbol{x}) \in [a, b]$ are obtained for each point in the vessel reference configuration as follows:

$$\begin{cases} s(\boldsymbol{x}) = \arg\min_{s\in[a,b]} \|\boldsymbol{x} - \boldsymbol{\gamma}(s)\| = \{s : [\boldsymbol{x} - \boldsymbol{\gamma}(s)] \cdot \boldsymbol{t}(s) = 0\}, \\ \theta(\boldsymbol{x}) = \arctan\left(\frac{[\boldsymbol{x}-\boldsymbol{\gamma}(s(\boldsymbol{x}))]\cdot\boldsymbol{n}_2(s(\boldsymbol{x}))}{[\boldsymbol{x}-\boldsymbol{\gamma}(s(\boldsymbol{x}))]\cdot\boldsymbol{n}_1(s(\boldsymbol{x}))}\right), \\ \rho(\boldsymbol{x}) = \|\boldsymbol{x} - \boldsymbol{\gamma}(s(\boldsymbol{x}))\| / r(s(\boldsymbol{x})). \end{cases}$$

(B) in this step the deformation of the curve is computed. Let $\{\boldsymbol{\mu}, \boldsymbol{\mu}'\}$ be the set of geometrical parameters. A radial basis functions (RBF) parametrization is employed to perform the deformation of the centerline, interpolating *(a)* the deformed positions $\{\boldsymbol{\gamma}(\vartheta_i) + \boldsymbol{\mu}_i\}_{i=1,\dots,N}$ of a small number N of *control points* (*centers, interpolation sites*) originally located at $\{(\vartheta_i, \boldsymbol{\gamma}(\vartheta_i))\}_{i=1,\dots,N}$ and *(b)* the prescribed values $\{\boldsymbol{\gamma}'(\boldsymbol{r}_j) + \boldsymbol{\mu}'_j\}_{j=1,\dots,M}$ of the first derivative at another (possibly overlapping) set of control points $\{\boldsymbol{r}_j\}_{j=1,\dots,M}$. Note

that, as we will see in Section 5.2.3, the latter allows to perform local modifications to the tangent vector. The definition of a RBF-based map is thus an interpolation problem of three scalar functions $\tau_k : \mathbb{R} \to \mathbb{R}$, $k = 1, \dots, 3$, of the form

$$\tau_k(s) = \pi_k(\boldsymbol{\gamma}(s)) + \sum_{i=1}^{N} w_i^k \sigma(\varepsilon\,|s - \mathfrak{s}_i|) - \sum_{j=1}^{M} u_j^k \partial_s \sigma(\varepsilon\,|s - \mathfrak{r}_j|); \tag{5.6}$$

where $\pi_k : \mathbb{R}^3 \to \mathbb{R}$ are polynomial functions of degree p, $\varepsilon > 0$ is a shape factor and $\sigma : \mathbb{R} \to \mathbb{R}$ is a fixed radial function such that $\sigma'(0) = 0$ (see Table 5.1 in Section 5.1.2 for some common radial functions). The coefficients w_i^k and u_j^k of the radial term and those of the polynomial π_k are determined so that τ_k and τ_k' are interpolatory at the control points

$$\tau_k(\mathfrak{s}_i) = [\boldsymbol{\gamma}(\mathfrak{s}_i) + \boldsymbol{\mu}_i]_k, \quad \forall i = 1, \dots, N, \quad \text{and} \quad \tau_k'(\mathfrak{r}_j) = [\boldsymbol{\gamma}'(\mathfrak{r}_j) + \boldsymbol{\mu}_j']_k, \quad \forall j = 1, \dots, M,$$

and satisfy the following *side constraints*

$$\sum_{i=1}^{N} w_i^k \phi(\boldsymbol{\gamma}(\mathfrak{s}_i)) + \sum_{j=1}^{M} u_j^k \partial_s(\phi \circ \boldsymbol{\gamma})|_{s=\mathfrak{r}_j} = 0 \qquad \forall \text{ polynomials } \phi \in \Pi^p,$$

being Π^p the space of polynomials of total degree up to p in three unknowns.
In particular, if π_k are chosen to be polynomials of degree $p = 1$, so that

$$\pi_k(\boldsymbol{\gamma}(s)) = c_k + \boldsymbol{a}_k \cdot \boldsymbol{\gamma}(s), \qquad \boldsymbol{a}_k \in \mathbb{R}^3,$$

the RBF parametrization results as follows

$$\begin{aligned}\boldsymbol{\gamma}(s; \boldsymbol{\mu}, \boldsymbol{\mu}') &= \boldsymbol{c}(\boldsymbol{\mu}, \boldsymbol{\mu}') + A(\boldsymbol{\mu}, \boldsymbol{\mu}')\boldsymbol{\gamma}(s) + W^T(\boldsymbol{\mu}, \boldsymbol{\mu}')\boldsymbol{r}(s) - U^T(\boldsymbol{\mu}, \boldsymbol{\mu}')\dot{\boldsymbol{r}}(s) = \\ &= \begin{bmatrix} W^T(\boldsymbol{\mu}, \boldsymbol{\mu}') & U^T(\boldsymbol{\mu}, \boldsymbol{\mu}') & \boldsymbol{c}(\boldsymbol{\mu}, \boldsymbol{\mu}') & A(\boldsymbol{\mu}, \boldsymbol{\mu}') \end{bmatrix} \begin{bmatrix} \boldsymbol{r}(s) \\ -\dot{\boldsymbol{r}}(s) \\ 1 \\ \boldsymbol{\gamma}(s) \end{bmatrix},\end{aligned}$$

where

$$\begin{aligned}[\boldsymbol{r}(s)]_{i=1,\dots,N} &= \sigma(\varepsilon\,|s - \mathfrak{s}_i|), \\ [\dot{\boldsymbol{r}}(s)]_{j=1,\dots,M} &= \partial_s \sigma(\varepsilon\,|s - \mathfrak{r}_j|).\end{aligned}$$

The coefficients

$$\begin{aligned}&\boldsymbol{c}(\boldsymbol{\mu}, \boldsymbol{\mu}') = [c_k]_k \in \mathbb{R}^3, \quad A(\boldsymbol{\mu}, \boldsymbol{\mu}') = [\boldsymbol{a}_1 | \boldsymbol{a}_2 | \dots | \boldsymbol{a}_3]^T \in \mathbb{R}^{3\times 3}, \\ &W(\boldsymbol{\mu}, \boldsymbol{\mu}') = [w_i^k]_{i=1,\dots,N}^{k=1,\dots,3} \in \mathbb{R}^{N\times 3}, \quad U(\boldsymbol{\mu}, \boldsymbol{\mu}') = [u_j^k]_{j=1,\dots,M}^{k=1,\dots,3} \in \mathbb{R}^{M\times 3},\end{aligned}$$

can thus be obtained as the solution of the following symmetric linear system of small size $(M + N + 4)$

$$\begin{bmatrix} S_{(0,0)} & S_{(0,1)} & \mathbf{1}_N & P \\ S_{(1,0)} & S_{(1,1)} & \mathbf{0}_M & T \\ \mathbf{1}_N^T & \mathbf{0}_M^T & 0 & \mathbf{0}_3^T \\ P^T & T^T & \mathbf{0}_3 & O_{3\times 3} \end{bmatrix} \begin{bmatrix} W(\boldsymbol{\mu}, \boldsymbol{\mu}') \\ U(\boldsymbol{\mu}, \boldsymbol{\mu}') \\ \boldsymbol{c}^T(\boldsymbol{\mu}, \boldsymbol{\mu}') \\ A^T(\boldsymbol{\mu}, \boldsymbol{\mu}') \end{bmatrix} = \begin{bmatrix} P + [\boldsymbol{\mu}] \\ T + [\boldsymbol{\mu}'] \\ \mathbf{0}_3^T \\ O_{3\times 3} \end{bmatrix} \tag{5.7}$$

being

$$
\begin{aligned}
&P = [\boldsymbol{\gamma}(\mathfrak{z}_1)|\boldsymbol{\gamma}(\mathfrak{z}_2)|\dots|\boldsymbol{\gamma}(\mathfrak{z}_N)]^T \in \mathbb{R}^{N\times 3}, \qquad [\boldsymbol{\mu}] = [\boldsymbol{\mu}_1|\boldsymbol{\mu}_2|\dots|\boldsymbol{\mu}_N]^T \in \mathbb{R}^{N\times 3},\\
&T = [\boldsymbol{\gamma}'(\mathfrak{r}_1)|\boldsymbol{\gamma}'(\mathfrak{r}_2)|\dots|\boldsymbol{\gamma}'(\mathfrak{r}_M)]^T \in \mathbb{R}^{M\times 3}, \qquad [\boldsymbol{\mu}'] = [\boldsymbol{\mu}'_1|\boldsymbol{\mu}'_2|\dots|\boldsymbol{\mu}'_N]^T \in \mathbb{R}^{M\times 3},\\
&[S_{(0,0)}]_{i=1,\dots,N}^{I=1,\dots,N} = \sigma(\varepsilon\,|s-\mathfrak{z}_I|)|_{s=\mathfrak{z}_i}, \quad S_{(0,0)} \in \mathbb{R}^{N\times N},\\
&[S_{(0,1)}]_{i=1,\dots,N}^{J=1,\dots,M} = -\partial_s\sigma(\varepsilon\,|s-\mathfrak{r}_J|)|_{s=\mathfrak{z}_i}, \quad S_{(0,1)} \in \mathbb{R}^{N\times M},\\
&[S_{(1,0)}]_{j=1,\dots,M}^{I=1,\dots,N} = \partial_s\sigma(\varepsilon\,|s-\mathfrak{z}_I|)|_{s=\mathfrak{r}_j}, \quad S_{(1,0)} \in \mathbb{R}^{M\times N},\\
&[S_{(1,1)}]_{j=1,\dots,M}^{J=1,\dots,M} = -\partial_{ss}\sigma(\varepsilon\,|s-\mathfrak{r}_J|))|_{s=\mathfrak{r}_j}, \quad S_{(1,1)} \in \mathbb{R}^{M\times M}.
\end{aligned}
$$

The main differences between this RBF interpolation and the one proposed for the volume-based parametrization are that *(i)* in this case the interpolation procedures (and, thus, deformation) are performed on the curve, rather than on the three-dimensional vessel, and *(ii)* interpolation of the tangent vector is also sought by means of the parameters $\boldsymbol{\mu}'$, in order to be able to perform local variations to angles.

Finally, after the deformation an updated moving coordinate frame ($\boldsymbol{t}(s;\boldsymbol{\mu},\boldsymbol{\mu}')$, $\boldsymbol{n}_1(s;\boldsymbol{\mu},\boldsymbol{\mu}')$, $\boldsymbol{n}_2(s;\boldsymbol{\mu},\boldsymbol{\mu}')$) can be computed.

(C) in the final step the vessel is deformed by the map $\boldsymbol{C}(\cdot;\boldsymbol{\mu},\boldsymbol{\mu}',\boldsymbol{\eta}) : \mathbb{R}^3 \to \mathbb{R}^3$,

$$
\begin{aligned}
\boldsymbol{C}(\boldsymbol{x};\boldsymbol{\mu},\boldsymbol{\mu}',\boldsymbol{\eta}) &= \boldsymbol{C}(\{\rho(\boldsymbol{x}),\theta(\boldsymbol{x}),s(\boldsymbol{x})\};\boldsymbol{\mu},\boldsymbol{\mu}',\boldsymbol{\eta})\\
&= \boldsymbol{\gamma}(s(\boldsymbol{x});\boldsymbol{\mu},\boldsymbol{\mu}') + \rho r(s(\boldsymbol{x});\boldsymbol{\eta})\,[\cos\theta(\boldsymbol{x})\;\boldsymbol{n}_1(s(\boldsymbol{x});\boldsymbol{\mu},\boldsymbol{\mu}')\\
&\qquad + \sin\theta(\boldsymbol{x})\;\boldsymbol{n}_2(s(\boldsymbol{x});\boldsymbol{\mu},\boldsymbol{\mu}')]\,.
\end{aligned}
\tag{5.8}
$$

The resulting map $\boldsymbol{C}(\cdot;\boldsymbol{\mu},\boldsymbol{\mu}',\boldsymbol{\eta})$ thus provides the deformation of the three-dimensional vessel between a reference configuration (say, a branch of the patient-specific network) and the deformed configuration, obtained as a function of the displacements $\boldsymbol{\mu}$, variations $\boldsymbol{\mu}'$ of the tangent vector, and local radius variations $\boldsymbol{\eta}$ of the centerline.

5.2.2.1 Stenoses variation

Analyzing the sensitivity of the haemodynamics with respect to the severity of a stenosis is interesting from a clinical standpoint. In fact, current medical experience suggests that surgery should be performed only for critical occlusions [124,218,224,225,251]. The challenge from a computational standpoint is, however, that local geometrical variations need to be performed to change the value of the stenosis severity. This task is easily carried out by the proposed parametrization, and in particular considering at step (C) a function

$$
r(s;\boldsymbol{\eta}) = r(s)\sqrt{1-\alpha\exp\left(-\frac{(s-\mu)^2}{\sigma^2}\right)}, \quad \boldsymbol{\eta} = (\alpha,\mu,\sigma)
$$

used to represent a stenosis at the point located at curvilinear abscissa μ, where the factor α is the surface reduction and the standard deviation σ controls, in this simplified model, the "extension" of the stenotic region.

5.2.3 Handling bifurcations and anastomoses

The main advantage of the centerline-based parametrization is the chance of deforming a three-dimensional shape acting on a one-dimensional object. However, the unidimensionality

assumption does not hold near bifurcations of native vessels or anastomoses of coronary arteries and bypass grafts. In these regions a three-dimensional parametrization, based on a volume-based RBF interpolation (Section 5.1.2), is employed.

Therefore, the proposed centerlines-based parametrization for a network of vessels (in particular, coronary arteries and bypass grafts) is:

- (5.8) away from bifurcations and anastomoses. Geometrical quantities of clinical interest can be chosen, such as stenosis variation;
- (5.4) close to bifurcations or anastomoses. To ensure continuity between one-dimensional and three-dimensional representations some control points of the three-dimensional representation need to be chosen, on the interfaces between the different representations. We explain how to choose such control points with the help of a relevant example in the clinical practice, namely the variation of end-to-side anastomosis between antegrade (same direction for graft flow and native vessel flow in the anastomosis), T-shaped (graft is perpendicular to the native vessel) and retrograde (opposite directions for graft flow and native vessel flow in the anastomosis) cases, which can be related to the variation of the grafting angle.

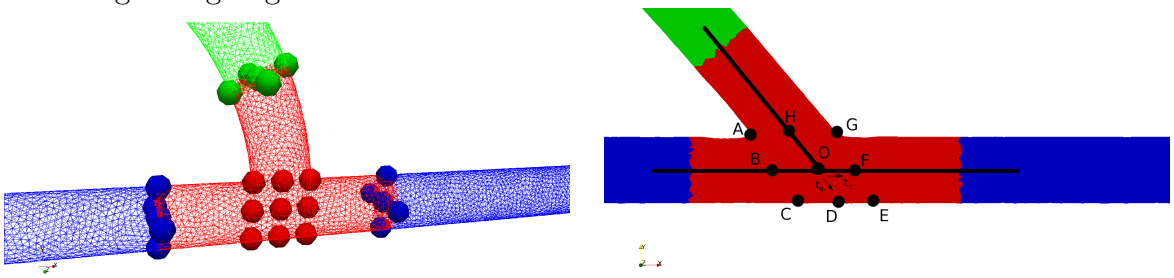

(a) *Reference domain and corresponding domain decomposition (blue and green: monodimensional parametrization* (5.8)*; red: three-dimensional representation* (5.4)*). Possible choices for control points of* (5.4)*.*

(b) *Possible choices for a subset of the control points of* (5.4)*.*

Figure 5.10: *Reference domain and possible control point choices.*

The current parametrization is able to deform a reference anastomosis between the previous cases, see e.g. Figure 5.11, preserving the mesh quality as much as possible. To this aim, only two parameters $(a, \delta\theta)$ are needed. We proceed as follows:

1. we rotate the tangential vector of the graft near the anastomosis as follows: denoting by $\boldsymbol{t}_c$ and $\boldsymbol{t}_g$ the tangent vectors of the coronary artery and the graft in the reference configuration and by $\boldsymbol{t}_g(\boldsymbol{\mu}')$ the tangent vector of the graft in the deformed configuration, the following choice of $\boldsymbol{\mu}' = \boldsymbol{\mu}'(a, \delta\theta)$

$$\boldsymbol{k} = \frac{\boldsymbol{t}_g \times \boldsymbol{t}_c}{\|\boldsymbol{t}_g \times \boldsymbol{t}_c\|}, \quad R = I_{3\times 3} + [\boldsymbol{k}]_\times \sin\delta\theta + (1 - \cos\delta\theta)[\boldsymbol{k}]_\times^2, \quad \boldsymbol{\mu}'(a, \theta) = (aR - I_{3\times 3})\boldsymbol{t}_g$$

enforces a rotation of $\boldsymbol{t}_g$ of an angle $\delta\theta$ in the plane of $(\boldsymbol{t}_c, \boldsymbol{t}_g)$, to obtain $\boldsymbol{t}_g(\boldsymbol{\mu}')$. $[\boldsymbol{k}]_\times \in \mathbb{R}^{3\times 3}$ denotes the cross-product matrix such that $[\boldsymbol{k}]_\times \boldsymbol{v} = \boldsymbol{k} \times \boldsymbol{v}$ for all $\boldsymbol{v} \in \mathbb{R}^3$. The scaling coefficient $a \approx 1$ controls the size of the neighborhood which is affected by the transformation (see Figure 5.11d for a comparison). The graft (green subdomain in Figure 5.10a) is then deformed by means of the unidimensional representation (5.8), enforcing the new tangent direction $\boldsymbol{t}_g(\boldsymbol{\mu}')$. After the deformation, the map (5.8) is computed *also* at the control points denoted by green markers, in

order to store their deformed position[6]. These deformed position are then used as interpolation constraints for the three-dimensional volume-based parametrization, which deforms the anastomosis region (denoted by the red subdomain) guaranteeing continuity of the global map.

2. additional control points should also be added in the anastomosis region, see Figures 5.10a (red markers) and 5.10b, to prevent undesired variations of the radius in the parametrized graft, especially when performing large rotations. However, in contrast to Section 5.1.4, their position in the deformed domain can be *automatically* computed. For example, the deformed position of the control point A is computed as the intersection between the straight lines AHG (lying on the plane $(\boldsymbol{t}_c, \boldsymbol{t}_g)$, parallel to $\boldsymbol{t}_c$ at a distance r_c from O, being r_c the local radius of the native coronary artery) and ABC (lying on the plane $(\boldsymbol{t}_c, \boldsymbol{t}_g)$, parallel to $\boldsymbol{t}_g(\boldsymbol{\mu}')$ at a distance r_g from O, being r_g the local radius of the graft).

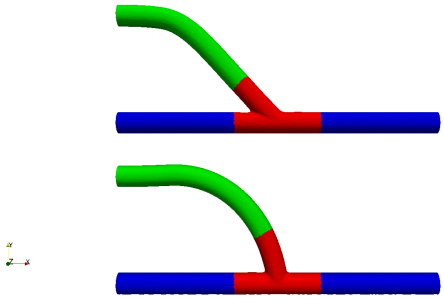

(a) *Antegrade (top) anastomosis obtained as a deformation of a T-shaped (bottom) anastomosis.*

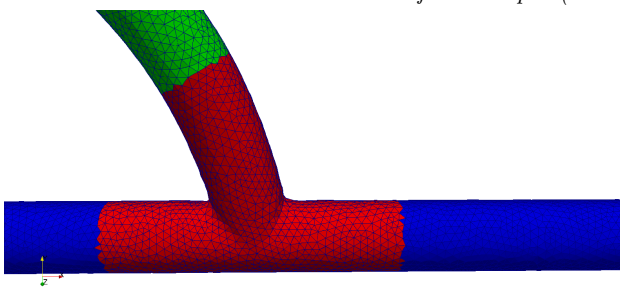

(b) *T-shaped anastomosis (zoom, mesh).*

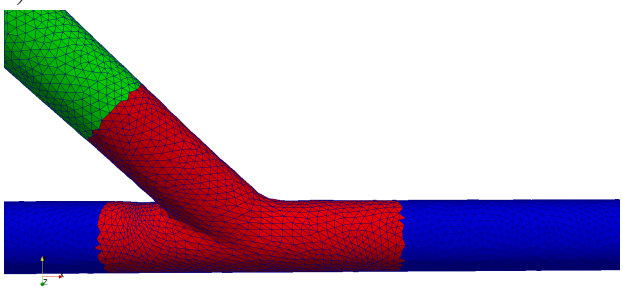

(c) *Antegrade anastomosis (zoom, mesh).*

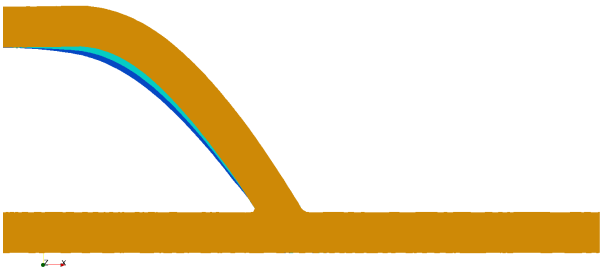

(d) *Deformed domain for different values of the parameter a: $a = 0.8$ (blue), $a = 1$ (cyan), $a = 1.2$ (orange).*

Figure 5.11: *Some examples of anastomosis variation.*

[6]The same operations are performed on the blue subdomain and at the blue control points, which are related to the native coronary artery. However, since no rotation is sought on the coronary artery, the resulting map is the identity.

5.3 Test case: anastomosis and residual flow variation

In this section we present a test case for the coupling between the centerlines-based parametrization and the POD-Galerkin ROM. We consider a steady flow in the idealized bypass configuration in Figure 5.10a, and two possible physical and geometrical parametrizations:

1. physical parametrization on the Reynolds number (two parameters: viscosity and magnitude of the inlet velocity on the graft), no residual flow in the native vessel, geometrical parametrization on anastomosis variation (two parameters: angle θ and scaling coefficient a);
2. physical parametrization on the Reynolds number (two parameters: viscosity and magnitude of the inlet velocity on the graft), parametrized residual flow in the native vessel (one parameter $\%_{fr}$, defined as the ratio between the magnitude of the inlet velocity at the native vessel over the magnitude of the inlet velocity at the graft), geometrical parametrization on anastomosis variation (two parameters: angle θ and scaling coefficient a).

Number of physical parameters	2 (case 1) or 3 (case 2)
Number of geometrical parameters	2
FE velocity order	2
FE pressure order	1
Total number of FE dofs	376,254
$N_{\text{train,EIM}}$	150
Affine expansions components for a, b, c	20, 10, 10
$N_{\text{train,POD-Galerkin}}$	50
$N_{\max}$	50
Offline CPU time	≈ 2 *days* $\times$ 36 processor

Table 5.4: *Details of the offline stage.*

Number of velocity basis functions	50 + 1 lifting (case 1) o 50 + 2 liftings (case 2)
Number of supremizer basis functions	50
Number of pressure basis functions	50
Online CPU time for each ROM solve	≈ 2 *min* $\times$ 1 processor

Table 5.5: *Details of the online stage.*

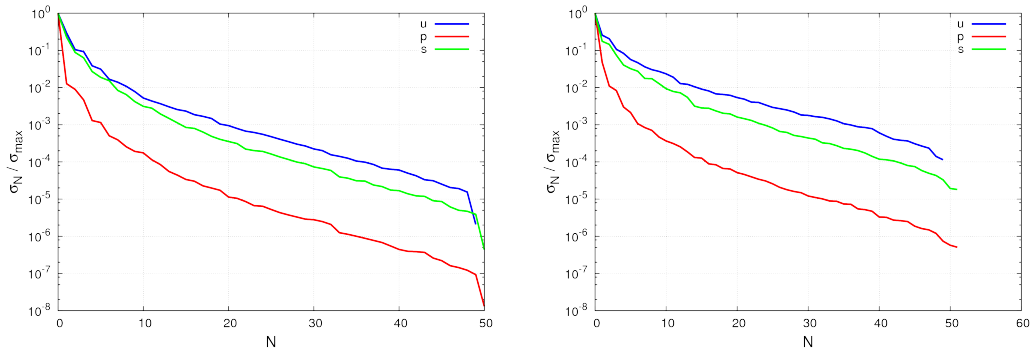

(a) *Case 1: POD singular values for velocity, supremizers, pressure.*

(b) *Case 2: POD singular values for velocity, supremizers, pressure.*

Figure 5.12: *Results of the offline stage: POD singular values for velocity, supremizers, pressure.*

5.3.1 Numerical results: case 1

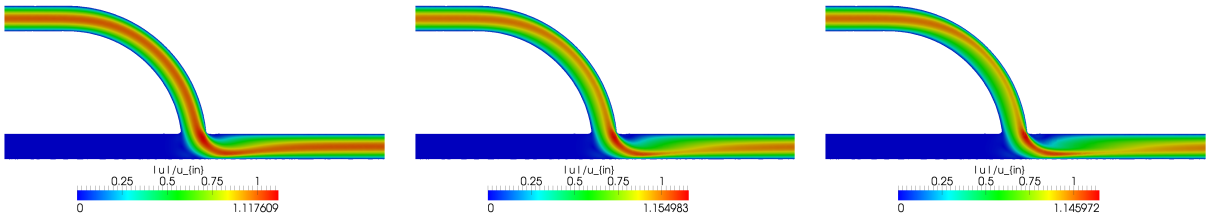

(a) $Re \approx 60$ **(b)** $Re \approx 100$ **(c)** $Re \approx 140$

Figure 5.13: Case 1, $\theta = 90°$, $a = 1$. *Magnitude of the velocity for increasing Reynolds numbers.*

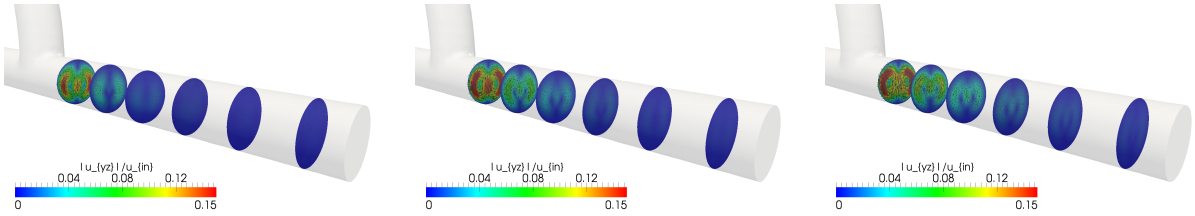

(a) $Re \approx 60$ **(b)** $Re \approx 100$ **(c)** $Re \approx 140$

Figure 5.14: Case 1, $\theta = 90°$, $a = 1$. *Magnitude of the transversal velocity for increasing Reynolds numbers.*

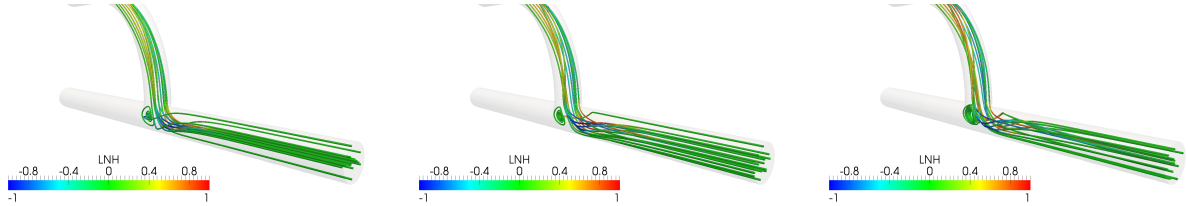

(a) $Re \approx 60$ **(b)** $Re \approx 100$ **(c)** $Re \approx 140$

Figure 5.15: Case 1, $\theta = 90°$, $a = 1$. *Streamlines and local normalized helicity for increasing Reynolds numbers.*

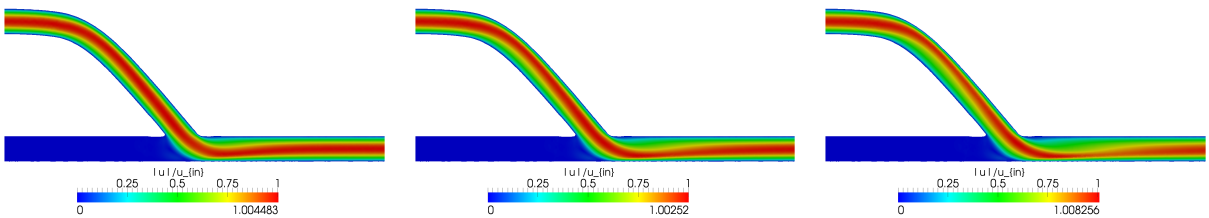

(a) $Re \approx 60$ **(b)** $Re \approx 100$ **(c)** $Re \approx 140$

Figure 5.16: Case 1, $\theta = 50°$, $a = 1$. *Magnitude of the velocity for increasing Reynolds numbers.*

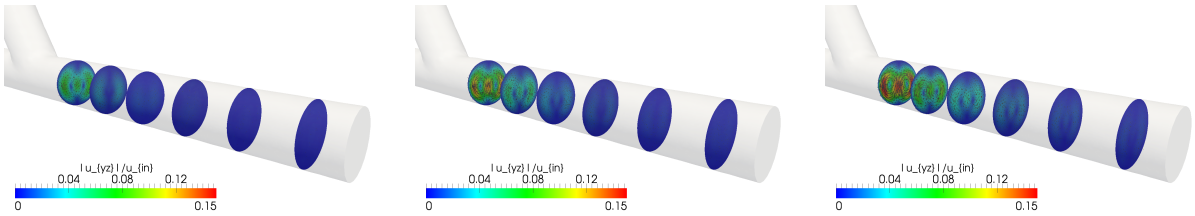

(a) $Re \approx 60$ **(b)** $Re \approx 100$ **(c)** $Re \approx 140$

Figure 5.17: Case 1, $\theta = 50°$, $a = 1$. *Magnitude of the transversal velocity for increasing Reynolds numbers.*

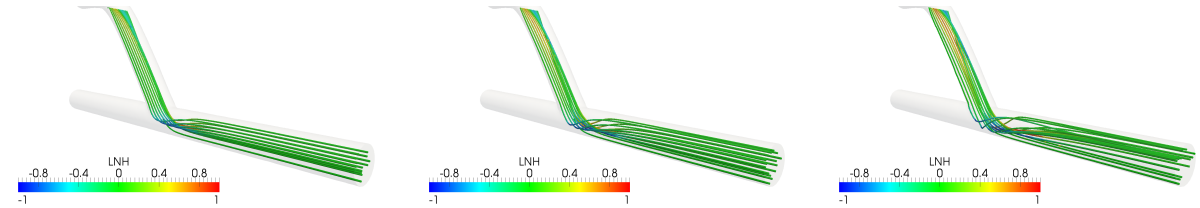

(a) $Re \approx 60$ **(b)** $Re \approx 100$ **(c)** $Re \approx 140$

Figure 5.18: Case 1, $\theta = 50°$, $a = 1$. *Streamlines and local normalized helicity for increasing Reynolds numbers.*

5.3.2 Numerical results: case 2

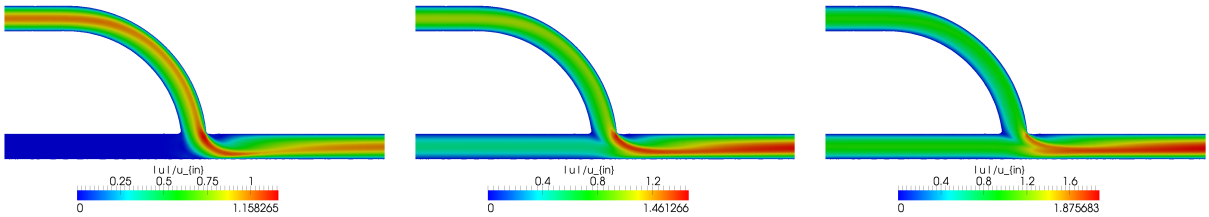

(a) $\%_{fr} = 0.0$ **(b)** $\%_{fr} = 0.5$ **(c)** $\%_{fr} = 1.0$

Figure 5.19: Case 2, $\theta = 90°$, $a = 1$. *Magnitude of the velocity for increasing residual flow, at* $Re = 100$.

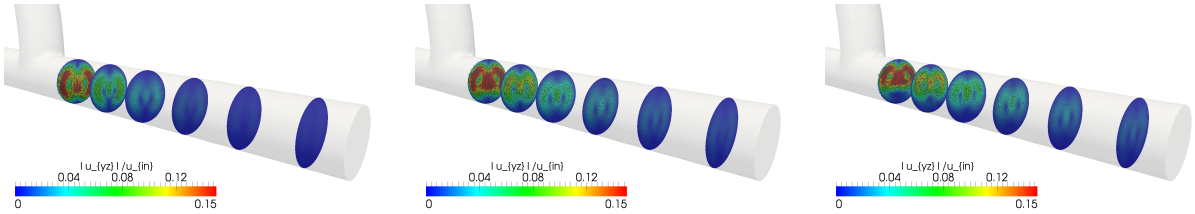

(a) $\%_{fr} = 0.0$ **(b)** $\%_{fr} = 0.5$ **(c)** $\%_{fr} = 1.0$

Figure 5.20: Case 2, $\theta = 90°$, $a = 1$. *Magnitude of the transversal velocity for increasing residual flow, at* $Re = 100$.

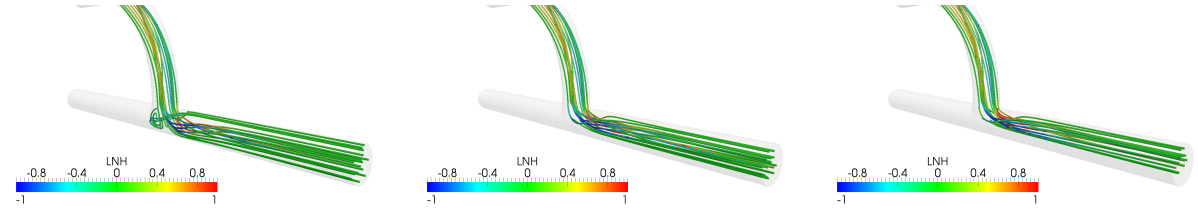

(a) $\%_{fr} = 0.0$ **(b)** $\%_{fr} = 0.5$ **(c)** $\%_{fr} = 1.0$

Figure 5.21: Case 2, $\theta = 90°$, $a = 1$. *Streamlines and local normalized helicity for increasing residual flow, at* $Re = 100$.

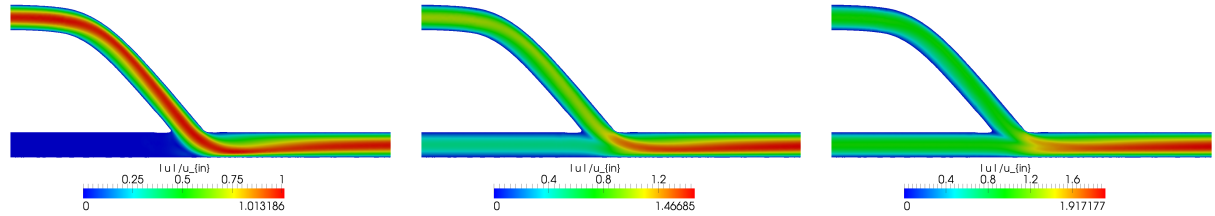

(a) $\%_{fr} = 0.0$ **(b)** $\%_{fr} = 0.5$ **(c)** $\%_{fr} = 1.0$

Figure 5.22: Case 2, $\theta = 50°$, $a = 1$. *Magnitude of the velocity for increasing residual flow, at* $Re = 100$.

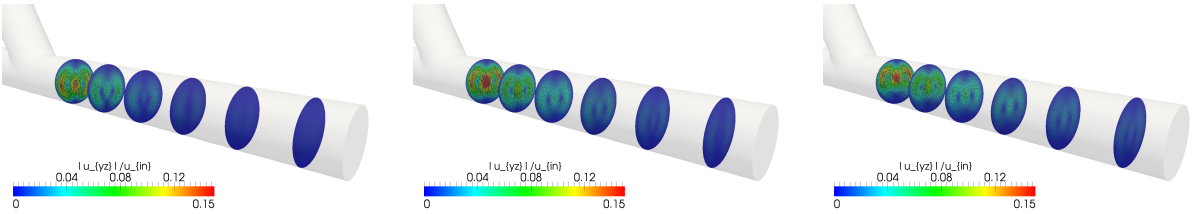

(a) $\%_{fr} = 0.0$ **(b)** $\%_{fr} = 0.5$ **(c)** $\%_{fr} = 1.0$

Figure 5.23: Case 2, $\theta = 50°$, $a = 1$. *Magnitude of the transversal velocity for increasing residual flow, at* $Re = 100$.

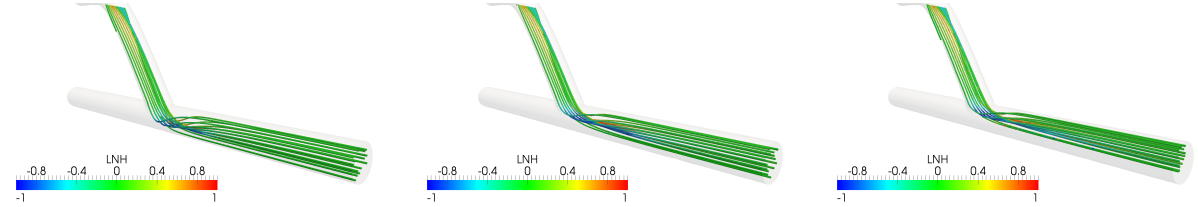

(a) $\%_{fr} = 0.0$ **(b)** $\%_{fr} = 0.5$ **(c)** $\%_{fr} = 1.0$

Figure 5.24: Case 2, $\theta = 50°$, $a = 1$. *Streamlines and local normalized helicity for increasing residual flow, at* $Re = 100$.

5.3.3 Discussion

Figure 5.12 shows a comparison of the POD singular values for velocity, supremizers, pressure. The additional physical parameter in case 2 causes a slower decay in the POD singular values. In both cases velocity and supremizers singular values exhibit slower decay than pressure singular values. Online results are shown in Figures 5.13-5.15 for case 1 on a T-shaped anastomosis ($\theta = 90°$), Figures 5.16-5.18 for case 1 on a flow-direction anastomosis ($\theta = 50°$), Figures 5.19-5.21 for case 2 on a T-shaped anastomosis ($\theta = 90°$) and Figures 5.22-5.24 for case 2 on a flow-direction anastomosis ($\theta = 50°$).

Plots of the magnitude of the velocity are reported in Figures 5.13, 5.16, 5.19, 5.22. In the case of no residual flow and T-shaped anastomosis (Figure 5.13), a jet of high velocity impacts on the arterial bed, while the toe of the graft shows a recirculation region. Both the maximum velocity and the size of the recirculation region increase with higher Reynolds numbers. In contrast, neither higher velocity nor a recirculation region are shown in a flow-direction anastomosis (Figure 5.16). The size of the recirculation region near the toe appears to decrease for increasing residual flow in the native artery, for both T-shaped (Figure 5.19) and flow-direction (Figure 5.22) anastomoses.

Plots of the magnitude of the transversal velocity are reported in Figures 5.14, 5.17, 5.20, 5.23. These figures highlight the formation of two Dean vortices just distally to the anastomosis, in all considered cases. The magnitude of the maximum transversal velocity increases with the Reynolds number; the two Dean vortices however quickly dissipate as the distance downstream the anastomosis increases. Flow-direction anastomoses (Figures 5.17 and 5.23) feature in general lower values of transversal velocity than T-shaped anastomoses (Figures 5.14 and 5.20), for both the cases with and without residual flow. Dean vortices are moved closer to the toe and farther from the arterial bed as residual flow grows (Figures 5.20 and 5.23).

Finally, streamlines and local normalized helicity (LNH) are shown in Figures 5.15, 5.18, 5.21, 5.24. High absolute values of LNH are observed near the arterial bed just distally to the anastomosis. In case 1 (no residual flow), T-shaped anastomosis feature a vortex near the heel of graft (Figure 5.15). However, case 2 shows that this recirculation region disappears with an increase of residual flow in the native artery (Figure 5.21). No recirculation region is highlighted instead for flow-direction anastomoses, neither in case 1 (Figure 5.18) nor in case 2 (Figure 5.24).

Part IV

Numerical results

CHAPTER 6

Numerical results for patient-specific coronary artery bypass grafts computationally reduced simulations

The proposed framework (medical imaging for reconstruction of patient-specific coronary artery bypass grafts, model order reduction techniques based on POD-Galerkin reduced-order models, and shape parametrization techniques such as the centerlines-based parametrization) is applied in this chapter to some patient-specific cases. Three possible classes of parameters of clinical interest (Section 6.2) are considered: physical parameters related to inflow profiles (Section 6.3), geometrical parameters related to coronary artery disease (Section 6.4), and to coronary artery bypass graft surgery (Section 6.5). Numerical results and a clinical discussion on the resulting flow patterns are discussed for each case.

6.1 State of the art

Occlusion of the grafts is a typical problem in the long term behavior of coronary artery bypass grafts (CABGs), as discussed in Section 1.3. A better understanding, both by means of experimental measurements or numerical simulations, of the haemodynamics in CABGs, and in particular near the anastomosis between two grafts (e.g. Y-graft) or between a graft and a native artery (termino-lateral or latero-lateral), has been sought in the last decades [107, 181, 184, 196, 254].

Early numerical results on three-dimensional idealized end-to-side anastomoses have been proposed by [94, 133, 152, 239], under the assumption of steady flow conditions, and in [38, 39, 83, 90, 164] for time-dependent flow profiles. Several topics have been addressed since these first studies.

Remarkable research focus has been devoted to *parametric studies* [141, 152, 195, 197, 223, 225, 251]. A first relevant parametric study is on *inlet boundary conditions*. From a physiological point of view, this is useful to take into account different exercise conditions of the patient (stress conditions or rest conditions), which entail a variation in the flow rate. Variation of graft flow rate is also observed in the clinical practice in the internal thoracic

artery [197, 223, 225], and numerical simulations to take this aspect into account have been recently performed in [195, 251], which studied (on a pig, and not on patient-specific cases) how different flow rates affect the local flow patterns in the anastomosis, combining invasive blood flow measurements, acquisition of the anatomical model and computational methods. Moreover, from a numerical point of view, a flow rate parametrization has been used on idealized geometries also to account for different coronary artery disease progression. In fact, for example, a study of the haemodynamics in an idealized distal anastomosis for different flow conditions in the native artery (to simulate partial occlusion, complete occlusion, retrograde flow) has been proposed in [141,152]. In our work, we propose a parametrization on the flow rate to account for different stress or rest conditions, rather than stenosis variation, which instead is accounted for thanks to its own parametrization.

Large attention has been also given to the *optimization of existing designs* [22,88,163,182, 205,229], and the resulting possible *proposal of new designs*, for example in Π-composite grafts [203], sequential grafts [137,138] or helical-type grafts [272]. Optimal grafts or new proposed designs have been obtained considering *local geometrical variations of the coronary arteries and grafts*. This topic has been also addressed in [87, 94, 101, 109, 135, 141, 238, 249] (grafting angles) and [42, 131, 209, 259, 276] (graft-to-host diameter ratio). However, these results are obtained mostly on idealized geometries. On one hand, as it has been shown in Chapter 2, patient-specific geometries are far more complex than simplified end-to-side anastomosis; moreover, only few of the previous studies consider sequential grafting procedures. On the other hand, many practical constraints need to be considered during the surgery, which may in fact limit the choice of grafting angles (for example, when operating on a patient with three-vessels disease the aim should be to revascularize the entire left and right coronary trees, and the length of the available grafts poses a severe constraint) or graft-to-host diameter ratios (for example, since grafts are autologous materials, it is difficult in practice to change graft diameters). For these reasons, it is important, even if performing just local variations, to start from a complete, sequential, *patient-specific* configuration. This is a major difference between the results proposed in this chapter and the cited literature.

Few studies have been carried out on *patient-specific* configurations, reconstructed from clinical data. Among them we mention [45, 65, 142] on native (healthy) coronary arteries, and [88, 100, 228] on coronary artery bypass grafts. Our current dataset is however larger, and more complete (with respect to anastomosis features, grafting procedures, coronary artery disease) than the previous references, and some methodological differences are also present. In particular, [100] proposed CFD simulations on only two patients, the first one featuring a single graft and the second one a double sequential graft. Both surgeries, however, were performed only with saphenous vein grafts, and more complex structures (such as Y-grafts) were not studied. Finally, variation of parameters of clinical interest was not considered. Geometrical variations were considered instead in [88], but they were performed on two-dimensional configurations and then applied to the three-dimensional patient-specific configuration in a post-processing stage. Moreover, the variation of grafting angles proposed in [228] requires a new segmentation for each new angle. Besides involving a time consuming procedure, the resulting method cannot be formulated in a parametrized framework, and thus it cannot take advantage of the model order reduction techniques proposed in this thesis to efficiently perform a sensitivity analysis of the flow patterns.

Finally, as already mentioned in the introduction to Part II, early results on the coupling between reduced-order models, parametrized formulations and idealized bypass configurations have been proposed in the last ten years in [4, 5, 154, 180, 211, 219, 220]. A peculiar characteristic of the present work is to present, for the first time, the results of the coupling between reduced-order models and *patient-specific* clinical data of CABGs.

6.2 Parameters of interest: boundary conditions and geometrical features

In this chapter the POD-Galerkin ROM is employed for fast computation of the haemodynamics in patient-specific configurations of coronary artery bypass grafts. Several parameters are of clinical interest; they represent:

- **physical parametrization on inflow boundary conditions** (right coronary artery, left coronary artery, internal thoracic artery): variation of inlet flow rates may be of clinical relevance e.g. when interested in the evaluation of the surgery under both rest or stress conditions.
  - For the **LCA**, clinical literature (see e.g. [8, 66, 126, 140, 256]) agrees on dominant diastolic flow, i.e. coronary blood flow peaks in diastole.
  - In the case of the **RCA**, instead, some studies suggest neither diastolic nor systolic dominance (see e.g. [46, 140, 257]), others systolic dominance [39, 263] and others diastolic dominance [279], featuring also very different time-averaged flow rates.
  - Finally, we refer e.g. to [26, 39, 56, 87, 134, 166, 169, 169, 227, 263] for some studies on the **LITA**. Moreover, the effect of graft adaptation should be considered also for the LITA [86, 195, 197, 223, 225, 251], which causes the flow (and also the diameter of the graft itself) to adapt over time. In [149], the flow is found to be predominantly diastolic in the short-term and in distal sections of the artery, but predominantly systolic in the long-term period after the surgery.

  Although possible, considering all these factors would entail a high dimensional parametric space (e.g. to change the RCA flow from predominantly systolic to predominantly diastolic) and to a more difficult interpretation of the results. For this reason only one case of systolic/diastolic dominance has been studied (LCA: diastolic dominance; RCA: neither diastolic nor systolic dominance; LITA: systolic dominance) and two physical parameters, $\text{factor}_{Re}^{ave,i}$ and $\text{factor}_{Re}^{ampl,i}$, have been considered for each inlet i, $i =$ LCA, RCA, LITA. The parametrized flow rate is then given by

$$q_i(t; \text{factor}_{Re}^{ave,i}, \text{factor}_{Re}^{ampl,i}) = \text{factor}_{Re}^{ave,i}\ \bar{q}_i + \text{factor}_{Re}^{ave,i}\ \text{factor}_{Re}^{ampl,i}\ q_i'(t).$$

  The parameter $\text{factor}_{Re}^{ave,i}$ (range $[2/3, 4/3]$) is a multiplicative factor on the time-averaged flow rate $\bar{q}_i$, while the amplitude $q_i'(t)$ of the oscillation during the period is multiplied by $\text{factor}_{Re}^{ampl,i}$ (range $[0.1, 1]$) times $\text{factor}_{Re}^{ave,i}$. These parameters are able to account rest/stress conditions; stress conditions are obtained e.g. increasing the time-averaged flow rate.

  The time-averaged flow rates $\bar{q}_i$ and the profiles of $q_i'(t)$ employed in the current numerical simulations have been adapted from [134] (LITA) and [140] (LCA and RCA). A plot is provided in Figure 6.1 for the reference cases $\text{factor}_{Re}^{ave,i} = \text{factor}_{Re}^{ampl,i} = 1$, corresponding to time-averaged Reynolds number equal to 130 (LITA) and 100 (LCA and RCA).

- **disease-related geometrical parameters**: we consider different values of stenosis severity. With the notation of Section 5.2.2.1, the section reduction parameter α of the centerlines-based shape parametrization is considered as the geometrical parameter related to native coronary artery disease. The location of the stenosis (denoted by μ in the aforementioned Section) and the extension of the stenosis region (previously denoted by σ) are instead obtained from the available clinical data. In case of double- or

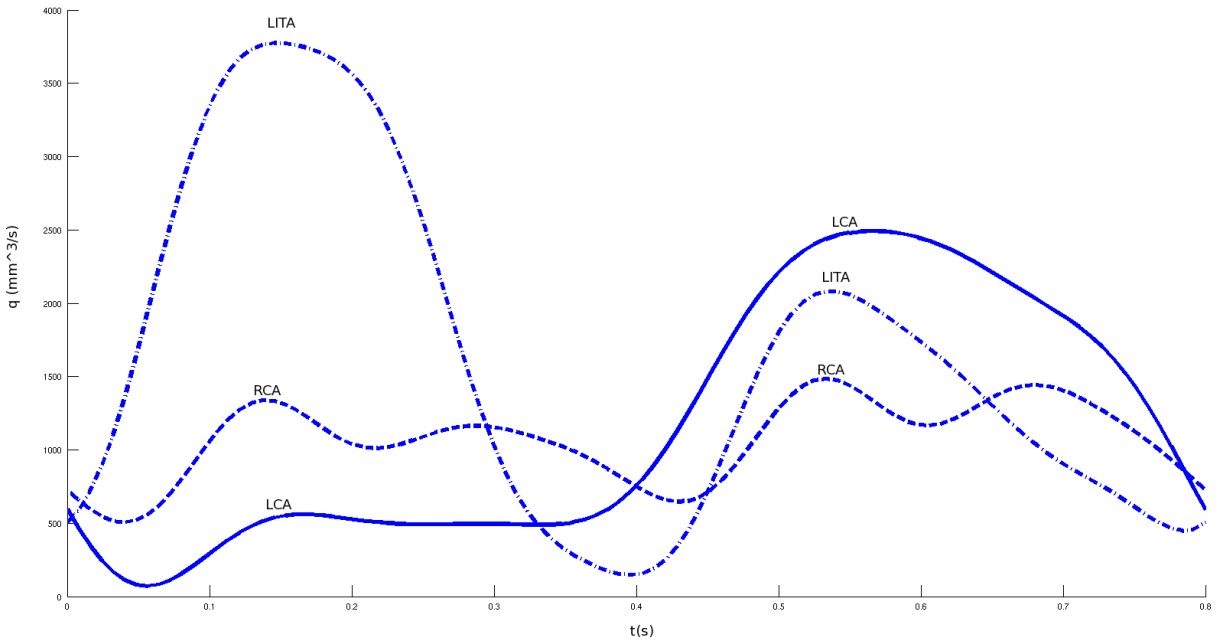

Figure 6.1: *Inlet flow rates (LITA [134], LCA and RCA [140]).*

triple-vessel coronary artery disease, multiple geometrical parameters α_j are consider, where j denotes the stenosed artery (e.g. j = LAD, LCX, RCA, etc.). Stenosis factors vary in the range $[0, 90\%]$, in order to compare critical cases ($\alpha_j \geq 70\%$) to non-critical ones ($\alpha_j < 70\%$). In fact, current clinical experience suggest that surgery should be performed only for critical occlusions [124, 218, 224, 225, 251].

- **surgery-related geometrical parameters**: local variation to anastomoses are performed by means of the centerlines-based shape parametrization, as detailed in Section 5.2.3. Current clinical experience suggests at least three possible termino-lateral (end-to-side) anastomosis are employed in the clinical practice: antegrade (same direction for graft flow and native vessel flow in the anastomosis), T-shaped (graft is perpendicular to the native vessel) and retrograde (opposite directions for graft flow and native vessel flow in the anastomosis). The ROM is employed to compare the haemodynamics in the different cases. The grafting angle is considered as geometrical parameter, in the range $[25°, 155°]$; antegrade cases correspond to angles approximately equal to 45°, T-shaped to 90°, and retrograde to 135°.

Flow patterns are analyzed in the following sections, for several patient-specific configurations, by means of some of the fluid dynamics indices mentioned in the Introduction to Part II. In particular, we will present and discuss results on wall shear stress (WSS), oscillatory shear index (OSI), transversal velocity profiles, and pressure drops. Regions of interest are the *heel* and *toe* of the graft, and the proximal and distal *arterial floor* near the anastomosis (see also Figure 1.7). We refer to heel of the graft as the location of the proximal suture line, while the toe of the graft refers to the distal suture line. The adjectives *proximal* and *distal* are defined with respect to the direction of the flow in the native coronary artery.

6.3 Fast haemodynamics simulations for several values of physical parameters

In this section we apply the POD-Galerkin ROM for a fast evaluation of the fluid dynamics in patient-specific CABGs, considering a variation of physical parameters (inflow boundary conditions) only, in order to quantify the sensitivity of the haemodynamics in the patient-specific configuration with respect to inlet flow rates.

6.3.1 Parametrization and reduced-order models details

Patient	**1**	**7**	**9**
Number of physical parameters	6	4	4
LCA inlet flow rate parameters	2	2	2
RCA inlet flow rate parameters	2	no	no
LITA inlet flow rate parameters	2	2	2
Number of geometrical parameters	0	0	0
FE velocity order	2		
FE pressure order	1		
Total number of FE dofs	1 325 530	970 618	1 261 527
Temporal step	0.01		
Number of time steps per cardiac cycle	80		
CPU time for one cardiac cycle	$11 \sim 13$ h	$8 \sim 9$ h	$10 \sim 12$ h
$N_{\mathbf{train}}$	50		
$N_{\mathbf{max}}$	50		
$M_{\mathbf{2\text{–}POD}}$	20		
Affine expansion components for m**,** a**,** $b \,\&\, c$	1, 1, 1	1, 1, 1	1, 1, 1

Table 6.1: *Details of the reduced-order model.*

Details of the reduced-order model are summarized in Table 6.1. The number of considered physical parameters is reported for each patient; physical parameters are related to the variation of inlet flow rates of left coronary artery, right coronary artery (if present) and bypass grafts.

A Taylor-Hood $\mathbb{P}_2 - \mathbb{P}_1$ FE discretization is employed for the space discretization; an Implicit Euler method is considered for the time discretization. N_{train} FE problems are solved for random values of the parameters. A compression of the temporal trajectory by means of the two-level POD, as detailed in Chapter 4, is performed considering only $M_{2\text{–POD}}$ POD modes in the innermost POD. The offline stage is performed in parallel, for $24 \sim 32$ processors.

The truth solution for each sample point (and for each cardiac cycle) requires approximately 10 hours (to be multiplied by the number of processors to obtain the actual CPU time). The online stage, instead, is performed on a single processor. Thanks to the considerable reduction in the number of degrees of freedom ($N_{\mathbf{u}} = N_{\mathbf{s}} = N_p = N_{\text{max}}$) and efficient offline-online procedure, each online ROM solution requires only a couple of minutes, with computational savings in terms of user time of approximately 99%.

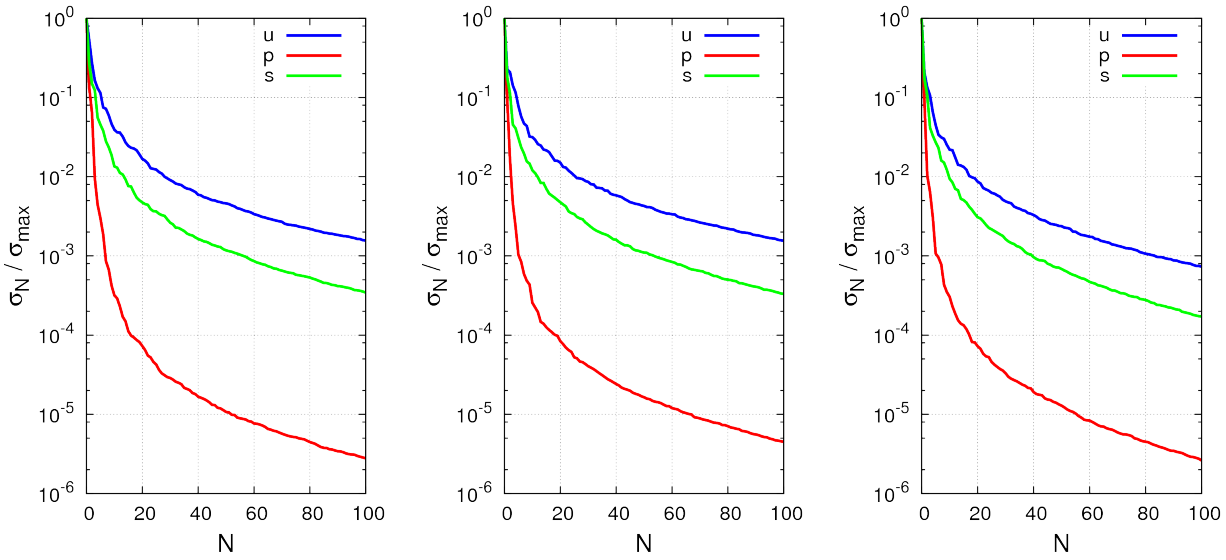

(a) ***Patient 1:*** *POD singular values for velocity, supremizers, pressure.*

(b) ***Patient 7:*** *POD singular values for velocity, supremizers, pressure.*

(c) ***Patient 9:*** *POD singular values for velocity, supremizers, pressure.*

Figure 6.2: *Results of the offline stage: POD singular values for velocity, supremizers, pressure.*

Figure 6.2 shows a plot of the POD singular values for velocity, supremizers, pressure. The pattern is similar for the three studied patients; in all cases velocity (and supremizers) feature a considerably slower decay than pressure.

6.3.2 Numerical results

Patient 1

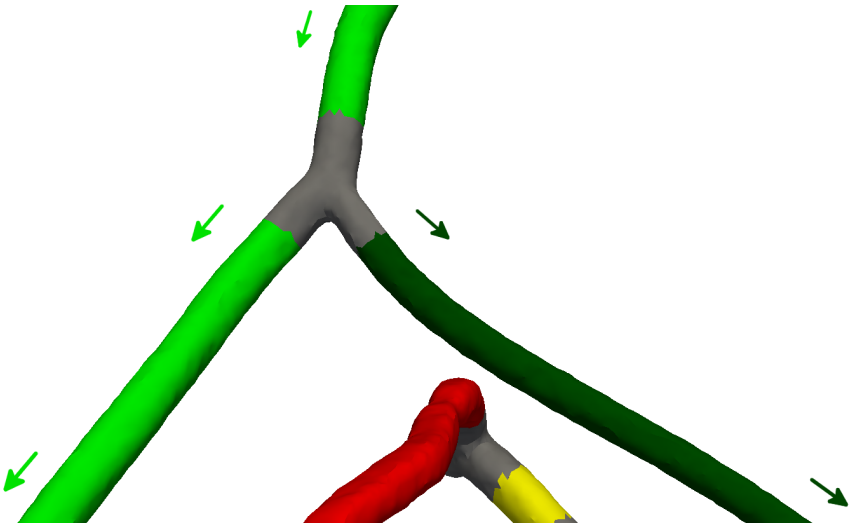

(a) *Bypass grafts near the studied anastomosis. Colored arrows denote blood flow direction.*

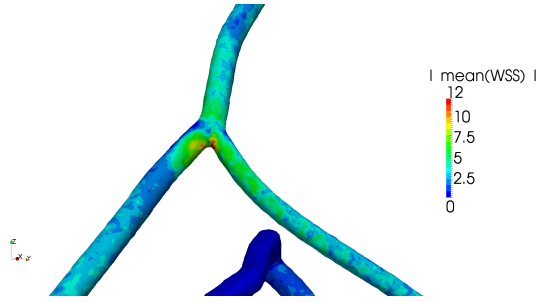

(b) $factor_{Re}^{ave,LITA} = 1$, $factor_{Re}^{ampl,LITA} = 1$
$factor_{Re}^{ave,LCA} = 1$, $factor_{Re}^{ampl,LCA} = 1$
$factor_{Re}^{ave,RCA} = 1$, $factor_{Re}^{ampl,RCA} = 1$

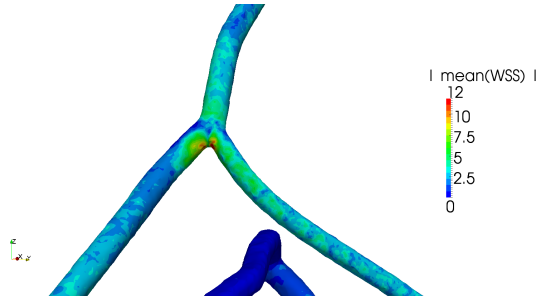

(c) $factor_{Re}^{ave,LITA} = 1$, $factor_{Re}^{ampl,LITA} = 0.1$
$factor_{Re}^{ave,LCA} = 1$, $factor_{Re}^{ampl,LCA} = 0.1$
$factor_{Re}^{ave,RCA} = 1$, $factor_{Re}^{ampl,RCA} = 0.1$

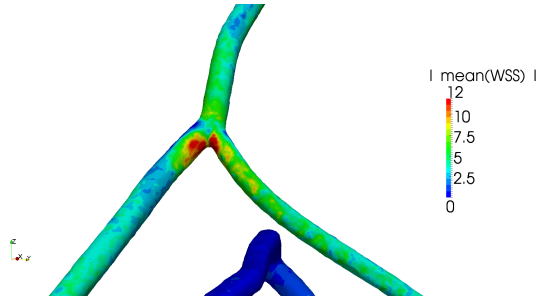

(d) $factor_{Re}^{ave,LITA} = 1.33$, $factor_{Re}^{ampl,LITA} = 1$
$factor_{Re}^{ave,LCA} = 0.66$, $factor_{Re}^{ampl,LCA} = 1$
$factor_{Re}^{ave,LCA} = 0.66$, $factor_{Re}^{ampl,LCA} = 1$

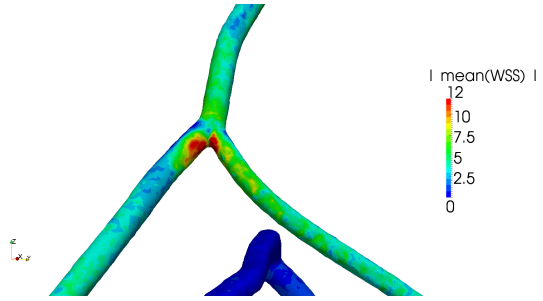

(e) $factor_{Re}^{ave,LITA} = 1.33$, $factor_{Re}^{ampl,LITA} = 0.5$
$factor_{Re}^{ave,LCA} = 0.66$, $factor_{Re}^{ampl,LCA} = 0.5$
$factor_{Re}^{ave,LCA} = 0.66$, $factor_{Re}^{ampl,LCA} = 0.5$

Figure 6.3: ***Patient 1 - Y-graft between LITA and Radial.*** *Comparison of time-averaged wall shear stress [Pa] for different inflow boundary conditions.*

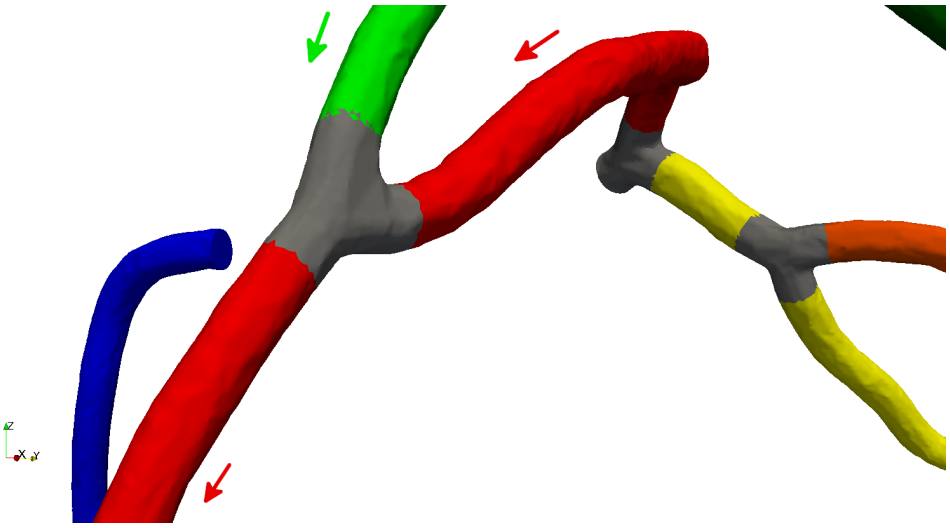

(a) *Coronary arteries and bypass grafts near the studied anastomosis. Colored arrows denote blood flow direction.*

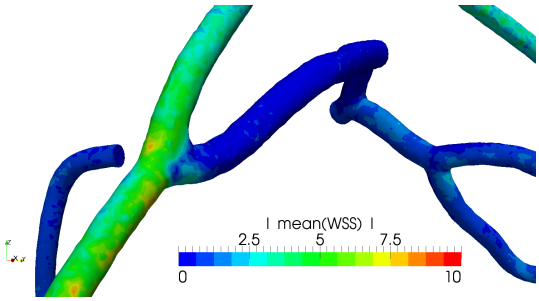

(b) $factor_{Re}^{ave,LITA} = 1$, $factor_{Re}^{ampl,LITA} = 1$
$factor_{Re}^{ave,LCA} = 1$, $factor_{Re}^{ampl,LCA} = 1$
$factor_{Re}^{ave,RCA} = 1$, $factor_{Re}^{ampl,RCA} = 1$

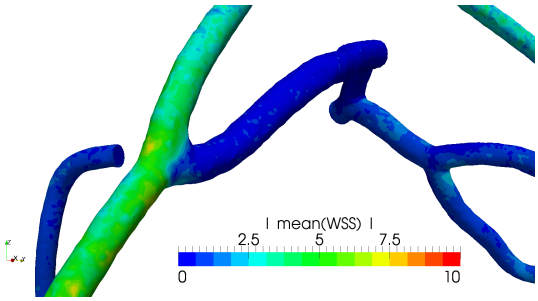

(c) $factor_{Re}^{ave,LITA} = 1$, $factor_{Re}^{ampl,LITA} = 0.1$
$factor_{Re}^{ave,LCA} = 1$, $factor_{Re}^{ampl,LCA} = 0.1$
$factor_{Re}^{ave,RCA} = 1$, $factor_{Re}^{ampl,RCA} = 0.1$

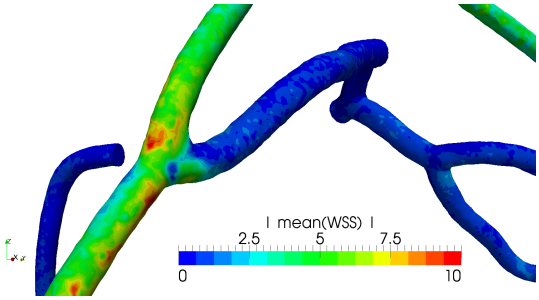

(d) $factor_{Re}^{ave,LITA} = 1.33$, $factor_{Re}^{ampl,LITA} = 1$
$factor_{Re}^{ave,LCA} = 0.66$, $factor_{Re}^{ampl,LCA} = 1$
$factor_{Re}^{ave,LCA} = 0.66$, $factor_{Re}^{ampl,LCA} = 1$

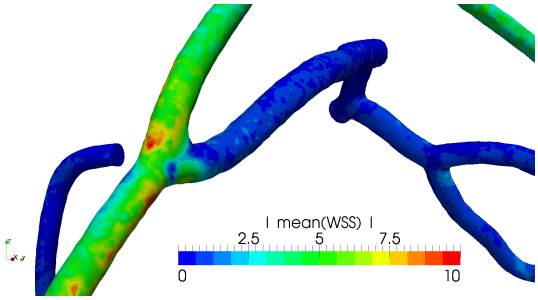

(e) $factor_{Re}^{ave,LITA} = 1.33$, $factor_{Re}^{ampl,LITA} = 0.5$
$factor_{Re}^{ave,LCA} = 0.66$, $factor_{Re}^{ampl,LCA} = 0.5$
$factor_{Re}^{ave,LCA} = 0.66$, $factor_{Re}^{ampl,LCA} = 0.5$

Figure 6.4: ***Patient 1 - LITA to LAD anastomosis (flow-direction, termino-lateral).*** *Comparison of time-averaged wall shear stress [Pa] for different inflow boundary conditions.*

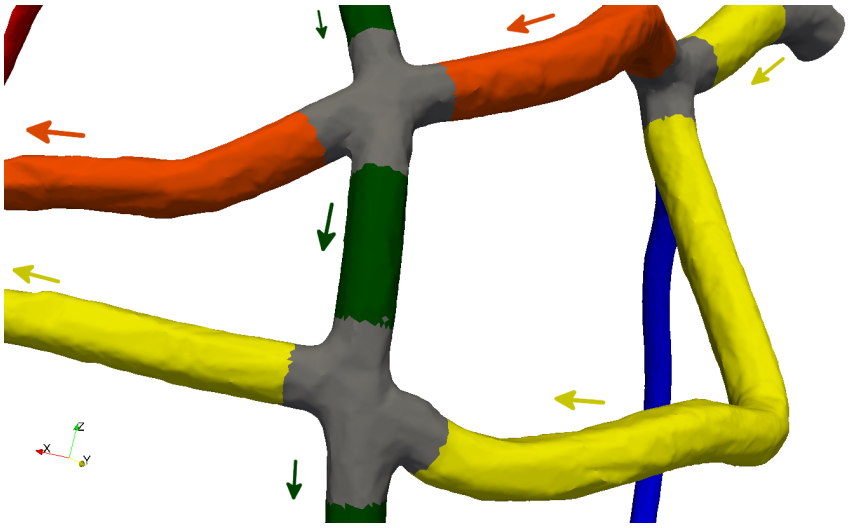

(a) *Coronary arteries and bypass grafts near the studied anastomosis. Colored arrows denote blood flow direction.*

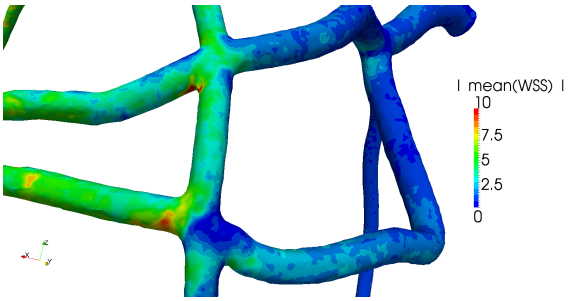

(b) $factor_{Re}^{ave,LITA} = 1$, $factor_{Re}^{ampl,LITA} = 1$
$factor_{Re}^{ave,LCA} = 1$, $factor_{Re}^{ampl,LCA} = 1$
$factor_{Re}^{ave,RCA} = 1$, $factor_{Re}^{ampl,RCA} = 1$

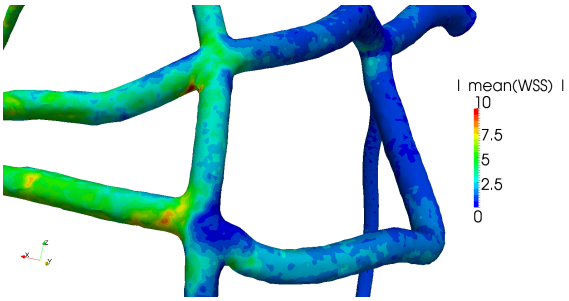

(c) $factor_{Re}^{ave,LITA} = 1$, $factor_{Re}^{ampl,LITA} = 0.1$
$factor_{Re}^{ave,LCA} = 1$, $factor_{Re}^{ampl,LCA} = 0.1$
$factor_{Re}^{ave,RCA} = 1$, $factor_{Re}^{ampl,RCA} = 0.1$

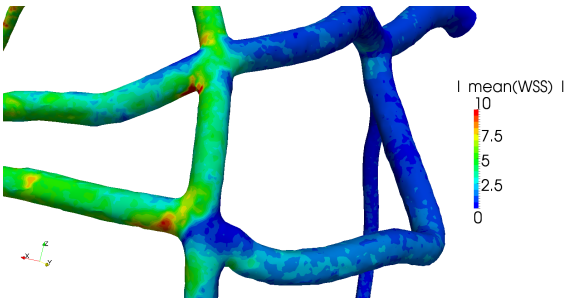

(d) $factor_{Re}^{ave,LITA} = 1.33$, $factor_{Re}^{ampl,LITA} = 1$
$factor_{Re}^{ave,LCA} = 0.66$, $factor_{Re}^{ampl,LCA} = 1$
$factor_{Re}^{ave,LCA} = 0.66$, $factor_{Re}^{ampl,LCA} = 1$

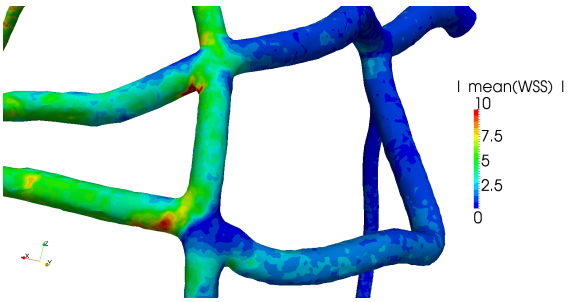

(e) $factor_{Re}^{ave,LITA} = 1.33$, $factor_{Re}^{ampl,LITA} = 0.5$
$factor_{Re}^{ave,LCA} = 0.66$, $factor_{Re}^{ampl,LCA} = 0.5$
$factor_{Re}^{ave,LCA} = 0.66$, $factor_{Re}^{ampl,LCA} = 0.5$

Figure 6.5: ***Patient 1 - Radial to OM and LCX anastomosis (cross, latero-lateral).*** *Comparison of time-averaged wall shear stress [Pa] for different inflow boundary conditions.*

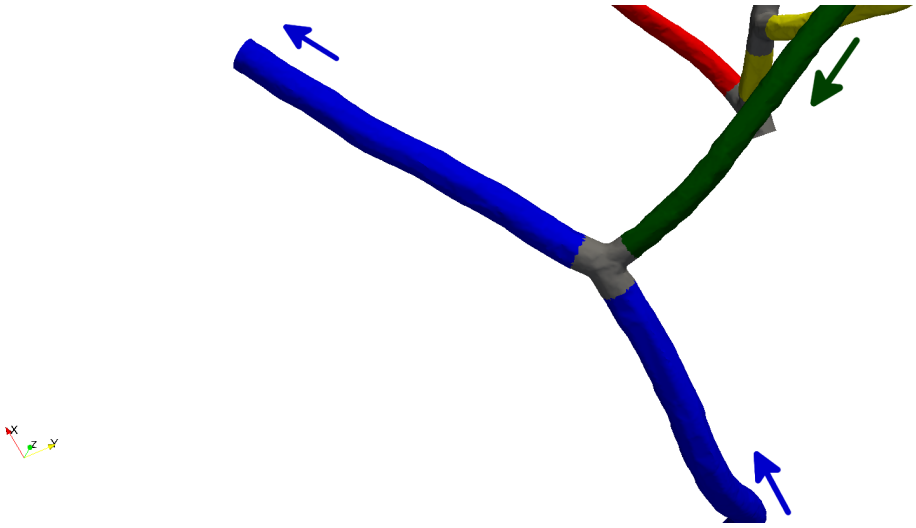

(a) *Coronary arteries and bypass grafts near the studied anastomosis. Colored arrows denote blood flow direction.*

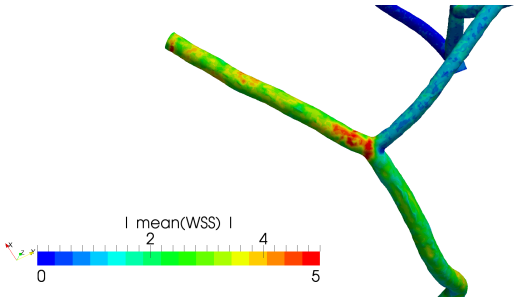

(b) $factor_{Re}^{ave,LITA} = 1$, $factor_{Re}^{ampl,LITA} = 1$
$factor_{Re}^{ave,LCA} = 1$, $factor_{Re}^{ampl,LCA} = 1$
$factor_{Re}^{ave,RCA} = 1$, $factor_{Re}^{ampl,RCA} = 1$

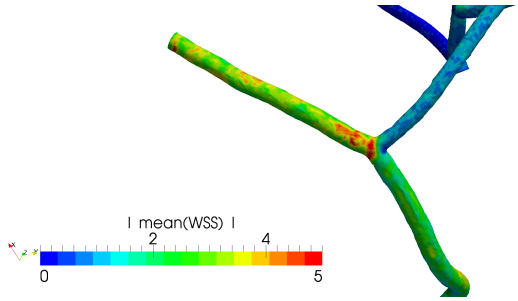

(c) $factor_{Re}^{ave,LITA} = 1$, $factor_{Re}^{ampl,LITA} = 0.1$
$factor_{Re}^{ave,LCA} = 1$, $factor_{Re}^{ampl,LCA} = 0.1$
$factor_{Re}^{ave,RCA} = 1$, $factor_{Re}^{ampl,RCA} = 0.1$

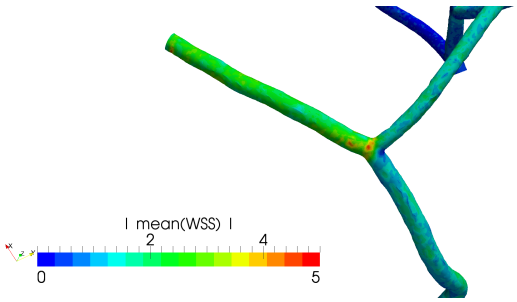

(d) $factor_{Re}^{ave,LITA} = 1.33$, $factor_{Re}^{ampl,LITA} = 1$
$factor_{Re}^{ave,LCA} = 0.66$, $factor_{Re}^{ampl,LCA} = 1$
$factor_{Re}^{ave,RCA} = 0.66$, $factor_{Re}^{ampl,RCA} = 1$

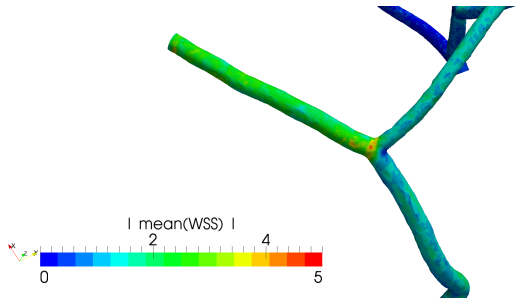

(e) $factor_{Re}^{ave,LITA} = 1.33$, $factor_{Re}^{ampl,LITA} = 0.5$
$factor_{Re}^{ave,LCA} = 0.66$, $factor_{Re}^{ampl,LCA} = 0.5$
$factor_{Re}^{ave,RCA} = 0.66$, $factor_{Re}^{ampl,RCA} = 0.5$

Figure 6.6: ***Patient 1 - Radial to PDA anastomosis (T-shaped, termino-lateral).*** *Comparison of time-averaged wall shear stress [Pa] for different inflow boundary conditions.*

Patient 7

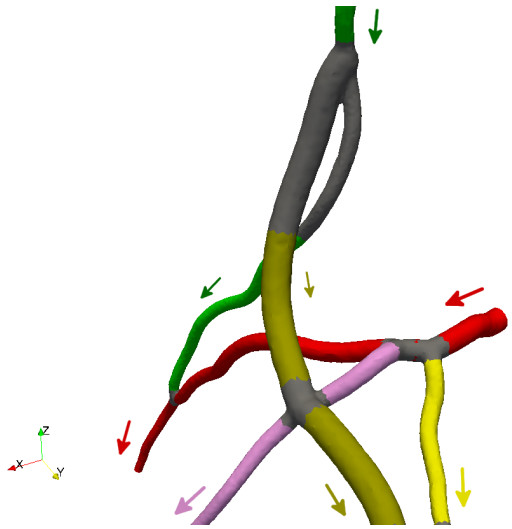

(a) *Coronary arteries and bypass grafts near the studied anastomosis. Colored arrows denote blood flow direction.*

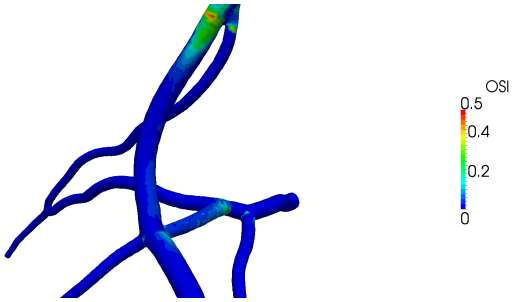

(b) $factor_{Re}^{ave,LITA} = 0.666$, $factor_{Re}^{ampl,LITA} = 0.5$
$factor_{Re}^{ave,LCA} = 0.666$, $factor_{Re}^{ampl,LCA} = 0.5$

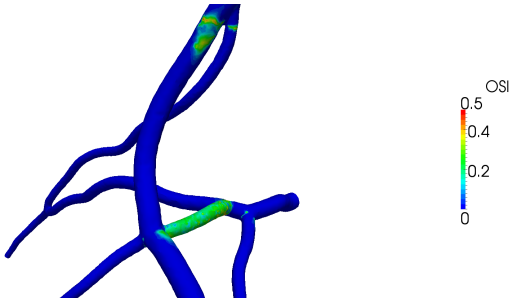

(c) $factor_{Re}^{ave,LITA} = 1.333$, $factor_{Re}^{ampl,LITA} = 0.5$
$factor_{Re}^{ave,LCA} = 0.666$, $factor_{Re}^{ampl,LCA} = 0.5$

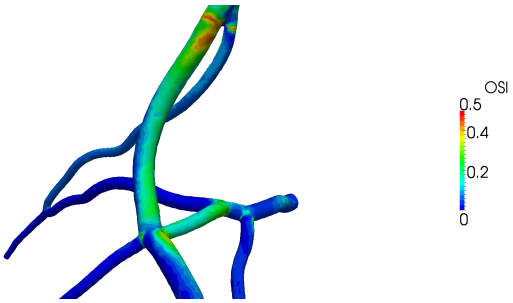

(d) $factor_{Re}^{ave,LITA} = 1.333$, $factor_{Re}^{ampl,LITA} = 1$
$factor_{Re}^{ave,LCA} = 0.666$, $factor_{Re}^{ampl,LCA} = 1$

Figure 6.7: ***Patient 7 - Y-graft between LITA and SVG, LITA to LAD (flow-direction, termino-lateral), SVG to Diag (cross, latero-lateral).*** *Comparison of oscillatory shear index for different inflow boundary conditions.*

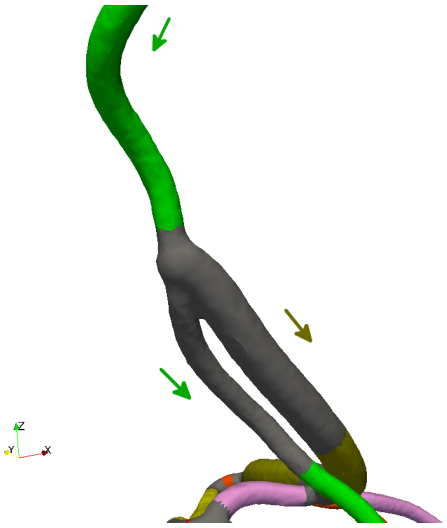

(a) *Bypass grafts near the studied anastomosis. Colored arrows denote blood flow direction.*

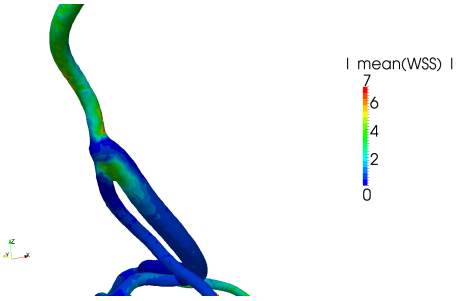

(b) $factor_{Re}^{ave,LITA} = 1$, $factor_{Re}^{ampl,LITA} = 1$
$factor_{Re}^{ave,LCA} = 1$, $factor_{Re}^{ampl,LCA} = 1$

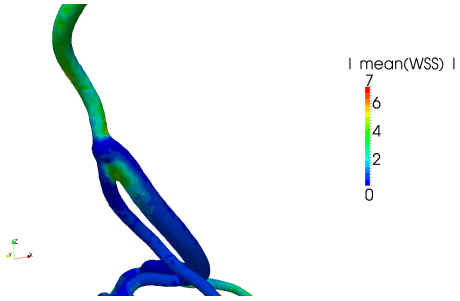

(c) $factor_{Re}^{ave,LITA} = 1$, $factor_{Re}^{ampl,LITA} = 0.1$
$factor_{Re}^{ave,LCA} = 1$, $factor_{Re}^{ampl,LCA} = 0.1$

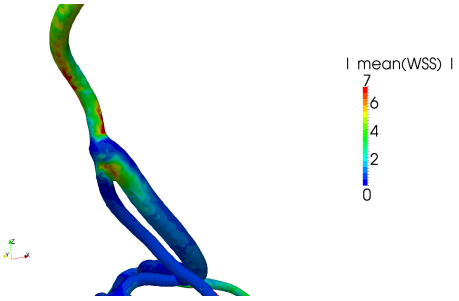

(d) $factor_{Re}^{ave,LITA} = 1.33$, $factor_{Re}^{ampl,LITA} = 1$
$factor_{Re}^{ave,LCA} = 0.66$, $factor_{Re}^{ampl,LCA} = 1$

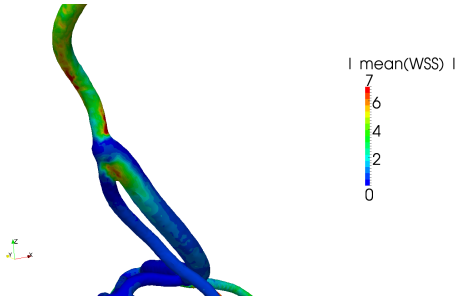

(e) $factor_{Re}^{ave,LITA} = 1.33$, $factor_{Re}^{ampl,LITA} = 0.5$
$factor_{Re}^{ave,LCA} = 0.66$, $factor_{Re}^{ampl,LCA} = 0.5$

Figure 6.8: ***Patient 7 - Y-graft between LITA and SVG****. Comparison of time-averaged wall shear stress [Pa] for different inflow boundary conditions.*

Patient 9

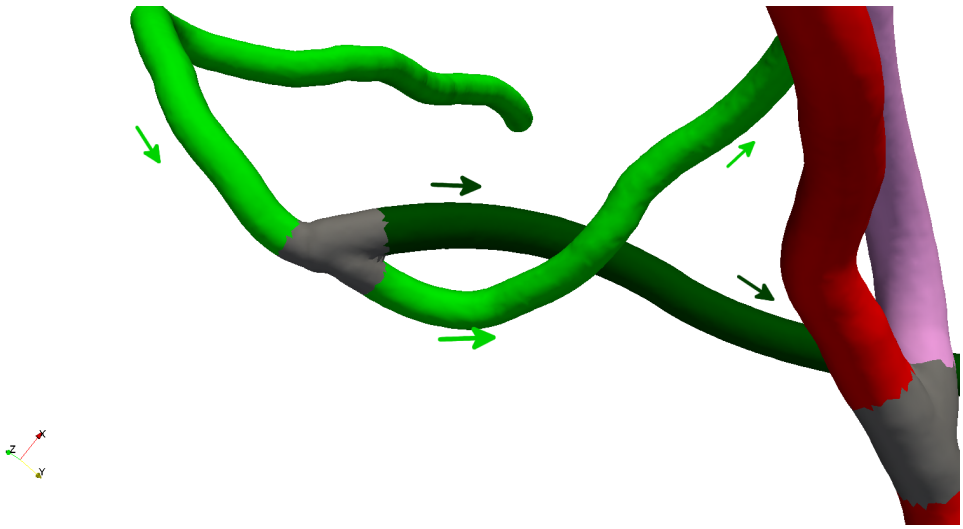

(a) *Bypass grafts near the studied anastomosis. Colored arrows denote blood flow direction.*

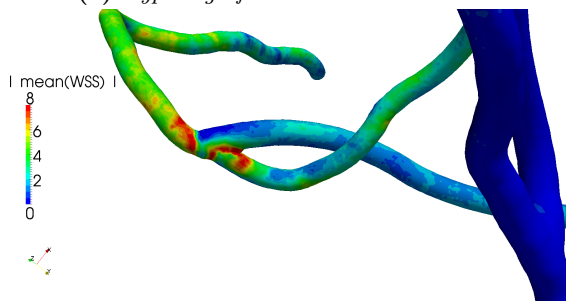

(b) $factor_{Re}^{ave,LITA} = 1$, $factor_{Re}^{ampl,LITA} = 1$
$factor_{Re}^{ave,LCA} = 1$, $factor_{Re}^{ampl,LCA} = 1$

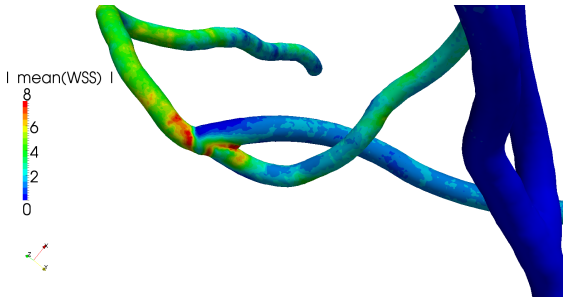

(c) $factor_{Re}^{ave,LITA} = 1$, $factor_{Re}^{ampl,LITA} = 0.1$
$factor_{Re}^{ave,LCA} = 1$, $factor_{Re}^{ampl,LCA} = 0.1$

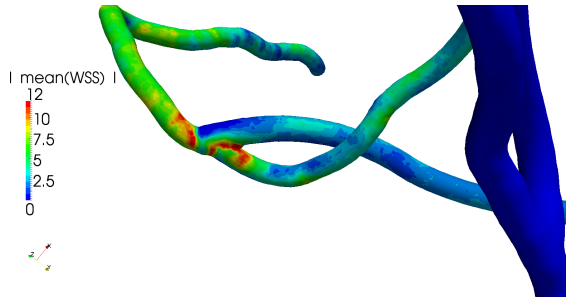

(d) $factor_{Re}^{ave,LITA} = 1.33$, $factor_{Re}^{ampl,LITA} = 1$
$factor_{Re}^{ave,LCA} = 0.66$, $factor_{Re}^{ampl,LCA} = 1$

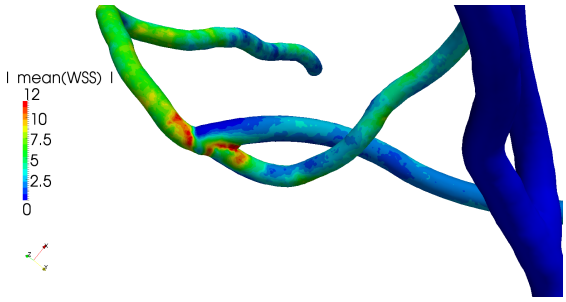

(e) $factor_{Re}^{ave,LITA} = 1.33$, $factor_{Re}^{ampl,LITA} = 0.5$
$factor_{Re}^{ave,LCA} = 0.66$, $factor_{Re}^{ampl,LCA} = 0.5$

Figure 6.9: ***Patient 9 - Y-graft between LITA and Radial artery****. Comparison of time-averaged wall shear stress [Pa] for different inflow boundary conditions.*

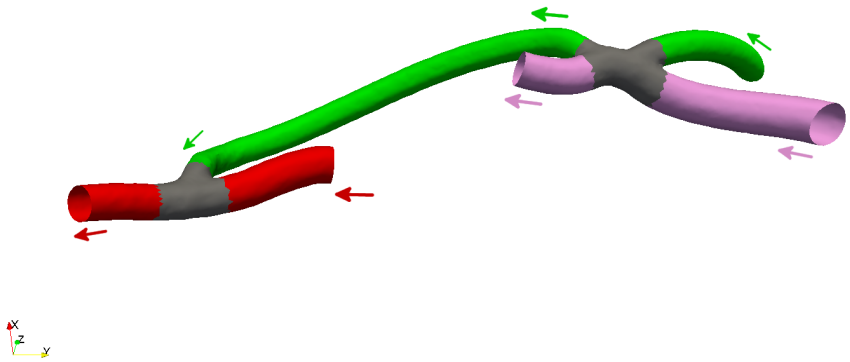

(a) *Coronary arteries and bypass grafts near the studied anastomosis. Colored arrows denote blood flow direction.*

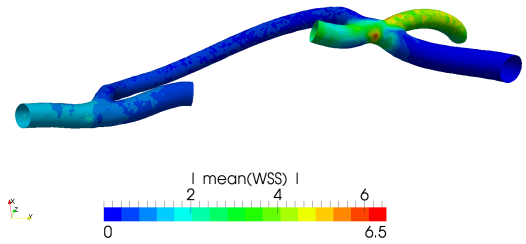

(b) $factor_{Re}^{ave,LITA} = 1$, $factor_{Re}^{ampl,LITA} = 1$
$factor_{Re}^{ave,LCA} = 1$, $factor_{Re}^{ampl,LCA} = 1$

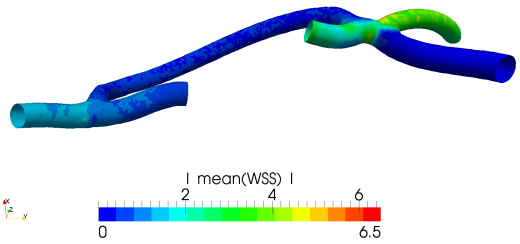

(c) $factor_{Re}^{ave,LITA} = 1$, $factor_{Re}^{ampl,LITA} = 0.1$
$factor_{Re}^{ave,LCA} = 1$, $factor_{Re}^{ampl,LCA} = 0.1$

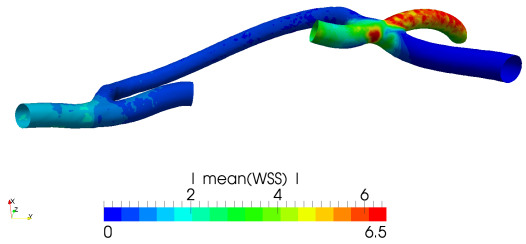

(d) $factor_{Re}^{ave,LITA} = 1.33$, $factor_{Re}^{ampl,LITA} = 1$
$factor_{Re}^{ave,LCA} = 0.66$, $factor_{Re}^{ampl,LCA} = 1$

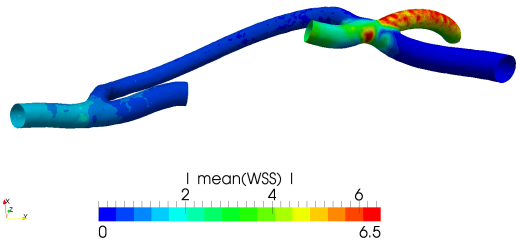

(e) $factor_{Re}^{ave,LITA} = 1.33$, $factor_{Re}^{ampl,LITA} = 0.5$
$factor_{Re}^{ave,LCA} = 0.66$, $factor_{Re}^{ampl,LCA} = 0.5$

Figure 6.10: ***Patient 9 - LITA to Diag anastomosis (flow-direction, latero-lateral) and LITA to LAD anastomosis (flow-direction, termino-lateral).*** *Comparison of time-averaged wall shear stress [Pa] for different inflow boundary conditions.*

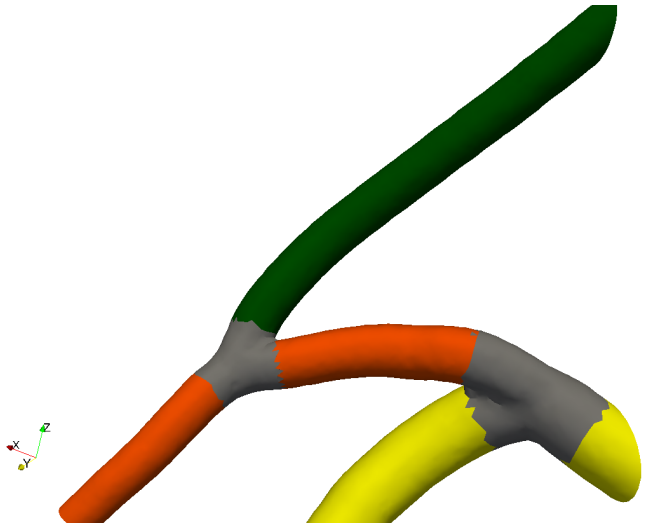

(a) *Coronary arteries and bypass grafts near the studied anastomosis. Colored arrows denote blood flow direction.*

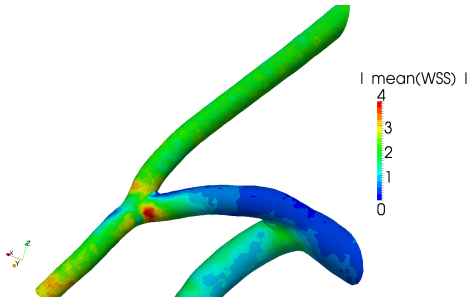

(b) $factor_{Re}^{ave,LITA} = 1$, $factor_{Re}^{ampl,LITA} = 1$
$factor_{Re}^{ave,LCA} = 1$, $factor_{Re}^{ampl,LCA} = 1$

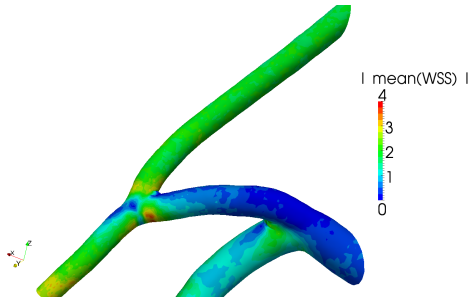

(c) $factor_{Re}^{ave,LITA} = 1$, $factor_{Re}^{ampl,LITA} = 0.1$
$factor_{Re}^{ave,LCA} = 1$, $factor_{Re}^{ampl,LCA} = 0.1$

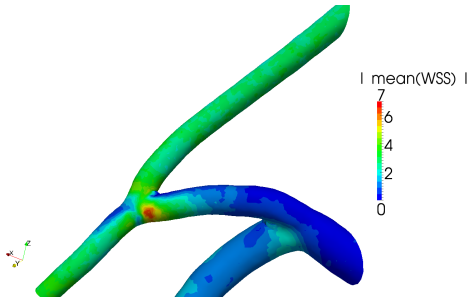

(d) $factor_{Re}^{ave,LITA} = 1.33$, $factor_{Re}^{ampl,LITA} = 1$
$factor_{Re}^{ave,LCA} = 0.66$, $factor_{Re}^{ampl,LCA} = 1$

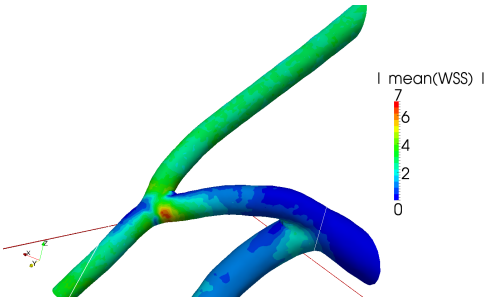

(e) $factor_{Re}^{ave,LITA} = 1.33$, $factor_{Re}^{ampl,LITA} = 0.5$
$factor_{Re}^{ave,LCA} = 0.66$, $factor_{Re}^{ampl,LCA} = 0.5$

Figure 6.11: ***Patient 9 - Radial to OM anastomosis (flow-direction, termino-lateral).*** *Comparison of time-averaged wall shear stress [Pa] for different inflow boundary conditions.*

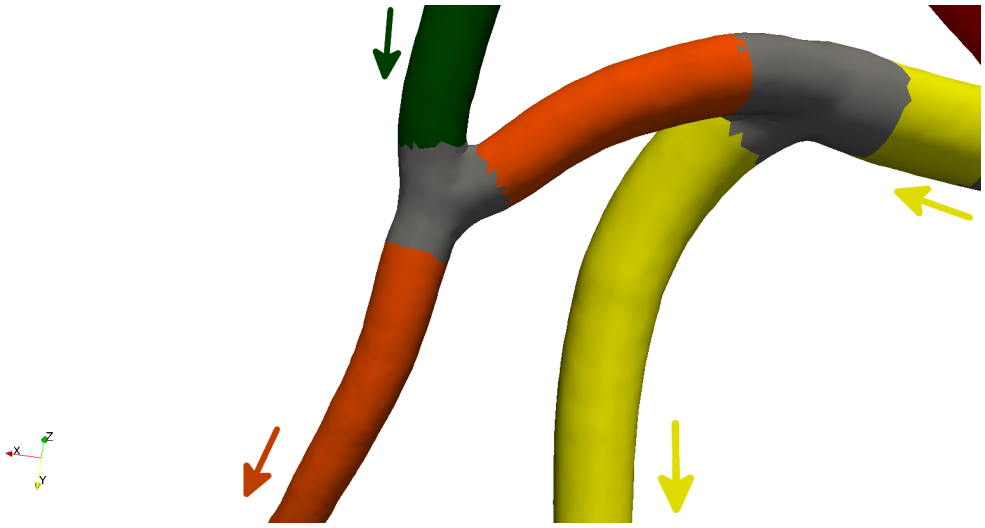

(a) *Coronary arteries and bypass grafts near the studied anastomosis. Colored arrows denote blood flow direction.*

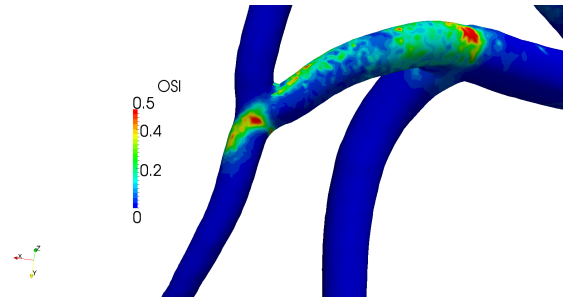

(b) $factor_{Re}^{ave,LITA} = 1$, $factor_{Re}^{ampl,LITA} = 1$
$factor_{Re}^{ave,LCA} = 1$, $factor_{Re}^{ampl,LCA} = 1$

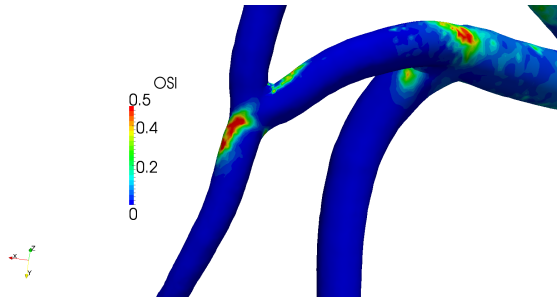

(c) $factor_{Re}^{ave,LITA} = 1.33$, $factor_{Re}^{ampl,LITA} = 1$
$factor_{Re}^{ave,LCA} = 0.66$, $factor_{Re}^{ampl,LCA} = 1$

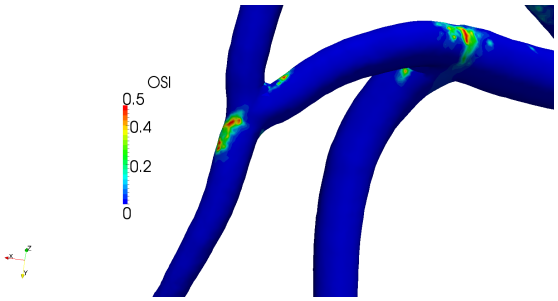

(d) $factor_{Re}^{ave,LITA} = 1.33$, $factor_{Re}^{ampl,LITA} = 0.5$
$factor_{Re}^{ave,LCA} = 0.66$, $factor_{Re}^{ampl,LCA} = 0.5$

Figure 6.12: ***Patient 9 - LCX-OM bifurcation, Radial to OM anastomosis (flow-direction, termino-lateral).*** *Comparison of oscillatory shear index for different inflow boundary conditions.*

6.3.3 Discussion

Patient 1.

- *Y-graft between LITA and Radial.* Figure 6.3 shows a comparison of time-averaged wall shear stress near the Y-graft for different inflow boundary conditions. *(i)* A region of high wall shear stress is found near the Y-graft, for both LITA and Radial artery. *(ii)* This region is highly sensitive to the graft flow ($\text{factor}_{Re}^{ave,LITA}$), and features a larger area for increasing graft flow.

- *LITA to LAD anastomosis (flow-direction, termino-lateral).* Figure 6.4 shows a comparison of time-averaged wall shear stress near the LITA to LAD flow-direction anastomosis for different inflow boundary conditions. *(i)* A region of high wall shear stress is found in the graft near the anastomosis, and in the LAD distal to the anastomosis. *(ii)* An increased $\text{factor}_{Re}^{ave,LITA}$ to $\text{factor}_{Re}^{ave,LCA}$ ratio causes an increase of maximum WSS value (compare figures (d) and (e) to (b) and (c)). *(iii)* Moreover, a larger region of intermediate wall shear stress is present on the distal arterial bed. *(iv)* The size of this region decreases with amplitude factors, especially for $\text{factor}_{Re}^{ave,LITA} = 1$ (compare figure (b) to figure (c)).

- *Radial to OM and LCX anastomosis (cross, latero-lateral).* Figure 6.5 shows a comparison of time-averaged wall shear stress near the Radial-OM-LCX cross anastomosis, for different inflow boundary conditions. *(i)* A region of high wall shear stress is found in the arterial beds of both OM and LCX distal to the anastomosis. *(ii)* However, in contrast to the pattern most noticeable in the Y-graft, an increased $\text{factor}_{Re}^{ave,LITA}$ to $\text{factor}_{Re}^{ave,LCA}$ ratio causes only a modest increment in the maximum WSS value. Also, WSS patterns are not sensible in this case to amplitude factors. *(iii)* Nevertheless, in all four parametrized cases the maximum WSS near the OM (first cross anastomosis from the top) is slightly larger than the one near the LCX (second cross anastomosis from the top).

- *Radial to PDA anastomosis (T-shaped, termino-lateral).* Figure 6.6 shows a comparison of time-averaged wall shear stress for different inflow boundary conditions. *(i)* The magnitude of WSS is higher in the PDA arterial bed distal to the anastomosis than in the proximal PDA and in the graft. Similar magnitude is also observed near the toe of the graft. *(ii)* In this case the most important amplitude factor is the one related to the RCA coronary artery itself rather than the LITA graft. In fact, a decrease of RCA inlet flow rates affects the resulting WSS in the distal PDA, which also decreases, while variation of inlet flow rate of LITA does not seem to affect this anastomosis. The latter is due to the fact that other two coronary arteries have been already bypassed with the radial artery (which was anastomized with a Y-graft to the LITA), so that the increased blood flow to the LITA has been already redistributed to other native coronary arteries. *(iii)* Moreover the WSS at the anastomosis is lower than the one observed on the Radial-OM-LCX cross anastomosis. This is in agreement with the previous discussion (Radial to OM and LCX cross latero-lateral anastomosis), and shows that in sequential grafts distal anastomoses feature lower time-averaged WSS than proximal anastomoses.

Patient 7.

- *Y-graft between LITA and SVG, LITA to LAD (flow-direction, termino-lateral), SVG to Diag (cross, latero-lateral).* Figure 6.7 features a comparison of oscillatory shear index for different inflow boundary conditions. *(i)* The Y-graft between the mammary artery

and the saphenous vein grafts features high OSI. *(ii)* An increased flow rate in the graft causes flow reversal in the diagonal branch. *(iii)* Moreover, an increased maximum to average flow ratio causes flow reversal in the diagonal branch and higher OSI in the saphenous vein graft.

- *Y-graft between LITA and SVG.* Figure 6.8 shows a comparison of time-averaged wall shear stress for different inflow boundary conditions. *(i)* A region of high wall shear stress is found near the Y-graft, for both LITA and SVG grafts. The region of high WSS is larger in the SVG graft than in the LITA. *(ii)* This region is highly sensitive to the graft flow ($\text{factor}_{Re}^{ave,LITA}$), and features a larger area for increasing graft flow. *(iii)* High WSS appear also in the LITA graft proximal to the Y-graft, especially where the centerline features higher curvature. *(iv)* Average WSS values in the distal LITA are lower than in the proximal LITA, because of the flow subdivision between the LITA and SVG grafts.

Patient 9.

- *Y-graft between LITA and Radial artery.* The time-averaged WSS near the Y-graft is shown in Figure 6.9. *(i)* The comparison of figures (b)-(c) and (d)-(e) reveals that, as in the previous patients, an increased graft flow causes higher maximum values of WSS. *(ii)* Regions of high WSS are located both proximally and distally to the suture line of the Y-graft. *(iii)* A region of high WSS appears also in the distal LITA, but not in the distal Radial artery. *(iv)* Amplitude factors have an influence mostly on the size of the latter region, rather than the one near the suture line (compare figures (b) and (c)).

- *LITA to Diag anastomosis (flow-direction, latero-lateral) and LITA to LAD anastomosis (flow-direction, termino-lateral).* A detailed view of the sequential LITA graft, which features first a latero-lateral flow-direction anastomosis on a diagonal branch and a termino-lateral flow-direction anastomosis on the LAD, is provided in Figure 6.10. *(i)* A region of high WSS is present at the arterial bed of the latero-lateral anastomosis. *(ii)* The magnitude of WSS on the arterial bed at the latero-lateral is sensible both to increased graft flow (compare figures (b) and (d)) and increased amplitude factors (compare figures (c) and (b)). *(iii)* The latero-lateral anastomosis features higher WSS on the arterial bed than the termino-lateral anastomosis.

- *LCX-OM bifurcation, Radial to OM anastomosis (flow-direction, termino-lateral).* Figures 6.11 and 6.12 study the Radial to OM anastomosis. *(i)* Region of maximum OSI are found at the LCX-OM bifurcation and at the radial-OM anastomosis, near the toe. *(ii)* An increased graft flow $\text{factor}_{Re}^{ave,LITA}$ causes an increase of the region of high OSI value for the radial-OM anastomosis. *(iii)* Moreover, a decrease in amplitude factors involves a reduction of the region of high OSI value for both LCX-OM bifurcation and radial-OM anastomosis. *(iv)* Regions of low WSS are found near the toe and the heel of the graft, while the arterial bed features highest WSS. *(v)* An increased graft flow causes higher WSS at the arterial bed (compare figures 6.11(b) and 6.11(d)). *(vi)* Decreased graft amplitude factors contribute in a larger region of low WSS (stagnation) near the toe of the graft and lower WSS at the arterial bed (compare figures 6.11(b) and 6.11(c)).

6.4 Fast haemodynamics simulations for several values of stenoses severity

In this section we apply the POD-Galerkin ROM and the centerlines-based parametrization for a fast evaluation of the haemodynamics in patient-specific CABGs considering different values of stenoses severity, in order to compare critical and non-critical stenoses, and possibly also allowing for a variation of physical parameters (inflow boundary conditions).

6.4.1 Parametrization and reduced-order models details

Patient	**1**	**3**	**4**	**7**	**12**	**13**
Num. physical parameters	6	4	4	4	4	6
LCA inlet flow rate parameters	2	2	2	2	2	2
RCA inlet flow rate parameters	2	no	no	no	no	2
LITA inlet flow rate parameters	2	2	2	2	2	2
Num. geometrical parameters	3	2	2	3	2	4
LCA parametrized stenosis	no	no	no	1	no	no
LAD/Diag parametrized stenosis	1	2	2	1	2	2
LCX/OM parametrized stenosis	1	no	no	1	no	1
RCA parametrized stenosis	1	no	no	no	no	1
FE velocity order	2					
FE pressure order	1					
Total number of FE dofs	1 325 530	813 197	1 325 044	970 618	1 624 370	1 426 060
Temporal step	0.01					
Num. time steps/cardiac cycle	80					
CPU time for one cardiac cycle	$11 \sim 13$ h	$4 \sim 7$ h	$11 \sim 13$ h	$9 \sim 12$ h	$12 \sim 15$ h	$9 \sim 11$ h
$N_{\mathbf{train}}$	50					
$N_{\mathbf{max}}$	50					
$M_{\mathbf{2\text{–}POD}}$	20					
Affine exp. comp. for m, a, $b \& c$	14, 36, 37	28, 53, 40	15, 39, 38	19, 42, 40	38, 57, 43	19, 48, 33

Table 6.2: *Details of the reduced-order model.*

Details of the reduced-order model are summarized in Table 6.2. The number of considered physical and geometrical parameters is reported for each patient; physical parameters are related to the variation of inlet flow rates of left coronary artery, right coronary artery (if present) and bypass grafts. The entities of several stenoses are considered as geometrical parameters. The location of the stenoses is also summarized.

As in the previous section, a Taylor-Hood $\mathbb{P}_2 - \mathbb{P}_1$ FE discretization is employed for the space discretization; an Implicit Euler method is considered for the time discretization. N_{train} time-dependent FE problems are solved for random values of the parameters, and $M_{\text{2–POD}}$ POD modes are retained in the two-level POD.

The offline stage is performed in parallel, for $24 \sim 32$ processors. The truth solution for each sample point (and for each cardiac cycle) requires approximately 10 hours (to be multiplied by the number of processors to obtain the actual CPU time). The online stage, instead, is performed on a single processor. When compared to the previous case (physical parametrization only), slightly higher CPU times are required; this is motivated by the fact that additional computations are required in the evaluation of the centerlines-based parametrization. Thanks to the considerable reduction in the number of degrees of freedom ($N_{\mathbf{u}} = N_{\mathbf{s}} = N_p = N_{\max}$) and efficient offline-online procedure, each online ROM solution requires from 5 to 15 minutes. Online CPU times are higher than the case with no geometrical

parameters because of larger affine expansions, but computational savings are still consistent (more than 95%).

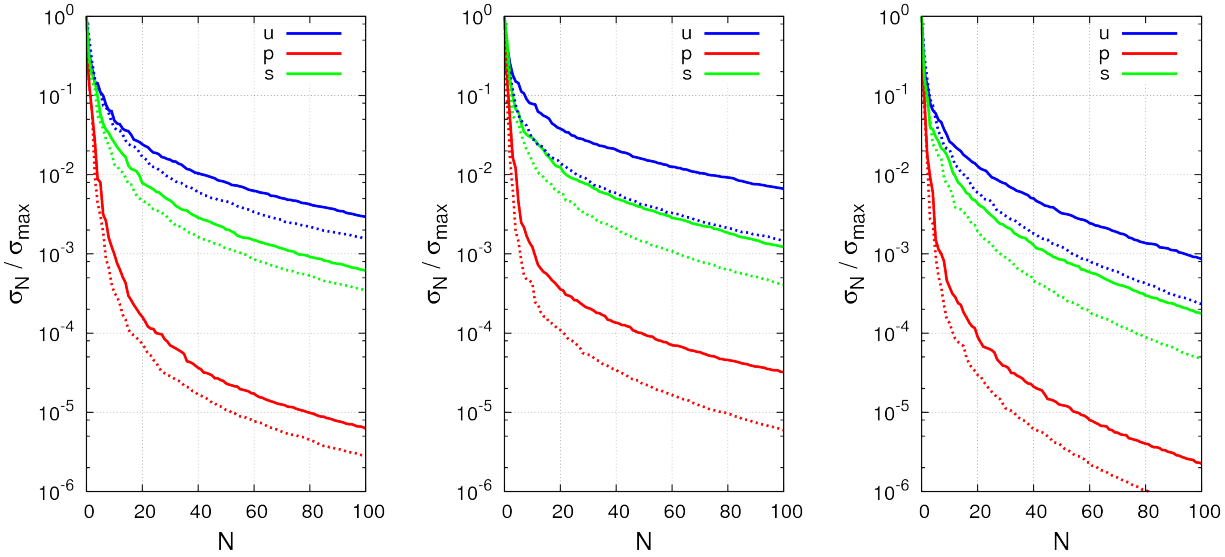

(a) ***Patient 1:*** *POD singular values for velocity, supremizers, pressure (solid lines).*

(b) ***Patient 4:*** *POD singular values for velocity, supremizers, pressure (solid lines).*

(c) ***Patient 12:*** *POD singular values for velocity, supremizers, pressure (solid lines).*

Figure 6.13: *Results of the offline stage: POD singular values for velocity, supremizers, pressure. Solid lines: physical parametrization and stenosis variation; dotted lines: physical parametrization only.*

Figure 6.13 shows a plot of the POD singular values for velocity, supremizers, pressure. The pattern is similar for the three studied patients; in all cases velocity (and supremizers) feature a considerably slower decay than pressure. A comparison, on the same patient, between the case of physical parametrization only (dotted lines) and physical parametrization and stenosis variation (solid lines) is also shown. Slower decay is the result of additional geometrical parameters.

6.4.2 Numerical results

Patient 4

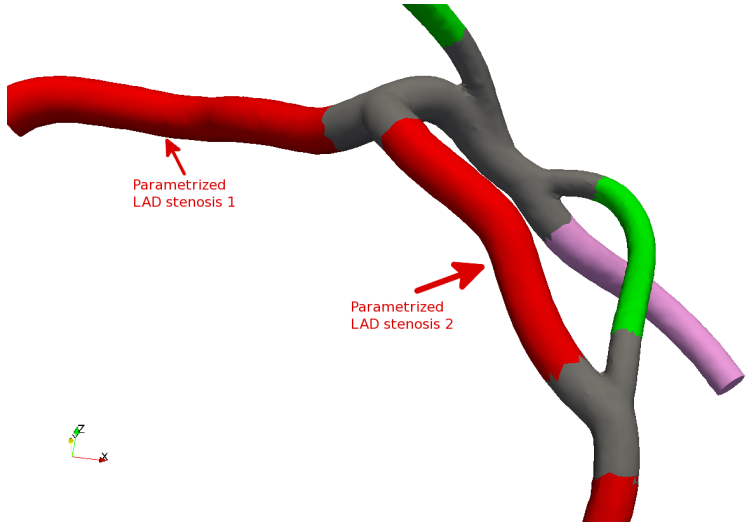

Figure 6.14: ***Patient 4 - location of parametrized stenoses***. *Two LAD stenoses have been considered. Their area reduction can be varied, and is denoted by* $\alpha_{LAD,1}$ *and* $\alpha_{LAD,2}$.

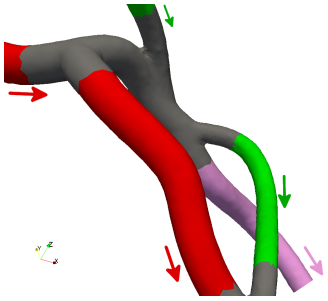

(a) *Coronary arteries and bypass grafts near the studied anastomosis. Colored arrows denote blood flow direction.*

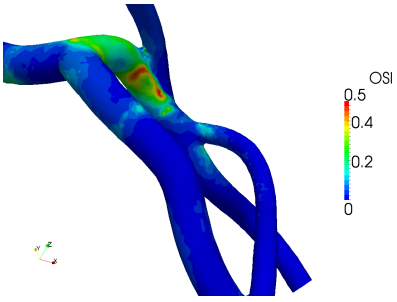

(b) $factor_{Re}^{ave,LITA} = 0.66$, $factor_{Re}^{ampl,LITA} = 1$
$factor_{Re}^{ave,LCA} = 0.66$, $factor_{Re}^{ampl,LCA} = 1$
$\alpha_{LAD,1} = 0\%$, $\alpha_{LAD,2} = 0\%$

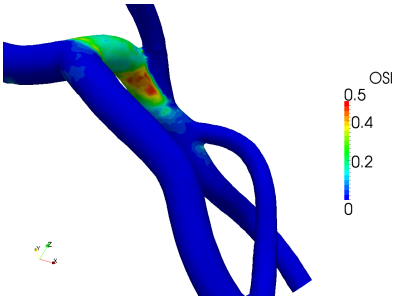

(c) $factor_{Re}^{ave,LITA} = 0.66$, $factor_{Re}^{ampl,LITA} = 0.5$
$factor_{Re}^{ave,LCA} = 0.66$, $factor_{Re}^{ampl,LCA} = 0.5$
$\alpha_{LAD,1} = 0\%$, $\alpha_{LAD,2} = 0\%$

Figure 6.15: ***Patient 4 - LITA to Diag anastomosis (flow-direction, latero-lateral), second LAD stenosis***. *Comparison of the oscillatory shear index for different inflow boundary conditions and stenosis.* (continued on next page).

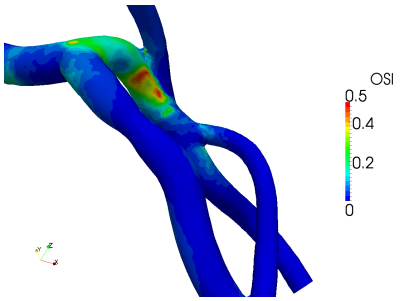

(d) $factor_{Re}^{ave,LITA} = 0.66$, $factor_{Re}^{ampl,LITA} = 1$
$factor_{Re}^{ave,LCA} = 0.66$, $factor_{Re}^{ampl,LCA} = 1$
$\alpha_{LAD,1} = 50\%$, $\alpha_{LAD,2} = 50\%$

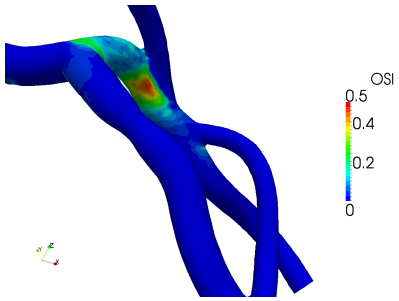

(e) $factor_{Re}^{ave,LITA} = 0.66$, $factor_{Re}^{ampl,LITA} = 0.5$
$factor_{Re}^{ave,LCA} = 0.66$, $factor_{Re}^{ampl,LCA} = 0.5$
$\alpha_{LAD,1} = 50\%$, $\alpha_{LAD,2} = 50\%$

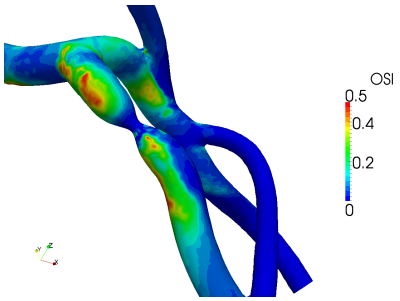

(f) $factor_{Re}^{ave,LITA} = 0.66$, $factor_{Re}^{ampl,LITA} = 1$
$factor_{Re}^{ave,LCA} = 0.66$, $factor_{Re}^{ampl,LCA} = 1$
$\alpha_{LAD,1} = 90\%$, $\alpha_{LAD,2} = 90\%$

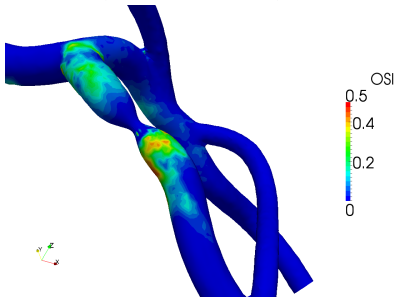

(g) $factor_{Re}^{ave,LITA} = 0.66$, $factor_{Re}^{ampl,LITA} = 0.5$
$factor_{Re}^{ave,LCA} = 0.66$, $factor_{Re}^{ampl,LCA} = 0.5$
$\alpha_{LAD,1} = 90\%$, $\alpha_{LAD,2} = 90\%$

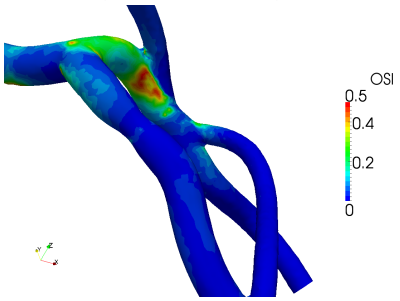

(h) $factor_{Re}^{ave,LITA} = 0.66$, $factor_{Re}^{ampl,LITA} = 1$
$factor_{Re}^{ave,LCA} = 0.66$, $factor_{Re}^{ampl,LCA} = 1$
$\alpha_{LAD,1} = 90\%$, $\alpha_{LAD,2} = 50\%$

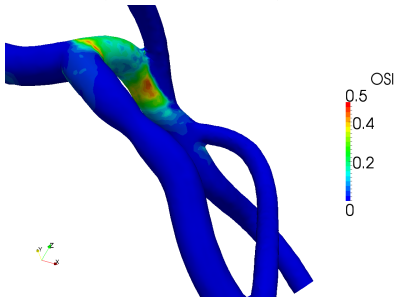

(i) $factor_{Re}^{ave,LITA} = 0.66$, $factor_{Re}^{ampl,LITA} = 0.5$
$factor_{Re}^{ave,LCA} = 0.66$, $factor_{Re}^{ampl,LCA} = 0.5$
$\alpha_{LAD,1} = 90\%$, $\alpha_{LAD,2} = 50\%$

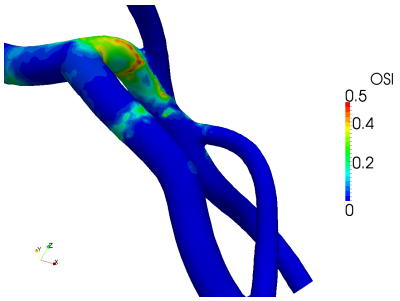

(j) $factor_{Re}^{ave,LITA} = 1.33$, $factor_{Re}^{ampl,LITA} = 1$
$factor_{Re}^{ave,LCA} = 0.66$, $factor_{Re}^{ampl,LCA} = 1$
$\alpha_{LAD,1} = 0\%$, $\alpha_{LAD,2} = 0\%$

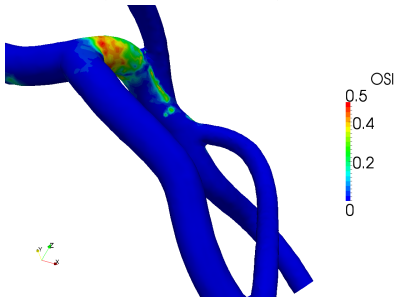

(k) $factor_{Re}^{ave,LITA} = 1.33$, $factor_{Re}^{ampl,LITA} = 0.5$
$factor_{Re}^{ave,LCA} = 0.66$, $factor_{Re}^{ampl,LCA} = 0.5$
$\alpha_{LAD,1} = 0\%$, $\alpha_{LAD,2} = 0\%$

Figure 6.15: ***Patient 4 - LITA to Diag anastomosis (flow-direction, latero-lateral), second LAD stenosis.*** *Comparison of the oscillatory shear index for different inflow boundary conditions and stenosis.* (continued on next page).

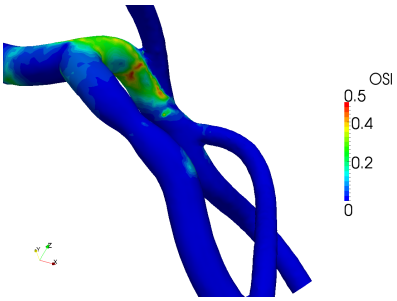

(l) $factor_{Re}^{ave,LITA} = 1.33$, $factor_{Re}^{ampl,LITA} = 1$
$factor_{Re}^{ave,LCA} = 0.66$, $factor_{Re}^{ampl,LCA} = 1$
$\alpha_{LAD,1} = 50\%$, $\alpha_{LAD,2} = 50\%$

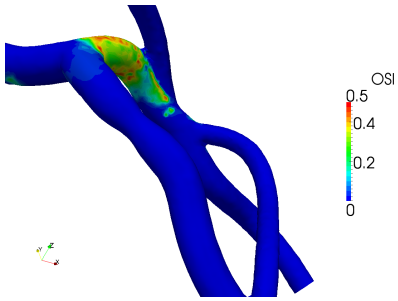

(m) $factor_{Re}^{ave,LITA} = 1.33$, $factor_{Re}^{ampl,LITA} = 0.5$
$factor_{Re}^{ave,LCA} = 0.66$, $factor_{Re}^{ampl,LCA} = 0.5$
$\alpha_{LAD,1} = 50\%$, $\alpha_{LAD,2} = 50\%$

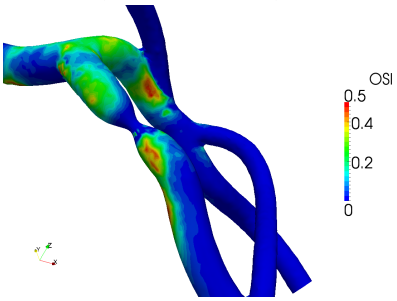

(n) $factor_{Re}^{ave,LITA} = 1.33$, $factor_{Re}^{ampl,LITA} = 1$
$factor_{Re}^{ave,LCA} = 0.66$, $factor_{Re}^{ampl,LCA} = 1$
$\alpha_{LAD,1} = 90\%$, $\alpha_{LAD,2} = 90\%$

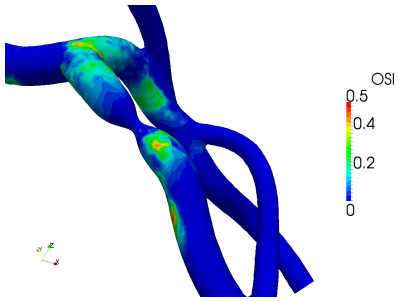

(o) $factor_{Re}^{ave,LITA} = 1.33$, $factor_{Re}^{ampl,LITA} = 0.5$
$factor_{Re}^{ave,LCA} = 0.66$, $factor_{Re}^{ampl,LCA} = 0.5$
$\alpha_{LAD,1} = 90\%$, $\alpha_{LAD,2} = 90\%$

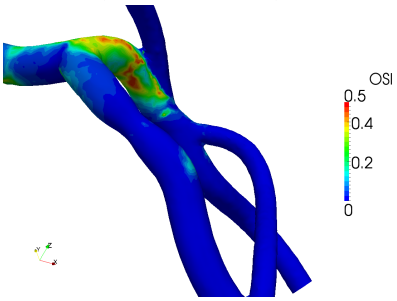

(p) $factor_{Re}^{ave,LITA} = 1.33$, $factor_{Re}^{ampl,LITA} = 1$
$factor_{Re}^{ave,LCA} = 0.66$, $factor_{Re}^{ampl,LCA} = 1$
$\alpha_{LAD,1} = 90\%$, $\alpha_{LAD,2} = 50\%$

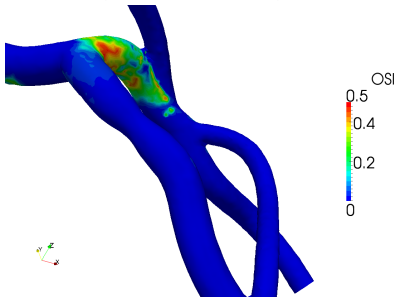

(q) $factor_{Re}^{ave,LITA} = 1.33$, $factor_{Re}^{ampl,LITA} = 0.5$
$factor_{Re}^{ave,LCA} = 0.66$, $factor_{Re}^{ampl,LCA} = 0.5$
$\alpha_{LAD,1} = 90\%$, $\alpha_{LAD,2} = 50\%$

Figure 6.15: ***Patient 4 - LITA to Diag anastomosis (flow-direction, latero-lateral), second LAD stenosis.*** *Comparison of the oscillatory shear index for different inflow boundary conditions and stenosis.*

Patient 7

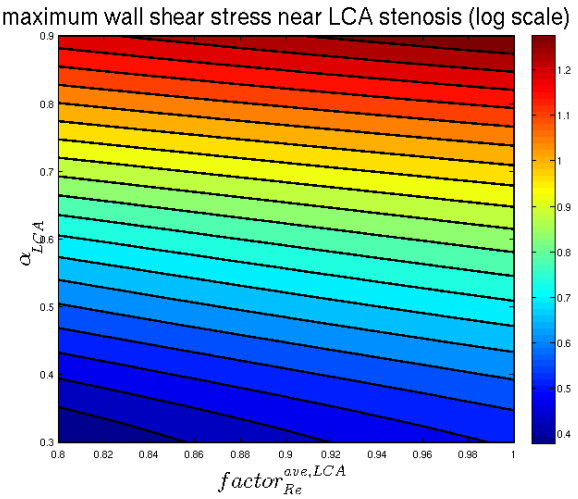

(a) *LCA stenosis*

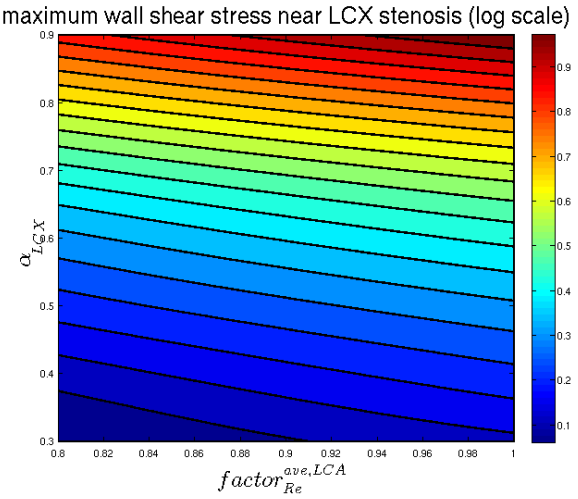

(b) *LCX stenosis*

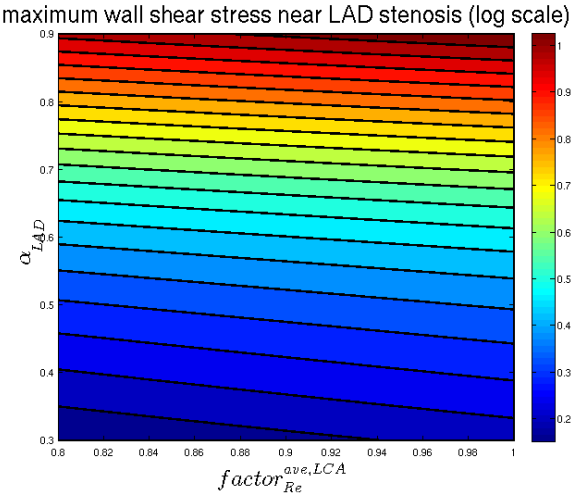

(c) *LAD stenosis*

Figure 6.16: ***Patient 7****. Dependence of the maximum wall shear stress [Pa] near the stenosis on Reynolds number and stenosis factors.*

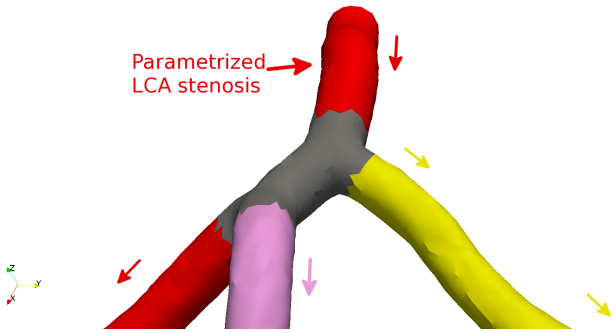

(a) *Coronary arteries near the studied bifurcation. Colored arrows denote blood flow direction.*

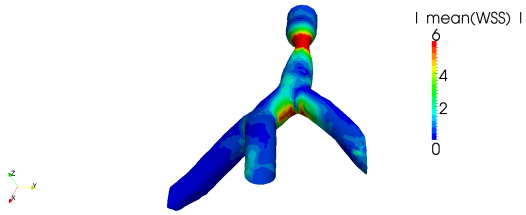

(b) $factor_{Re}^{ave,LCA} = 1,\ \alpha_{LAD} = 80\%$

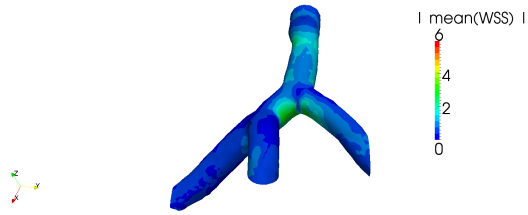

(c) $factor_{Re}^{ave,LCA} = 1,\ \alpha_{LAD} = 30\%$

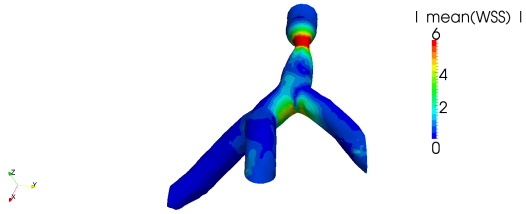

(d) $factor_{Re}^{ave,LCA} = 0.8,\ \alpha_{LAD} = 80\%$

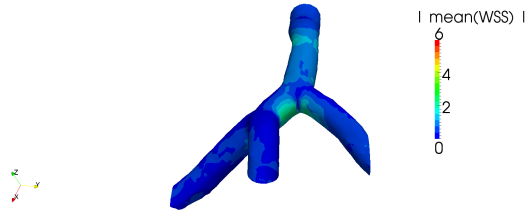

(e) $factor_{Re}^{ave,LCA} = 0.8,\ \alpha_{LAD} = 30\%$

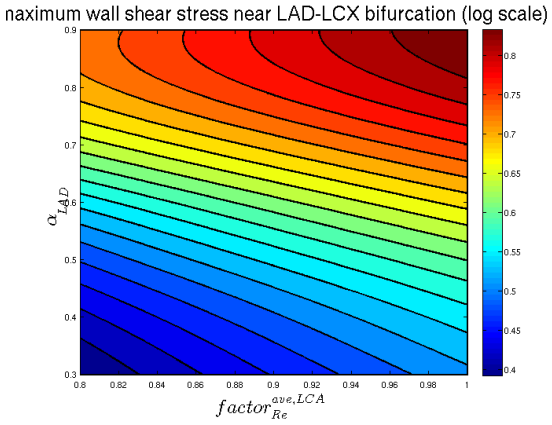

(f) *Summary*

Figure 6.17: ***Patient 7 - LAD-LCX bifurcation.*** *Comparison of time-averaged wall shear stress [Pa] for different inflow boundary conditions and stenosis.*

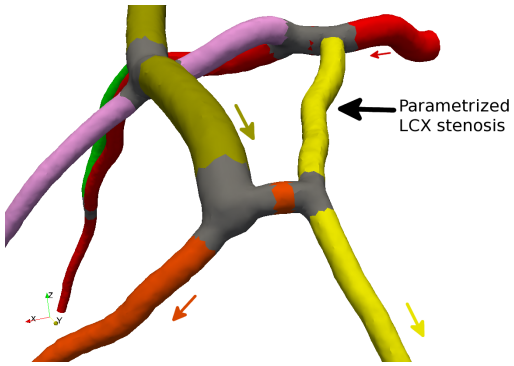

(a) *Coronary arteries and bypass grafts near the studied bifurcation. Colored arrows denote blood flow direction.*

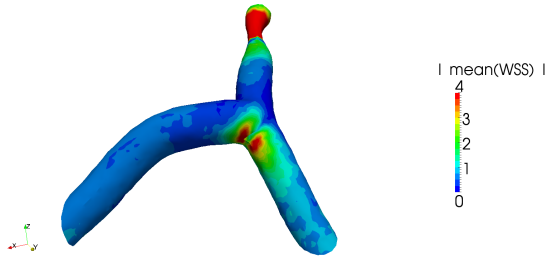

(b) Pre-surgery: $factor_{Re}^{ave,LCA} = 1$, $\alpha_{LAD} = 80\%$

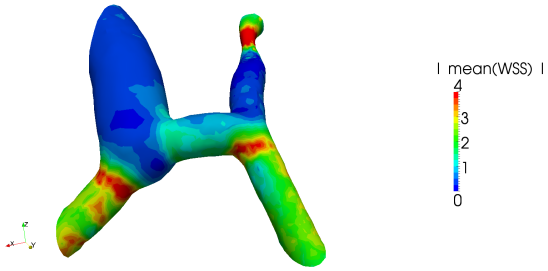

(c) Post-surgery: $factor_{Re}^{ave,LCA} = 1$, $\alpha_{LAD} = 80\%$

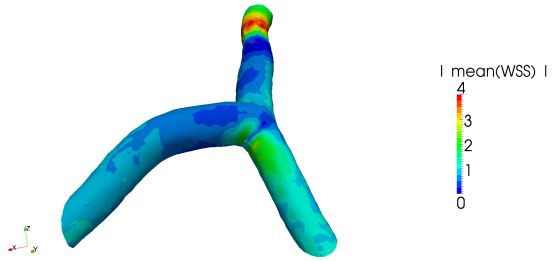

(d) Pre-surgery: $factor_{Re}^{ave,LCA} = 1$, $\alpha_{LAD} = 30\%$

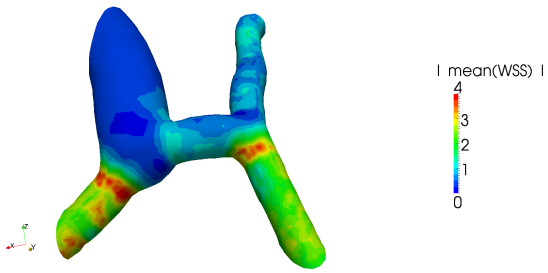

(e) Post-surgery: $factor_{Re}^{ave,LCA} = 1$, $\alpha_{LAD} = 30\%$

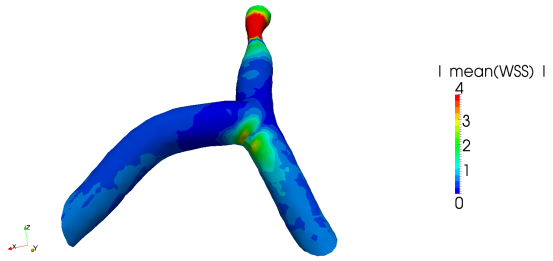

(f) Pre-surgery: $factor_{Re}^{ave,LCA} = 0.8$, $\alpha_{LAD} = 80\%$

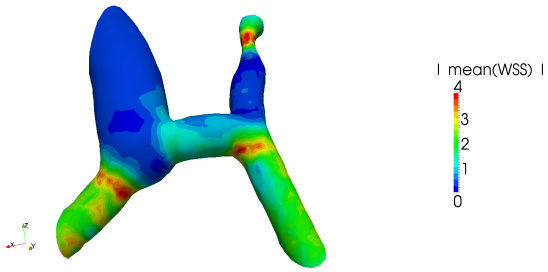

(g) Post-surgery: $factor_{Re}^{ave,LCA} = 0.8$, $\alpha_{LAD} = 80\%$

Figure 6.18: ***Patient 7 - LCX-OM bifurcation.*** *Comparison of time-averaged wall shear stress [Pa], both pre- and post-surgery, for different inflow boundary conditions and stenosis.* (continued on next page)

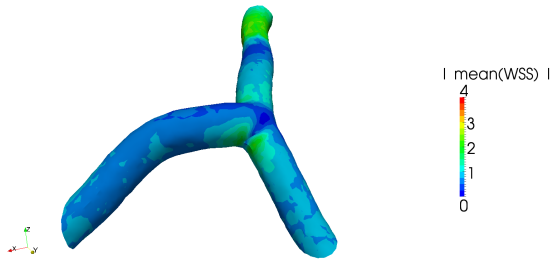

(h) Pre-surgery: $factor_{Re}^{ave,LCA} = 0.8$, $\alpha_{LAD} = 30\%$

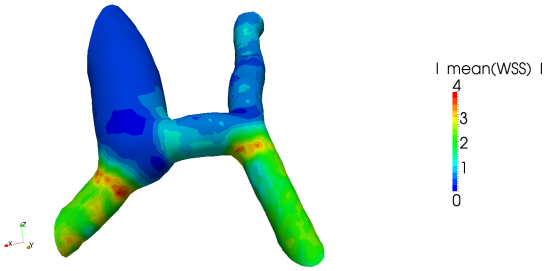

(i) Post-surgery: $factor_{Re}^{ave,LCA} = 0.8$, $\alpha_{LAD} = 30\%$

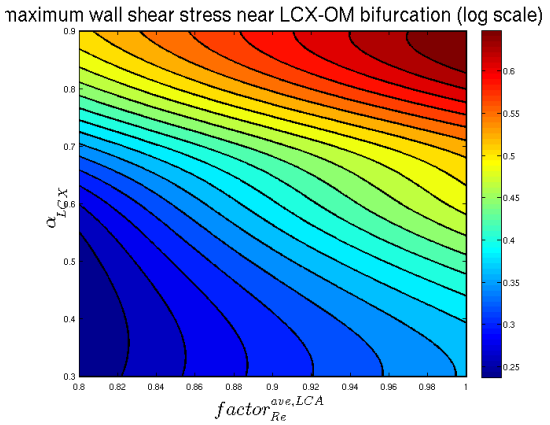

(j) Pre-surgery: *summary*

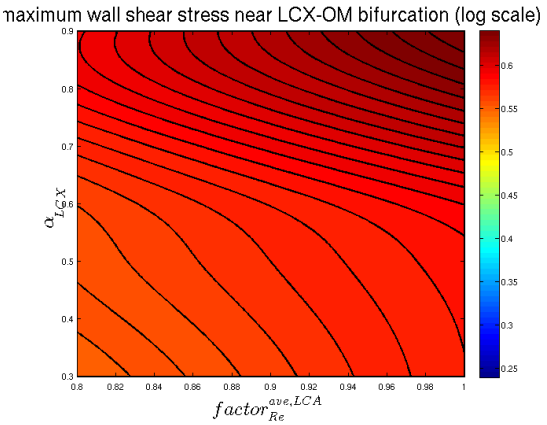

(k) Post-surgery: *summary*

Figure 6.18: ***Patient 7 - LCX-OM bifurcation***. *Comparison of time-averaged wall shear stress [Pa], both pre- and post-surgery, for different inflow boundary conditions and stenosis.*

Patient 3

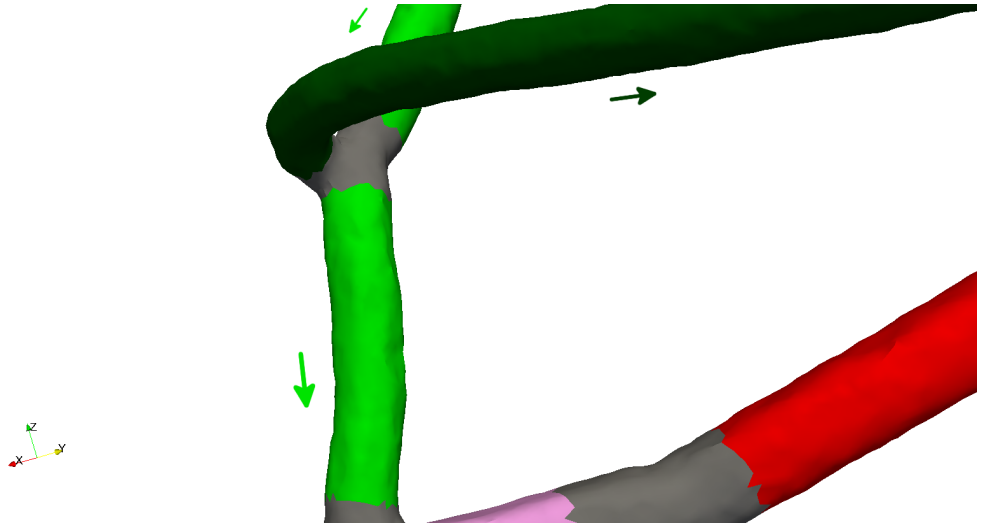

(a) *Bypass grafts near the studied anastomosis. Colored arrows denote blood flow direction.*

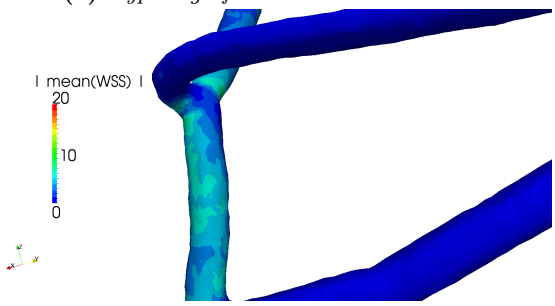

(b) $factor_{Re}^{ave,LITA} = 0.666$

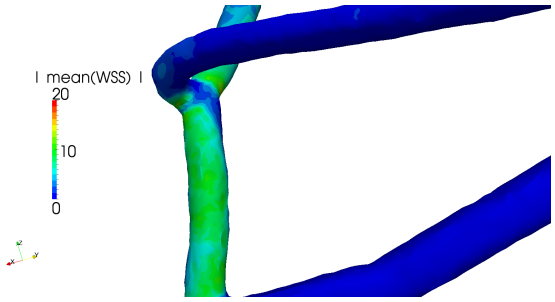

(c) $factor_{Re}^{ave,LITA} = 1$

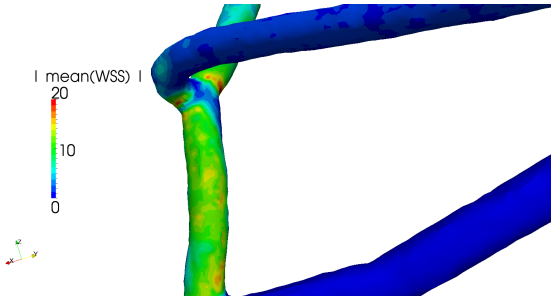

(d) $factor_{Re}^{ave,LCA} = 1.333$

Figure 6.19: ***Patient 3 - Y-graft between LITA and Radial artery.*** *Comparison of time-averaged wall shear stress [Pa] for different inflow boundary conditions.*

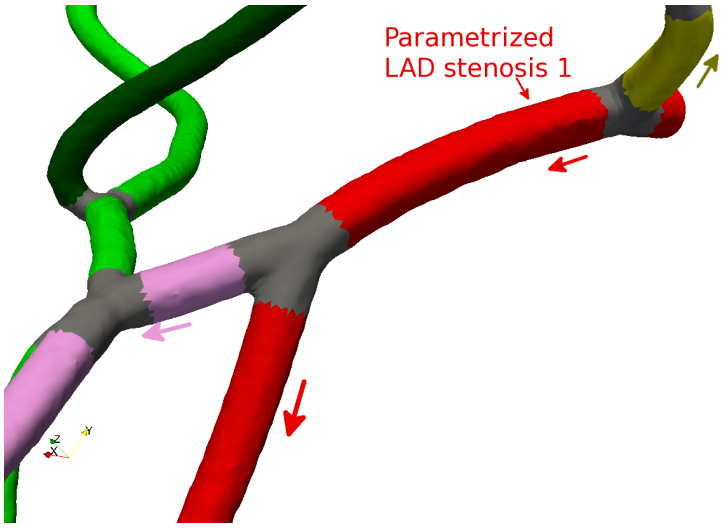

(a) *Coronary arteries near the studied bifurcations. Colored arrows denote blood flow direction.*

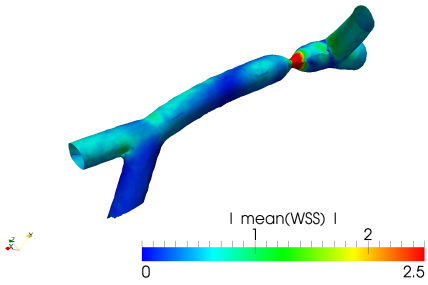

(b) $factor_{Re}^{ave,LCA} = 0.666$, $\alpha_{LAD,1} = 90\%$

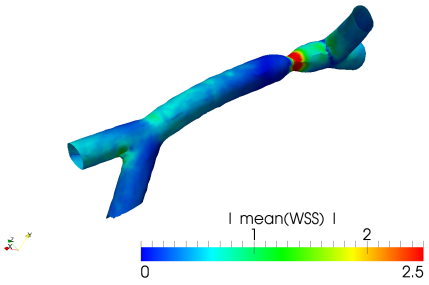

(c) $factor_{Re}^{ave,LCA} = 0.666$, $\alpha_{LAD,1} = 70\%$

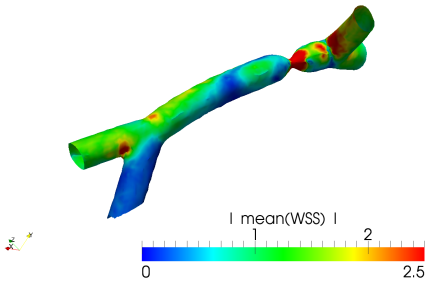

(d) $factor_{Re}^{ave,LCA} = 1.333$, $\alpha_{LAD} = 90\%$

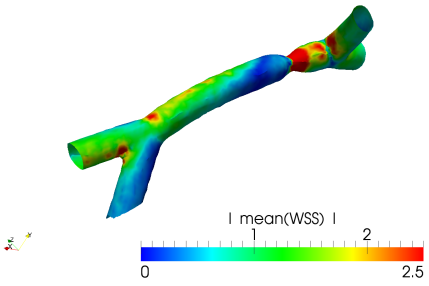

(e) $factor_{Re}^{ave,LCA} = 1.333$, $\alpha_{LAD,1} = 70\%$

Figure 6.20: ***Patient 3 - LAD-LCX and LAD-Diag bifurcations****. Comparison of time-averaged wall shear stress [Pa] for different inflow boundary conditions and stenosis.*

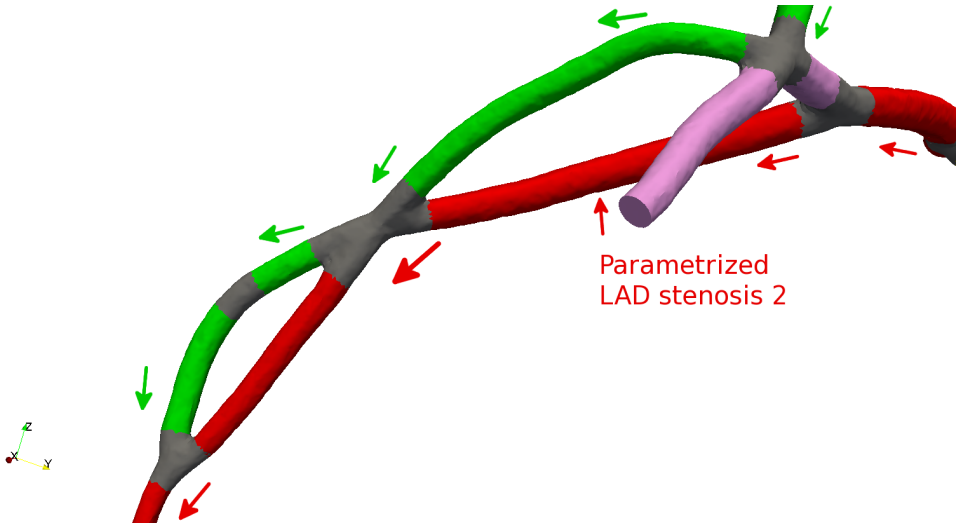

(a) *Coronary arteries and bypass grafts near the studied anastomoses. Colored arrows denote blood flow direction.*

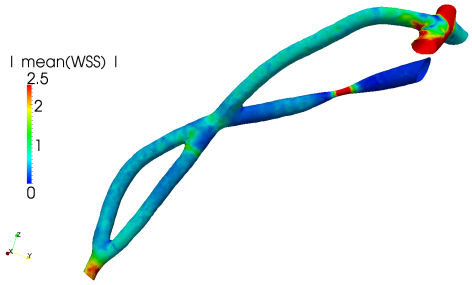

(b) $factor_{Re}^{ave,LCA} = factor_{Re}^{ave,LITA} = 0.666$, $\alpha_{LAD,2} = 90\%$

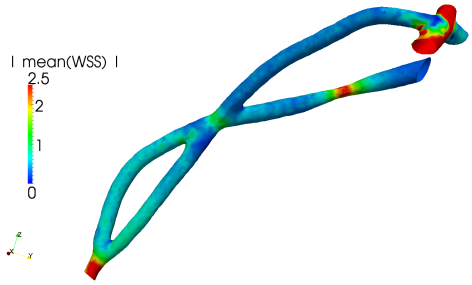

(c) $factor_{Re}^{ave,LCA} = factor_{Re}^{ave,LITA} = 0.666$, $\alpha_{LAD,2} = 70\%$

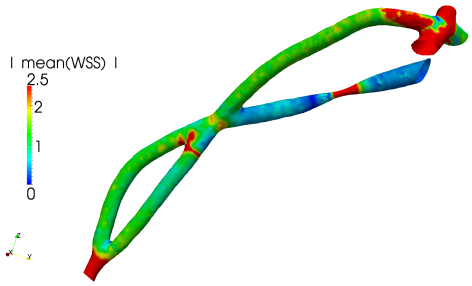

(d) $factor_{Re}^{ave,LCA} = factor_{Re}^{ave,LITA} = 1.333$, $\alpha_{LAD,2} = 90\%$

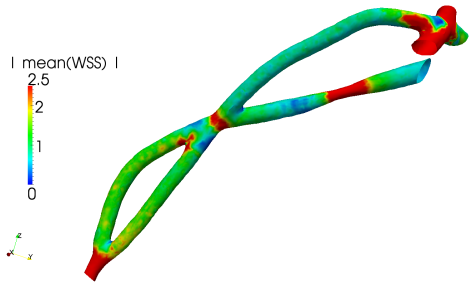

(e) $factor_{Re}^{ave,LCA} = factor_{Re}^{ave,LITA} = 1.333$, $\alpha_{LAD,2} = 70\%$

Figure 6.21: ***Patient 3 - From top-right to bottom-left: LITA-Diag anastomosis (flow-direction, latero-lateral), LITA-LAD anastomosis (flow-direction, latero-lateral), LITA-LAD anastomosis (flow-direction, termino-lateral).*** *Comparison of time-averaged wall shear stress [Pa] for different inflow boundary conditions and stenosis.*

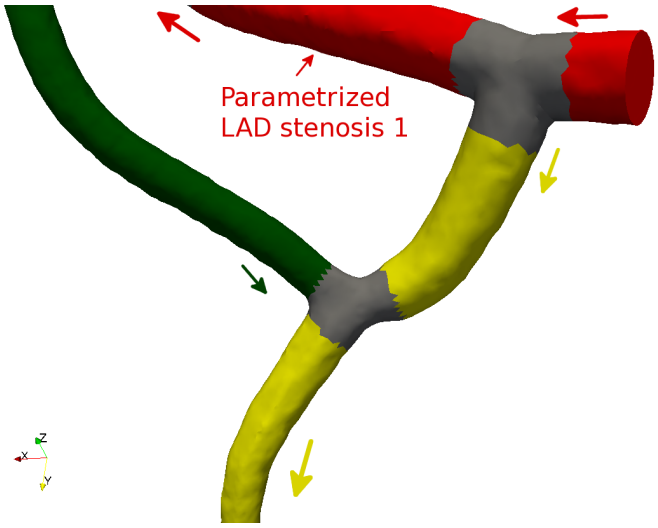

(a) *Coronary arteries and bypass grafts near the studied anastomosis. Colored arrows denote blood flow direction.*

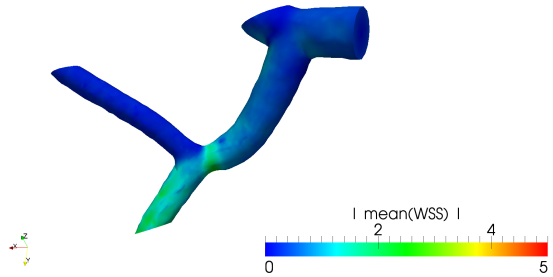

(b) $factor_{Re}^{ave,LITA} = 0.666$, $factor_{Re}^{ave,LCA} = 0.666$, $\alpha_{LAD,1} = 90\%$

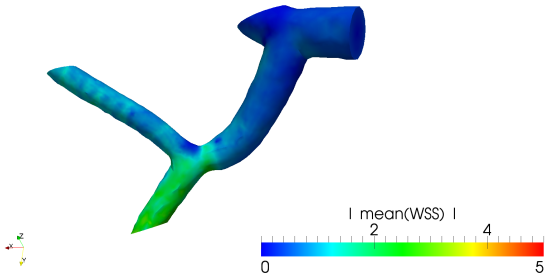

(c) $factor_{Re}^{ave,LITA} = 1.333$, $factor_{Re}^{ave,LCA} = 0.666$, $\alpha_{LAD,1} = 90\%$

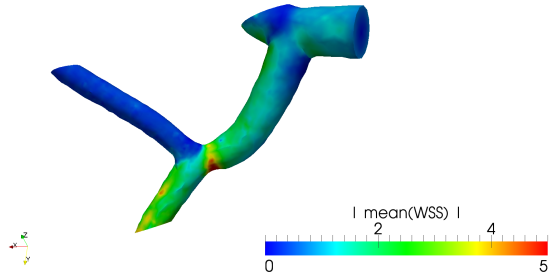

(d) $factor_{Re}^{ave,LITA} = 0.666$, $factor_{Re}^{ave,LCA} = 1.333$, $\alpha_{LAD,1} = 90\%$

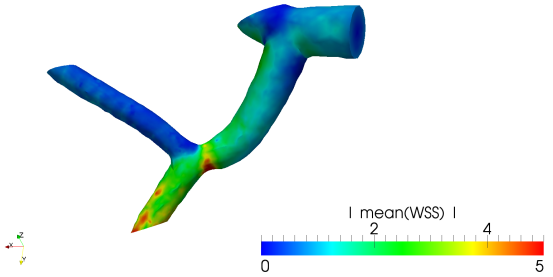

(e) $factor_{Re}^{ave,LITA} = 1.333$, $factor_{Re}^{ave,LCA} = 1.333$, $\alpha_{LAD,1} = 90\%$

Figure 6.22: ***Patient 3 - Radial-LCX anastomosis (flow-direction, termino-lateral).*** *Comparison of time-averaged wall shear stress [Pa] for different inflow boundary conditions and stenosis.*

Patient 1

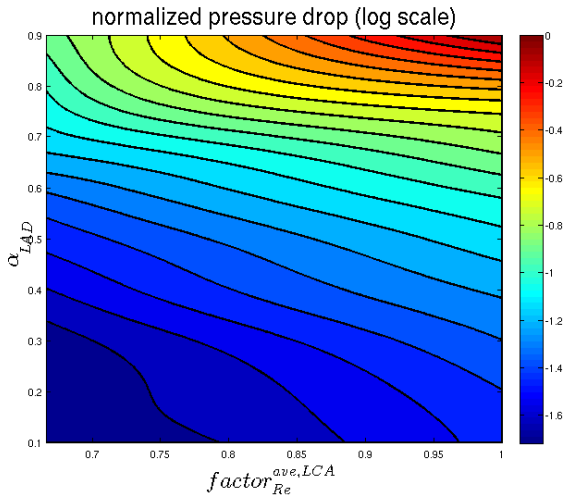

(a) *LAD stenosis*

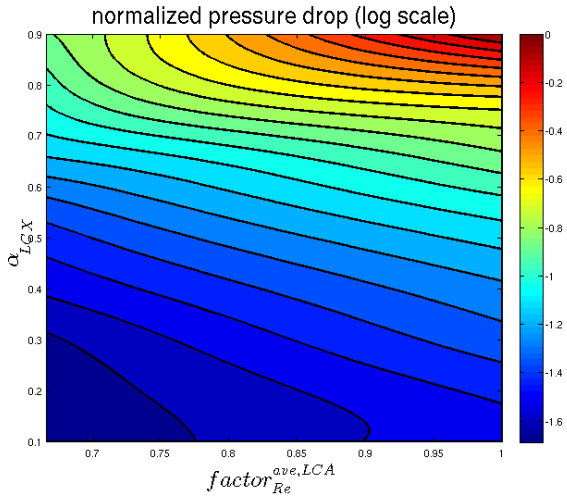

(b) *LCX stenosis*

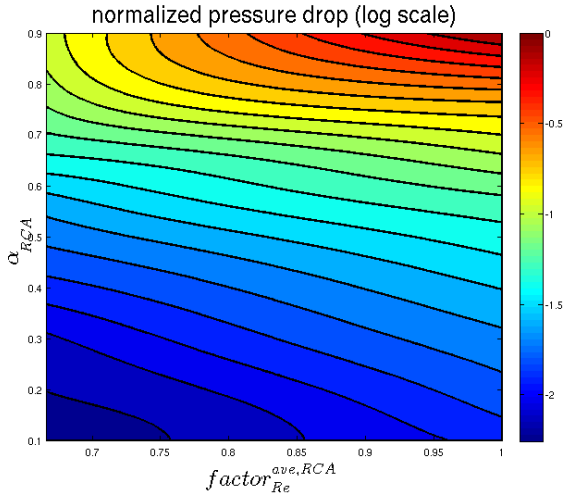

(c) *RCA stenosis*

Figure 6.23: ***Patient 1****. Dependence of the normalized pressure drop at the stenosis on Reynolds number and stenosis factors.*

Patient 12

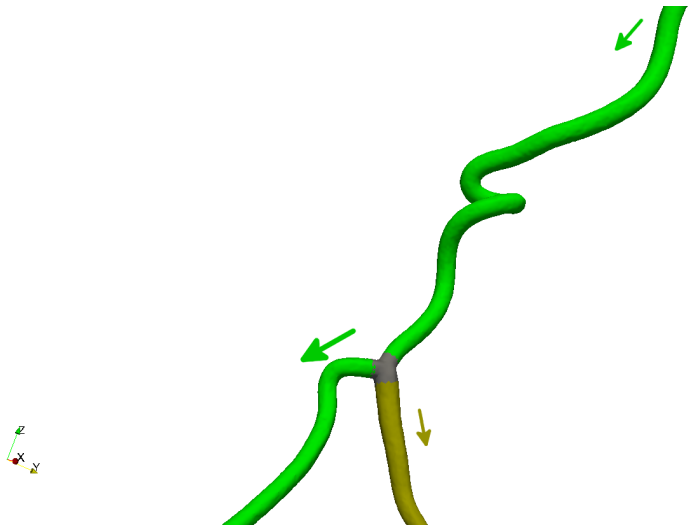

(a) *Bypass grafts near the studied anastomosis. Colored arrows denote blood flow direction.*

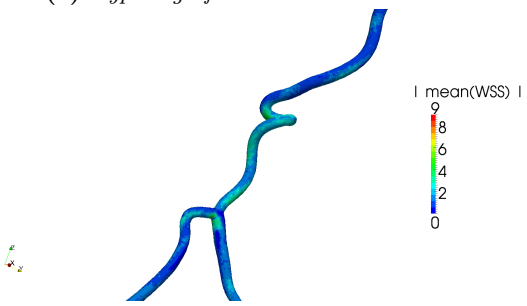

(b) $factor_{Re}^{ave,LITA} = 0.666$

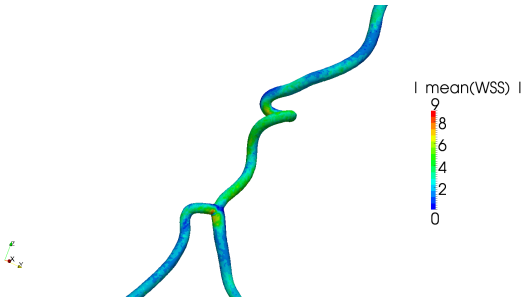

(c) $factor_{Re}^{ave,LITA} = 1$

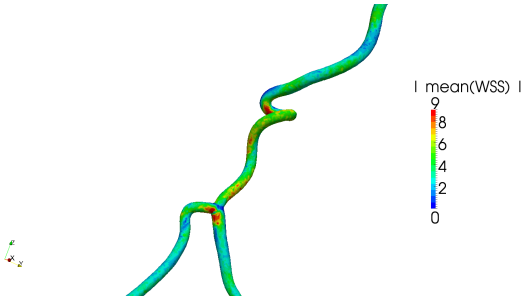

(d) $factor_{Re}^{ave,LCA} = 1.333$

Figure 6.24: ***Patient 12 - Y-graft between LITA and SVG.*** *Comparison of time-averaged wall shear stress [Pa] for different inflow boundary conditions.*

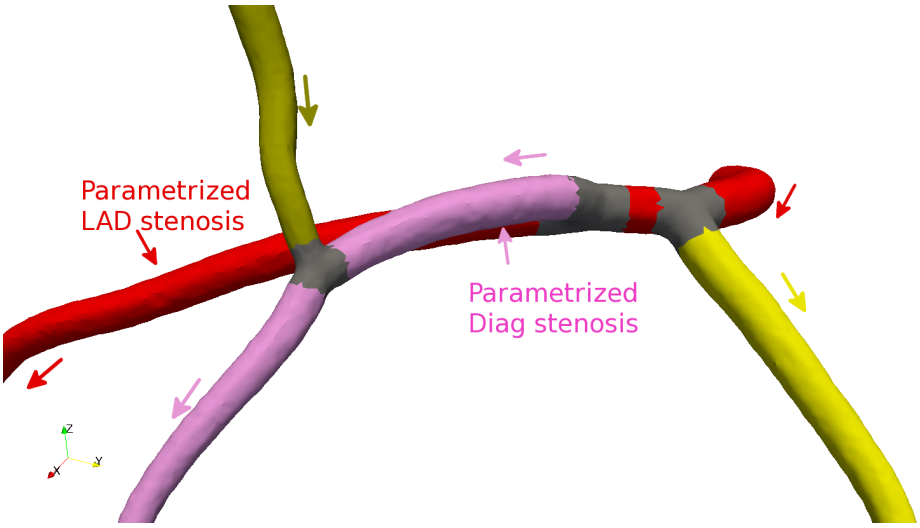

(a) *Coronary arteries near the studied bifurcations. Colored arrows denote blood flow direction.*

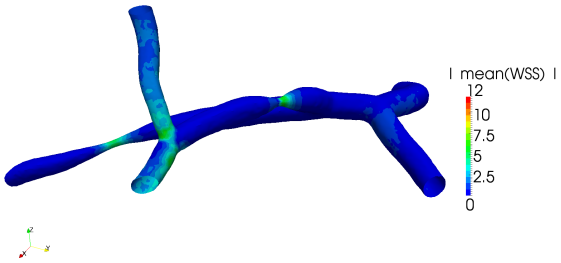

(b) $factor_{Re}^{ave,LCA} = factor_{Re}^{ave,LCA} = 0.666$, $\alpha_{LAD} = \alpha_{Diag} = 90\%$

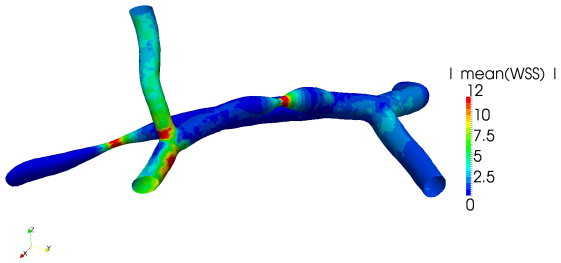

(c) $factor_{Re}^{ave,LCA} = factor_{Re}^{ave,LCA} = 1.333$, $\alpha_{LAD} = \alpha_{Diag} = 90\%$

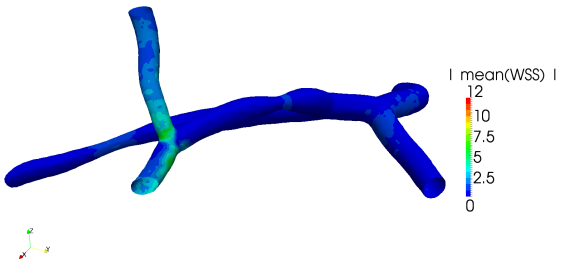

(d) $factor_{Re}^{ave,LCA} = factor_{Re}^{ave,LCA} = 0.666$, $\alpha_{LAD} = \alpha_{Diag} = 70\%$

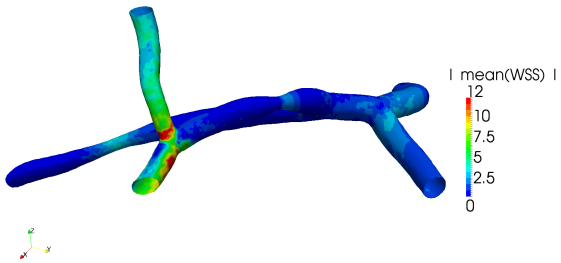

(e) $factor_{Re}^{ave,LCA} = factor_{Re}^{ave,LCA} = 1.333$, $\alpha_{LAD} = \alpha_{Diag} = 70\%$

Figure 6.25: ***Patient 12 - From top-right to bottom-left: LAD-LCX and LAD-Diag bifurcations, SVG-Diag anastomosis (flow-direction, termino-lateral).*** *Comparison of time-averaged wall shear stress [Pa] for different inflow boundary conditions and stenosis.*

Patient 13

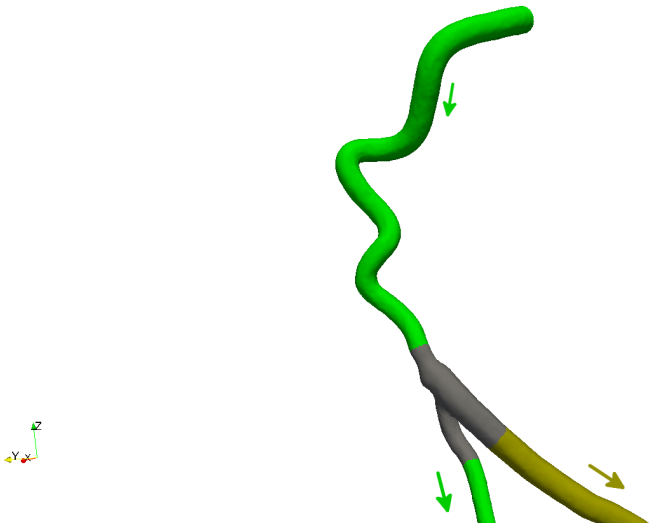

(a) *Bypass grafts near the studied anastomosis. Colored arrows denote blood flow direction.*

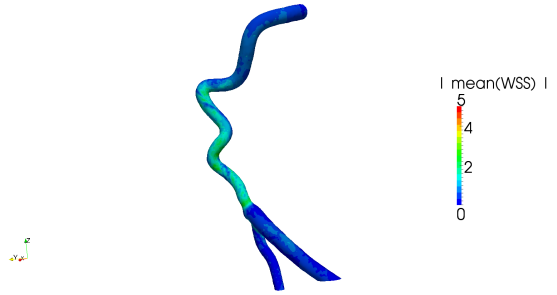

(b) $factor_{Re}^{ave,LITA} = 0.666$

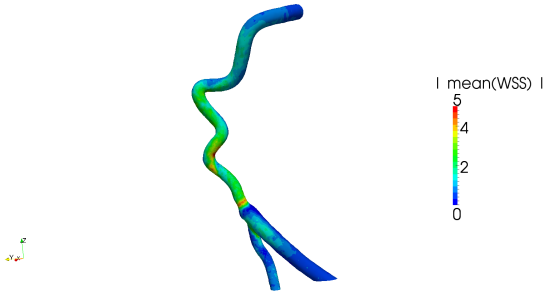

(c) $factor_{Re}^{ave,LITA} = 1$

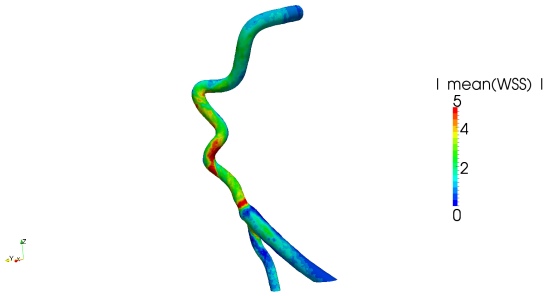

(d) $factor_{Re}^{ave,LCA} = 1.333$

Figure 6.26: ***Patient 13 - Y-graft between LITA and SVG.*** *Comparison of time-averaged wall shear stress for different inflow boundary conditions.*

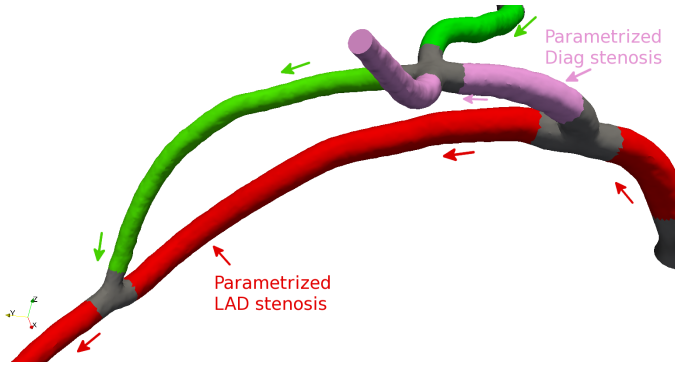

(a) *Coronary arteries near the studied bifurcations. Colored arrows denote blood flow direction.*

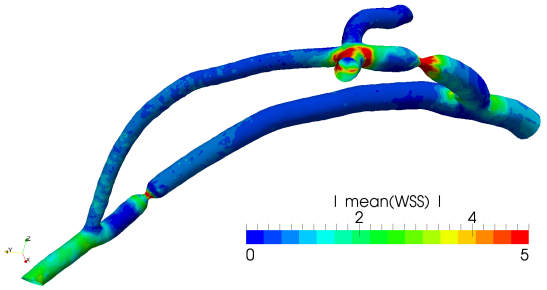

(b) $factor_{Re}^{ave,LCA} = 0.666$, $factor_{Re}^{ave,LCA} = 1.333$, $\alpha_{LAD} = \alpha_{Diag} = 90\%$

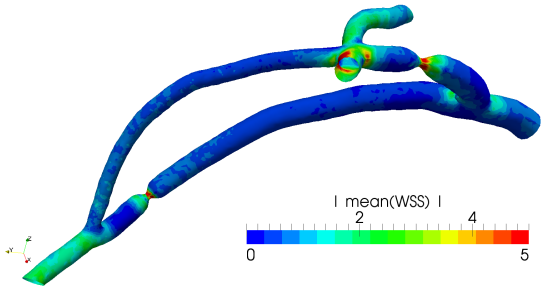

(c) $factor_{Re}^{ave,LCA} = 0.666$, $factor_{Re}^{ave,LCA} = 1.333$, $\alpha_{LAD} = \alpha_{Diag} = 70\%$

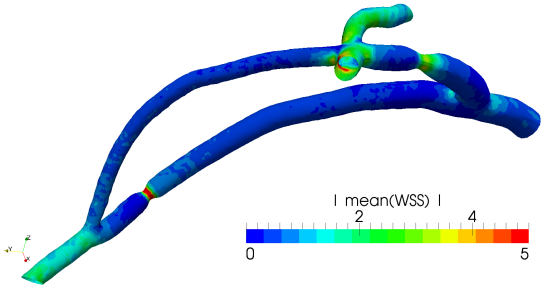

(d) $factor_{Re}^{ave,LCA} = 1$, $factor_{Re}^{ave,LCA} = 1$, $\alpha_{LAD} = \alpha_{Diag} = 90\%$

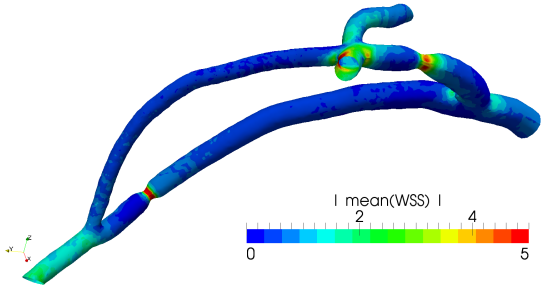

(e) $factor_{Re}^{ave,LCA} = 1$, $factor_{Re}^{ave,LCA} = 1$, $\alpha_{LAD} = \alpha_{Diag} = 70\%$

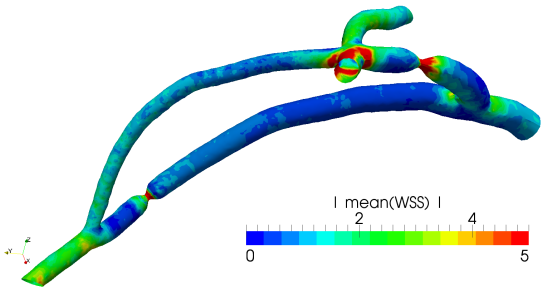

(f) $factor_{Re}^{ave,LCA} = 1.333$, $factor_{Re}^{ave,LCA} = 1.333$, $\alpha_{LAD} = \alpha_{Diag} = 90\%$

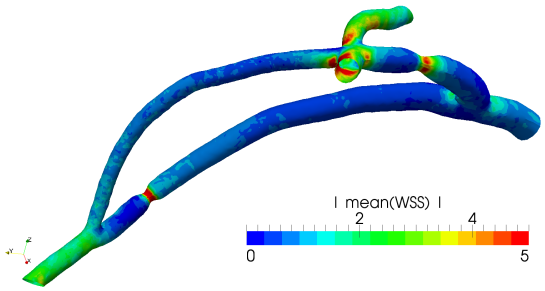

(g) $factor_{Re}^{ave,LCA} = 1.333$, $factor_{Re}^{ave,LCA} = 1.333$, $\alpha_{LAD} = \alpha_{Diag} = 70\%$

Figure 6.27: ***Patient 13 - From top-right to bottom-left: LAD-Diag bifurcation, LITA-Diag anastomosis (flow-direction, latero-lateral), LITA-LAD anastomosis (flow-direction, termino-lateral).*** *Comparison of time-averaged wall shear stress for different inflow boundary conditions and stenosis.*

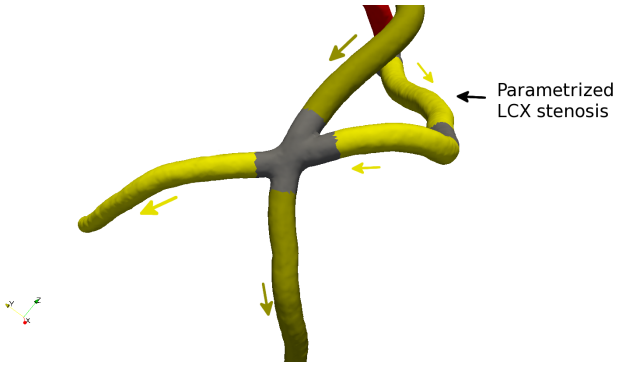

(a) *Coronary arteries and bypass grafts near the studied anastomoses. Colored arrows denote blood flow direction.*

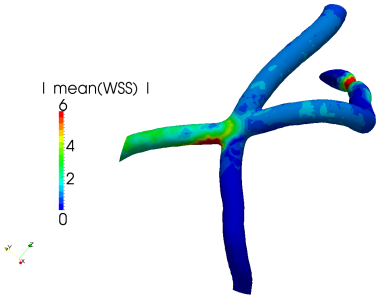

(b) $factor_{Re}^{ave,LCA} = 0.666$, $factor_{Re}^{ave,LCA} = 1.333$, $\alpha_{LCX} = 90\%$

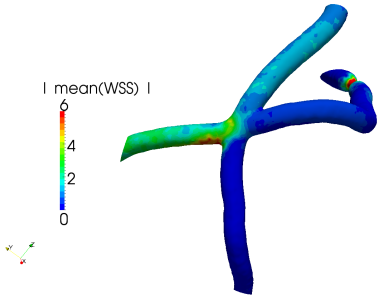

(c) $factor_{Re}^{ave,LCA} = 0.666$, $factor_{Re}^{ave,LCA} = 1.333$, $\alpha_{LCX} = 70\%$

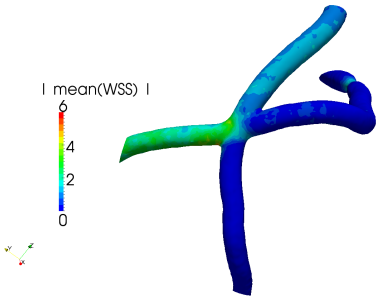

(d) $factor_{Re}^{ave,LCA} = 1$, $factor_{Re}^{ave,LCA} = 1$, $\alpha_{LCX} = 90\%$

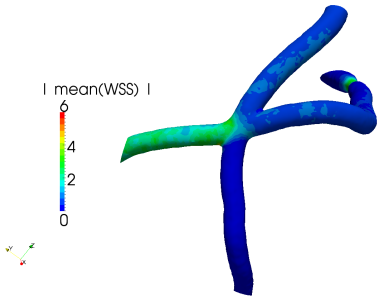

(e) $factor_{Re}^{ave,LCA} = 1$, $factor_{Re}^{ave,LCA} = 1$, $\alpha_{LCX} = 70\%$

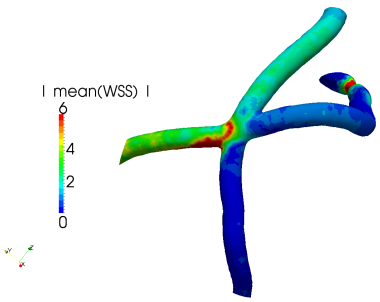

(f) $factor_{Re}^{ave,LCA} = 1.333$, $factor_{Re}^{ave,LCA} = 1.333$, $\alpha_{LCX} = 90\%$

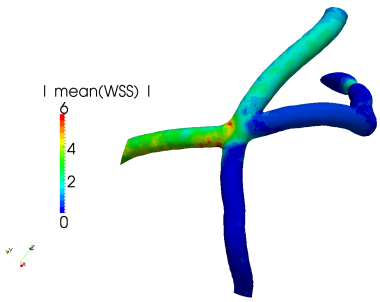

(g) $factor_{Re}^{ave,LCA} = 1.333$, $factor_{Re}^{ave,LCA} = 1.333$, $\alpha_{LCX} = 70\%$

Figure 6.28: ***Patient 13 - SVG-LCX anastomosis (cross, latero-lateral).*** *Comparison of time-averaged wall shear stress for different inflow boundary conditions and stenosis.*

6.4.3 Discussion

Patient 4.

- *LITA to Diag anastomosis (flow-direction, latero-lateral), second LAD stenosis.* Results in Figure 6.15 highlight that:
  - *Amplitude factors:* comparing the figures by row (e.g. (b) and (c), (d) and (e), etc.) it can be noted that amplitude factors do not have significant effects on the OSI for healthy ($\alpha_{LAD,2} = 0\%$) or non critical stenosis ($\alpha_{LAD,2} = 50\%$). However, a complex variation of OSI patterns with respect to amplitude factors can be noted for the case with critical stenoses ($\alpha_{LAD,2} = 90\%$), comparing Figures (f) and (g), (n) and (o).
  - *LITA time-averaged flow factor:* comparing figures (a)-(i) and (j)-(o) it can be remarked that larger LITA flow rates has significant effect in the stenotic case, causing a larger OSI value in the LITA-Diag anastomosis and entailing also smaller OSI values in the region proximal to the second LAD stenosis.
  - *Stenoses:* regions both proximal and distal to the second LAD stenoses feature high OSI in the critical case ($\alpha_{LAD,2} = 90\%$), being more widespread for increasing amplitude factors and decreasing LITA time-averaged flow factor. Moreover, all healthy and non-critical cases feature high OSI in the LITA to Diag anastomosis, because an high residual flow can still go through the native vessel. Instead, for critical $LAD-1$ and $LAD-2$ stenoses, three out of four cases (figures (f), (g), (o), but not figure (n)), feature smaller OSI. Finally, in the study of this anastomosis the $LAD-2$ stenosis is more critical then the $LAD-1$: in fact, no significantly different flow patterns can be observed for non-critical $LAD-2$ and critical $LAD-1$ (compare e.g. figures (d) and (h), (e) and (i)).

Patient 7.

- *Dependence of the maximum WSS near the stenosis on Reynolds number and stenosis factors.* A test to assess the reliability of the reduced-order model, and its ability to span over the entire parametric range (increasing inlet flow rates, and critical to non critical stenoses) is performed. The maximum value of wall shear stress in each one of the three stenosis (LCA, LCX, LAD) is computed. Resulting patterns are shown in Figure 6.16, and show a monotonically increasing value of WSS, both with respect to inlet flow rates and stenosis severity. WSS is higher in the LCA stenosis than in the LCX and LAD ones; this is motivated by the fact that the blood flow in the LCA is split between LAD and LCX.

- *LAD-LCX bifurcation.* Figure 6.17 provides a detailed view of the LCA stenosis and LAD-LCX bifurcation. The arterial wall near the bifurcation features high WSS; maximum WSS values are influenced both by the inlet flow rate at the LCA ostium and the severity of the LCA stenosis. In fact, lower values of the former parameter cause a smaller region of high WSS (compare figures (b)-(c) to (d)-(e)). Moreover, the impingement of the jet of high velocity, formed by critical stenosis, on the arterial wall, is an additional cause of higher WSS, regardless of the inlet flow rates (compare figures (b)-(d) to (c)-(e)). Figure (f) provides a confirmation of this phenomena for a wide range of stenosis severity and inlet flow rates.

- *LCX-OM bifurcation.* A similar study is performed for the LCX-OM bifurcation. Figure 6.18 shows the time-averaged wall shear stress patterns both before and after the surgery.

The pattern of WSS at the bifurcation before the surgery, summarized in figure (j), is similar to the one at the LAD-LCX bifurcation (although smaller values of WSS are identified). In contrast, after the surgery maximum values of WSS are not sensible anymore to neither LCA inlet flow rate and stenosis factor. This is motivated by the fact that, in this case, the SVG graft is the main source of blood flow for both LCX and OM branches.

Patient 3.

- *Y-graft between LITA and Radial artery.* A comparison of the WSS near the Y-graft for increasing inlet flow rates at the LITA graft is shown in Figure 6.19. The anastomosis near the Y-graft features local high values of WSS, both distally and proximally. Higher WSS is present in the LITA graft than in the Radial artery.
- *LAD-LCX and LAD-Diag bifurcations.* Figure 6.20 studies the LAD-LCX and LAD-Diag bifurcations, and LAD stenosis. As in the previous patient, local high regions of WSS are located at arterial walls near bifurcations. A recirculation region is also apparent downstream the stenosis (figures (d) and (e)), as highlighted by WSS approximately equal to zero.
- *LITA-Diag anastomosis (flow-direction, latero-lateral), LITA-LAD anastomosis (flow-direction, latero-lateral), LITA-LAD anastomosis (flow-direction, termino-lateral).* The sequential LITA graft is studied in Figure 6.21. It is composed of three anastomoses: LITA-Diag anastomosis (flow-direction, latero-lateral), LITA-LAD anastomosis (flow-direction, latero-lateral) and LITA-LAD anastomosis (flow-direction, termino-lateral). The first anastomosis is the most critical, as it features the highest WSS values; WSS gradually decreases at the remaining anastomoses. LAD is divided in two segments by the second anastomosis (the first one contains a stenosis); higher WSS are present in the second segment, because it is perfused by the blood coming from the LITA graft, especially in the case of increased coronary flow rates. In a similar way, higher WSS is observed in the LITA (especially in its second segment) if graft flow rate is increased.
- *Radial-LCX anastomosis (flow-direction, termino-lateral).* Finally, the anastomosis between Radial artery and LCX is shown in Figure 6.22. A region of high WSS is located at the arterial bed (figures (d) and (e)). In this anastomosis, in contrast to the sequential graft, an increased flow rate does not cause significant differences (compare figures (b) and (c), (d) and (e)). The additional blood flow is thus fully routed to the triple sequential LITA graft.

Patient 1.

- *Dependence of the pressure drop at the stenosis on Reynolds number and stenosis factors.* Figure 6.23 shows the result of a test to assess the capability of the pressure recovery of the supremizer-stabilized ROM on patient-specific geometries, computing the pressure drop at the stenosis. For each one of the considered stenosis, an increasing pressure drop is observed both with Reynolds number and stenosis severity. It is relevant to be able to produce such plots in the medical practice, especially in the pre-surgical phase. In fact, some clinical exams to detect the presence of a stenosis are based on experimental measures of pressure drops. A plot similar to Figure 6.23 can then be employed to precisely quantify the severity of the stenosis.

Patient 12.

- *Y-graft between LITA and SVG.* Figure 6.24 provides a comparison of the WSS at the Y-graft between LITA and SVG, for increasing LITA flow rate. The anastomosis of the Y-graft is a critical region, as in the previous cases (e.g. Patient 3). Other regions of high WSS are located where the LITA graft features high curvature. A correlation between increased graft flow rate and increased maximum WSS can be detected.
- *LAD-LCX and LAD-Diag bifurcations, SVG-Diag anastomosis (flow-direction, termino-lateral).* A study of the SVG-Diag anastomosis is performed in Figure 6.25. The anastomosis features high WSS. A recirculation region (highlighted by zero magnitude of WSS) is observed in the distal native coronary artery, near the toe of the graft. Instead, the arterial bed features high WSS, because of the blood flow from the graft.

Patient 13.

- *Y-graft between LITA and SVG.* Figure 6.26 provides a comparison of the WSS at the Y-graft between LITA and SVG, for increasing LITA flow rate. Both the anastomosis of the Y-graft and LITA segments characterized by high curvature are critical regions. However, in contrast to the previous patient, values of WSS are higher proximally to the anastomosis than distally; this is related to the larger diameter that characterizes the SVG in this case.
- *LAD-Diag bifurcation, LITA-Diag anastomosis (flow-direction, latero-lateral), LITA-LAD anastomosis (flow-direction, termino-lateral).* Figure 6.27 details the double sequential graft (LITA-Diag-LAD). Higher values of WSS are observed for the latero-lateral LITA-Diag anastomosis, than the termino-lateral LITA-LAD. The effect of increased LCA flow rates is visible at the LAD-Diag bifurcation, and is the source of a region of locally higher WSS at the LAD wall both proximally and distally the bifurcation. Increased LITA flow rates are a possible cause of larger critical regions both on the arterial bed and at the anastomosis at the LITA-Diag anastomosis.
- *SVG-LCX anastomosis (cross, latero-lateral).* The SVG-LCX anastomosis is studied in Figure 6.28. A region of high WSS is located on the arterial bed distal to the cross anastomosis. Increased LCX flow rates, both as a consequence of increased native LCA flow rates or decreased stenosis, have a significant impact on the local pattern of the WSS in this region.

6.5 Fast haemodynamics simulations for several types of anastomosis

In this section we apply the POD-Galerkin ROM and the centerlines-based parametrization for a fast evaluation of the fluid dynamics in patient-specific CABGs considering a variation of stenoses severity and anastomoses type (antegrade, T-shaped, retrograde), in order to perform a comparison based on both "input data" (stenoses severity) and "surgical control variables" (anastomoses type).

6.5.1 Parametrization and reduced-order models details

Patient	**2**	**6**	**15**
Number of physical parameters	0	0	0
Number of geometrical parameters	3	3	2
LCA parametrized stenosis	no	no	no
LAD/Diag parametrized stenosis	1	1	1
LCX/OM parametrized stenosis	no	no	no
RCA parametrized stenosis	1	1	no
Parametrized anastomosis	1 (Rad-PL)	1 (SVG-PDA)	1 (LITA-LAD)
FE velocity order	2		
FE pressure order	1		
Total number of FE dofs	1 826 495	2 038 891	1 219 918
Temporal step	0.01		
Number of time steps per cardiac cycle	80		
CPU time for one cardiac cycle	$12 \sim 15$ h	$15 \sim 18$ h	$11 \sim 13$ h
$N_{\mathbf{train}}$	50		
$N_{\mathbf{max}}$	50		
$M_{\mathbf{2\text{–}POD}}$	20		
Affine expansion components for m**,** a**,** $b\&c$	49, 163, 61	45, 154, 60	37, 133, 53

Table 6.3: *Details of the reduced-order model.*

Details of the reduced-order model are summarized in Table 6.3. The number of considered geometrical parameters is reported for each patient; no physical parameters are considered in this analysis (the multiplicative and amplitude factors on the flow rate are chosen equal to one). Both entities of one or more stenoses and variation of end-to-side anastomosis are considered as geometrical parameters. The location of the stenoses is summarized, alongside with the parametrized anastomosis.

As in the previous sections, a Taylor-Hood $\mathbb{P}_2 - \mathbb{P}_1$ FE discretization is employed for the space discretization; an Implicit Euler method is considered for the time discretization. N_{train} time-dependent FE problems are solved for random values of the parameters, and $M_{2\text{–POD}}$ POD modes are retained in the two-level POD.

The offline stage is performed in parallel, for $24 \sim 32$ processors. The truth solution for each sample point (and for each cardiac cycle) requires approximately 13 hours (to be multiplied by the number of processors to obtain the actual CPU time). The online stage, instead, is performed on a single processor. Thanks to the considerable reduction in the number of degrees of freedom ($N_{\mathbf{u}} = N_{\mathbf{s}} = N_p = N_{\max}$) and efficient offline-online procedure, each online ROM solution requires from 25 to 35 minutes. As in the previous section, online CPU times are higher than the case with no geometrical parameters because of considerably larger affine expansions, but computational savings are still remarkable (more than 95%).

6.5.2 Numerical results

Patient 15

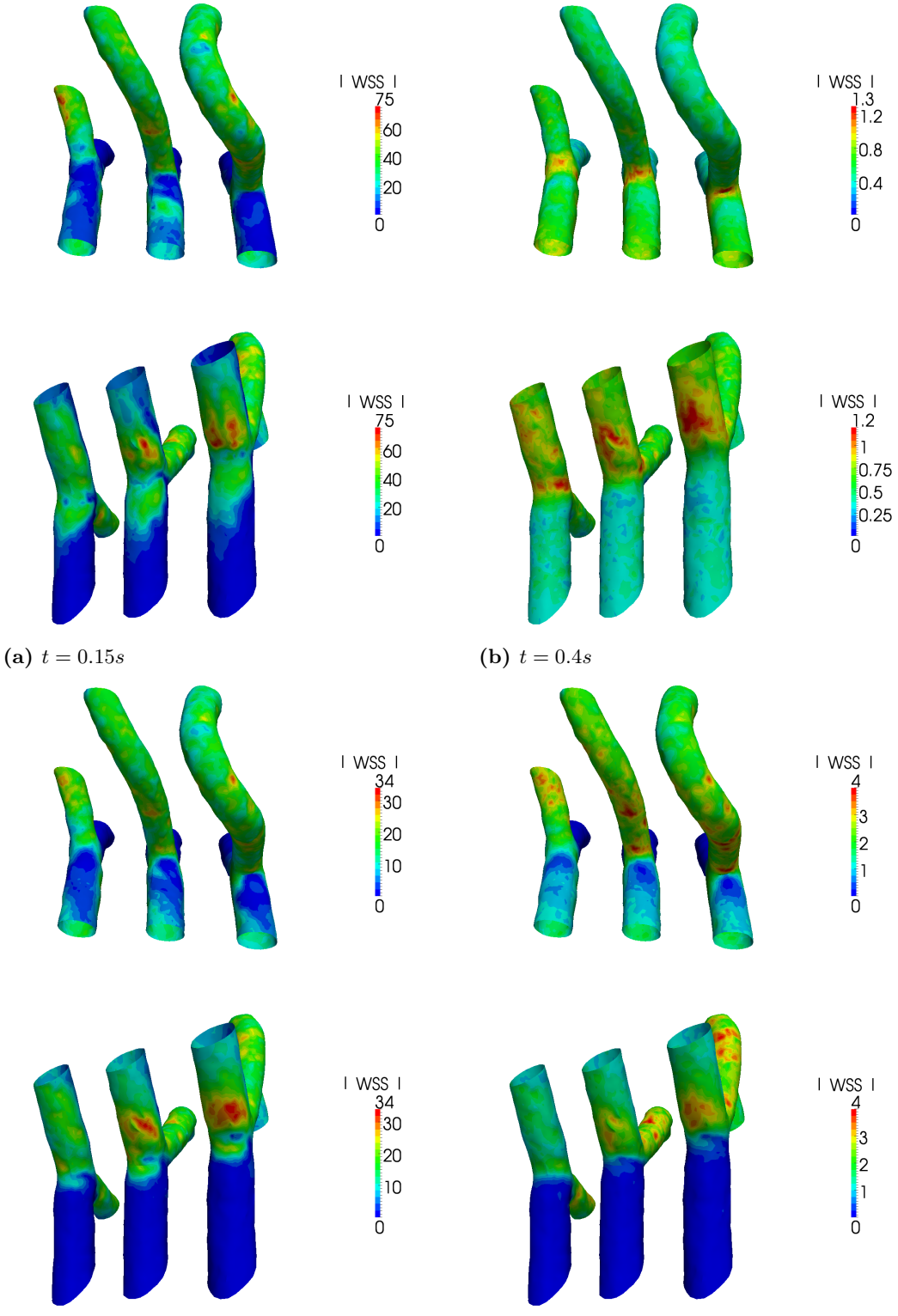

(a) $t = 0.15s$ **(b)** $t = 0.4s$

(c) $t = 0.55s$ **(d)** $t = 0.8s$

Figure 6.29: ***Patient 15 - LITA to LAD anastomosis (termino-lateral).*** *Comparison of wall shear stress [Pa] at different phases of the cardiac cycle for three anastomoses types (from left to right: antegrade, T-shaped, retrograde). Proximal stenosis: 90%.*

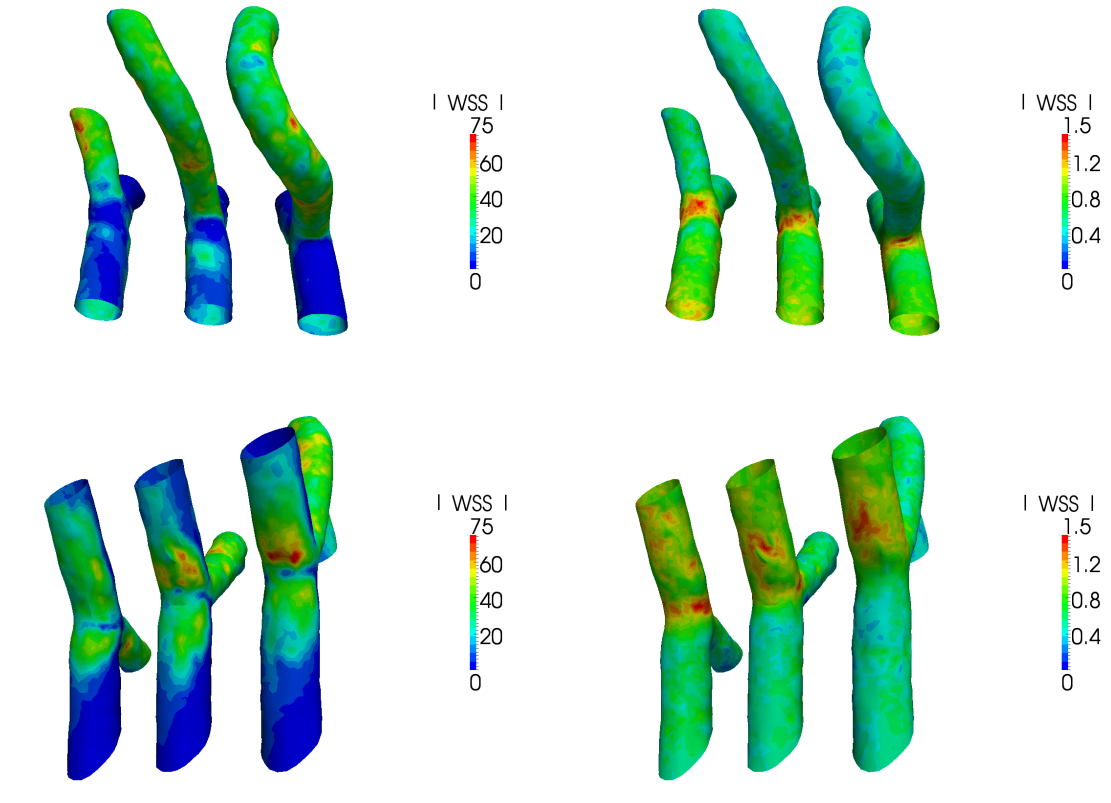

(a) $t = 0.15s$ **(b)** $t = 0.4s$

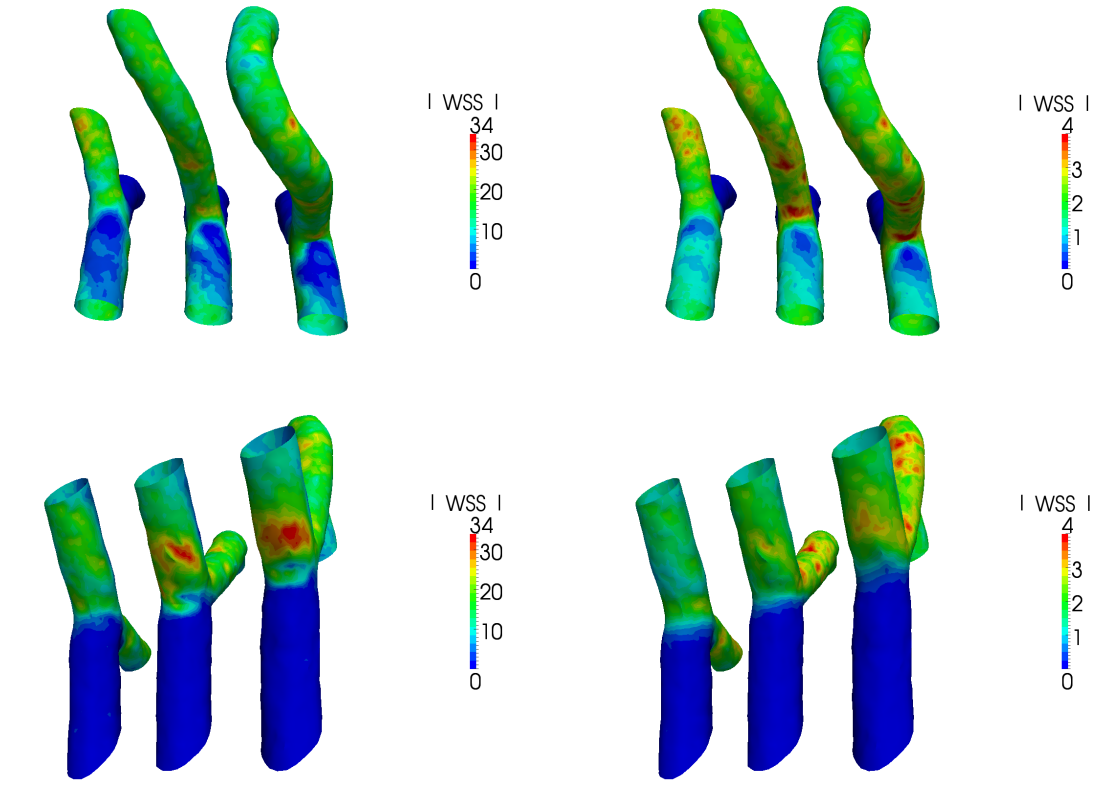

(c) $t = 0.55s$ **(d)** $t = 0.8s$

Figure 6.30: ***Patient 15 - LITA to LAD anastomosis (termino-lateral).*** *Comparison of wall shear stress [Pa] at different phases of the cardiac cycle for three anastomoses types (from left to right: antegrade, T-shaped, retrograde). Proximal stenosis: 60%.*

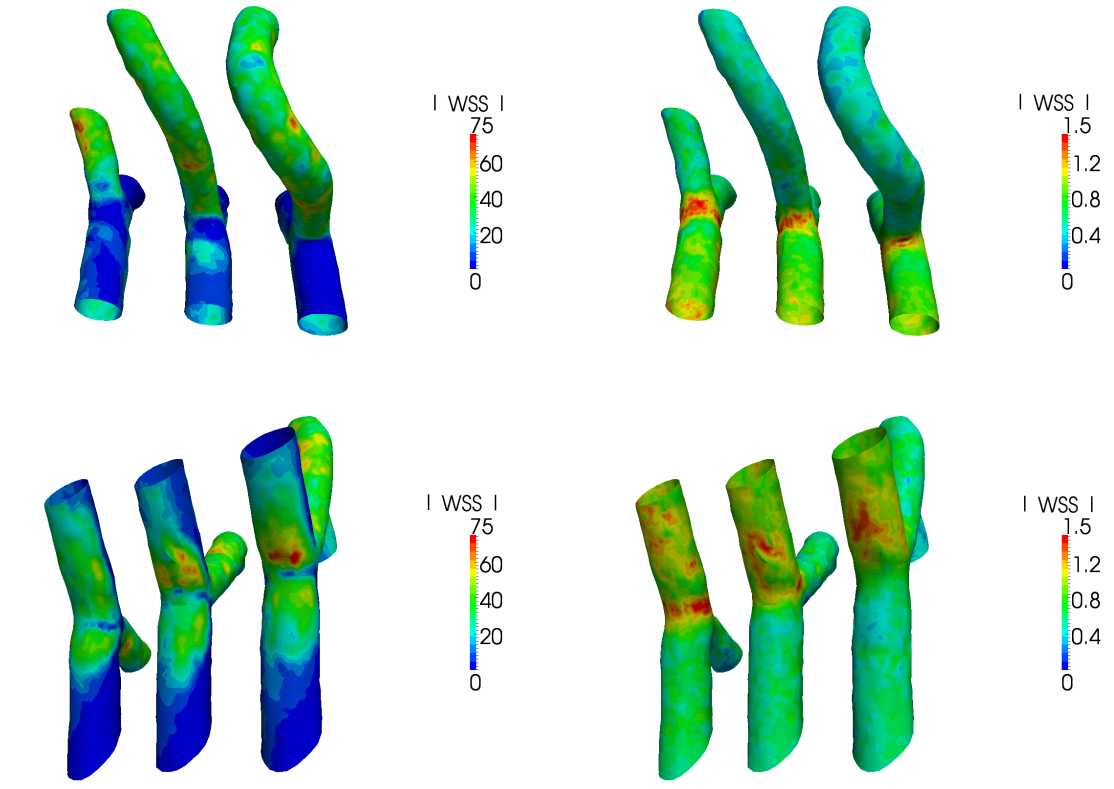

(a) $t = 0.15s$ **(b)** $t = 0.4s$

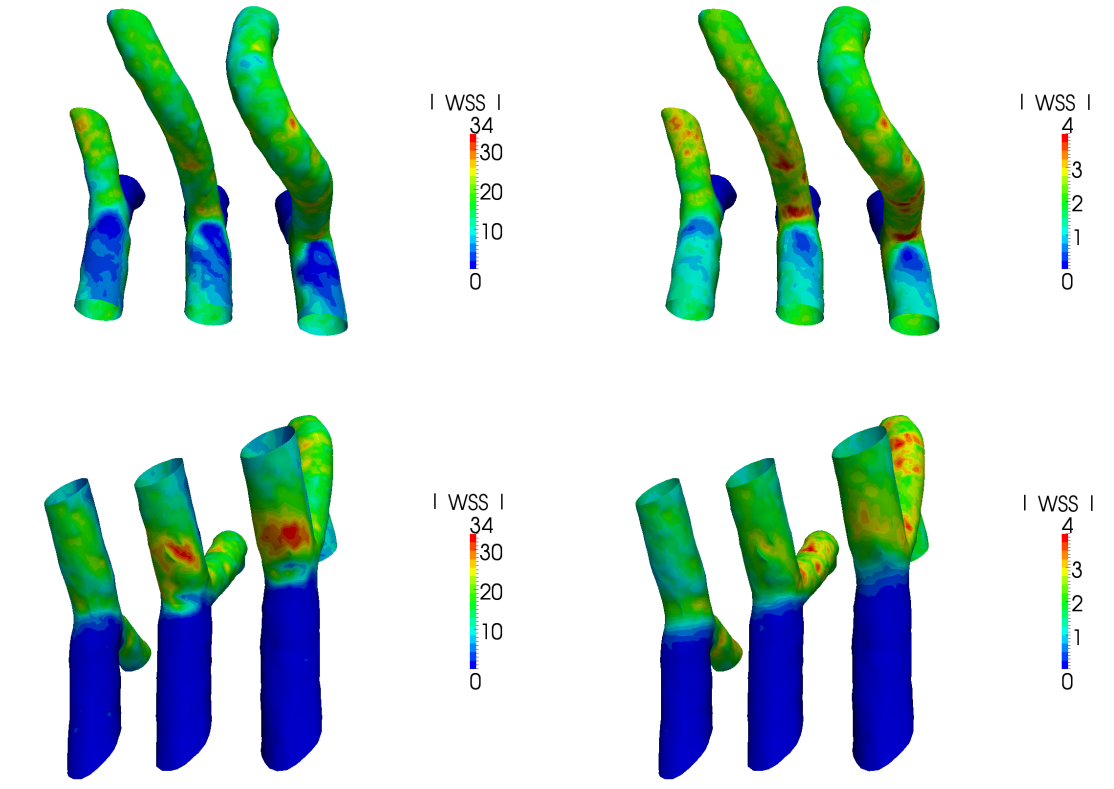

(c) $t = 0.55s$ **(d)** $t = 0.8s$

Figure 6.31: ***Patient 15 - LITA to LAD anastomosis (termino-lateral).*** *Comparison of wall shear stress [Pa] at different phases of the cardiac cycle for three anastomoses types (from left to right: antegrade, T-shaped, retrograde). Proximal stenosis: 0%.*

(a) $t = 0.15s$ (b) $t = 0.4s$ (c) $t = 0.55s$ (d) $t = 0.8s$

Figure 6.32: *Patient 15 - LITA to LAD anastomosis (termino-lateral).* *Comparison of normalized transversal velocity profiles at different phases of the cardiac cycle for three anastomoses types (from top to bottom: antegrade, T-shaped, retrograde; from left to right: increasing distance from the anastomosis). Proximal stenosis: 90%.*

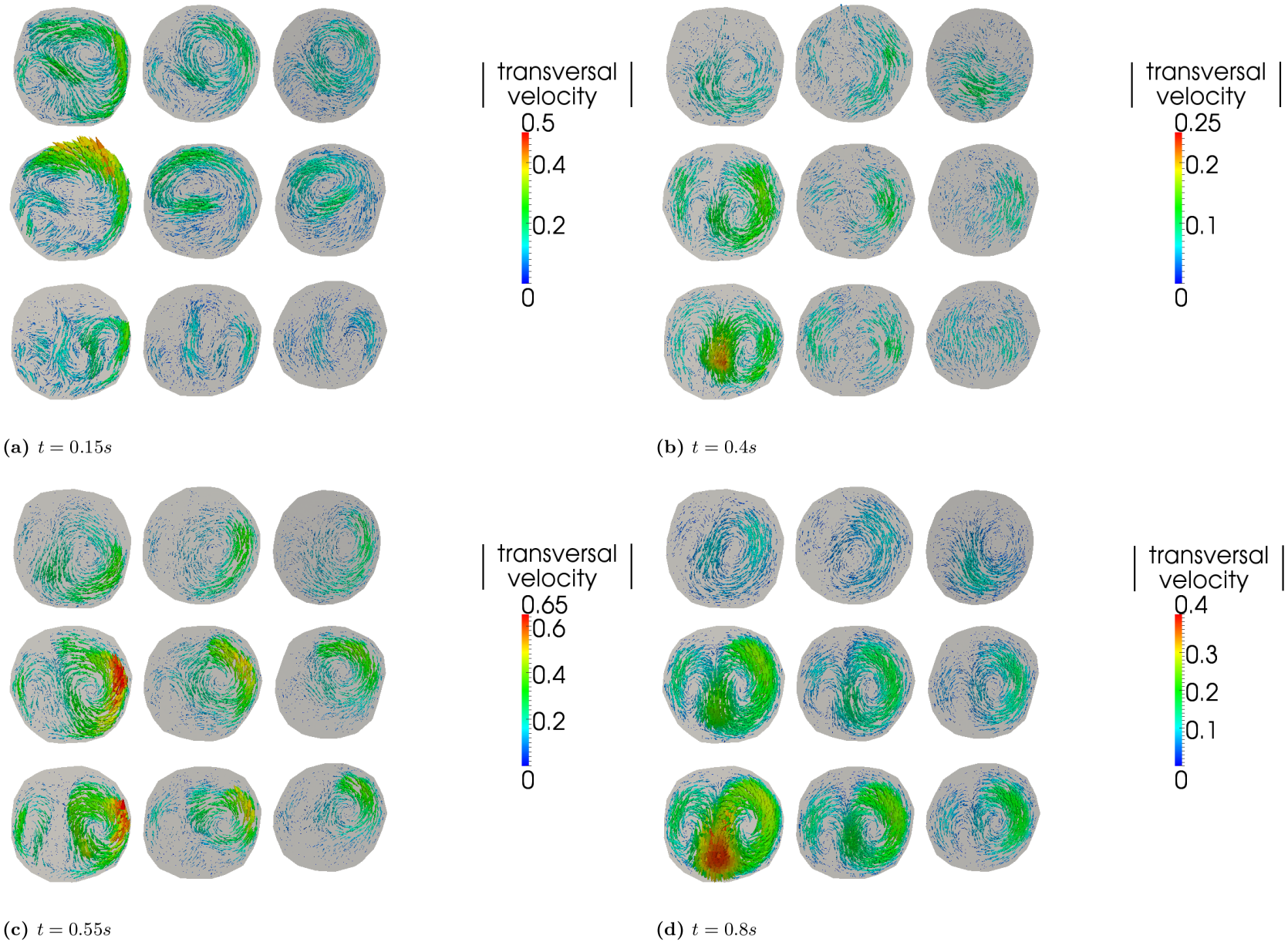

(a) $t = 0.15s$ **(b)** $t = 0.4s$

(c) $t = 0.55s$ **(d)** $t = 0.8s$

Figure 6.33: ***Patient 15 - LITA to LAD anastomosis (termino-lateral)***. *Comparison of normalized transversal velocity profiles at different phases of the cardiac cycle for three anastomoses types (from top to bottom: antegrade, T-shaped, retrograde; from left to right: increasing distance from the anastomosis). Proximal stenosis: 60%.*

(a) $t = 0.15s$ (b) $t = 0.4s$ (c) $t = 0.55s$ (d) $t = 0.8s$

Figure 6.34: *Patient 15 - LITA to LAD anastomosis (termino-lateral).* *Comparison of normalized transversal velocity profiles at different phases of the cardiac cycle for three anastomoses types (from top to bottom: antegrade, T-shaped, retrograde; from left to right: increasing distance from the anastomosis). Proximal stenosis: 0%.*

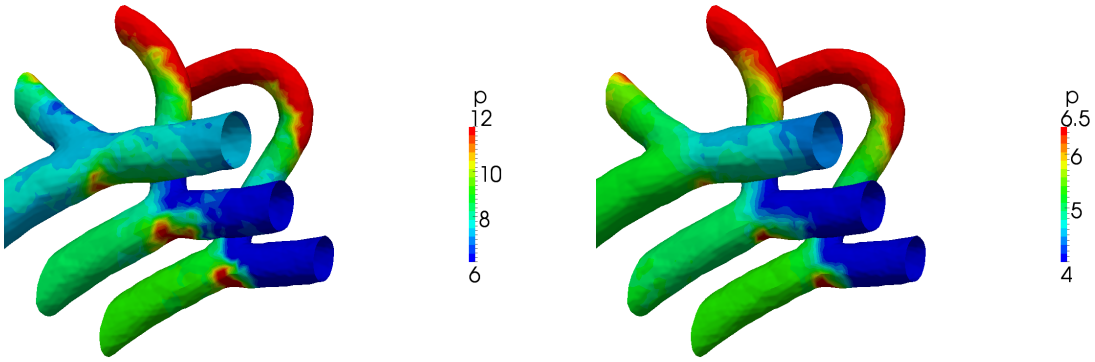

(a) $t = 0.15s$ **(b)** $t = 0.55s$

Figure 6.35: ***Patient 15 - LITA to LAD anastomosis (termino-lateral)****. Comparison of the pressure drop [mmHg] in the anastomosis at different phases of the cardiac cycle for three anastomoses types (from left to right: antegrade, T-shaped, retrograde). Proximal stenosis: 90%.*

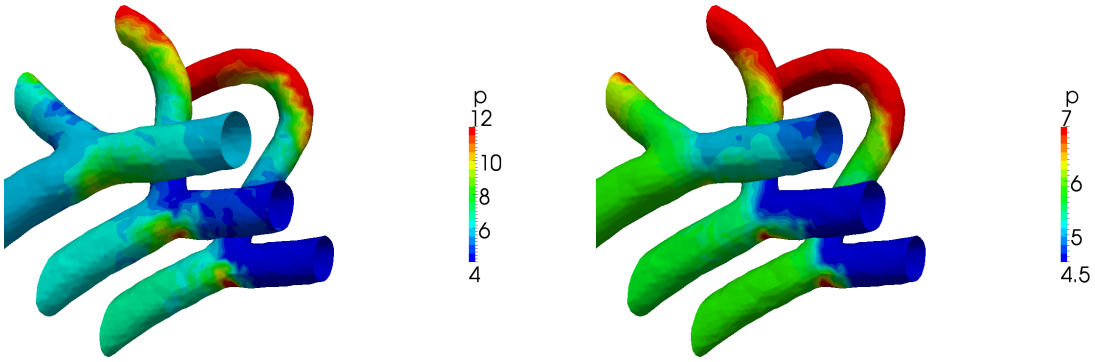

(a) $t = 0.15s$ **(b)** $t = 0.55s$

Figure 6.36: ***Patient 15 - LITA to LAD anastomosis (termino-lateral)****. Comparison of the pressure drop [mmHg] in the anastomosis at different phases of the cardiac cycle for three anastomoses types (from left to right: antegrade, T-shaped, retrograde). Proximal stenosis: 60%.*

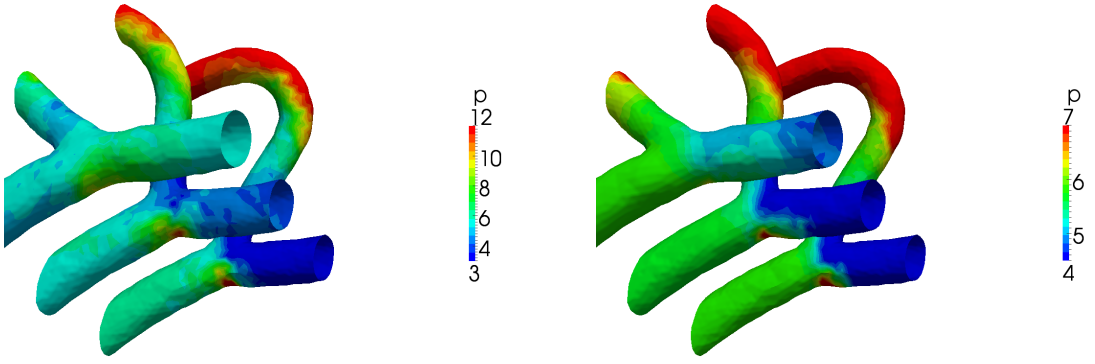

(a) $t = 0.15s$ **(b)** $t = 0.55s$

Figure 6.37: ***Patient 15 - LITA to LAD anastomosis (termino-lateral)****. Comparison of the pressure drop [mmHg] in the anastomosis at different phases of the cardiac cycle for three anastomoses types (from left to right: antegrade, T-shaped, retrograde). Proximal stenosis: 0%.*

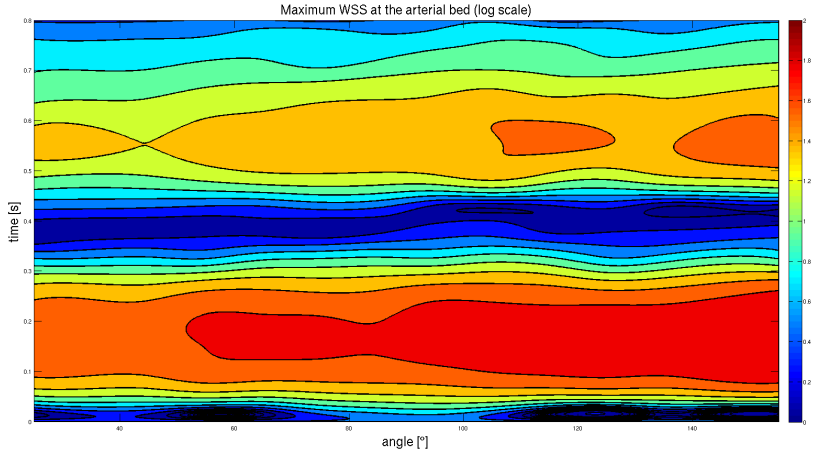

(a) *Maximum wall shear stress [Pa] at the arterial bed as a function of the anastomosis angle.*

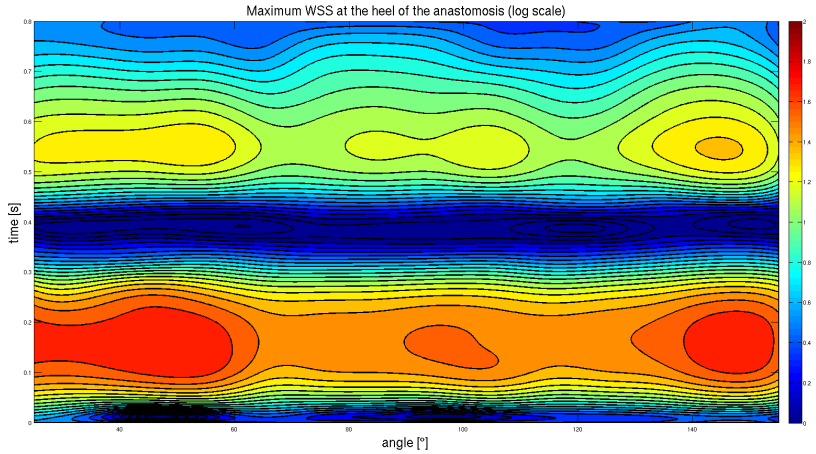

(b) *Maximum wall shear stress [Pa] at the heel of the anastomosis as a function of the anastomosis angle.*

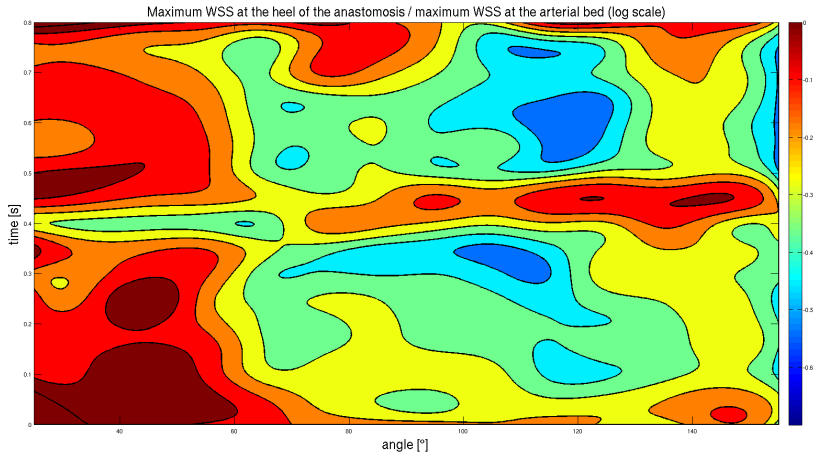

(c) *Ratio between maximum wall shear stress at the heel of the anastomosis over maximum wall shear stress at the arterial bed as a function of the anastomosis angle.*

Figure 6.38: ***Patient 15 - LITA to LAD anastomosis (termino-lateral).*** *Dependence of the maximum wall shear stress [Pa] on the anastomosis angle, at different locations near the anastomosis.*

Patient 6

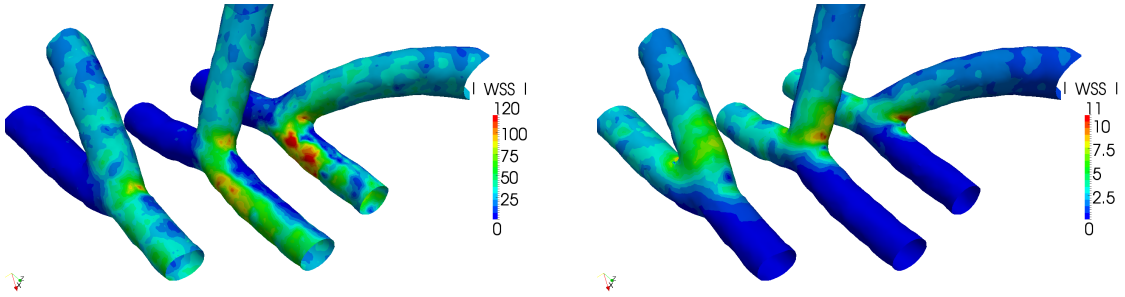

(a) $t = 0.15s$ **(b)** $t = 0.4s$

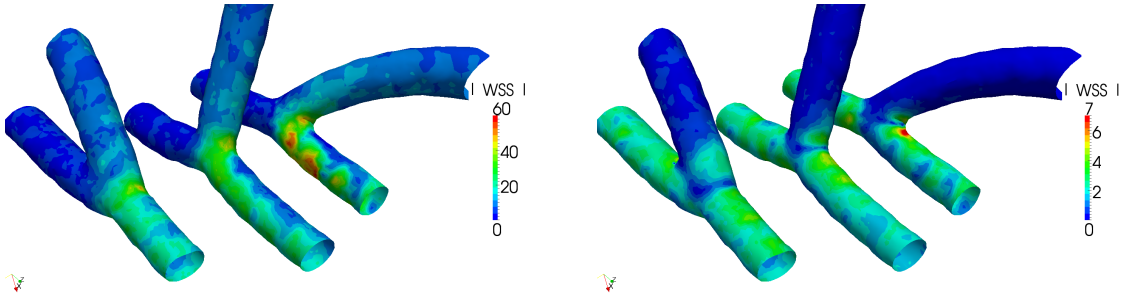

(c) $t = 0.55s$ **(d)** $t = 0.8s$

Figure 6.39: ***Patient 6 - SVG to PDA anastomosis (termino-lateral).*** *Comparison of wall shear stress [Pa] at different phases of the cardiac cycle for three anastomoses types (from left to right: antegrade, T-shaped, retrograde). Proximal stenosis: 90%.*

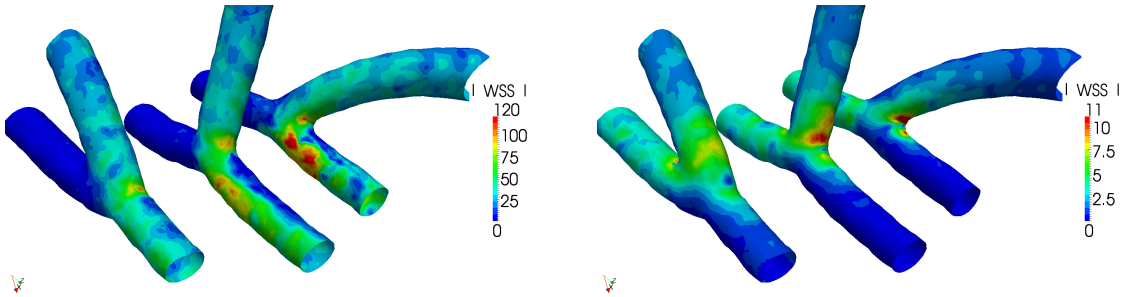

(a) $t = 0.15s$ **(b)** $t = 0.4s$

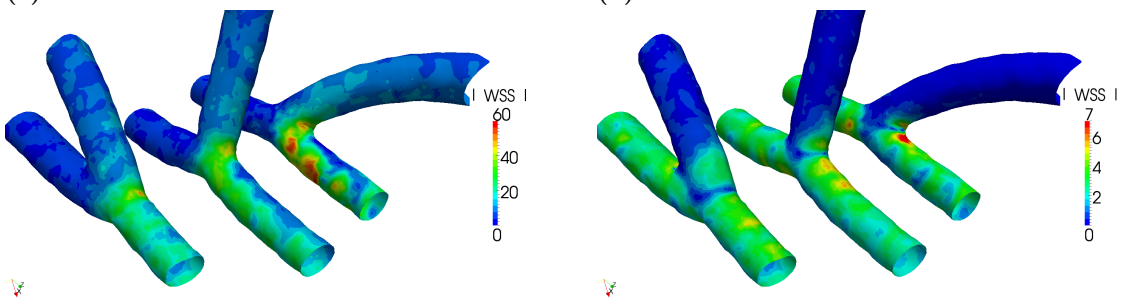

(c) $t = 0.55s$ **(d)** $t = 0.8s$

Figure 6.40: ***Patient 6 - SVG to PDA anastomosis (termino-lateral).*** *Comparison of wall shear stress [Pa] at different phases of the cardiac cycle for three anastomoses types (from left to right: antegrade, T-shaped, retrograde). Proximal stenosis: 80%.*

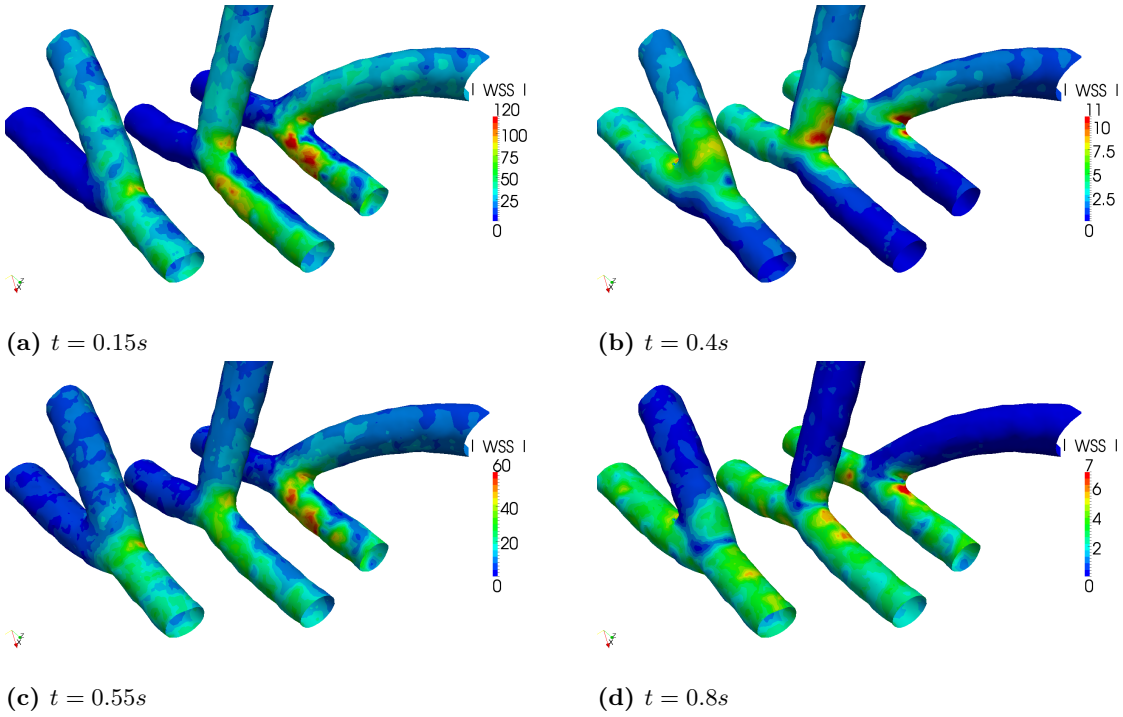

(a) $t = 0.15s$ **(b)** $t = 0.4s$

(c) $t = 0.55s$ **(d)** $t = 0.8s$

Figure 6.41: ***Patient 6 - SVG to PDA anastomosis (termino-lateral).*** *Comparison of wall shear stress [Pa] at different phases of the cardiac cycle for three anastomoses types (from left to right: antegrade, T-shaped, retrograde). Proximal stenosis: 60%.*

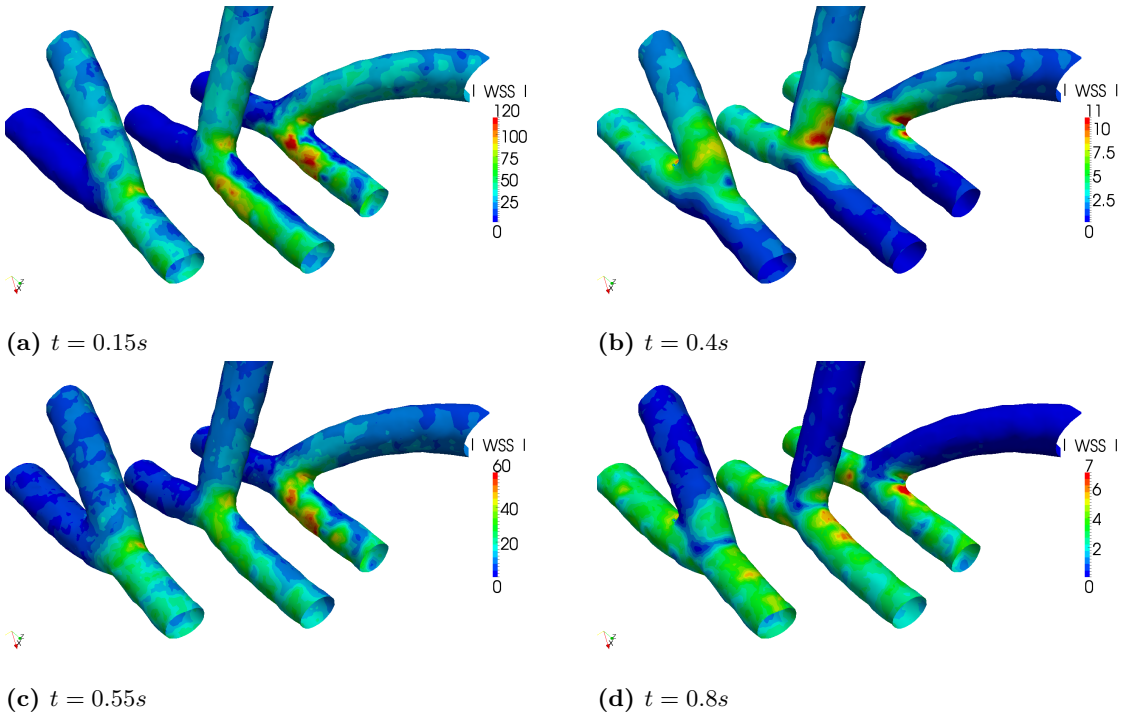

(a) $t = 0.15s$ **(b)** $t = 0.4s$

(c) $t = 0.55s$ **(d)** $t = 0.8s$

Figure 6.42: ***Patient 6 - SVG to PDA anastomosis (termino-lateral).*** *Comparison of wall shear stress [Pa] at different phases of the cardiac cycle for three anastomoses types (from left to right: antegrade, T-shaped, retrograde). Proximal stenosis: 0%.*

Patient 2

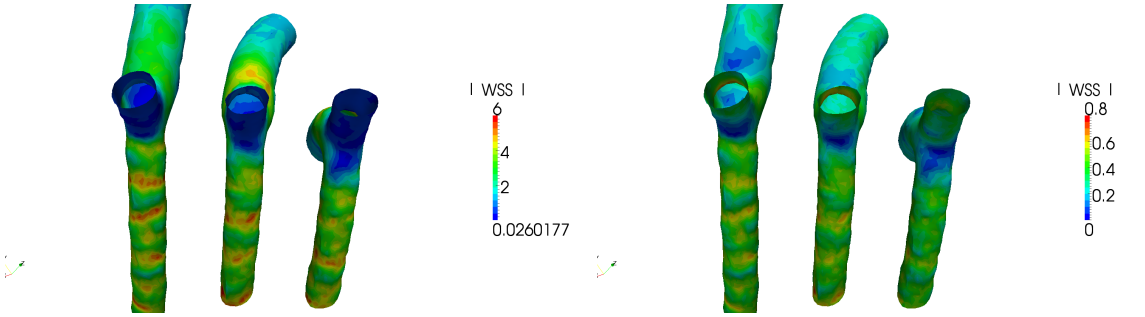

(a) $t = 0.4s$ **(b)** $t = 0.8s$

Figure 6.43: ***Patient 2 - Radial to PL anastomosis (termino-lateral)***. *Comparison of wall shear stress [Pa] at different phases of the cardiac cycle for three anastomoses types (from left to right: antegrade, T-shaped, retrograde). Proximal stenosis: 90%.*

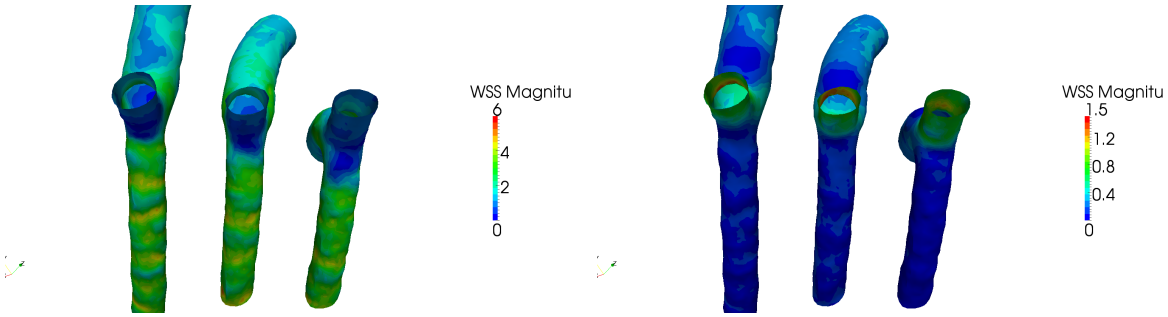

(a) $t = 0.4s$ **(b)** $t = 0.8s$

Figure 6.44: ***Patient 2 - Radial to PL anastomosis (termino-lateral)***. *Comparison of wall shear stress [Pa] at different phases of the cardiac cycle for three anastomoses types (from left to right: antegrade, T-shaped, retrograde). Proximal stenosis: 80%.*

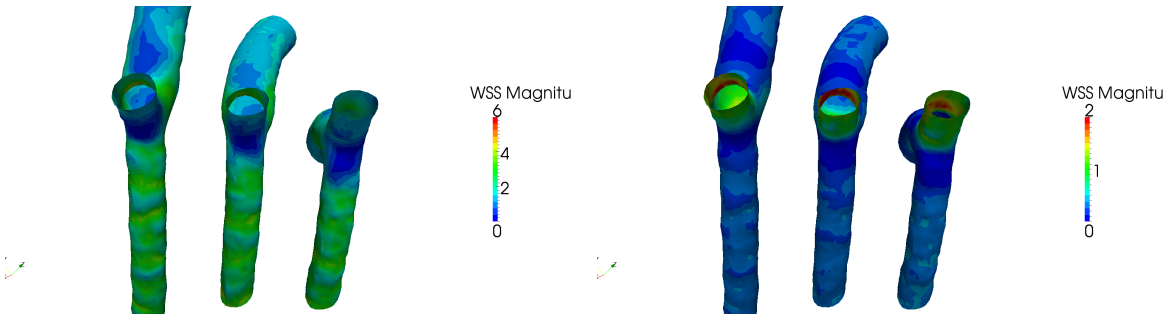

(a) $t = 0.4s$ **(b)** $t = 0.8s$

Figure 6.45: ***Patient 2 - Radial to PL anastomosis (termino-lateral)***. *Comparison of wall shear stress [Pa] at different phases of the cardiac cycle for three anastomoses types (from left to right: antegrade, T-shaped, retrograde). Proximal stenosis: 60%.*

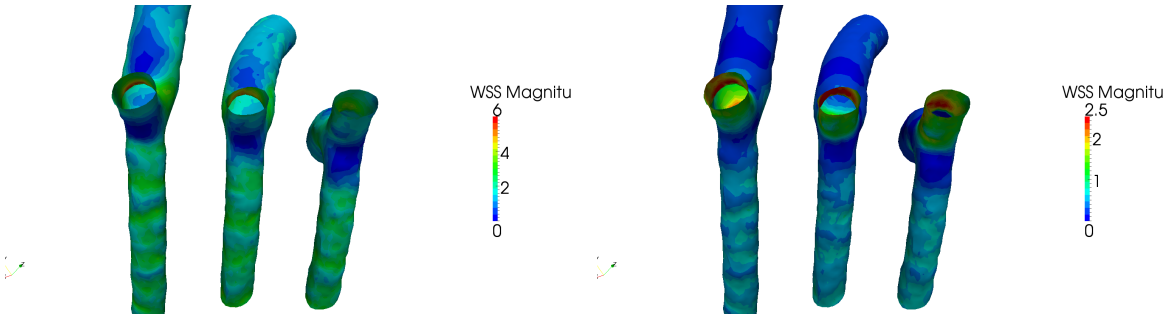

(a) $t = 0.4s$ **(b)** $t = 0.8s$

Figure 6.46: ***Patient 2 - Radial to PL anastomosis (termino-lateral).*** *Comparison of wall shear stress [Pa] at different phases of the cardiac cycle for three anastomoses types (from left to right: antegrade, T-shaped, retrograde). Proximal stenosis: 0%.*

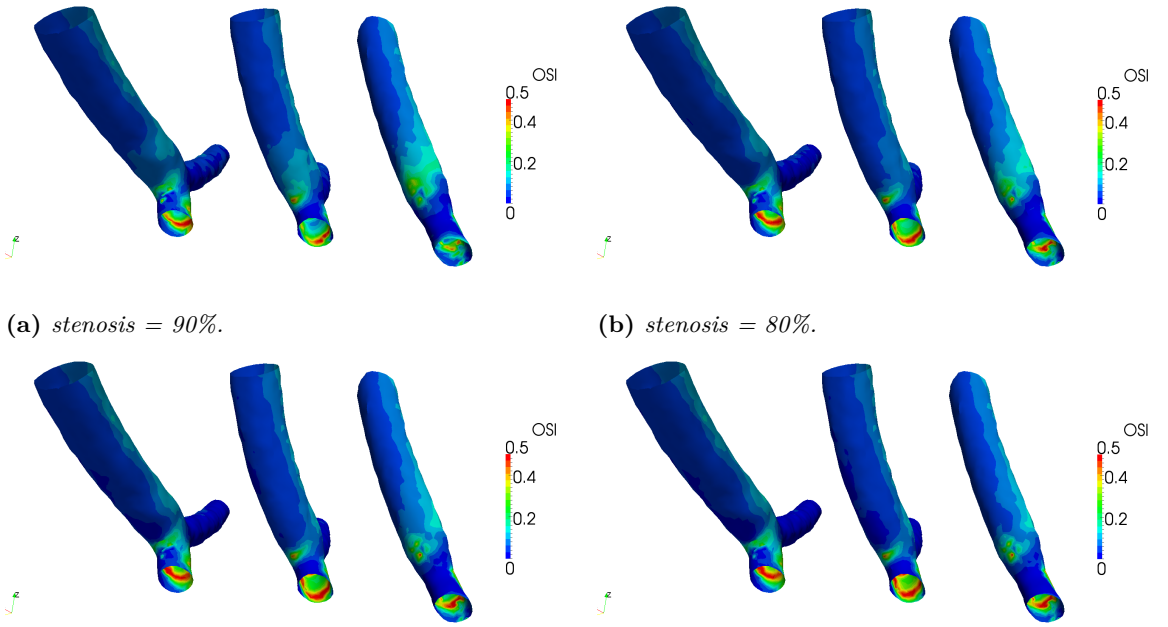

(a) *stenosis = 90%.* **(b)** *stenosis = 80%.*

(c) *stenosis = 60%.* **(d)** *stenosis = 0%.*

Figure 6.47: ***Patient 2 - Radial to PL anastomosis (termino-lateral).*** *Comparison of oscillatory shear index at different phases of the cardiac cycle for three anastomoses types (from left to right: antegrade, T-shaped, retrograde).*

(a) $t = 0.15s$

(b) $t = 0.4s$

(c) $t = 0.55s$

Figure 6.48: *Patient 2 - Radial to PL anastomosis (termino-lateral).* *Comparison of normalized transversal velocity profiles at different phases of the cardiac cycle for three anastomoses types (from top to bottom: antegrade, T-shaped, retrograde; from left to right: increasing distance from the anastomosis). Proximal stenosis: 90%.*

(a) $t = 0.15s$ **(b)** $t = 0.4s$ **(c)** $t = 0.55s$

Figure 6.49: *Patient 2 - Radial to PL anastomosis (termino-lateral).* *Comparison of normalized transversal velocity profiles at different phases of the cardiac cycle for three anastomoses types (from top to bottom: antegrade, T-shaped, retrograde; from left to right: increasing distance from the anastomosis). Proximal stenosis: 80%.*

(a) $t = 0.15s$ **(b)** $t = 0.4s$ **(c)** $t = 0.55s$

Figure 6.50: ***Patient 2 - Radial to PL anastomosis (termino-lateral).*** *Comparison of normalized transversal velocity profiles at different phases of the cardiac cycle for three anastomoses types (from top to bottom: antegrade, T-shaped, retrograde; from left to right: increasing distance from the anastomosis). Proximal stenosis: 60%.*

(a) $t = 0.15s$ **(b)** $t = 0.4s$ **(c)** $t = 0.55s$

Figure 6.51: ***Patient 2 - Radial to PL anastomosis (termino-lateral).*** *Comparison of normalized transversal velocity profiles at different phases of the cardiac cycle for three anastomoses types (from top to bottom: antegrade, T-shaped, retrograde; from left to right: increasing distance from the anastomosis). Proximal stenosis: 0%.*

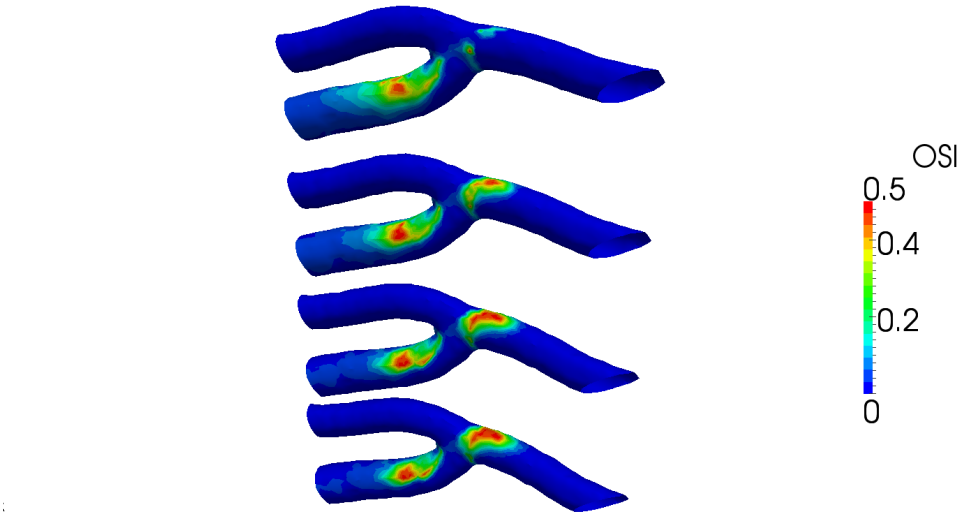

Figure 6.52: ***Patient 2 - LITA to LAD anastomosis (termino-lateral).*** *Comparison of oscillatory shear index at for decreasing proximal stenosis (from top to bottom: 90%, 80%, 60%, 0%).*

6.5.3 Discussion

The comparison is carried out for four different times: $t = 0.15\ s$ (peak LITA flow in systolic phase), $t = 0.4\ s$ (minimum LITA flow), $t = 0.55\ s$ (maximum LITA and LCA flow), $t = 0.8s$ (end diastole).

Patient 15.

- *LITA to LAD anastomosis (termino-lateral) – WSS comparison.* Figures 6.29, 6.30 and 6.31 show a comparison of wall shear stress at different phases of the cardiac cycle for three anastomoses types (from left to right: antegrade, T-shaped, retrograde) and for three different values of stenosis (90%, 60%, 0%).
  - $t = 0.15\ s$ and $t = 0.55\ s$: both T-shaped and retrograde anastomosis feature worse patterns than the antegrade anastomosis. This conclusion is based on the following facts: *(i)* at the distal arterial floor, maximum WSS values in the T-shaped and retrograde cases are approximately two times higher than the antegrade case. This pattern is unaltered with different stenosis severities. *(ii)* Intermediate WSS values are also observed in the proximal part of the arterial floor. This region is larger for T-shaped and retrograde anastomoses than the antegrade, although minimum and maximum value are not affected by the anastomosis type. Moreover, this region appears to enlarge (in particular at $t = 0.15\ s$) as the degree of proximal stenosis decreases, because of the higher residual flow in the native coronary. *(iii)* The region downstream to the toe features low WSS; for the T-shaped anastomosis, however, a smaller area of slightly higher WSS is present. *(iv)* Overall, higher WSS is present in the graft and in the distal coronary artery than in the proximal native artery, due to the higher blood flow.
  - $t = 0.4\ s$: no sensible differences can be observed among the three anastomosis types at this time step. In particular: *(i)* WSS of the same order of magnitude is observed in both the graft and the LAD. *(ii)* The toe of the graft features high values of WSS; the area of the region of high WSS slightly increases as the proximal

stenosis decreases. *(iii)* The region of highest WSS on the arterial floor is more downstream in the T-shaped and retrograde cases than in the antegrade case; however, apart from this region, the magnitude of the WSS on the proximal arterial floor is comparable to the magnitude on the distal part. *(iv)* The magnitude of the maximum WSS increases for decreasing stenosis.

- $t = 0.8\ s$: both T-shaped and retrograde anastomosis feature worse patterns than the antegrade anastomosis. In particular: *(i)* a region of high WSS is present near the toe of the graft for both T-shaped and retrograde; this region is however not present in the antegrade case. Maximum WSS in the former case are approximately two times higher than the latter. This behavior is not influenced by the stenosis. *(iii)* The proximal arterial floor features low WSS, while the distal arterial floor features higher values of WSS. This behavior is different than the one observed at $t = 0.15\ s$. *(iv)* Low WSS is also computed in the region downstream to the toe; T-shaped and retrograde anastomosis feature a wider region of low WSS.

Thanks to the fast evaluation of the reduced-order model it is possible to study the behavior of the WSS for several different configurations of antegrade, T-shaped and retrograde grafts, characterized by different grafting angles θ (antegrade: $\theta \ll 90°$, T-shaped: $\theta \approx 90°$, retrograde: $\theta \gg 90°$). Figure 6.38(a) shows the maximum WSS at the arterial bed as a function of the anastomosis angle and time. This plot shows, in agreement with the previous discussion, that WSS increases with the grafting angle at $t = 0.15\ s$ and $t = 0.55\ s$. Figures 6.38(b)-(c) study also the WSS at the heel of the anastomosis. For small anastomosis angles (antegrade anastomoses) WSS at the heel and at the arterial floor are comparable in the whole time interval, except that in a neighborhood of $t = 0.4$, when WSS at the heel is smaller than WSS at the bed. This is the most favorable condition. In contrast, for larger anastomosis angles, the ratio between WSS at the heel and WSS at the arterial floor is smaller than one, except for $t = 0.4\ s$. Local minima are found near T-shaped configurations: this is caused both by the increasing WSS at the arterial floor, and WSS at the heel that is decreasing for $\theta < 90°$ and increasing for $\theta > 90°$.

- *LITA to LAD anastomosis (termino-lateral) – transversal velocity profiles comparison.* The analysis of transversal velocity profiles (normalized by the maximum velocity in the anastomosis, at the same time), carried out in Figures 6.32, 6.33 and 6.34, highlights the formation of Dean vortices in the region of the anastomosis. A comparison of transversal velocity profiles at different phases of the cardiac cycle for three anastomoses types, different values of stenosis (90%, 60%, 0%) is carried out at increasing distance from the anastomosis. The formation of at least two Dean vortices is observed in all cases, and at all times. *(i)* Peak values of transversal velocity are reached at $t = 0.55\ s$, when both LITA and LCA feature maximum flow. *(ii)* Minimum values over the whole time interval are reached at $t = 0.4\ s$, when LITA flow is minimum. *(iii)* Dean vortices are dissipated more quickly in the antegrade anastomosis than in the T-shaped and retrograde ones. *(iv)* Although it is apparent that antegrade anastomosis features lower transversal than both T-shaped and retrograde anastomoses in the section closest to the anastomosis, a comparison among the latter cases yields different results for different time steps ($t = 0.15\ s$: T-shaped features higher transversal velocity; the opposite is true instead for $t = 0.4\ s$ and $t = 0.8\ s$, while a similar behavior among the two cases is observed for $t = 0.55\ s$). *(v)* A third vortex may be formed in retrograde anastomosis, especially for high stenosis and a peak LITA flow. This is particularly apparent in the second slice on the third row of Figure 6.32(a).

- *LITA to LAD anastomosis (termino-lateral) – pressure drop comparison.* Figures 6.35, 6.36 and 6.37 show a comparison of the pressure drop in the anastomosis. The pressure drop is minimum for antegrade anastomosis; T-shaped and retrograde anastomoses feature instead an higher pressure drop. An higher pressure drop is obtained decreasing the stenosis severity; this is a strong confirmation of the clinical experience that a CABG surgery should be performed only for critical stenoses (greater than 70%).

Patient 6.

- *SVG to PDA anastomosis (termino-lateral) – WSS comparison.* Figures 6.39, 6.40, 6.41 and 6.42 show a comparison of wall shear stress at different phases of the cardiac cycle for three anastomoses types and for four different values of stenosis (90%, 80%, 60%, 0%). Remarkable differences can be highlighted with respect to Patient 15. Those differences are because of the different graft material. In fact, while a LITA (arterial) graft was employed in Patient 15, in this case a SVG (venous) graft is studied, which is characterized by a larger radius. *(i)* WSS on the graft is lower than WSS in the distal arterial floor. This is in contrast to the arterial anastomosis case, where those WSS values were of the same order of magnitude. This is motivated by the larger diameter of the SVG graft. *(ii)* In the retrograde case, maximum values of WSS are observed on the lateral arterial surface distal to the anastomosis and near the toe of the graft. The magnitude in these regions is almost twice the magnitude in the antegrade and T-shaped cases. *(iii)* Antegrade and T-shaped anastomoses behave similarly at $t = 0.15\ s$, $t = 0.55\ s$ and $t = 0.8\ s$; intermediate WSS values (approximately half than the retrograde case) are obtained near the toe and distal to the anastomosis. At $t = 0.4\ s$, instead, retrograde and T-shaped anastomoses behave in similar way, with comparable values of WSS near the toe.

Patient 2.

- *Radial to PL anastomosis (termino-lateral) – WSS comparison, OSI comparison.* Figures 6.43, 6.44, 6.45 and 6.46 show a comparison of wall shear stress at different phases of the cardiac cycle for three anastomoses types and for four different values of stenosis (90%, 80%, 60%, 0%). OSI is showed in Figure 6.47. The analysis in this case is similar to the one carried out for Patient 6. Moreover: *(i)* the arterial floor close to the anastomosis features a region of low WSS at $t = 0.4\ s$ and $t = 0.8\ s$. This is in contrast to Patient 15, where local maxima of WSS were present in the same region. This different behavior is also related to the larger radius of the Radial artery graft than the LITA graft. The same region features high OSI values. *(ii)* Maximum WSS values at $t = 0.8\ s$ increase as the stenosis decreases: this is in agreement with the current clinical practice, that prescribes the usage of radial artery as a graft only when stenosis is greater than 70%. Maximum values are located near the heel of the graft. The region also features intermediate OSI values.

- *Radial to PL anastomosis (termino-lateral) – transversal velocity profiles comparison.* The analysis of transversal velocity profiles, carried out in Figures 6.48, 6.49, 6.50 and 6.51, highlights that Dean vortices may appear in the region of the anastomosis. In contrast to the LITA-LAD anastomosis in Patient 15: *(i)* transversal velocity maximum value is the same for $t = 0.15\ s$ and $t = 0.55\ s$. *(ii)* No Dean vortices appear at $t = 0.4\ s$. *(iii)* The magnitude of transversal velocity is lower than the one observed in Patient 15, for all considered time steps. *(iv)* A third vortex does not appear in the retrograde case.

- *LITA to LAD anastomosis (termino-lateral) – OSI comparison.* Figure 6.52 shows the OSI for the LITA to LAD anastomosis. OSI assumes its maximum value in the LAD,

proximal to the anastomosis, and near the toe of the graft. Moreover, a larger area of maximum OSI can be noted near the toe of the graft for decreasing proximal stenosis; this is motivated by the higher residual flow in the LAD.

CHAPTER 7

Conclusions and perspectives

7.1 Conclusions

A computational framework for the study of the haemodynamics in patient-specific configurations of coronary artery bypass grafts (CABGs) has been proposed in this thesis. This framework is composed of three Parts:

I. in the first Part, concerning clinical data and medical imaging, a pipeline for the acquisition of patient-specific geometries has been described.

   The current clinical dataset presents a broad variability of both disease and surgical intervention, with the aim of being representative of the most common cases. To the best of our knowledge, although few recent works have been devoted to the study of patient-specific CABGs, our current dataset is significantly wider than any of the previous studies. This is an important contribution of the present work, especially in the study of complex sequential grafting procedures (Y-graft of the internal mammary artery with radial artery or saphenous vein, and successive anastomoses to obtain a complete revascularization of the heart) that are widely employed in the clinical practice but not yet completely studied from a numerical standpoint.

   A medical imaging pipeline has been setup to build a mesh from CT-scan clinical data. Even though it is partially based on existing software toolboxes, their combination (filters to enhance the image, level set segmentation, centerline extraction, tubular structure representation), their specialization to the case of CABGs and its extensive application to a large dataset of patient-specific CABGs is an important contribution of the current work. The proposed pipeline has in fact been then applied to each one of the fourteen patients in the current clinical dataset.

II. the focus of the second Part has been instead on the methodological development of model order reduction techniques. Parametric studies are relevant in the present CABG study, since the interest of the clinician is to evaluate the outcome of the surgery not only

for a single physical or geometrical configuration, but for several related ones obtained either because of different flow conditions (such as inlet flow rates at the grafts) caused by an increased blood request due to physical activity, or because of the interest in the comparison of the outcome of the surgery for relevant local variations of the geometry, related both to native coronary artery disease (stenosis severity) or surgery (different anastomosis geometry). In the context of parametrized problems, reduced-order models have been introduced in the last decades to decrease the required computational costs.

A POD-Galerkin reduced-order model (ROM) has been introduced in this Part. Two aspects have been addressed in particular, namely the proposal of a ROM for the simultaneous approximation of velocity and pressure in unsteady incompressible Navier-Stokes flows, and efficient compression of the temporal trajectory. For the first issue, we proposed an enrichment procedure of the reduced velocity space by means of supremizer solutions in order to obtain an inf-sup stable reduced-order model. A theoretical result to detect the existence of spurious pressure modes in the online stage has been proved, and the relation between the online stability factors and the online dimension of the reduced spaces has been studied, characterizing in this way the minimum number of supremizer basis functions that are needed to obtain a stable ROM. For the second issue, we proposed a two-level POD to provide a compression of the temporal trajectory.

III. in the third Part, shape parametrization techniques are discussed.

A new idea of shape parametrization has been introduced, and has been named centerlines-based parametrization. It is based on the assumption that coronary arteries and bypass grafts are represented as a network of tubular geometries. This parametrization is an additional model order reduction technique itself, since deformation of three-dimensional vessels is ascribed to the variation of few relevant parameters defined on the unidimensional centerlines, such as local radii or local tangent vectors. These account in particular for stenosis severity and anastomosis features, respectively.

The proposed framework has then been applied to some patient-specific CABG configurations. As a first case, we considered variation of physical parameters only related to inlet flow rates. These results have shown that such parameters have a significant impact on the magnitude of wall shear stress (WSS) and the extension of the region of high oscillatory shear index (OSI). We also noted that the Y-graft features in general highest WSS, and that WSS in the successive side-to-side and end-to-side anastomoses gradually decreases. Regions with high and oscillatory stresses are clearly identified by the proposed reduced computational framework, leading to several insights on the locations where the intimal hyperplasia may occur in each patient-specific configuration.

As a second scenario, we considered the variation of both inlet flow rates and stenosis severity. Critical and non-critical cases are compared; in particular, the variation of the regions of high OSI, both upstream and downstream stenoses and near anastomoses, with respect to physical and geometrical parameters have been shown on patient-specific cases. Moreover, the exploration of the entire parameter space by means of the ROM allows, for example, to investigate the relation between stenosis severity and pressure drop or maximum WSS in the stenosis. These relations are in fact of particular interest in the pre-surgical phase since, for example, pressure measurements are used to assess the coronary artery disease. The effect of the severity of the stenosis is evaluated both near anastomoses and at native coronary arteries bifurcations; both regions are critical from a fluid dynamics standpoint, and increased stenosis severity causes in fact higher WSS at native bifurcations. Moreover, a comparison on the same patient before and after the surgery is performed, to evaluate the variation induced by bypass grafts on these patterns.

As a third case, the variation of both stenosis and end-to-side anastomoses has been studied. Some differences are observed between mammary artery, saphenous vein and radial artery cases; in particular, we have observed that in the mammary artery case flow-direction anastomosis presents better haemodynamic indicators than T-shaped anastomosis, while in the saphenous vein the two anastomosis are comparable. Local patterns of transversal velocity distal to the anastomosis show the formation of two Dean vortices. Critical regions are located near the heel and the toe of the graft, and on the arterial bed of the native vessel. Querying the ROM allows for example to draw a plot of the maximum WSS at these critical regions with respect to the grafting angle, showing that WSS on the arterial bed increases with the the grafting angle.

In all cases, after a computationally intensive offline stage performed on HPC architectures, our POD-Galerkin ROM has allowed to obtain haemodynamics simulations at greatly reduced computational costs, with savings up to 99% of user time for each new online query.

7.2 Perspectives

Several improvements are possible for the proposed framework and in the study of patient-specific coronary artery bypass grafts. In particular, we mention the following aspects:

- *compliance and rheological properties of the grafts:* as discussed in Section 1.3, remarkable differences have been observed in the clinical practice on the outcome (patency rates) of the surgery depending on the graft employed (mammary artery, saphenous vein, radial artery). The proposed model has allowed us to consider a first relevant aspect that differentiates these materials: the average radius of the vessel. Numerical results (see in particular Section 6.5) have shown that the different graft-to-host diameter ratios alone are able to account for different results in the comparison between flow-direction, T-shaped and retrograde anastomoses. These results are in good agreement with the current clinical practice. However, as an improvement of the proposed computational model, compliance effects should be taken into account. The rigid walls assumption should then be relaxed and a *fluid-structure interaction (FSI)* problem shall be solved. This is a very challenging aspect. In fact, a thorough analysis on the structural properties of the grafts needs to be performed. On one hand, different rheological models should be used to differentiate between arterial and vein grafts. On the other hand, even in the sole class of arterial grafts, the structural model should be able to capture the remarkable differences that occur in the clinical practice between mammary artery grafts and radial artery grafts. In fact, it is nowadays agreed in the clinical community that the mammary artery graft is the gold standard for the revascularization of the left anterior descending, and that the same performance *cannot* be obtained when employing a radial artery graft.

- *heart motion:* another important development could be oriented to the inclusion of myocardial motion, since coronary arteries lie on the myocardium. Although cyclic curvature deformation of coronary arteries do have strong effect on the local distribution of wall shear stress [187, 206, 273], it typically changes the magnitude rather than the macroscopic characteristics of the flow. For these reasons, this aspect has been neglected in this thesis. As noted in [270], this topic is significantly challenging. From the modeling point of view, a *fluid-structure interaction (FSI)* problem shall be solved in this case [206, 256, 258]. Two effects need to be taken into account for the structural model: myocardial motion, and the contraction/dilation of the coronary arteries during the

cardiac cycle. The current medical imaging pipeline shall be improved in order to extract (if possible) such information from the clinical data.

- *graft adaptation and flow competition:* these two aspects are particularly relevant in the study of mammary artery grafts, and concern the variation over time of the flow rate in the graft [117]. In fact, it has been observed that mammary artery grafts are able to adapt their flow rate in response to the severity of the stenosis in the native coronary arteries. The latter phenomena, which in the clinical literature is usually referred to as flow competition, entails a monotonically increasing dependence between the flow rate in the mammary artery graft and the severity of the stenosis. Sources of additional complexity arise from the nonlinear nature of this relation, that cannot be fully taken into account by a multiplicative factor on the graft flow rate. In fact, also the geometrical features of the graft (in the whole vessel, not just at the inlet from the subclavian artery) are affected by this phenomena, since the flow rate adaptation is obtained through a variation of the radius of the graft and, thus, cannot be completely modelled by a multiplicative factor on the boundary condition. As a final source of complexity, these phenomena usually occur years after the surgery.

- *extension of the centerlines-based parametrization*: the proposed parametrization could also be extended to capture more accurately local geometrical features of the patient-specific configuration. In particular, a more general shape (rather than a circle with variable radius) could be swept along the centerlines in the generation of the tubular network of coronary arteries and grafts.

- *more complex outflow boundary conditions:* the feasibility of the application of more advanced boundary conditions on the outflow sections, such as multiscale lumped parameters models [142, 228] or empirical flow-diameter relations [261], should be assessed. Their integration with required clinical data (ventricular volumes, ventricular pressures, etc.) should also be investigated.

- *patient-specific coronary arteries flow rates:* a considerable effort has been made throughout the thesis to develop personalized (patient-specific) simulations. A possible improvement, still in view of a better personalization, would be to replace the flow rates in Section 6.2 with patient-specific ones. This will pose a significant challenge from the technical point of the acquisition of clinical data, since methods for the measurements of velocities and flow rates are still too invasive to be used in the daily clinical practice.

- *integration between different patients:* numerical results in Chapter 6 have shown that the proposed computational framework is able to provide numerical simulations on patient-specific geometries at greatly reduced computational costs. A computationally expensive phase needs to be performed once, for each patient. The next step for the extensive application of reduced-order models in the clinical practice would then be to store a database of offline basis functions for *each* patient (say, for each one of the fourteen patients reconstructed in this thesis) and to be able to query it each time a *new* patient arrives. Formidable challenges need to be undertaken to implement this idea. From a technical point of view, possibly a better integration between the software employed at the radiology departments of the hospitals and the computational mesh generation pipeline (such as the one proposed in Chapter 2) should be sought. In this way, the mesh generation step itself would be deployed in the clinical environment. From a methodological point of view, techniques like the reduced basis element method, or reduced basis hybrid methods, or more in general reduced-order models based on a

domain decomposition approach (see [129] and references therein) should be integrated in this application. This is an area of ongoing research, even on simplified geometrical configurations and test cases. These methods would, in principle, allow to decompose the patient-specific geometry in a sequence of subdomains (say, one for the LAD, one for the LAD-LCX bifurcation, one for the LITA-LAD anastomosis, etc.), and then combine them for each new patient. A considerable challenge for this idea is, finally, that no one-to-one correspondence between the vessels of two patients can be obtained in general, because of different anatomical features (for instance, left or right dominance, or presence or absence of the ramus intermedius) and grafting procedures (different revascularized coronary arteries, different anastomosis locations, single or sequential grafts).

7.3 Acknowledgements

The collaboration with clinicians at Ospedale Luigi Sacco in Milan has been the leading motivation and most stimulating aspect of this work. I am most grateful to my supervisor Dr. Roberto Scrofani, M.D. (Division of Cardiac Surgery), for his invaluable insights on coronary artery bypass grafts, countless suggestions, strong interest and enthusiasm in the application of computational methods to cardiovascular applications. I am grateful to each one of the fifteen patients who have accepted to be part of this study. I also acknowledge Dr. Sonia Ippolito, M.D. (Division of Radiology), for her collaboration in the acquisition of the clinical data, and her insights and suggestions on the clinical and anatomical description of each patient.

I acknowledge Prof. Alfio Quarteroni for his supervision of this work, and the opportunity to be part of both his research group at MOX and the project in collaboration with Ospedale Sacco. I am also grateful to my co-advisors Prof. Gianluigi Rozza (SISSA mathLab), Dr. Elena Faggiano, Dr. Andrea Manzoni (EPFL CMCS), for their collaboration facing the several different aspects involved in this project. This work has also benefited from the collaboration with Dott. Riccardo Ferrero (Politecnico di Torino), who carried out his master thesis under my co-supervision.

The work of this thesis lead to the development of an object-oriented C++ library, based on `rbOOmit & libMesh` [143, 146] for finite element computations, `PETSc & SLEPc` [21, 123] for parallel linear algebra, sparse linear solvers and eigenproblem solvers, `GiNaC` [32] for symbolic computations and `VTK & vmtk` [11] for medical imaging. I am grateful to the developers and user support communities of these libraries. The computational support of high performance computing facilities at CINECA (PLX, Eurora; "Convenzione di Ateneo" agreement between Politecnico di Milano and CINECA, and project COGESTRA) and Istituto Nazionale di Fisica Nucleare (Zefiro; project SUMA, through an agreement with SISSA mathLab) is also gratefully acknowledged.

Bibliography

[1] C. Acar, V. A. Jebara, M. Portoghese, B. Beyssen, J. Y. Pagny, P. Grare, J. C. Chachques, J.-N. Fabiani, A. Deloche, J. L. Guermonprez, and A. F. Carpentier. Revival of the radial artery for coronary artery bypass grafting. *The Annals of Thoracic Surgery*, 54(4):652–660, 1992.

[2] C. Acar, A. Ramsheyi, J.-Y. Pagny, V. Jebara, P. Barrier, J.-N. Fabiani, A. Deloche, J.-L. Guermonprez, and A. Carpentier. The radial artery for coronary artery bypass grafting: clinical and angiographic results at five years. *The Journal of Thoracic and Cardiovascular Surgery*, 116(6):981–989, 1998.

[3] F. D. Affonso da Costa, I. Affonso da Costa, R. Poffo, D. Abuchaim, R. Gaspar, L. Garcia, and D. L. Faraco. Myocardial revascularization with the radial artery: a clinical and angiographic study. *The Annals of Thoracic Surgery*, 62(2):475–480, 1996.

[4] V. Agoshkov, A. Quarteroni, and G. Rozza. A mathematical approach in the design of arterial bypass using unsteady Stokes equations. *Journal of Scientific Computing*, 28:139–165, 2006.

[5] V. Agoshkov, A. Quarteroni, and G. Rozza. Shape design in aorto-coronaric bypass anastomoses using perturbation theory. *SIAM Journal On Numerical Analysis*, 44(1):367–384, 2007.

[6] I. Akhtar, A. H. Nayfeh, and C. J. Ribbens. On the stability and extension of reduced-order Galerkin models in incompressible flows. *Theoretical and Computational Fluid Dynamics*, 23(3):213–237, 2009.

[7] E. I. Amoiralis and I. K. Nikolos. Freeform deformation versus B-spline representation in inverse airfoil design. *Journal of Computing and Information Science in Engineering*, 8(2):1–13, 2008.

[8] H. V. Anderson, M. J. Stokes, M. Leon, S. A. Abu-Halawa, Y. Stuart, and R. L. Kirkeeide. Coronary artery flow velocity is related to lumen area and regional left ventricular mass. *Circulation*, 102(1):48–54, 2000.

[9] L. Antiga. *Patient-Specific Modeling of Geometry and Blood Flow in Large Arteries*. PhD thesis, Dipartimento di Bioingegneria, Politecnico di Milano, 2002.

[10] L. Antiga, B. Ene-Iordache, and A. Remuzzi. Computational geometry for patient-specific reconstruction and meshing of blood vessels from MR and CT angiography. *IEEE Transactions on Medical Imaging*, 22(5):674–684, 2003.

[11] L. Antiga, M. Piccinelli, L. Botti, B. Ene-Iordache, A. Remuzzi, and D. Steinman. An image-based modeling framework for patient-specific computational hemodynamics. *Medical and Biological Engineering and Computing*, 46:1097–1112, 2008.

[12] L. Antiga and D. A. Steinman. Robust and objective decomposition and mapping of bifurcating vessels. *IEEE Transactions on Medical Imaging*, 23(6):704–713, 2004.

[13] N. Aubry. On the hidden beauty of the proper orthogonal decomposition. *Theoretical and Computational Fluid Dynamics*, 2:339–352, 1991.

[14] N. Aubry, P. Holmes, J. Lumley, and E. Stone. The dynamics of coherent structures in the wall region of a turbulent boundary layer. *Journal of Fluid Mechanics*, 192:115–173, 1988.

[15] C. Audouze, F. De Vuyst, and P. B. Nair. Reduced-order modeling of parameterized PDEs using time–space-parameter principal component analysis. *International Journal for Numerical Methods in Engineering*, 80(8):1025–1057, 2009.

[16] C. Audouze, F. De Vuyst, and P. B. Nair. Nonintrusive reduced-order modeling of parametrized time-dependent partial differential equations. *Numerical Methods for Partial Differential Equations*, 29(5):1587–1628, 2013.

[17] W. Austen, J. Edwards, R. Frye, G. Gensini, V. Gott, L. Griffith, D. McGoon, M. Murphy, and B. Roe. A reporting system on patients evaluated for coronary artery disease. Report of the ad hoc committee for grading of coronary artery disease, Council on cardiovascular surgery, American Heart Association. *Circulation*, 51(4):5–40, 1975.

[18] J. Baiges, R. Codina, and S. Idelsohn. A domain decomposition strategy for reduced order models. Application to the incompressible Navier–Stokes equations. *Computer Methods in Applied Mechanics and Engineering*, 267:23–42, 2013.

[19] J. Baiges, R. Codina, and S. Idelsohn. Explicit reduced-order models for the stabilized finite element approximation of the incompressible Navier–Stokes equations. *International Journal for Numerical Methods in Fluids*, 72(12):1219–1243, 2013.

[20] J. Baiges, R. Codina, and S. R. Idelsohn. Reduced-order modelling strategies for the finite element approximation of the incompressible Navier-Stokes equations. In S. R. Idelsohn, editor, *Numerical Simulations of Coupled Problems in Engineering*, volume 33 of *Computational Methods in Applied Sciences*, pages 189–216. Springer International Publishing, 2014.

[21] S. Balay, W. D. Gropp, L. C. McInnes, and B. F. Smith. Efficient management of parallelism in object oriented numerical software libraries. In E. Arge, A. M. Bruaset, and H. P. Langtangen, editors, *Modern Software Tools in Scientific Computing*, pages 163–202. Birkhäuser Press, 1997.

[22] F. Ballarin. Shape optimization for three-dimensional viscous flows in cardiovascular geometries (in Italian). Master's thesis, MOX, Dipartimento di matematica, Politecnico di Milano, 2011. `http://mox.polimi.it/it/progetti/pubblicazioni/viewtesi.php?id=490&en=en`.

[23] F. Ballarin, A. Manzoni, A. Quarteroni, and G. Rozza. Supremizer stabilization of POD–Galerkin approximation of parametrized steady incompressible Navier–Stokes equations. International Journal for Numerical Methods in Engineering (in press, published online at `http://onlinelibrary.wiley.com/doi/10.1002/nme.4772/abstract`), 2014.

[24] F. Ballarin, A. Manzoni, G. Rozza, and S. Salsa. Shape optimization by Free-Form Deformation: existence results and numerical solution for Stokes flows. *Journal of Scientific Computing*, 60(3):537–563, 2014.

[25] J. Barboriak, G. Batayias, K. Pintar, T. Tieu, D. Van Horn, and M. Korns. Late lesions in aorta-coronary artery vein grafts. *The Journal of Thoracic and Cardiovascular Surgery*, 73(4):596–601, 1977.

[26] O. Barnea and W. P. Santamore. Intraoperative monitoring of IMA flow: what does it mean? *The Annals of Thoracic Surgery*, 63(6, Supplement 1):S12–S17, 1997.

[27] H. Barner, J. Standeven, and J. Reese. Twelve-year experience with internal mammary artery for coronary artery bypass. *The Journal of Thoracic and Cardiovascular Surgery*, 90(5):668–675, 1985.

[28] M. Barrault, Y. Maday, N. C. Nguyen, and A. T. Patera. An 'empirical interpolation' method: application to efficient reduced-basis discretization of partial differential equations. *Comptes Rendus Mathematique*, 339(9):667–672, 2004.

[29] T. D. Bartley, J. C. Bigelow, and U. S. Page. Aortocoronary bypass grafting with multiple sequential anastomoses to a single vein. *Archives of Surgery*, 105(6):915–917, 1972.

[30] H. S. Bassiouny, S. White, S. Glagov, E. Choi, D. P. Giddens, and C. K. Zarins. Anastomotic intimal hyperplasia: mechanical injury or flow induced. *Journal of Vascular Surgery*, 15(4):708–717, 1992.

[31] K. Bathe. The inf-sup condition and its evaluation for mixed finite element methods. *Computers & Structures*, 79(2):243–252, 2001.

[32] C. Bauer, A. Frink, and R. Kreckel. Introduction to the ginac framework for symbolic computation within the c++ programming language. *Journal of Symbolic Computation*, 33(1):1–12, 2002.

[33] C. S. Beck. The development of a new blood supply to the heart by operation. *Annals of Surgery*, 102(5):801–813, 1935.

[34] A. Beckert and H. Wendland. Multivariate interpolation for fluid-structure-interaction problems using radial basis functions. *Aerospace Science and Technology*, 5(2):125–134, 2001.

[35] M. Bergmann, C.-H. Bruneau, and A. Iollo. Enablers for robust POD models. *Journal of Computational Physics*, 228(2):516–538, 2009.

[36] G. Berkooz, P. Holmes, and J. Lumley. The Proper Orthogonal Decomposition in the analysis of turbulent flows. *Annual Review of Fluid Mechanics*, 25(1):539–575, 1993.

[37] L. Bertagna and A. Veneziani. A model reduction approach for the variational estimation of vascular compliance by solving an inverse fluid–structure interaction problem. *Inverse Problems*, 30(5):055006:1–055006:23, 2014.

[38] C. Bertolotti and V. Deplano. Three-dimensional numerical simulations of flow through a stenosed coronary bypass. *Journal of Biomechanics*, 33(8):1011–1022, 2000.

[39] C. Bertolotti, V. Deplano, J. Fuseri, and P. J. Dupouy. Numerical and experimental models of post-operative realistic flows in stenosed coronary bypasses. *Journal of Biomechanics*, 34(8):1049–1064, 2001.

[40] R. L. Bishop. There is more than one way to frame a curve. *American Mathematical Monthly*, 82(3):246–251, 1975.

[41] A. Blitz, R. M. Osterday, and R. F. Brodman. Harvesting the radial artery. *Annals of Cardiothoracic Surgery*, 2(4):533–542, 2013.

[42] M. Bonert, J. Myers, S. Fremes, J. Williams, and C. Ethier. A numerical study of blood flow in coronary artery bypass graft side-to-side anastomoses. *Annals of Biomedical Engineering*, 30(5):599–611, 2002.

[43] M. Boulakia, E. Schenone, and J.-F. Gerbeau. Reduced-order modeling for cardiac electrophysiology. Application to parameter identification. *International Journal for Numerical Methods in Biomedical Engineering*, 28(6-7):727–744, 2012.

[44] M. Bourassa, L. Fisher, L. Campeau, M. Gillespie, M. McConney, and J. Lesperance. Long-term fate of bypass grafts: the Coronary Artery Surgery Study (CASS) and Montreal Heart Institute experiences. *Circulation*, 72(6 Pt 2):V71–V78, 1985.

[45] E. Boutsianis, H. Dave, T. Frauenfelder, D. Poulikakos, S. Wildermuth, M. Turina, Y. Ventikos, and G. Zund. Computational simulation of intracoronary flow based on real coronary geometry. *European Journal of Cardio-Thoracic Surgery*, 26(2):248–256, 2004.

[46] A. Brandts, S. D. Roes, J. Doornbos, R. G. Weiss, A. de Roos, M. Stuber, and J. J. Westenberg. Right coronary artery flow velocity and volume assessment with spiral K-space sampled breathhold velocity-encoded MRI at 3 tesla: accuracy and reproducibility. *Journal of Magnetic Resonance Imaging*, 31(5):1215–1223, 2010.

[47] F. Brezzi and K. Bathe. A discourse on the stability conditions for mixed finite element formulations. *Computer Methods in Applied Mechanics and Engineering*, 82(1–3):27–57, 1990.

[48] F. Brezzi and M. Fortin. *Mixed and hybrid finite element methods*. Springer-Verlag New York, 1991.

[49] M. D. Buhmann. Radial basis functions. *Acta Numerica 2000*, 9:1–38, 2000.

[50] M. D. Buhmann. *Radial Basis Functions: theory and implementations*. Cambridge University Press, 2003.

[51] B. H. Bulkley and G. M. Hutchins. Accelerated "atherosclerosis". A morphologic study of 97 saphenous vein coronary artery bypass grafts. *Circulation*, 55(1):163–169, 1977.

[52] J. Burkardt, M. Gunzburger, and H.-C. Lee. POD and CVT-based reduced-order modeling of Navier–Stokes flows. *Computer Methods in Applied Mechanics and Engineering*, 196(1–3):337–355, 2006.

[53] J. Butany, T. David, and M. Ojha. Histological and morphometric analyses of early and late aortocoronary vein grafts and distal anastomoses. *The Canadian Journal of Cardiology*, 14(5):671–677, 1998.

[54] B. F. Buxton and P. A. Hayward. The art of arterial revascularization–total arterial revascularization in patients with triple vessel coronary artery disease. *Annals of Cardiothoracic Surgery*, 2(4):543–551, 2013.

[55] F. Cademartiri, G. Runza, M. Belgrano, G. Luccichenti, N. R. Mollet, P. Malagutti, M. Silvestrini, M. Midiri, M. Cova, R. Pozzi Mucelli, and G. P. Krestin. Introduction to coronary imaging with 64-slice computed tomography. *La radiologia medica*, 110(1-2):16–41, 2005.

[56] K. Cagli, M. Emir, A. Kunt, K. Ergun, M. Tola, M. Topbas, K. Vural, and E. Sener. Evaluation of flow characteristics of the left internal thoracic artery graft: perioperative color Doppler ultrasonography versus intraoperative free-bleeding technique. *Texas Heart Institute Journal*, 31(4):376–381, 2004.

[57] A. Caiazzo, T. Iliescu, V. John, and S. Schyschlowa. A numerical investigation of velocity-pressure reduced order models for incompressible flows. *Journal of Computational Physics*, 259:598–616, 2014.

[58] A. Cameron, K. B. Davis, G. Green, and H. V. Schaff. Coronary bypass surgery with internal-thoracic-artery grafts – effects on survival over a 15-year period. *New England Journal of Medicine*, 334(4):216–220, 1996.

[59] L. Campeau, M. Enjalbert, J. Lespérance, C. Vaislic, C. Grondin, and M. Bourassa. Atherosclerosis and late closure of aortocoronary saphenous vein grafts: sequential angiographic studies at 2 weeks, 1 year, 5 to 7 years, and 10 to 12 years after surgery. *Circulation*, 68(3 Pt 2):II1–II7, 1983.

[60] F. Campolongo, J. Cariboni, and A. Saltelli. An effective screening design for sensitivity analysis of large models. *Environmental Modelling & Software*, 22(10):1509–1518, 2007.

[61] K. Carlberg, C. Bou-Mosleh, and C. Farhat. Efficient non-linear model reduction via a least-squares Petrov-Galerkin projection and compressive tensor approximations. *International Journal for Numerical Methods in Engineering*, 86(2):155–181, 2011.

[62] K. Carlberg, C. Farhat, J. Cortial, and D. Amsallem. The GNAT method for nonlinear model reduction: effective implementation and application to computational fluid dynamics and turbulent flows. *Journal of Computational Physics*, 242:623–647, 2013.

[63] A. Carpentier, J. Guermonprez, A. Deloche, C. Frechette, and C. DuBost. The aorta-to-coronary radial artery bypass graft: a technique avoiding pathological changes in grafts. *The Annals of Thoracic Surgery*, 16(2):111–121, 1973.

[64] W. Cazemie, R. Verstappen, and A. Veldman. Proper orthogonal decomposition and low-dimensional models for driven cavity flows. *Physics of Fluids*, 10(7):1685–1699, 1998.

[65] T. Chaichana, Z. Sun, and J. Jewkes. Computation of hemodynamics in the left coronary artery with variable angulations. *Journal of Biomechanics*, 44(10):1869–1878, 2011.

[66] T. Chaichana, Z. Sun, and J. Jewkes. Computational fluid dynamics analysis of the effect of plaques in the left coronary artery. *Computational and Mathematical Methods in Medicine*, 2012(10):1–9, 2012.

[67] B. R. Chaitman, E. L. Alderman, L. T. Sheffield, T. Tong, L. Fisher, M. B. Mock, R. D. Weins, G. C. Kaiser, D. Roitman, R. Berger, B. Gersh, H. Schaff, M. G. Bourassa, and T. Killip. Use of survival analysis to determine the clinical significance of new Q waves after coronary bypass surgery. *Circulation*, 67(2):302–309, 1983.

[68] D. Chapelle, A. Gariah, P. Moireau, and J. Sainte-Marie. A Galerkin strategy with Proper Orthogonal Decomposition for parameter-dependent problems – analysis, assessments and applications to parameter estimation. *ESAIM: Mathematical Modelling and Numerical Analysis*, 47(6):1821–1843, 2013.

[69] D. Chapelle, A. Gariah, and J. Sainte-Marie. Galerkin approximation with Proper Orthogonal Decomposition: new error estimates and illustrative examples. *ESAIM: Mathematical Modelling and Numerical Analysis*, 46:731–757, 2012.

[70] S. Chaturantabut and D. Sorensen. Nonlinear model reduction via discrete empirical interpolation. *SIAM Journal on Scientific Computing*, 32(5):2737–2764, 2010.

[71] A. H. Chen, T. Nakao, R. F. Brodman, M. Greenberg, R. Charney, M. Menegus, M. Johnson, R. Grose, R. Frame, E. C. Hu, H.-K. Choi, and S. Safyer. Early postoperative angiographic assessment of radial artery grafts used for coronary artery bypass grafting. *The Journal of Thoracic and Cardiovascular Surgery*, 111(6):1208–1212, 1996.

[72] J. H. Chesebro, V. Fuster, L. R. Elveback, I. P. Clements, H. C. Smith, D. R. Holmes, W. T. Bardsley, J. R. Pluth, R. B. Wallace, F. J. Puga, T. A. Orszulak, J. M. Piehler, G. K. Danielson, H. V. Schaff, and R. L. Frye. Effect of dipyridamole and aspirin on late vein-graft patency after coronary bypass operations. *New England Journal of Medicine*, 310(4):209–214, 1984.

[73] E. Christensen, M. Brøns, and J. Sørensen. Evaluation of Proper Orthogonal Decomposition–based decomposition techniques applied to parameter-dependent nonturbulent flows. *SIAM Journal on Scientific Computing*, 21:1419–1434, 2000.

[74] L. H. Cohn. *Cardiac surgery in the adult*. McGraw-Hill Medical, 2008.

[75] C. M. Colciago. *Reduced Order Fluid-Structure Interaction Models for Haemodynamics Applications*. PhD thesis, École Polytechnique Fédérale de Lausanne, N. 6285, 2014.

[76] D. Cosgrove, F. Loop, B. Lytle, M. Goormastic, R. Stewart, C. Gill, and L. Golding. Does mammary artery grafting increase surgical risk? *Circulation*, 72(3 Pt 2):II170–II174, 1985.

[77] E. Cueto and F. Chinesta. Real time simulation for computational surgery: a review. *Advanced Modeling and Simulation in Engineering Sciences*, 1(1):11:1–11:18, 2014.

[78] A. de Boer, M. van der Schoot, and H. Bijl. Mesh deformation based on radial basis function interpolation. *Computers & Structures*, 85(11–14):784–795, 2007.

[79] A. de Boer, A. van Zuijlen, and H. Bijl. Review of coupling methods for non-matching meshes. *Computer Methods in Applied Mechanics and Engineering*, 196(8):1515–1525, 2007.

[80] A. de Boer, A. van Zuijlen, and H. Bijl. Comparison of conservative and consistent approaches for the coupling of non-matching meshes. *Computer Methods in Applied Mechanics and Engineering*, 197(49–50):4284–4297, 2008.

[81] L. Dedè, A. Quarteroni, and S. Zhu. Isogeometric analysis and proper orthogonal decomposition for parabolic problems. Technical report EPFL MATHICSE 44.2014, 2014.

[82] S. Deparis and G. Rozza. Reduced basis method for multi-parameter-dependent steady Navier-Stokes equations: applications to natural convection in a cavity. *Journal of Computational Physics*, 228(12):4359–4378, 2009.

[83] V. Deplano, C. Bertolotti, and O. Boiron. Numerical simulations of unsteady flows in a stenosed coronary bypass graft. *Medical and Biological Engineering and Computing*, 39(4):488–499, 2001.

[84] N. D. Desai, E. A. Cohen, C. D. Naylor, and S. E. Fremes. A randomized comparison of radial-artery and saphenous-vein coronary bypass grafts. *New England Journal of Medicine*, 351(22):2302–2309, 2004.

[85] C. A. Dietl and C. H. Benoit. Radial artery graft for coronary revascularization: technical considerations. *The Annals of Thoracic Surgery*, 60(1):102–110, 1995.

[86] J. Ding, Y. Liu, F. Wang, and F. Bai. Impact of competitive flow on hemodynamics in coronary surgery: numerical study of ITA-LAD model. *Computational and Mathematical Methods in Medicine*, 2012:356187:1–356187:7, 2012.

[87] H. Do, A. A. Owida, W. Yang, and Y. S. Morsi. Numerical simulation of the haemodynamics in end-to-side anastomoses. *International Journal for Numerical Methods in Fluids*, 67:638–650, 2011.

[88] O. Dur, S. Coskun, K. Coskun, D. Frakes, L. Kara, and K. Pekkan. Computer-aided patient-specific coronary artery graft design improvements using CFD coupled shape optimizer. *Cardiovascular Engineering and Technology*, 2:35–47, 2011.

[89] F. H. Edwards, R. E. Clark, and M. Schwartz. Impact of internal mammary artery conduits on operative mortality in coronary revascularization. *The Annals of Thoracic Surgery*, 57(1):27–32, 1994.

[90] C. R. Ethier, D. Steinman, X. Zhang, S. Karpik, and M. Ojha. Flow waveform effects on end-to-side anastomotic flow patterns. *Journal of Biomechanics*, 31(7):609–617, 1998.

[91] European Coronary Surgery Study Group. Prospective randomized study of coronary artery bypass surgery in stable angina pectoris: a progress report on survival. *Circulation*, 65(7 Pt 2):67–71, 1982.

[92] R. G. Favaloro. Saphenous vein autograft replacement of severe segmental coronary artery occlusion: operative technique. *The Annals of Thoracic Surgery*, 5(4):334–339, 1968.

[93] A. Fedorov, R. Beichel, J. Kalpathy-Cramer, J. Finet, J.-C. Fillion-Robin, S. Pujol, C. Bauer, D. Jennings, F. Fennessy, M. Sonka, J. Buatti, S. Aylward, J. V. Miller, S. Pieper, and R. Kikinis. 3D Slicer as an image computing platform for the quantitative imaging network. *Magnetic Resonance Imaging*, 30(9):1323–1341, 2012.

[94] D.-Y. Fei, J. D. Thomas, and S. E. Rittgers. The effect of angle and flow rate upon hemodynamics in distal vascular graft anastomoses: a numerical model study. *Journal of Biomechanical Engineering*, 116(3):331–336, 1994.

[95] R. Ferrero. Numerical study of the fluid-dynamics in patient-specific coronary artery bypass grafts. Master's thesis, Politecnico di Torino, 2014.

[96] R. Flemma, W. Johnson, and D. Lepley Jr. Triple aorto-coronary vein bypass as treatment for coronary insufficiency. *Archives of Surgery*, 103(1):82–83, 1971.

[97] L. Formaggia, A. Quarteroni, and A. Veneziani. *Cardiovascular mathematics: modeling and simulation of the circulatory system*, volume 1 of *MS&A series*. Springer-Verlag Italia, 2009.

[98] D. Forti and G. Rozza. Efficient geometrical parametrisation techniques of interfaces for reduced-order modelling: application to fluid–structure interaction coupling problems. *International Journal of Computational Fluid Dynamics*, 28(3-4):158–169, 2014.

[99] A. Frangi, W. Niessen, K. Vincken, and M. Viergever. Multiscale vessel enhancement filtering. In W. Wells, A. Colchester, and S. Delp, editors, *Medical Image Computing and Computer-Assisted Interventation – MICCAI'98*, volume 1496 of *Lecture Notes in Computer Science*, pages 130–137. Springer Berlin Heidelberg, 1998.

[100] T. Frauenfelder, E. Boutsianis, T. Schertler, L. Husmann, S. Leschka, D. Poulikakos, B. Marincek, and H. Alkadhi. Flow and wall shear stress in end-to-side and side-to-side anastomosis of venous coronary artery bypass grafts. *BioMedical Engineering OnLine*, 6(1):35:1–35:13, 2007.

[101] I. J. Freshwater, Y. S. Morsi, and T. Lai. The effect of angle on wall shear stresses in a LIMA to LAD anastomosis: numerical modelling of pulsatile flow. *Proceedings of the Institution of Mechanical Engineers, Part H: Journal of Engineering in Medicine*, 220(7):743–757, 2006.

[102] G. Friesinger, E. Page, and R. Ross. Prognostic significance of coronary arteriography. *Transactions of the Association of American Physicians*, 83:78–92, 1970.

[103] J. Gain and D. Bechmann. A survey of spatial deformation from a user-centered perspective. *ACM Transactions on Graphics*, 27(4):107:1–107:21, 2008.

[104] J. E. Gain and N. A. Dodgson. Preventing self-intersection under free-form deformation. *IEEE Transactions on Visualization and Computer Graphics*, 7:289–298, 2001.

[105] H. Garrett, E. Dennis, and M. DeBakey. Aortocoronary bypass with saphenous vein graft: seven-year follow-up. *JAMA: The Journal of the American Medical Association*, 223(7):792–794, 1973.

[106] A. Gerner and K. Veroy. Certified reduced basis methods for parametrized saddle point problems. *SIAM Journal on Scientific Computing*, 34(5):A2812–A2836, 2012.

[107] D. Ghista and F. Kabinejadian. Coronary artery bypass grafting hemodynamics and anastomosis design: a biomedical engineering review. *BioMedical Engineering OnLine*, 12(1):129:1–129:28, 2013.

[108] J. H. Gibbon Jr. Application of a mechanical heart and lung apparatus to cardiac surgery. *Minnesota medicine*, 37(3):171–185, 1954.

[109] S. Giordana, S. Sherwin, J. Peiró, D. Doorly, J. Crane, K. Lee, N. Cheshire, and C. Caro. Local and global geometric influence on steady flow in distal anastomoses of peripheral bypass grafts. *Journal of Biomechanical Engineering*, 127:1087–1098, 2005.

[110] A. S. Go, D. Mozaffarian, V. L. Roger, E. J. Benjamin, J. D. Berry, M. J. Blaha, S. Dai, E. S. Ford, et al. Heart disease and stroke statistics–2014 update: a report from the American Heart Association. *Circulation*, 129:e28–e292, 2014.

[111] R. Goetz, M. Rohman, J. Haller, R. Dee, and S. S. Rosenak. Internal mammary-coronary artery anastomosis. A nonsuture method employing tantalum rings. *The Journal of Thoracic and Cardiovascular Surgery*, 41:378–386, 1961.

[112] L. Grinberg, M. Deng, A. Yakhot, and G. Karniadakis. Window Proper Orthogonal Decomposition: application to continuum and atomistic data. In A. Quarteroni and G. Rozza, editors, *Reduced Order Methods for Modeling and Computational Reduction*, volume 9, pages 275–304. Springer Milano, MS&A Series, 2013.

[113] F. L. Grover, R. R. Johnson, G. Marshall, K. E. Hammermeister, and Department of Veterans Affairs Cardiac Surgeons. Impact of mammary grafts on coronary bypass operative mortality and morbidity. *The Annals of Thoracic Surgery*, 57(3):559–569, 1994.

[114] J. Grow and C. Brantigan. The diamond anastomosis: a technique for creating a right-angle side-to-side vascular anastomosis. *The Journal of Thoracic and Cardiovascular Surgery*, 69(2):188–189, 1975.

[115] R. Guibert, K. McLeod, A. Caiazzo, T. Mansi, M. A. Fernández, M. Sermesant, X. Pennec, I. E. Vignon-Clementel, Y. Boudjemline, and J.-F. Gerbeau. Group-wise construction of reduced models for understanding and characterization of pulmonary blood flows from medical images. *Medical Image Analysis*, 18(1):63–82, 2014.

[116] M. D. Gunzburger, J. S. Peterson, and J. N. Shadid. Reduced-order modeling of time-dependent PDEs with multiple parameters in the boundary data. *Computer Methods in Applied Mechanics and Engineering*, 196(4–6):1030–1047, 2007.

[117] O. Gurné, P. Chenu, M. Buche, Y. Louagie, P. Eucher, B. Marchandise, E. Rombaut, D. Blommaert, and E. Schroeder. Adaptive mechanisms of arterial and venous coronary bypass grafts to an increase in flow demand. *Heart*, 82(3):336–342, 1999.

[118] B. Haasdonk. Convergence rates of the POD–Greedy method. *ESAIM: Mathematical Modelling and Numerical Analysis*, 47:859–873, 2013.

[119] B. Haasdonk and M. Ohlberger. Reduced basis method for finite volume approximations of parametrized linear evolution equations. *ESAIM: Mathematical Modelling and Numerical Analysis*, 42(02):277–302, 2008.

[120] J. Habets, R. van den Brink, R. Uijlings, A. Spijkerboer, W. Mali, S. Chamuleau, and R. Budde. Coronary artery assessment by multidetector computed tomography in patients with prosthetic heart valves. *European Radiology*, 22(6):1278–1286, 2012.

[121] A. J. Hanson and H. Ma. Parallel transport approach to curve framing. Technical report TR425, Indiana University, 1995.

[122] A. Hay, J. Borggaard, and D. Pelletier. Local improvements to reduced-order models using sensitivity analysis of the proper orthogonal decomposition. *Journal of Fluid Mechanics*, 629:41–72, 2009.

[123] V. Hernandez, J. E. Roman, and V. Vidal. Slepc: A scalable and flexible toolkit for the solution of eigenvalue problems. *ACM Transactions on Mathematical Software*, 31(3):351–362, 2005.

[124] L. D. Hillis, P. K. Smith, et al. 2011 ACCF/AHA guideline for coronary artery bypass graft surgery – a report of the American College of Cardiology Foundation/American Heart Association task force on practice guidelines developed in collaboration with the american association for thoracic surgery, society of cardiovascular anesthesiologists, and society of thoracic surgeons. *Journal of the American College of Cardiology*, 58(24):e123–e210, 2011.

[125] M. Hofer, G. Rappitsch, K. Perktold, W. Trubel, and H. Schima. Numerical study of wall mechanics and fluid dynamics in end-to-side anastomoses and correlation to intimal hyperplasia. *Journal of Biomechanics*, 29(10):1297–1308, 1996.

[126] Y. Huo and G. S. Kassab. Pulsatile blood flow in the entire coronary arterial tree: theory and experiment. *American Journal of Physiology - Heart and Circulatory Physiology*, 291(3):H1074–H1087, 2006.

[127] J. Hurst, R. O'Rourke, R. Walsh, and V. Fuster. *Hurst's the heart manual of cardiology.* McGraw-Hill Medical, 2009.

[128] A. L. Iacò, G. Teodori, G. D. Giammarco, M. D. Mauro, L. Storto, V. Mazzei, G. Vitolla, B. Mostafa, and A. M. Calafiore. Radial artery for myocardial revascularization: long-term clinical and angiographic results. *The Annals of Thoracic Surgery*, 72(2):464–468, 2001.

[129] L. Iapichino. *Reduced Basis Methods for the Solution of Parametrized PDEs in Repetitive and Complex Networks with Application to CFD.* PhD thesis, École Polytechnique Fédérale de Lausanne, N. 5529, 2012.

[130] L. Iapichino, A. Quarteroni, and G. Rozza. A reduced basis hybrid method for the coupling of parametrized domains represented by fluidic networks. *Computer Methods in Applied Mechanics and Engineering*, 221–222:63–82, 2012.

[131] M. Idu, J. Buth, W. Hop, P. Cuypers, E. van de Pavoordt, and J. Tordoir. Factors influencing the development of vein-graft stenosis and their significance for clinical management. *European Journal of Vascular and Endovascular Surgery*, 17(1):15–21, 1999.

[132] T. Iliescu and Z. Wang. Are the snapshot difference quotients needed in the proper orthogonal decomposition? *SIAM Journal on Scientific Computing*, 36(3):A1221–A1250, 2014.

[133] F. Inzoli, F. Migliavacca, and G. Pennati. Numerical analysis of steady flow in aorto-coronary bypass 3-D model. *Journal of Biomechanical Engineering*, 118(2):172–179, 1996.

[134] N. Ishida, H. Sakuma, B. P. Cruz, T. Shimono, T. Tokui, I. Yada, K. Takeda, and C. B. Higgins. MR flow measurement in the internal mammary artery–to–coronary artery bypass graft: comparison with graft stenosis at radiographic angiography. *Radiology*, 220(2):441–447, 2001.

[135] Z. S. Jackson, H. Ishibashi, A. I. Gotlieb, and B. Langille. Effects of anastomotic angle on vascular tissue responses at end-to-side arterial grafts. *Journal of Vascular Surgery*, 34(2):300–307, 2001.

[136] E. L. Jones, O. Lattouf, J. F. Lutz, and S. B. King III. Important anatomical and physiological considerations in performance of complex mammary–coronary artery operations. *The Annals of Thoracic Surgery*, 43(5):469–477, 1987.

[137] F. Kabinejadian, L. Chua, D. Ghista, M. Sankaranarayanan, and Y. Tan. A novel coronary artery bypass graft design of sequential anastomoses. *Annals of Biomedical Engineering*, 38(10):3135–3150, 2010.

[138] F. Kabinejadian and D. N. Ghista. Compliant model of a coupled sequential coronary arterial bypass graft: effects of vessel wall elasticity and non-Newtonian rheology on blood flow regime and hemodynamic parameters distribution. *Medical Engineering & Physics*, 34(7):860–872, 2012.

[139] I. Kakadiaris, A. Santamaria-Pang, and A. Pednekar. Functional morphology analysis of the left anterior descending coronary artery in EBCT images. *IEEE Transactions on Biomedical Engineering*, 57(8):1886–1896, 2010.

[140] J. Keegan, P. D. Gatehouse, G.-Z. Yang, and D. N. Firmin. Spiral phase velocity mapping of left and right coronary artery blood flow: correction for through-plane motion using selective fat-only excitation. *Journal of Magnetic Resonance Imaging*, 20(6):953–960, 2004.

[141] R. Keynton, M. Shu, and S. Rittgers. The effect of angle and flow rate upon hemodynamics in distal vascular graft anastomoses: an in vitro model study. *Journal of Biomechanical Engineering*, 113(4):458–463, 1991.

[142] H. Kim, I. Vignon-Clementel, C. Figueroa, K. Jansen, and C. Taylor. Developing computational methods for three-dimensional finite element simulations of coronary blood flow. *Finite Elements in Analysis and Design*, 46(6):514–525, 2010.

[143] B. S. Kirk, J. W. Peterson, R. H. Stogner, and G. F. Carey. libMesh: a C++ library for parallel adaptive mesh refinement/coarsening simulations. *Engineering with Computers*, 22(3-4):237–254, 2006.

[144] J. W. Kirklin and B. G. Barratt-Boyes. *Cardiac surgery: morphology, diagnostic criteria, natural history, techniques, results, and indications*. Churchill Livingstone New York, 1988.

[145] C. Kleinstreuer, M. Nazemi, and J. P. Archie. Hemodynamics analysis of a stenosed carotid bifurcation and its plaque-mitigating design. *Journal of Biomechanical Engineering*, 113(3):330–335, 1991.

[146] D. J. Knezevic and J. W. Peterson. A high-performance parallel implementation of the certified reduced basis method. *Computer Methods in Applied Mechanics and Engineering*, 200(13–16):1455–1466, 2011.

[147] V. I. Kolessov. Mammary artery-coronary artery anastomosis as method of treatment for angina pectoris. *The Journal of Thoracic and Cardiovascular Surgery*, 54(4):535–544, 1967.

[148] D. N. Ku, D. P. Giddens, C. K. Zarins, and S. Glagov. Pulsatile flow and atherosclerosis in the human carotid bifurcation. Positive correlation between plaque location and low oscillating shear stress. *Arteriosclerosis, Thrombosis, and Vascular Biology*, 5(3):293–302, 1985.

[149] S. Kumazaki, J. Koyama, K. Aizawa, H. Kasai, M. Koshikawa, A. Izawa, T. Tomita, M. Takahashi, and U. Ikeda. Effect of graft adaptation of the internal mammary artery on longitudinal phasic blood flow velocity characteristics after surgery. *Heart and Vessels*, 25(6):515–521, 2010.

[150] K. Kunisch and S. Volkwein. Galerkin Proper Orthogonal Decomposition methods for a general equation in fluid dynamics. *SIAM Journal On Numerical Analysis*, 40(2):492–515, 2003.

[151] K. Kunisch and S. Volkwein. Optimal snapshot location for computing POD basis functions. *ESAIM: Mathematical Modelling and Numerical Analysis*, 44(3):509–529, 2010.

[152] S. M. Kute and D. A. Vorp. The effect of proximal artery flow on the hemodynamics at the distal anastomosis of a vascular bypass graft: computational study. *Journal of Biomechanical Engineering*, 123(3):277–283, 2001.

[153] H. J. Lamousin and W. N. Waggenspack Jr. NURBS-based free-form deformations. *IEEE Computer Graphics and Applications*, 14(6):59–65, 1994.

[154] T. Lassila, A. Manzoni, A. Quarteroni, and G. Rozza. Boundary control and shape optimization for the robust design of bypass anastomoses under uncertainty. *ESAIM: Mathematical Modelling and Numerical Analysis*, 47(4):1107–1131, 2013.

[155] T. Lassila, A. Manzoni, A. Quarteroni, and G. Rozza. A reduced computational and geometrical framework for inverse problems in hemodynamics. *International Journal for Numerical Methods in Biomedical Engineering*, 29(7):741–776, 2013.

[156] T. Lassila, A. Manzoni, A. Quarteroni, and G. Rozza. Model order reduction in fluid dynamics: challenges and perspectives. In A. Quarteroni and G. Rozza, editors, *Reduced Order Methods for Modeling and Computational Reduction*, volume 9, pages 235–274. Springer MS&A Series, 2014.

[157] T. Lassila and G. Rozza. Parametric free-form shape design with PDE models and reduced basis method. *Computer Methods in Applied Mechanics and Engineering*, 199(23-24):1583–1592, 2010.

[158] G. M. Lawrie, J. Lie, G. C. Morris Jr, and H. L. Beazley. Vein graft patency and intimal proliferation after aortocoronary bypass: early and long-term angiopathologic correlations. *The American Journal of Cardiology*, 38(7):856–862, 1976.

[159] F. Lazarus, S. Coquillart, and P. Jancène. Interactive axial deformations. In *Modeling in Computer Graphics*, pages 241–254. Springer-Verlag, 1993.

[160] C. Leblond, C. Allery, and C. Inard. An optimal projection method for the reduced-order modeling of incompressible flows. *Computer Methods in Applied Mechanics and Engineering*, 200(33–36):2507–2527, 2011.

[161] S.-W. Lee, L. Antiga, and D. A. Steinman. Correlations among indicators of disturbed flow at the normal carotid bifurcation. *Journal of Biomechanical Engineering*, 131(6):061013–1:061013–7, 2009.

[162] K. H. Lehmann, L. von Segesser, W. Müller-Glauser, R. Siebenmann, K. Schneider, T. F. Lüscher, and M. Turina. Internal-mammary coronary artery grafts: is their superiority also due to a basically intact endothelium? *The Thoracic and Cardiovascular Surgeon*, 37(03):187–189, 1989.

[163] M. Lei, J. Archie, and C. Kleinstreuer. Computational design of a bypass graft that minimizes wall shear stress gradients in the region of the distal anastomosis. *Journal of Vascular Surgery*, 25(4):637–646, 1997.

[164] M. Lei, D. P. Giddens, S. A. Jones, F. Loth, and H. Bassiouny. Pulsatile flow in an end-to-side vascular graft model: comparison of computations with experimental data. *Journal of Biomechanical Engineering*, 123(1):80–87, 2000.

[165] J. Leipsic, S. Abbara, S. Achenbach, R. Cury, J. P. Earls, G. J. Mancini, K. Nieman, G. Pontone, and G. L. Raff. SCCT guidelines for the interpretation and reporting of coronary CT angiography: a report of the Society of Cardiovascular Computed Tomography guidelines committee. *Journal of Cardiovascular Computed Tomography*, 8(5):342–358, 2014.

[166] M. Lemma, A. Innorta, M. Pettinari, A. Mangini, G. Gelpi, M. Piccaluga, P. Danna, and C. Antona. Flow dynamics and wall shear stress in the left internal thoracic artery: composite arterial graft versus single graft. *European Journal of Cardio-Thoracic Surgery*, 29(4):473–478, 2006.

[167] G. N. Levine, E. R. Bates, J. C. Blankenship, S. R. Bailey, J. A. Bittl, B. Cercek, C. E. Chambers, et al. 2011 ACCF/AHA/SCAI guideline for percutaneous coronary intervention: executive summary. A report of the American College of Cardiology Foundation/American Heart Association task force on practice guidelines and the Society for Cardiovascular Angiography and Interventions. *Circulation*, 124(23):e574–e651, 2011.

[168] I. Llamas, A. Powell, J. Rossignac, and C. D. Shaw. Bender: a virtual ribbon for deforming 3D shapes in biomedical and styling applications. In *Proceedings of the 2005 ACM symposium on solid and physical modeling*, pages 89–99, 2005.

[169] J. G. Lobo Filho, M. C. Leitão, A. J. Forte, H. G. Lobo Filho, A. A. Silva, E. S. Bastos, and H. Murad. Flow analysis of left internal thoracic artery in myocardial revascularization surgery using Y graft. *Texas Heart Institute Journal*, 33(4):430–436, 2006.

[170] W. P. Longmire, J. A. Cannon, and A. A. Kattus. Direct-vision coronary endarterectomy for angina pectoris. *New England Journal of Medicine*, 259(21):993–999, 1958.

[171] F. D. Loop, B. W. Lytle, D. M. Cosgrove, R. W. Stewart, M. Goormastic, G. W. Williams, L. A. Golding, C. C. Gill, P. C. Taylor, W. C. Sheldon, and W. L. Proudfit. Influence of the internal-mammary-artery graft on 10-year survival and other cardiac events. *New England Journal of Medicine*, 314(1):1–6, 1986.

[172] W. E. Lorensen and H. E. Cline. Marching cubes: a high resolution 3D surface construction algorithm. *Computer Graphics*, 21(4):163–169, 1987.

[173] F. Loth, P. F. Fischer, and H. S. Bassiouny. Blood flow in end-to-side anastomoses. *Annual Review of Fluid Mechanics*, 40:367–393, 2008.

[174] Z. Luo. A reduced-order extrapolation algorithm based on SFVE method and POD technique for non-stationary Stokes equations. *Applied Mathematics and Computation*, 247:976–995, 2014.

[175] Z. Luo, J. Chen, I. Navon, and X. Yang. Mixed finite element formulation and error estimates based on Proper Orthogonal Decomposition for the nonstationary Navier–Stokes equations. *SIAM Journal on Numerical Analysis*, 47(1):1–19, 2009.

[176] Z. Luo, H. Li, P. Sun, and J. Gao. A reduced-order finite difference extrapolation algorithm based on POD technique for the non-stationary Navier–Stokes equations. *Applied Mathematical Modelling*, 37(7):5464–5473, 2013.

[177] A. Manzoni. *Reduced models for optimal control, shape optimization and inverse problems in haemodynamics*. PhD thesis, École Polytechnique Fédérale de Lausanne, N. 5402, 2012.

[178] A. Manzoni. An efficient computational framework for reduced basis approximation and a posteriori error estimation of parametrized Navier–Stokes flows. *ESAIM: Mathematical Modelling and Numerical Analysis*, 48:1199–1226, 2014.

[179] A. Manzoni, A. Quarteroni, and G. Rozza. Model reduction techniques for fast blood flow simulation in parametrized geometries. *International Journal for Numerical Methods in Biomedical Engineering*, 28(6–7):604–625, 2012.

[180] A. Manzoni, A. Quarteroni, and G. Rozza. Shape optimization for viscous flows by reduced basis methods and free-form deformation. *International Journal for Numerical Methods in Fluids*, 70(5):646–670, 2012.

[181] A. L. Marsden. Optimization in cardiovascular modeling. *Annual Review of Fluid Mechanics*, 46(1):519–546, 2014.

[182] A. L. Marsden, J. A. Feinstein, and C. A. Taylor. A computational framework for derivative-free optimization of cardiovascular geometries. *Computer Methods in Applied Mechanics and Engineering*, 197(21-24):1890–1905, 2008.

[183] K. McLeod, A. Caiazzo, M. Fernández, T. Mansi, I. Vignon-Clementel, M. Sermesant, X. Pennec, Y. Boudjemline, and J.-F. Gerbeau. Atlas-based reduced models of blood flows for fast patient-specific simulations. In O. Camara, M. Pop, K. Rhode, M. Sermesant, N. Smith, and A. Young, editors, *Statistical Atlases and Computational Models of the Heart*, volume 6364 of *Lecture Notes in Computer Science*, pages 95–104. Springer Berlin / Heidelberg, 2010.

[184] F. Migliavacca and G. Dubini. Computational modeling of vascular anastomoses. *Biomechanics and Modeling in Mechanobiology*, 3(4):235–250, 2005.

[185] N. Mills. Physiologic and technical aspects of internal mammary artery coronary artery bypass grafts. *Modern techniques in surgery. Cardio-thoracic Surgery. Mt. Kisco NY: Futura*, 48:1–19, 1982.

[186] M. B. Mock, I. Ringqvist, L. D. Fisher, K. B. Davis, B. R. Chaitman, N. T. Kouchoukos, G. C. Kaiser, E. Alderman, T. J. Ryan, R. O. Russell, S. Mullin, D. Fray, and T. Killip. Survival of medically treated patients in the Coronary Artery Surgery Study (CASS) registry. *Circulation*, 66(3):562–568, 1982.

[187] J. E. Moore, Jr., E. S. Weydahl, and A. Santamarina. Frequency dependence of dynamic curvature effects on flow through coronary arteries. *Journal of Biomechanical Engineering*, 123(2):129–133, 2000.

[188] S. V. Moran, R. Baeza, E. Guarda, R. Zalaquett, M. J. Irarrazaval, E. Marchant, and C. Deck. Predictors of radial artery patency for coronary bypass operations. *The Annals of Thoracic Surgery*, 72(5):1552–1556, 2001.

[189] U. Morbiducci, R. Ponzini, M. Grigioni, and A. Redaelli. Helical flow as fluid dynamic signature for atherogenesis risk in aortocoronary bypass. A numeric study. *Journal of Biomechanics*, 40(3):519–534, 2007.

[190] M. D. Morris. Factorial sampling plans for preliminary computational experiments. *Technometrics*, 33(2):161–174, 1991.

[191] N.-C. Nguyen, G. Rozza, and A. Patera. Reduced basis approximation and a posteriori error estimation for the time-dependent viscous Burgers' equation. *Calcolo*, 46:157–185, 2009.

[192] S. Niroomandi, I. Alfaro, E. Cueto, and F. Chinesta. Real-time deformable models of non-linear tissues by model reduction techniques. *Computer Methods and Programs in Biomedicine*, 91(3):223–231, 2008.

[193] S. Niroomandi, I. Alfaro, D. González, E. Cueto, and F. Chinesta. Real-time simulation of surgery by reduced-order modeling and X-FEM techniques. *International Journal for Numerical Methods in Biomedical Engineering*, 28(5):574–588, 2012.

[194] S. Niroomandi, D. González, I. Alfaro, F. Bordeu, A. Leygue, E. Cueto, and F. Chinesta. Real-time simulation of biological soft tissues: a PGD approach. *International Journal for Numerical Methods in Biomedical Engineering*, 29(5):586–600, 2013.

[195] H. Nordgaard, A. Swillens, D. Nordhaug, I. Kirkeby-Garstad, D. Van Loo, N. Vitale, P. Segers, R. Haaverstad, and L. Lovstakken. Impact of competitive flow on wall shear stress in coronary surgery: computational fluid dynamics of a LIMA–LAD model. *Cardiovascular Research*, 88(3):512–519, 2010.

[196] A. A. Owida, H. Do, and Y. S. Morsi. Numerical analysis of coronary artery bypass grafts: an over view. *Computer Methods and Programs in Biomedicine*, 108(2):689–705, 2012.

[197] S. Pagni, J. Storey, J. Ballen, W. Montgomery, N. K. Qaqish, S. Etoch, and P. A. Spence. Factors affecting internal mammary artery graft survival: how is competitive flow from a patent native coronary vessel a risk factor? *Journal of Surgical Research*, 71(2):172–178, 1997.

[198] P. Pavone and M. Fioranelli. *Malattia coronarica: fisiopatologia e diagnostica non invasiva con TC*. Springer-Verlag Italia, 2008.

[199] P. Pavone, M. Fioranelli, and D. A. Dowe. *CT evaluation of coronary artery disease*. Springer, 2009.

[200] P. Perona and J. Malik. Scale-space and edge detection using anisotropic diffusion. *IEEE Transactions on Pattern Analysis and Machine Intelligence*, 12(7):629–639, 1990.

[201] J. Peterson. The reduced basis method for incompressible viscous flow calculations. *SIAM Journal on Scientific Computing*, 10:777–786, 1989.

[202] M. Piccinelli, A. Veneziani, D. A. Steinman, A. Remuzzi, and L. Antiga. A framework for geometric analysis of vascular structures: application to cerebral aneurysms. *IEEE Transactions on Medical Imaging*, 28(8):1141–1155, 2009.

[203] A. K. Politis, G. P. Stavropoulos, M. N. Christolis, P. G. Panagopoulos, N. S. Vlachos, and N. C. Markatos. Numerical modelling of simulated blood flow in idealized composite arterial coronary grafts: transient flow. *Journal of Biomechanics*, 41(1):25–39, 2008.

[204] G. Possati, M. Gaudino, F. Alessandrini, N. Luciani, F. Glieca, C. Trani, C. Cellini, C. Canosa, and G. D. Sciascio. Midterm clinical and angiographic results of radial artery grafts used for myocardial revascularization. *The Journal of Thoracic and Cardiovascular Surgery*, 116(6):1015–1021, 1998.

[205] M. Probst, M. Lülfesmann, M. Nicolai, H. M. Bücker, M. Behr, and C. H. Bischof. Sensitivity of optimal shapes of artificial grafts with respect to flow parameters. *Computer Methods in Applied Mechanics and Engineering*, 199(17-20):997–1005, 2010.

[206] M. Prosi, K. Perktold, Z. Ding, and M. H. Friedman. Influence of curvature dynamics on pulsatile coronary artery flow in a realistic bifurcation model. *Journal of Biomechanics*, 37(11):1767–1775, 2004.

[207] W. J. Proudfit, A. V. Bruschke, J. P. MacMillan, G. W. Williams, and F. M. Sones. Fifteen year survival study of patients with obstructive coronary artery disease. *Circulation*, 68(5):986–997, 1983.

[208] J. D. Puskas, H. L. Lazar, M. J. Mack, J. F. Sabik III, and D. P. Taggart. State-of-the-art coronary artery bypass graft. *Seminars in Thoracic and Cardiovascular Surgery*, 26(1):76–94, 2014.

[209] A. Qiao and Y. Liu. Influence of graft-host diameter ratio on the hemodynamics of cabg. *Bio-Medical Materials and Engineering*, 16(3):189–201, 2006.

[210] A. Quarteroni. *Numerical Models for Differential Problems*, volume 8 of *Modeling, Simulation and Applications (MS&A)*. Springer-Verlag Italia, Milano, 2014.

[211] A. Quarteroni and G. Rozza. Optimal control and shape optimization of aorto-coronaric bypass anastomoses. *Mathematical Models and Methods in Applied Sciences*, 13(12):1801–1824, 2003.

[212] A. Quarteroni and G. Rozza. Numerical solution of parametrized Navier–Stokes equations by reduced basis methods. *Numerical Methods for Partial Differential Equations*, 23(4):923–948, 2007.

[213] A. Quarteroni and G. Rozza. *Reduced Order Methods for Modeling and Computational Reduction*, volume 9. Springer Milano, MS&A Series, 2014.

[214] A. Quarteroni, G. Rozza, and A. Manzoni. Certified reduced basis approximation for parametrized partial differential equations and applications. *Journal of Mathematics in Industry*, 1(1):1–49, 2011.

[215] M.-L. Rapún and J. M. Vega. Reduced order models based on local POD plus Galerkin projection. *Journal of Computational Physics*, 229(8):3046–3063, 2010.

[216] S. Ravindran. A reduced-order approach for optimal control of fluids using proper orthogonal decomposition. *International Journal for Numerical Methods in Fluids*, 34:425–448, 2000.

[217] C. S. Rihal, D. L. Raco, B. J. Gersh, and S. Yusuf. Indications for coronary artery bypass surgery and percutaneous coronary intervention in chronic stable angina: review of the evidence and methodological considerations. *Circulation*, 108(20):2439–2445, 2003.

[218] G. G. Rowe, J. H. Thomsen, R. R. Stenlund, D. H. Mckenna, S. Sialer, and R. J. Corliss. A study of hemodynamics and coronary blood flow in man with coronary artery disease. *Circulation*, 39(1):139–148, 1969.

[219] G. Rozza. On optimization, control and shape design of an arterial bypass. *International Journal for Numerical Methods in Fluids*, 47(10-11):1411–1419, 2005.

[220] G. Rozza. *Shape design by optimal flow control and reduced basis techniques: applications to bypass configurations in haemodynamics*. PhD thesis, École Polytechnique Fédérale de Lausanne, N. 3400, 2005.

[221] G. Rozza, D. Huynh, and A. Manzoni. Reduced basis approximation and a posteriori error estimation for Stokes flows in parametrized geometries: roles of the inf-sup stability constants. *Numerische Mathematik*, 125(1):115–152, 2013.

[222] G. Rozza and K. Veroy. On the stability of the reduced basis method for Stokes equations in parametrized domains. *Computer Methods in Applied Mechanics and Engineering*, 196(7):1244–1260, 2007.

[223] J. F. Sabik III and E. H. Blackstone. Coronary artery bypass graft patency and competitive flow. *Journal of the American College of Cardiology*, 51(2):126–128, 2008.

[224] J. F. Sabik III, B. W. Lytle, E. H. Blackstone, P. L. Houghtaling, and D. M. Cosgrove. Comparison of saphenous vein and internal thoracic artery graft patency by coronary system. *The Annals of Thoracic Surgery*, 79(2):544–551, 2005.

[225] J. F. Sabik III, B. W. Lytle, E. H. Blackstone, M. Khan, P. L. Houghtaling, and D. M. Cosgrove. Does competitive flow reduce internal thoracic artery graft patency? *The Annals of Thoracic Surgery*, 76(5):1490–1497, 2003.

[226] D. C. Sabiston Jr. Direct surgical management of congenital and acquired lesions of the coronary circulation. *Progress in cardiovascular diseases*, 6(3):299–316, 1963.

[227] H. Sakuma, S. Globits, M. O'sullivan, A. Shimakawa, M. A. Bernstein, T. K. F. Foo, T. M. Amidon, K. Takeda, T. Nakagawa, and C. B. Higgins. Breath-hold MR measurements of blood flow velocity in internal mammary arteries and coronary artery bypass grafts. *Journal of Magnetic Resonance Imaging*, 6(1):219–222, 1996.

[228] S. Sankaran, M. Esmaily Moghadam, A. Kahn, E. Tseng, J. Guccione, and A. Marsden. Patient-specific multiscale modeling of blood flow for coronary artery bypass graft surgery. *Annals of Biomedical Engineering*, 40:2228–2242, 2012.

[229] S. Sankaran and A. L. Marsden. The impact of uncertainty on shape optimization of idealized bypass graft models in unsteady flow. *Physics of Fluids*, 22(12):1–16, 2010.

[230] S. Sarakinos, E. Amoiralis, and I. Nikolos. Exploring freeform deformation capabilities in aerodynamic shape parameterization. In *Proceedings of the International Conference on Computer as a tool, November 21-24, 2005*, volume 1, pages 535–538, 2005.

[231] L. R. Sauvage, H.-D. Wu, T. E. Kowalsky, C. C. Davis, J. C. Smith, E. A. Rittenhouse, D. G. Hall, P. B. Mansfield, S. R. Mathisen, Y. Usui, et al. Healing basis and surgical techniques for complete revascularization of the left ventricle using only the internal mammary arteries. *The Annals of Thoracic Surgery*, 42(4):449–465, 1986.

[232] L. Schwartz, K. E. Kip, R. L. Frye, E. L. Alderman, H. V. Schaff, and K. M. Detre. Coronary bypass graft patency in patients with diabetes in the Bypass Angioplasty Revascularization Investigation (BARI). *Circulation*, 106(21):2652–2658, 2002.

[233] T. W. Sederberg and S. R. Parry. Free-form deformation of solid geometric models. *SIGGRAPH Computer Graphics*, 20:151–160, 1986.

[234] P. Sen, J. Daulatram, S. Kinare, T. Udwadia, and G. Parulkar. Further studies in multiple transmyocardial acupuncture as a method of myocardial revascularization. *Surgery*, 64(5):861–870, 1968.

[235] P. Sergeant, E. Lesaffre, W. Flameng, and R. Suy. Internal mammary artery: methods of use and their effect on survival after coronary bypass surgery. *European Journal of Cardio-Thoracic Surgery*, 4(2):72–78, 1990.

[236] P. Serruys, F. Unger, B. Van Hout, M. van den Brand, L. van Herwerden, G. Van Es, J. Bonnier, R. Simon, J. Cremer, A. Colombo, et al. The ARTS study (Arterial Revascularization Therapies Study). In *Seminars in interventional cardiology: SIIC*, volume 4, pages 209–219, 1999.

[237] W. H. Sewell. Improved coronary vein graft patency rates with side-to-side anastomoses. *The Annals of Thoracic Surgery*, 17(6):538–544, 1974.

[238] S. Sherwin and D. Doorly. Flow dynamics within model distal arterial bypass grafts. *Advances in Fluid Mechanics*, 34:327–374, 2003.

[239] S. J. Sherwin, O. Shah, D. J. Doorly, J. Peiro, Y. Papaharilaou, N. Watkins, C. G. Caro, and C. L. Dumoulin. The influence of out-of-plane geometry on the flow within a distal end-to-side anastomosis. *Journal of Biomechanical Engineering*, 122(1):86–95, 1999.

[240] T. W. Sheu and H. Y. Chen. A transient analysis of incompressible fluid flow in vessels with moving boundaries. *International Journal of Numerical Methods for Heat & Fluid Flow*, 9(8):833–846, 1999.

[241] H. Shima, K. Ohno, K. Michi, K. Egawa, and R. Takiguchi. An anatomical study on the forearm vascular system. *Journal of Cranio-Maxillofacial Surgery*, 24(5):293–299, 1996.

[242] J. R. Singler. New POD error expressions, error bounds, and asymptotic results for reduced order models of parabolic PDEs. *SIAM Journal on Numerical Analysis*, 52(2):852–876, 2014.

[243] S. Sirisup and G. E. Karniadakis. Stability and accuracy of periodic flow solutions obtained by a POD-penalty method. *Physica D: Nonlinear Phenomena*, 202(3–4):218–237, 2005.

[244] L. Sirovich. Turbulence and the dynamics of coherent structures. *Quarterly of applied mathematics*, 45:561–590, 1987.

[245] S. Smith and J. Geer. Morphology of saphenous vein-coronary artery bypass grafts: seven to 116 months after surgery. *Archives of pathology & laboratory medicine*, 107(1):13–18, 1983.

[246] C. Smuclovisky. *Coronary Artery CTA. A Case-Based Atlas.* Springer, 2010.

[247] I. J. Sobey. On flow through furrowed channels. Part 1. Calculated flow patterns. *Journal of Fluid Mechanics*, 96(01):1–26, 1980.

[248] F. Sones Jr and E. K. Shirey. Cine coronary arteriography. *Modern concepts of cardiovascular disease*, 31:735–738, 1962.

[249] N.-H. Staalsen, M. Ulrich, J. Winther, E. M. Pedersen, T. How, and H. Nygaard. The anastomosis angle does change the flow fields at vascular end-to-side anastomoses in vivo. *Journal of Vascular Surgery*, 21(3):460–471, 1995.

[250] K. Stephanoff, I. J. Sobey, and B. Bellhouse. On flow through furrowed channels. Part 2. Observed flow patterns. *Journal of Fluid Mechanics*, 96(01):27–32, 1980.

[251] A. Swillens, M. De Witte, H. Nordgaard, L. Løvstakken, D. Van Loo, B. Trachet, J. Vierendeels, and P. Segers. Effect of the degree of LAD stenosis on "competitive flow" and flow field characteristics in LIMA-to-LAD bypass surgery. *Medical & Biological Engineering & Computing*, 50(8):839–849, 2012.

[252] Y. Takami and H. Ina. Effects of skeletonization on intraoperative flow and anastomosis diameter of internal thoracic arteries in coronary artery bypass grafting. *The Annals of Thoracic Surgery*, 73(5):1441–1445, 2002.

[253] J. Tatoulis, B. F. Buxton, and J. A. Fuller. Patencies of 2,127 arterial to coronary conduits over 15 years. *The Annals of Thoracic Surgery*, 77(1):93–101, 2004.

[254] C. Taylor and M. Draney. Experimental and computational methods in cardiovascular fluid mechanics. *Annual Review of Fluid Mechanics*, 36:197–231, 2004.

[255] A. J. Tector, S. Amundsen, T. M. Schmahl, D. C. Kress, and M. Peter. Total revascularization with T grafts. *The Annals of Thoracic Surgery*, 57(1):33–39, 1994.

[256] A. Theodorakakos, M. Gavaises, A. Andriotis, A. Zifan, P. Liatsis, I. Pantos, E. P. Efstathopoulos, and D. Katritsis. Simulation of cardiac motion on non-Newtonian, pulsating flow development in the human left anterior descending coronary artery. *Physics in Medicine and Biology*, 53(18):4875–4892, 2008.

[257] R. Torii, J. Keegan, N. B. Wood, A. W. Dowsey, A. D. Hughes, G.-Z. Yang, D. N. Firmin, S. A. Mcg Thom, and X. Y. Xu. The effect of dynamic vessel motion on haemodynamic parameters in the right coronary artery: a combined MR and CFD study. *The British Journal of Radiology*, 82:S24–S32, 2009.

[258] R. Torii, N. B. Wood, N. Hadjiloizou, A. W. Dowsey, A. R. Wright, A. D. Hughes, J. Davies, D. P. Francis, J. Mayet, G.-Z. Yang, S. A. M. Thom, and X. Y. Xu. Fluid–structure interaction analysis of a patient-specific right coronary artery with physiological velocity and pressure waveforms. *Communications in Numerical Methods in Engineering*, 25(5):565–580, 2009.

[259] J. Towne, D. Schmitt, G. Seabrook, and D. Bandyk. The effect of vein diameter on patency of in situ grafts. *The Journal of cardiovascular surgery*, 32(2):192–196, 1991.

[260] Y. Utturkar, B. Zhang, and W. Shyy. Reduced-order description of fluid flow with moving boundaries by proper orthogonal decomposition. *International Journal of Heat and Fluid Flow*, 26(2):276–288, 2005.

[261] A. G. van der Giessen, H. C. Groen, P.-A. Doriot, P. J. de Feyter, A. F. van der Steen, F. N. van de Vosse, J. J. Wentzel, and F. J. Gijsen. The influence of boundary conditions on wall shear stress distribution in patients specific coronary trees. *Journal of Biomechanics*, 44(6):1089–1095, 2011.

[262] K. Veroy and A. Patera. Certified real-time solution of the parametrized steady incompressible Navier-Stokes equations: rigorous reduced-basis a posteriori error bounds. *International Journal for Numerical Methods in Fluids*, 47(8-9):773–788, 2005.

[263] J. Vimmr, A. Jonáová, and O. Bublík. Effects of three geometrical parameters on pulsatile blood flow in complete idealised coronary bypasses. *Computers & Fluids*, 69:147–171, 2012.

[264] J. Vimmr and A. Jonásová. Non-Newtonian effects of blood flow in complete coronary and femoral bypasses. *Mathematics and Computers in Simulation*, 80(6):1324–1336, 2010.

[265] J. Vimmr, A. Jonásová, and O. Bublík. Numerical analysis of non-Newtonian blood flow and wall shear stress in realistic single, double and triple aorto-coronary bypasses. *International Journal for Numerical Methods in Biomedical Engineering*, 29(10):1057–1081, 2013.

[266] A. Vineberg and G. Miller. Internal mammary coronary anastomosis in the surgical treatment of coronary artery insuffidency. *Canadian Medical Association Journal*, 64:204–210, 1951.

[267] Z. Vlodaver and J. E. Edwards. Pathologic changes in aortic-coronary arterial saphenous vein grafts. *Circulation*, 44(4):719–728, 1971.

[268] W. Wang, B. Jüttler, D. Zheng, and Y. Liu. Computation of rotation minimizing frames. *ACM Transactions on Graphics*, 27(1):2:1–2:18, 2008.

[269] Z. Wang, I. Akhtar, J. Borggaard, and T. Iliescu. Proper orthogonal decomposition closure models for turbulent flows: a numerical comparison. *Computer Methods in Applied Mechanics and Engineering*, 237–240:10–26, 2012.

[270] S. L. Waters, J. Alastruey, D. A. Beard, P. H. Bovendeerd, P. F. Davies, G. Jayaraman, O. E. Jensen, J. Lee, K. H. Parker, A. S. Popel, T. W. Secomb, M. Siebes, S. J. Sherwin, R. J. Shipley, N. P. Smith, and F. N. van de Vosse. Theoretical models for coronary vascular biomechanics: progress & challenges. *Progress in Biophysics and Molecular Biology*, 104(1–3):49–76, 2011.

[271] J. Weller, E. Lombardi, M. Bergmann, and A. Iollo. Numerical methods for low-order modeling of fluid flows based on POD. *International Journal for Numerical Methods in Fluids*, 63(2):249–268, 2010.

[272] J. Wen, T. Zheng, W. Jiang, X. Deng, and Y. Fan. A comparative study of helical-type and traditional-type artery bypass grafts: numerical simulation. *American Society of Artificial Internal Organs Journal*, 57(5):399–406, 2011.

[273] E. S. Weydahl and J. E. Moore Jr. Dynamic curvature strongly affects wall shear rates in a coronary artery bifurcation model. *Journal of Biomechanics*, 34(9):1189–1196, 2001.

[274] P. L. Whitlow, A. P. Dimas, T. M. Bashore, R. M. Califf, M. G. Bourassa, B. R. Chaitman, A. D. Rosen, K. E. Kip, M. L. Stadius, and E. L. Alderman. Relationship of extent of revascularization with angina at one year in the Bypass Angioplasty Revascularization Investigation (BARI). *Journal of the American College of Cardiology*, 34(6):1750–1759, 1999.

[275] D. Xiao, F. Fang, A. Buchan, C. Pain, I. Navon, J. Du, and G. Hu. Non-linear model reduction for the Navier-Stokes equations using the residual DEIM method. *Journal of Computational Physics*, 263:1–18, 2014.

[276] F. L. Xiong and C. K. Chong. A parametric numerical investigation on haemodynamics in distal coronary anastomoses. *Medical Engineering & Physics*, 30(3):311–320, 2008.

[277] M. Yadav, T. Palmerini, A. Caixeta, M. V. Madhavan, E. Sanidas, A. J. Kirtane, G. W. Stone, and P. Généreux. Prediction of coronary risk by SYNTAX and derived scores: synergy between percutaneous coronary intervention with taxus and cardiac surgery. *Journal of the American College of Cardiology*, 62(14):1219–1230, 2013.

[278] S.-H. Yoon and M.-S. Kim. Sweep-based freeform deformations. *Computer Graphics Forum*, 25(3):487–496, 2006.

[279] D. Zeng, Z. Ding, M. Friedman, and C. Ethier. Effects of cardiac motion on right coronary artery hemodynamics. *Annals of Biomedical Engineering*, 31(4):420–429, 2003.